X-RAY SCALING LAWS
FOR GALAXY CLUSTERS AND GROUPS

by

Donald J. Horner

Dissertation submitted to the Faculty of the Graduate School of the
University of Maryland, College Park in partial fulfillment
of the requirements for the degree of
Doctor of Philosophy
2001

Advisory Committee:

Professor Richard F. Mushotzky, Advisor
Professor Andrew S. Wilson, Chairman
Professor Sylvain Veilleux
Professor M. Coleman Miller
Professor Theodore Jacobson
Professor Craig L. Sarazin

ABSTRACT

Title of Dissertation: X-RAY SCALING LAWS
FOR GALAXY CLUSTERS AND GROUPS

Donald J. Horner, Doctor of Philosophy, 2001

Dissertation directed by: Professor Richard F. Mushotzky
Department of Astronomy

Scaling laws between galaxy cluster properties, such as the x-ray luminosity–temperature relation (L–T), the total mass-temperature relation (M–T), and velocity dispersion – temperature relation (σ–T) reflect the underlying physics in cluster formation and evolution. The differences between empirically determined and theoretically predicted scaling laws can give useful insights into physical processes happening in clusters. To determine these scaling laws, we have developed a data reduction pipeline for clusters observed by the ASCA x-ray satellite to create a sample of 273 clusters and groups with measured x-ray luminosities, average temperatures, and metal abundances. This is the largest such sample yet created and will form a baseline for future studies with improved instruments like Chandra and XMM-Newton.

We compare our ASCA cluster catalog to data in the literature to examine some of the biases and systematics that affect measurement of x-ray properties, and illuminate issues that affect the science results derived from such x-ray samples. We derive the L–T relationship over several orders of magnitude in luminosity, from rich clusters to groups. In combination with data from the literature, we examine the M-T relationship for a variety of mass estimators. We then examine the σ–T relationship and other correlations between the optical and x-ray properties of

galaxy clusters. In general, we find that these scaling laws are affected by non-gravitational processes which require additional physics, e.g., energy injection by supernovae. We also see little evolution of galaxy cluster properties with redshift to $z \sim 0.5$.

Preface

This thesis was written under the supervision of Dr. Richard Mushotzky at the Laboratory for High Energy Astrophysics (LHEA) at Goddard Space Flight Center (GSFC). It is divided into nine chapters and two appendices. The figures in Chapter 2, which reviews x-ray instrumentation and data analysis, are nearly all taken from Appendix E of the ASCA Technical Description. The remaining figures in the chapter were taken from the web site of the High Energy Astrophysics Science Archive Research Center (HEASARC). The initial version of the ASCA cluster catalog described in Chapter 3 was created by Dr. Keith Gendreau. Using this as a basis, I rewrote and improved the reduction and analysis routines to the present version described in Chapter 3. Except for parts of Chapter 7 which were previously published as Horner et al. (1999) in collaboration with Dr. Mushotzky and Dr. Caleb Scharf, the rest of the thesis is original work.

This thesis has also utilized a number of on-line resources, including data obtained from the High Energy Astrophysics Science Archive Research Center (HEASARC), the NASA/IPAC Extragalactic Database (NED), and NASA's Astrophysics Data System (ADS) Abstract Service.

DEDICATION

To Yanga Rolando Fernández-Ponte Martin, who sent me the most postcards.

ACKNOWLEDGEMENTS

I would like to thank my advisor, Richard Mushotzky, for his advice, ideas, and patience. I also need to thank my thesis committee and all the people who read earlier versions of this thesis. It was greatly improved by their comments. At Goddard, I would like to thank Keith Arnaud, Keith Gendreau, and Koji Mukai for answering my many questions about x-ray astronomy, data reduction, and analysis. I also have to thank the WARPS team for giving me the opportunity to become involved in the project, with a special thanks to Caleb Scharf who helped usher me through the early days of my research work. At the University of Maryland, I have to thank John Trasco and Mary Ann Phillips for helping me navigate through the dangerous water of the University and departmental administration.

On a more personal note, I would also like to thank my office mates past and present, especially Wayne Baumgartner. I also need to thank Craig Markwardt, not only for his IDL expertise, but also for his sarcasm and Tali Figueroa for also writing his thesis at the same time. It helped to have someone else around dealing with similar pressures. I also thank Steve Fantasia and Mike Arida for not throwing me out when I stopped by their offices for no good reason and for keeping me with candy and gum. A special thanks to everyone in T–Club for the entertainment and cookies over the years, although this is somewhat offset by the repeated mocking. And to Maggie Masetti, I'm sorry you got fired.

I would also like to thank fellow (former) graduate students Yan Fernandez and Laura Woodney for all the postcards they sent me (not to mention the love and support and all that stuff) and making grad school bearable. Even though they didn't send me as many postcards, I would like to thank Kip Kuntz, Leslie Looney, Arunav Kundu, Neil Nagar, Scott Miller and (most) of the rest of the grad students for their

friendship. I also thank everyone else who sent me a postcard, especially Barb Mattson, who is truly insane. I also have to mention Robert Greundl, Phil Esterle, and Jim Braatz for helping me get through the first few years of grad school.

TABLE OF CONTENTS

LIST OF TABLES

LIST OF FIGURES

Chapter 1

Introduction

What is a cluster of galaxies? In some sense, the answer depends on how you look at them. Optically, a cluster is what the name implies: a gravitationally bound aggregate of 100–1000 galaxies in a relatively small volume ($\sim$ 1 Mpc^3). In the richest clusters, $\approx$75% of the galaxies are ellipticals or S0s, and a large, dominant galaxy (a cD galaxy) is often found at the center. The galaxies orbit in the cluster with a velocity dispersion of $\approx$ 500–1400 km s^{-1}. In x-rays, a cluster appears as a large amount of hot ($T_{\rm x} \sim 10^7$–10^8 K) and luminous ($L_{\rm x} \sim 10^{43}$–10^{45} ergs s^{-1}) gas filling a volume similar to the galaxies. This is the Intracluster Medium (ICM). The gas emits x-rays through thermal bremsstrahlung radiation and atomic emission lines (mainly from iron) and can also be detected at radio wavelengths as a decrement in the Cosmic Microwave Background (CMB) via the Sunyaev–Zeldovich effect. However, clusters are mainly composed of dark matter that can only be detected through its gravitational influence. Clusters usually have a total mass of $\sim 10^{14}$ – 10^{16} M$_\odot$ with $\lesssim$30% of this due to the baryons (the stars plus the ICM). The mass of the gas is about 2–10 times that of the stars, meaning that the galaxies themselves are, in some ways, the least part of a cluster.

To first order, groups of galaxies are scaled down versions of clusters. They have a few to tens of members and velocity dispersions of a few hundred km s^{-1}. All except for perhaps the poorest are filled with hot gas (i.e., the Intragroup Medium or IGM) similar to clusters although the gas in groups has lower x-ray luminosities and temperatures. Since the mass spectrum of collapsed objects in the universe is continuous, no firm dividing line exists between clusters and groups. A working definition of a group is a system with a velocity dispersion of $\lesssim$ 500 km s^{-1} or luminosity $L_{\rm x} \lesssim 10^{43}$ ergs s^{-1}. However, different physical mechanisms can be important in groups. Since the velocity dispersions within the individual galaxies are comparable to the velocity dispersion of the galaxies in the group, processes like galaxy-galaxy mergers are expected to be more common while processes that are important in rich clusters, like ram pressure stripping of gas from galaxies, are

not expected to be important in groups. Other differences can be attributed to energetics. Because the total amount of gas is smaller in groups than in clusters, energy injection due to supernovae or AGN driven winds can significantly change the entropy of the gas or expel gas from the relatively shallow potential wells of groups.

The quantitative properties of large, representative samples of clusters and groups are important for understanding their formation and history. Even the most detailed studies of individual objects are of limited use unless they can be placed in the context of the overall population. Among the measurable optical properties of a cluster are its richness (a measure of the number of galaxies in the cluster), total optical light, and velocity dispersion. The measurable quantities from x-rays are the x-ray surface brightness distribution, luminosity, temperature, and the metal abundance of the gas. From these properties, some fundamental parameters of clusters can be calculated, such as the total mass, the mass in stars, and mass in gas. The correlations between these properties, in the form of *scaling laws*, and the evolution of these scaling laws with time (i.e., redshift) can be predicted from theories of structure formation and evolution. Therefore, empirically deriving these scaling laws constrains these theories.

We have created a semi-automated software pipeline to analyze all the clusters in the public archives of the ASCA x-ray satellite ($\approx$ 300 clusters and groups). With ASCA we can obtain accurate x-ray temperatures, metal abundances, and luminosities to create the largest homogeneously analyzed sample of clusters and groups of galaxies available. Using this sample, we evaluate scaling laws in ways that have not been achievable previously.

The rest of this chapter reviews the basic optical and x-ray properties of clusters that will be necessary for understanding the rest of this thesis. Similarly, Chapter 2 covers the basics of x-ray astronomy and data reduction. Chapter 3 describes the creation of our ASCA cluster catalog (ACC). In Chapter 4, the ACC is compared to previous catalogs of clusters and groups. Chapter 5 covers the relationship between x-ray luminosity and temperature. Chapter 6 discusses the metal abundance of clusters of galaxies and its relation to other properties. Chapter 7 covers the mass – temperature relationship. Chapter 8 discusses scaling laws between the optical and x-ray properties of clusters. Lastly, in Chapter 9 we summarize our results and draw some conclusions about clusters as a whole.

Throughout this thesis, we will use $H_0 = 50\,h_{50}$ km s^{-1} Mpc^{-1} (where $h_{50} = 1$ unless otherwise specified) and $q_0 = 0.5$ for any calculations requiring a definite cosmology. Quoted errors are 90% confidence levels unless otherwise stated. Note that for simplicity, we sometimes use the term cluster to refer to all the objects in the catalog, even groups.

1.1 Optical Observations

1.1.1 Catalogs

Historically, clusters were first defined as overdensities in the spatial distribution of galaxies. Since clustering occurs over a wide range of angular scales, the difference between rich clusters and groups was a matter of overdensity and scale length. Identifying clusters in optical images usually takes the form of specifying a threshold surface density enhancement within a particular linear or angular scale. This is equivalent to specifying the number of galaxies (i.e., the richness) within a particular radius. Because the number of galaxies increases with decreasing brightness and galaxies become fainter with increasing distance, an apparent magnitude range and limiting distance or redshift must be specified to make a statistically complete sample.

The most extensive and widely used catalog of rich clusters was created by Abell (1958) from plates taken for the Palomar Observatory Sky Survey (POSS). Abell surveyed the plates by eye identifying clusters which met certain criteria. Abell's criteria for inclusion in his sample were at least 50 galaxies within 3 h_{50}^{-1} Mpc (now known as the Abell radius) and within two magnitudes of the third brightest cluster member (m_3 to $m_3 + 2$). Abell also applied a redshift cut of $0.02 < z < 0.2$. Abell estimated many of these redshifts based on the magnitude of the tenth brightest cluster member. Abell's sample contained 1682 objects which met his criteria plus an additional 1030 clusters he identified but were not part of the statistical sample. Like most cluster catalogs, Abell also avoided regions within galactic latitude $|b| \leq 30^\circ$ due to the obscuration created by the Galactic plane. Abell et al. (1989) extended the Abell catalog to the southern sky survey creating a catalog of over 5000 clusters.

Another rich cluster catalog created from POSS plates was constructed by Zwicky et al. (1969) (the Catalogue of Galaxies and Clusters of Galaxies or CGCG). Zwicky's criteria were much less strict than Abell's, requiring at least 50 galaxies within three magnitudes of the brightest cluster member in an isopleth of twice the background galaxy density. Zwicky's catalog contains many more poor clusters (i.e., those with fewer galaxies) than Abell's catalog. Specific searches for poor clusters using the POSS were carried out by Morgan et al. (1975) and Albert et al. (1977) who compiled a catalog of 23 poor clusters (the MKW and AWM clusters) containing cD galaxies. White et al. (1999) applied an automated finding algorithm to the CGCG to construct a catalog of 732 poor clusters with at least 3 galaxies with photographic magnitudes brighter than 15.7 and a galaxy surface overdensity of $\geq 10^{4/3}$.

At even poorer richnesses, Hickson (1982) created an optical catalog of 100

groups (Hickson Compact Groups or HCGs) from the POSS. A Hickson group was required to have more than 4 galaxies within 3 magnitudes of the brightest, no other galaxies in this magnitude range within 3 radii of the group (the smallest circle that contains the centers of the galaxies), and a total surface brightness of ≤ 26.0 mag arcsec^{-2}. More diffuse or "loose" groups have also been identified around nearby galaxies (e.g., Mulchaey & Zabludoff 1998) but with no strict selection criteria.

At higher redshifts ($z > 0.2$) beyond the limit of sky survey plates, clusters have been identified in smaller numbers. The GHO catalog (Gunn et al. 1986) identified 418 possible clusters in deep photographic images. More recently, searches have been based on CCD imaging and automated, objective finding algorithms. Postman et al. (1996) used a matched filter algorithm to identify 79 clusters in two color Palomar 5m images by using positional and photometric data simultaneously. Work on improved cluster finding algorithms and searches continues to this day (e.g., Kepner et al. 1999; Olsen et al. 1999; Zaritsky et al. 1997).

The difficulty with optical surveys is that they are subject to selection effects due to projections of background and foreground galaxies on the cluster, which can lead to false identifications (e.g., Frenk et al. 1990). This is particularly problematic for poor clusters and those at high redshift where the contrast with the background galaxy surface density is low. This has motivated much of the work in developing computer based algorithms and in surveys in other wavelengths (e.g., x-rays).

1.1.2 Morphology and Spatial Distribution

The optical morphology of clusters is usually based on some measure of their regularity (i.e., a smooth, spherical appearance). It is assumed that that irregular looking clusters are the product of mergers that will eventually lead to regular clusters. The two most common systems for classifying clusters were created by Bautz & Morgan (1970) and Rood & Sastry (1971). The Bautz-Morgan (BM) system is based on the degree that clusters are dominated by a cD galaxy. Bautz-Morgan Type I clusters have a large, central cD galaxy. Type II clusters have a dominant galaxy between a cD and a normal elliptical in size. Type III clusters have no dominant galaxy at all. Intermediate classes are Type I-II and Type II-III. The Rood-Sastry (RS) system has six classes based on the distribution of the brightest galaxies in the cluster: cD, dominated by a central cD galaxy; B (binary), dominated by a pair of luminous galaxies; L (line), at least three of the brightest galaxies appear in a straight line; C (core), at least four of the ten brightest galaxies form a central core; F (flat), the brightest galaxies form a flattened distribution; and I (irregular), the distribution of the brightest galaxies is irregular. Regular clusters tend to be BM Type I or RS type cD or B.

The number density distribution of galaxies in a regular cluster is usually

parameterized by a King approximation for the particle distribution in a self-gravitating isothermal sphere (King 1972):

$$n(r) = n_0 \left[1 + \left(\frac{r}{r_c}\right)^2\right]^{-3/2}, \tag{1.1}$$

where n_0 is the central galaxy density, r is the distance from the cluster center, and r_c is the core radius, typically $\sim 250\, h_{50}^{-1}$ Mpc for a rich cluster.

For the King distribution the projected surface density of galaxies is:

$$\Sigma(b) = \Sigma_0 \left[1 + \left(\frac{b}{r_c}\right)^2\right]^{-1}, \tag{1.2}$$

where b is the projected radius and $\Sigma_0 = 2n_0 r_c$. This King distribution is only reasonable in the inner regions of clusters because it diverges at large radius. In the outer portions of cluster ($r \gg r_c$), the number density profile tends to $r^{-2.4}$ (Bahcall 1999).

1.1.3 Luminosity Function of Galaxies

The luminosity function (LF) of a cluster is the number density distribution of the luminosities of the galaxies. The differential $n(L)dL$ is the number of galaxies with luminosities in the range L to $L + dL$. The LF is usually characterized by the analytic function of Schechter (1976):

$$n(L)\, dL = N^* \left(L/L^*\right)^{-\alpha} \exp\left(-L/L^*\right) d(L/L^*), \tag{1.3}$$

where L^* is a characteristic luminosity typically corresponding to an absolute magnitude $M^*_{B_j} = -20.16$, and the slope α is typically around 1.2 (e.g., Girardi et al. 2000). The total optical luminosity of a cluster, L_{opt}, can be obtained by integrating Equation 1.3. For rich clusters, $L_{opt} \sim 10^{12} L_\odot$ (Bahcall 1999).

1.1.4 Velocity Distribution of Galaxies

The optical redshift of a cluster is determined from the mean radial velocity of the galaxies. For a regular, relaxed cluster, the velocity distribution tends to follow a Gaussian distribution. This distribution is conventionally characterized by the radial velocity dispersion of the galaxies, σ_r, defined as:

$$\sigma_r = \left\langle \left(v_r - \langle v_r \rangle\right)^2 \right\rangle^{1/2}, \tag{1.4}$$

where v_r represents the velocity of a cluster galaxy along the line of sight. For rich clusters, $\sigma_r \sim 750$ km s^{-1} but drops to ~ 250 km s^{-1} for poor clusters and groups Bahcall (1999).

The velocity dispersion reflects the depth of the potential well of clusters. Therefore, the total mass of a cluster can be estimated from the velocity dispersion via the virial theorem ($2U + T = 0$). This is called the "virial mass" of the cluster:

$$M_{vir} = \frac{3}{G}\,\sigma_r^2\,r_{vir}, \tag{1.5}$$

where r_{vir} is the virial radius of the system, the boundary separating the material which is close to hydrostatic equilibrium from the matter which is still infalling. Both σ_r and r_{vir} can be calculated from observations of the galaxy distribution if it is assumed that the velocity vectors of the galaxies and their positions are uncorrelated.

Equation 1.5 makes a number of additional assumptions. First, it assumes that the galaxies are distributed similarly to the total mass (i.e., mass follows light). Second, the velocity distribution is assumed to be isotropic. If velocity anisotropies exist or the assumption that mass follows light does not hold, the virial mass estimator may produce misleading results (The & White 1986; Merritt 1988). Also, if the entire system is not included in the observational sample, as is common for galaxy clusters, Equation 1.5 overestimates the mass since the external pressure from the matter outside the included region reduces the mass needed to bind the system (see Girardi et al. 1998b; Carlberg et al. 1997). The virial theorem must be modified to include the "surface term", $2U + T = 3PV$, where P is the external pressure and V is the cluster volume.

1.1.5 Galactic Content of Clusters

Rich, regular clusters of galaxies generally have a higher fraction of elliptical (E) and S0 galaxies than found in the field population of galaxies, about ∼70% of field galaxies are spirals compared to ∼20% in rich, regular clusters (Bahcall 1999). The fraction of ellipticals also increases towards the center of clusters. The fraction of spirals may be close to zero in the cores of some rich clusters. This is often referred to as the morphology–density relation (Dressler 1980). Two classes of ideas are used to explain this relationship. One is that the relationship is due to initial conditions at the formation of the cluster. In hierarchical models of structure formation, such as cold dark matter theories, different mass scales become nonlinear simultaneously, so that the initial conditions of galaxy formation in cluster and group environments may differ from those in the field. The other class of theories require some mechanisms to change spirals into ellipticals and S0s, such as ram pressure stripping, merging, or tidal stripping.

The brightest galaxies in clusters are the cD galaxies which are essentially very luminous elliptical galaxies embedded in extended, low surface brightness halos. They are found near the positional and velocity centers of clusters, presumably at the bottom of the cluster potential well. Theories to explain the formation of cD galaxies include galactic cannibalism and deposition of cool gas from the ICM.

1.2 X-ray Observations

In 1966, x-ray emission was first detected from an extra-galactic object, M87 in the Virgo cluster (Byram et al. 1966; Bradt et al. 1967). Later observations found emission in the direction of the Coma and Perseus clusters, suggesting that clusters might generally be x-ray sources. The all sky survey conducted by the *Uhuru* satellite (Giacconi et al. 1972) indicated that many nearby clusters were bright x-ray sources. It also established that cluster x-ray emission was spatially extended on scales comparable to the galaxy distribution, and had x-ray luminosities 10^{43}–10^{45} erg s^{-1} with no temporal variability (Kellogg et al. 1972; Forman et al. 1972). Several mechanisms for the source of the x-ray emission were proposed, but the detection of iron-line emission in the spectra of the Virgo, Perseus, and Coma clusters (Mitchell et al. 1976; Serlemitsos et al. 1977) provided solid evidence for a thermal origin.

The presence of x-ray emission requires that clusters be filled with hot ($\sim 10^8$ K and therefore nearly completely ionized), low density ($\sim 10^{-3}$ cm^{-3}) gas with a total mass comparable to or greater than the mass of stars in galaxies. The gas is thought to be primordial in origin. It has fallen into the potential well of the cluster and heated by adiabatic compression. Since the iron abundance of the gas is nearly solar and the only known source of iron is nuclear reactions in stars, the gas must have been enriched by a substantial amount of material ejected from the stars and galaxies within the cluster. Therefore, the physics and history of the gas in clusters is not necessarily simple (i.e., driven solely by gravitational processes).

1.2.1 Catalogs

Most clusters observed in x-rays were initially detected in optical catalogs like Abell's. In principle, x-ray surveys for clusters have the advantage of being relatively free of the projections effects which plague optical catalogs. The detection of x-ray emission represents direct evidence of a deep gravitational well within which the hot gas is trapped.

X-ray searches for clusters generally fall into two classes: wide area, but shallow surveys that are limited to low redshifts or deep surveys that cover only a small portion of the sky. Surveys of the first type are now usually based on the ROSAT

All Sky Survey (RASS). Examples are the Northern ROSAT All-Sky Galaxy Cluster Survey (NORAS; Böhringer et al. 2000), the ROSAT Brightest Cluster Sample (BCS; Ebeling et al. 1998), the RASS1 survey (De Grandi et al. 1999a) and the ROSAT-ESO Flux-Limited X-ray Survey (REFLEX; Collins et al. 2000), although the last authors have not yet published their catalog. These surveys cover nearly the whole sky (at least the northern or southern hemispheres excluding the Galactic plane) and contain several hundred clusters (as opposed to about two thousand in Abell's original catalog) to $z \sim 0.3$. Deeper surveys are based on serendipitous detections of clusters in targeted observations. The prototype is the Einstein Observatory Extended Medium-Sensitivity Survey (EMSS; Gioia et al. 1990) which found about 100 clusters in the field around sources observed by the Einstein satellite. More modern surveys are based on serendipitous ROSAT detections. Examples are the CfA 160 deg^2 Survey (Vikhlinin et al. 1998) and SHARC (Romer et al. 2000), which have published catalogs. Other surveys of this type, WARPS (Scharf et al. 1997) and RDCS (Rosati et al. 1998) have not yet published catalogs.

All of these surveys still rely on optical imaging of x-ray candidates to confirm the cluster identity. The spatial resolution of x-ray instruments has not been good enough to distinguish an extended source, like a cluster, from blends of close point sources. Even then the extended cluster emission may still be contaminated by unresolved point sources (e.g., Stanford et al. 2001). Optical spectroscopic follow up is also required to measure the redshift of the cluster. These surveys can usually measure only the x-ray extent and flux of a cluster since the detections have low signal-to-noise ratios. Obtaining spectra requires deeper follow up x-ray observations.

1.2.2 The X-ray Spectrum from Hot Plasma

Much of our information about galaxy clusters comes from analysis of the x-ray spectra of the ICM. Since the ICM is an optically thin hot plasma (i.e., $kT_x \gtrsim 0.2$ keV), it radiates predominately in the x-ray regime via thermal bremsstrahlung. The emissivity at energy E for a gas at T_x is given by:

$$\epsilon_E = \frac{2^5 \pi e^6}{3 m_e c^3} \left(\frac{2\pi}{3 m_e k} \right)^{1/2} \sum_i Z_i^2 n_e n_i \overline{g_{ff}} T_x^{-1/2} \exp\left(-E/kT_x\right) \tag{1.6}$$

where Z_i and n_i are the charge and number density for ion i, n_e is the electron density, and g_{ff} is the Gaunt factor (of order unity), a slowly varying function of temperature and energy (Sarazin 1988).

In addition to the continuum emission, atomic emission lines are also important. For hotter clusters ($T_x \gtrsim 5$ keV), emission is primarily due to K-shell transitions from H/He-like iron because other elements are completely ionized. At lower

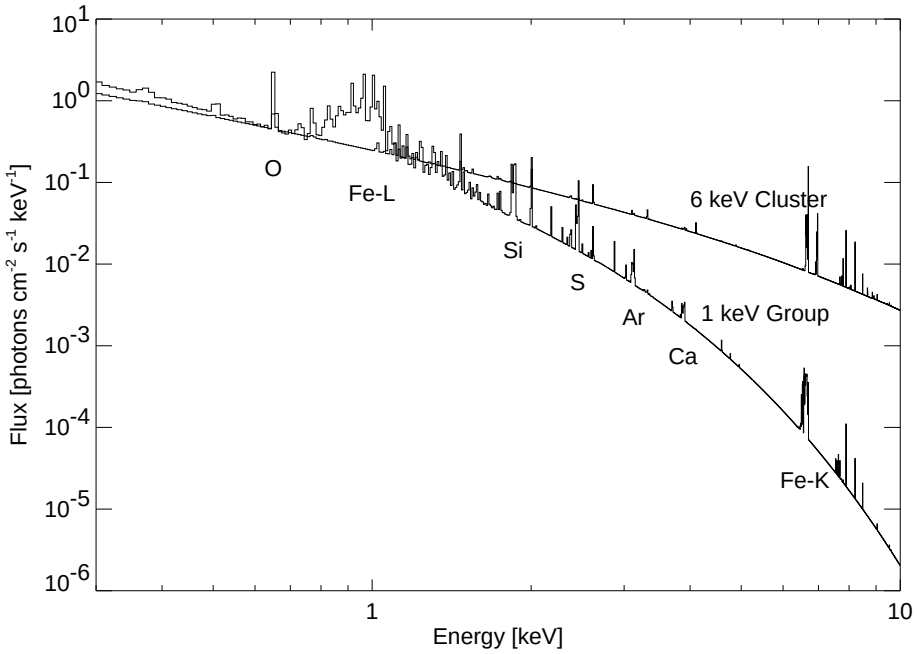

Figure 1.1: Comparison of spectra generated using the MEKAL model for a 6 keV cluster and 1 keV group at redshift zero and metal abundance 0.3 $Z_{\odot}$.

temperatures, K shell lines from other elements, such as O, Si, and S, enter the spectrum. Lower ionization states of iron also add numerous L-shell lines at $\sim$1 keV to the spectrum. The emissivity of the lines at low temperatures can be comparable to the continuum emission. Figure 1.1 shows the predicted spectra for a group at 1 keV and a cluster at 6 keV. At lower temperatures, strong K-lines of many elements are evident as is the Fe-L complex and a steep decline in continuum emission at higher energies. At higher temperatures, the continuum is flatter and the only strong lines are due to Fe-K.

The metal abundance and temperature of the gas can be determined by comparing the spectra to calculated plasma emission codes. However, the treatment of the Fe-L complex differs significantly among such codes. The two most often used are the Raymond-Smith code (Raymond & Smith 1977) and MEKAL code (Mewe et al. 1995). Unfortunately, recent results suggest that these codes may all fall short in comprehensively treating low temperature plasmas.

The spectral lines also provide a way to measure the redshift of the cluster independent of the galaxies. However, the signal-to-noise, energy resolution, and energy range of x-ray instruments has made this difficult (e.g., for ASCA) or im-

possible (e.g., for ROSAT), but it should become routine with Chandra and XMM.

1.2.3 Spatial Distribution of the Gas

The surface brightness of the ICM is usually assumed to follow a modified version of the King profile, called a "β-profile":

$$I(b) = I_0 \left[1 + \left(\frac{b}{r_c}\right)^2\right]^{-3\beta+1/2} \tag{1.7}$$

where b is the projected radius, r_c is the core radius, I_0 is the central density, and β is the asymptotic slope, usually $\sim 2/3$ for clusters.

Assuming the gas is isothermal, the gas density is then (Cavaliere & Fusco-Femiano 1976):

$$\rho(r) = \rho_0 \left[1 + \left(\frac{r}{r_c}\right)^2\right]^{-3\beta/2}, \tag{1.8}$$

which can be integrated to measure M_{gas}, the mass of the gas in the ICM.

Note that Equation 1.8 and Equation 1.1 imply that:

$$\rho_{gas}(r) \propto \rho_{gal}(r)^{\beta}. \tag{1.9}$$

Thus, the parameter β is a measure of the ratio of the scale heights of the gas and galaxies.

The bolometric x-ray luminosity of a cluster depends on the density as:

$$L_{\rm bol} = \int \rho_{gas}^2(r)\Lambda(T_{\rm x}(r))\, dV \tag{1.10}$$

where $\Lambda(T_{\rm x})$ is the radiative cooling function ($\propto {T_{\rm x}}^{1/2}$ for thermal bremsstrahlung).

1.2.4 Mass Estimates

X-ray mass estimates are based on the assumptions that the ICM is in hydrostatic equilibrium and supported solely by thermal pressure. With the further assumption of spherical symmetry, the gas density, temperature, and pressure are related to the mass by:

$$\frac{dP_g}{dr} = \rho_g \frac{GM(<r)}{r^2} \tag{1.11}$$

$$P_g = \frac{\rho_g k T_x}{\mu m_p}, \tag{1.12}$$

where k is Boltzmann's constant, and $\mu m_{\rm p}$ is the mean molecular weight of the gas. The enclosed mass at a radius, r, is then:

$$M(< r) = -\frac{kT_{\rm x}(r)}{G\mu m_{\rm p}} r \left[\frac{d\ log\ \rho_g(r)}{d\ log\ r} + \frac{d\ log\ T_{\rm x}(r)}{d\ log\ r} \right], \tag{1.13}$$

which depends on both the gas density and temperature profiles.

Historically, x-ray detectors have had either good spatial or good spectral resolution but not both. Measuring the actual temperature profiles of clusters has really only become practical with the advent of ASCA and its ability to obtain spatially resolved spectra. However, estimating the temperature profile is complicated by the spatial and energy dependence of the ASCA PSF (see Chapter 2). Markevitch et al. (1998) found strongly decreasing temperature profiles in many clusters using one technique while White (2000) found flat temperature profiles using the same data but a different method. The difficulty of measuring the temperature profiles means that far larger samples of clusters exist for which only the average x-ray temperature and isothermal mass estimates are available.

Therefore, the most often used x-ray mass estimator has been the isothermal β-model which assumes that the gas is isothermal and that the gas density follows Equation 1.8. Under these assumptions, Equation 1.13 then becomes:

$$M(< r) = 1.13 \times 10^{14} \beta \left(\frac{T_{\rm x}}{\rm keV} \right) \left(\frac{r}{\rm Mpc} \right) \frac{(r/r_{\rm c})^2}{1 + (r/r_{\rm c})^2} M_{\odot} \tag{1.14}$$

assuming $\mu = 0.59$.

Cluster masses can also be estimated via gravitational lensing of background galaxies as their light passes through the potential well of the cluster. In general, lensing and x-ray mass estimates agree fairly well (Allen 1998). There have been discrepancies between x-ray and lensing mass estimates measured in the central parts of the clusters, but as techniques and instrumentation have improved, these discrepancies have become less of an issue. For example, Arabadjis et al. (2001) using recent Chandra observation of EMMS 1358+6245 find good agreement between the mass profiles from x-ray and weak lensing mass estimates although the strong lensing estimate is still higher. The comparison of optical virial masses (as defined in Section 1.1.4) to x-ray masses will be examined in Chapter 7.

1.2.5 Cooling Flows

The basic idea behind cooling flows is simple. The radiative cooling time of a gas which emits x-rays is roughly $t_{cool} \propto {T_{\rm x}}^{1/2}/\rho_{gas}$. For the relatively dense parts of the ICM near the center of clusters, this is much less than the age of the system, i.e., $\sim H_0^{-1}$. Therefore, within the cooling radius, r_{cool}, a subsonic inflow

towards the center will develop as the gas cools and the pressure drops. The mass deposition rate, $\dot{M}$, can be estimated from its luminosity within r_{cool} assuming that it is all due to radiation of thermal energy plus the work done on the gas (PdV), $\dot{M} \propto L_{cool}/T_x$. Cooling flow clusters typically have deposition rates of 50–100 $M_\odot$ yr^{-1}. See Fabian (1994) for a comprehensive review of cooling flows.

Cooling flows should be stable and long lived, although possibly disturbed by major mergers. Observationally, cooling flows are characterized by a strong peak in the center of the surface brightness profile above a fit to the β-model made to the outer parts of the cluster. Spectral evidence also suggests that cooler gas resides in the central parts of clusters. X-ray observations suggest that 70%-90% of clusters may harbor cooling flows (Peres et al. 1998). However, where all the gas goes once it has cooled is unclear, and little evidence is seen for accumulated mass at other wavelengths.

Chapter 2

X-ray Instrumentation and Data Analysis

In this chapter, we review the basics of x-ray instrumentation and data analysis that will be necessary for understanding the discussion in later chapters. We will concentrate mainly on the ASCA satellite which is the main source of data used in this thesis. Several other missions will also be briefly reviewed.

2.1 The ASCA Satellite

The Advanced Satellite for Cosmology and Astrophysics (ASCA) was developed by Japan's Institute of Space and Astronautical Science (ISAS) as a Japanese-US collaboration (Tanaka et al. 1994). Launched in February 1993, ASCA operated until July 2000 when attitude control was lost due to a large solar flare. It reentered Earth's atmosphere and burned up in March 2001.

Figure 2.1 shows the in-orbit configuration of ASCA. ASCA has four identical, co-aligned grazing incidence x-ray telescopes (XRTs) each equipped with an imaging spectrometer detector. The four detectors operate simultaneously, increasing the total effective area and adding the benefit of consistency checks between the instruments. Two of the detectors are Solid-state Imaging Spectrometers (SIS0 and SIS1) each of which consists of four CCD chips arranged in a square with a total field of view of approximately $22' \times 22'$. The other two detectors are the Gas Imaging Spectrometers (GIS2 and GIS3) which are gas scintillation proportional counters with a circular field of view of approximately $40'$ diameter. The SIS has up to four times better energy resolution than the GIS. The nominal energy range of the detectors is 0.5–10 keV although the GIS is practically insensitive below ~ 1 keV and accumulated radiation damage to the SIS CCDs limited their usefulness to 0.8 keV or higher later in the mission.

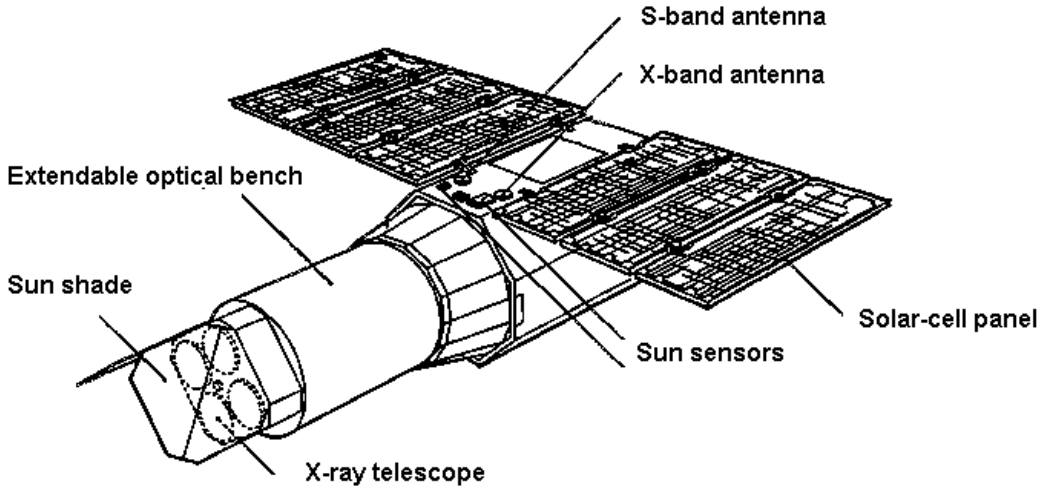

Figure 2.1: Diagram of the ASCA satellite.

2.1.1 The X-ray Telescope

The reflection of x-rays requires small grazing angles ($\lesssim 0.5^\circ$ for a 7 keV photon); otherwise, they will be absorbed by the mirror or not focused at all. Focusing off-axis x-rays also requires at least two reflections.

While conventional x-ray mirrors consists of a pair of hyperbolic and parabolic surfaces, the XRTs on ASCA are based on a nested foil design (Serlemitsos et al. 1995) that allowed them to be lightweight enough to launch four of them on ASCA. Each XRT consists of two sets of 120 foils (one set for each reflection) which are arranged concentrically to occupy a large fraction ($\sim 50\%$) of the geometric area of the aperture. The nesting lets the foils be nearly parallel to the mirror axis and still allows for two reflections. The effective focal length of the mirrors is 3.5m and the plate scale $\sim 1'/\mathrm{mm}$.

The foils are made of aluminum coated with acrylic and then with gold to improve reflectivity. Since the foils cannot be polished like other mirrors, the process introduces a small scale roughness. With alignment errors and non-perfect shape, the half power diameter is $3'$ for point sources, nearly independent of photon energy. In comparison, the German-US-UK ROSAT satellite, which uses conventional mirrors, has a half power diameter of $15''$, but the ROSAT XRT can only focus photons with energy $\lesssim 2.4$ keV. Although it has now been superseded by Chandra and XMM, ASCA's resolution was better and its collecting area larger than any previous mission at energies greater than 4 keV.

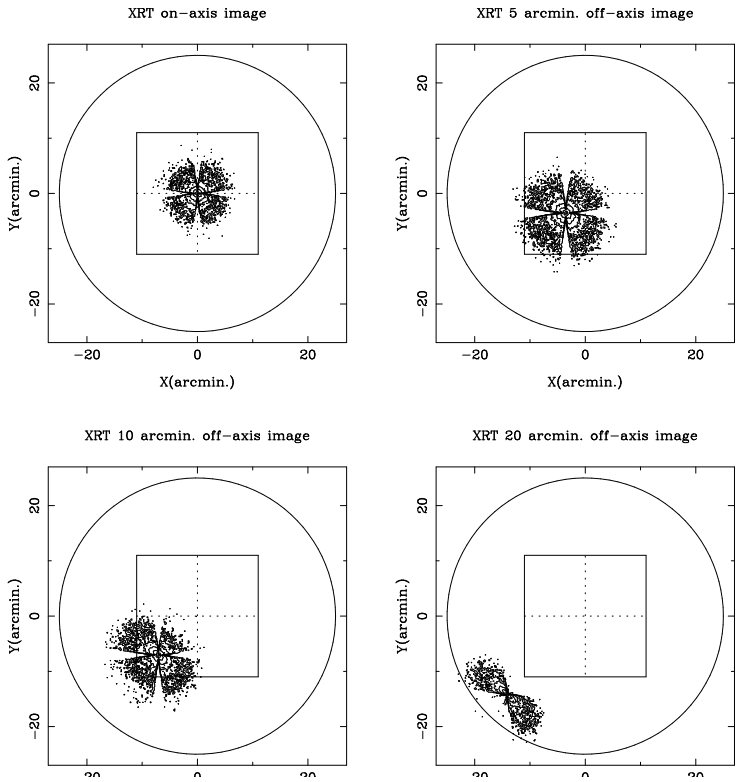

Figure 2.2: The dependence of the XRT PSF derived from ray-tracing calculations for on-axis and three off-axis angles (5′, 10′, and 20′). The circle indicates the GIS field of view. The solid square is the SIS field of view.

Figure 2.2 shows an image of the on-axis and off-axis point spread function (PSF) of ASCA. The cross shape of the PSF is due to the mirror supports (arranged in quadrants). To first order, the off-axis PSF is broadened because the grazing angle is increased. The PSF is also distorted by vignetting (shadowing by mirror foils and supports that reduces the projected area of the mirrors). Small scale surface roughness adds an energy dependent tail increasing the amount of flux scattered beyond 6′ by 8% at 1.5 keV and 17% at 8 keV.

2.1.2 The SIS

Each SIS (SIS0 and SIS1) consists of four 422×420 pixel Charge Coupled Device (CCD) chips arranged in a square (see Figure 2.2) with a field-of-view of $\approx 22'$ with gaps of $\approx 30''$ between chips. Each chip is composed of substrate of silicon. An electric field is applied across part of the substrate forming a region called the

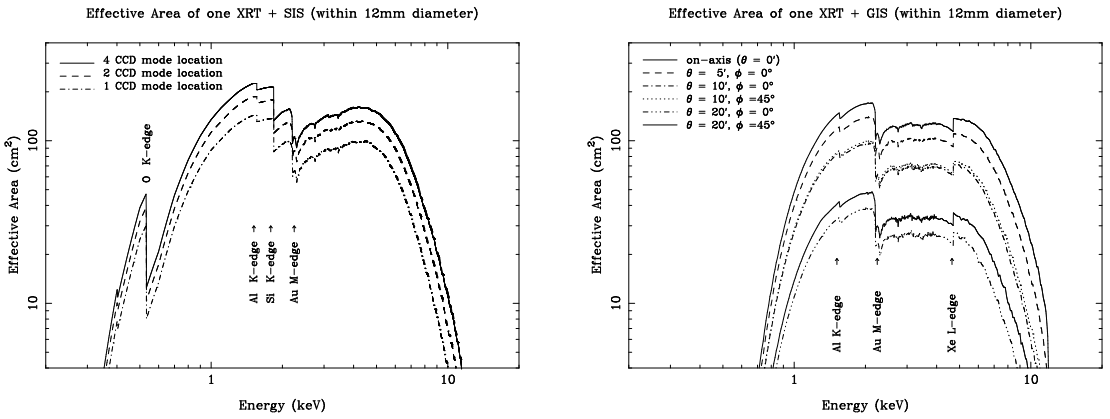

Figure 2.3: Left: The effective area of a single SIS and XRT combined for three off-axis angles. Right: The effective area of a single GIS and XRT for five off-axis angles.

depletion layer. Below this is the base layer, composed of the same material, but with no electric field. An ionizing photon absorbed in the depletion layer creates one electron per 3.65 eV of energy. The electron cloud is forced by the electric field into a potential well between the base layer and the depletion layer. The electrons are transferred from one potential well to the next by pulsing electrodes located above each pixel and eventually read out by the pre-amplifier. The net charge is converted to a pulse height amplitude (PHA). The PHA is proportional to the energy of the photon corrected for charge transfer losses and excess cosmic ray hits.

After the CCD is read out, "events" are identified as pixels with PHA values above a given threshold. Each event is assigned a time, position, and the PHA values of the center and adjacent pixels (9 PHA values total). This is referred to as FAINT mode data. Each event is then assigned a grade based on the distribution of events in neighboring pixels. Events likely to be associated with non-x-ray events (e.g., particle events, light leaks) are rejected. The graded events are referred to as BRIGHT mode data. Using BRIGHT mode data requires less telemetry since the processing occurs on on-board the satellite but can produce errors in the zero level determination and other effects which must be incorporated into spectral responses. For the sources considered in this thesis, statistical errors dominate over such systematic errors.

The SIS can be operated with one, two, or four CCDs operating. Due to the effects of radiation damage on charge transfer efficiency, 1-CCD mode has been preferred since 1994 to reduce the spectral degradation. The damage to the chips has also degraded the quantum efficiency and resolution of the SIS instruments with time, complicating the analysis of SIS data and interpretation of the results.

SIS0 resolution has degraded somewhat more slowly than that of SIS1. The initial energy resolution of the SIS ($\Delta E/E$) was about 2% at 5.9 keV.

The effective area of the SIS is shown is Figure 2.3. Effective area is defined as the percentage of photons that reach the detector multiplied by the XRT geometric area as a function of energy.

2.1.3 The GIS

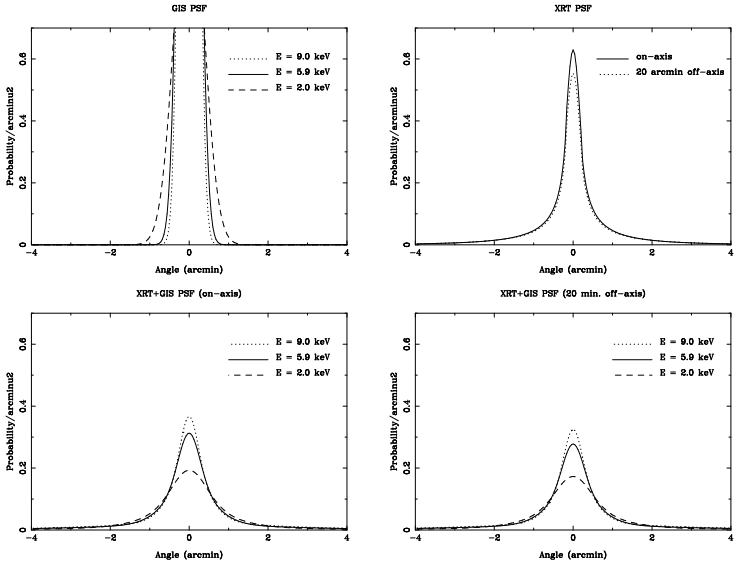

Figure 2.4: Upper-left: The GIS PSF for three different incident x-ray energies. Upper-right: The XRT PSF on-axis and 20′ off-axis. Lower-left: Convolution of the on-axis XRT and GIS PSFs. Lower-right: Convolution of the 20′ off-axis XRT and GIS PSFs.

A photon enters the GIS though a beryllium window held in place by a thin metal grid and ionizes xenon atoms creating an electron cloud in a "drift" region. Three meshes produce an electric field across the drift region with potentials of -8000 V, -7000 V, and 0 V. The electron cloud drifts slowly across the first region with potential of 1000 V, then accelerates across the 7000 V potential region (the scintillation region) exciting xenon atoms along the way. The xenon atoms emit ultra-violet (UV) photons which pass through a quartz window and are detected by position-sensitive phototube (PSPT). The x-ray photon position is determined by calculating the center of the scintillation photon distribution. The positional uncertainty is significant relative to the spatial resolution of the XRT and broadens the GIS PSF relative to the XRT PSF (and, hence, the SIS PSF). The PSF

approximates a Gaussian with a FWHM of $0.5\sqrt{5.9\,\mathrm{keV}/E}$ arcminutes, but has an additional "tail" above 4 keV because photons from L-shell xenon recombinations produce additional scintillation clouds that broaden the size of the primary cloud before it hits the PSPT. The spectral resolution of the GIS ($\Delta E/E$) is dominated by counting statistics and is about 8% at 5.9 keV (compared to 2% for the SIS, see Figure 2.5). The effective area of the GIS is shown in Figure 2.3.

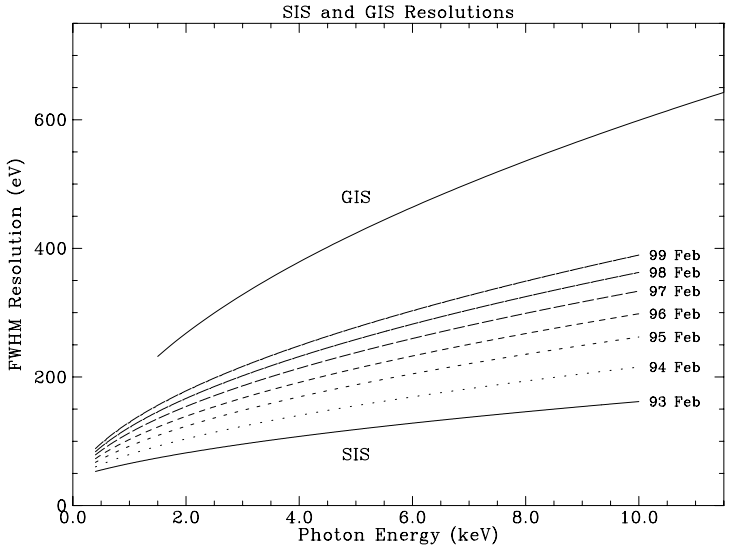

Figure 2.5: The energy resolution of the GIS and SIS. The estimated/extrapolated resolution of SIS1 in 1-CCD mode is plotted for at launch and 1, 2, 3, 4 , 5 and 6 years after launch.

2.1.4 Processing of ASCA data

The data telemetered from ASCA is placed in specific files for each instrument and telemetry bit rate. Data in the ASCA public archives is subjected to several standard processing steps which significantly improve the signal-to-noise ratio (SNR) for spatial, spectral, and temporal analysis. The outer rim of the GIS, which has a high particle background, is excluded as are events from the on-board calibration source, which is used only if the GIS gain determination is suspect. The PHA values are converted to pulse-height invariant (PI) values corrected for gain non-linearities and spatial dependencies. The GIS calibration is fairly stable with time and new calibration files released periodically. However, the calibration has to be recomputed for each observation for the SIS.

Times with high background rates are excluded as are times when ASCA is pointing within 5° of Earth, when ASCA is in the South Atlantic Anomaly (SSA), or when the source is not in the field-of view or the pointing deviates from the

nominal source position by $0.6'$. Events are also rejected if the cut off rigidity (COR) is less than 6 MeV/c. COR is a measure of the ability of the geomagnetic field to repel cosmic rays, defined as the minimum momentum required to reach the satellite from infinity.

2.2 Other X-ray Astrophysical Missions

Another x-ray satellite which will be mentioned repeatedly in this thesis is the Röntgensatellit (ROSAT), a German-US-UK collaboration launched in June 1990. ROSAT performed an all sky survey for its first six months of operation before beginning pointed operations, which then ended in February 1999. Figure 2.6 show a schematic of the ROSAT satellite. Unlike the foil design used in the ASCA XRT, ROSAT XRT used four fold nested Wolter Type I mirrors. These mirrors can be polished and give a half power radius of $5''$ on-axis as opposed to the $\sim 1.5'$ for the ASCA XRT. However, the energy range of the mirrors is limited to 0.1–2.4 keV. The two focal plane instruments on ROSAT are the High Resolution Imager (HRI) and the Position Sensitive Proportional Counter (PSPC). The HRI has no effective energy resolution but makes full use of the spatial resolution provided by the mirror. The PSPC is an imaging x-ray spectrometer similar to the ASCA GIS, and, like the GIS, significantly broadens the XRT PSF. The PSPC half power radius is $\sim 25''$ at 1 keV while the energy resolution about 40%.

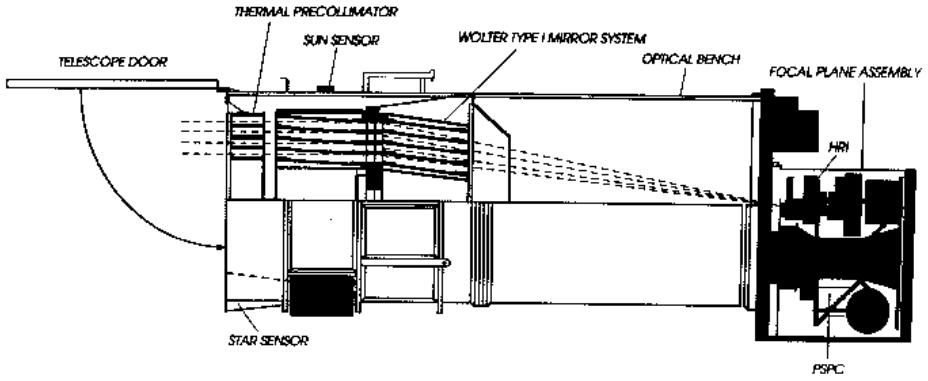

Figure 2.6: Diagram of ROSAT satellite.

The predecessor to ROSAT, the Einstein satellite, was launched in 1978 with a number of instruments on-board. The Einstein IPC was a position sensitive proportional counter with moderate spatial ($\sim 1'$) and poor spectral resolution

with an energy range of 0.4–4.0 keV. The Einstein MPC was a non-focal plane instrument that monitored the 1–20 keV X-ray flux of the source being observed simultaneously by the focal plane instrument. The MPC was a collimated (i.e., non-imaging) proportional counter filled with argon and carbon dioxide and had circular field of view of 1.5° and an energy resolution of 20% at 6 keV.

European Space Agency's X-ray Observatory, EXOSAT, was launched in 1983. The primary instrument of concern here is the Medium Energy (ME) Proportional Counter which consisted of an array of eight proportional counters with an energy resolution of about 20% at 6 keV. It was non-imaging with a $45'$ field of view.

BeppoSAX is a major program of the Italian Space Agency with participation of the Netherlands Agency for Aerospace Programs. It was launched on April 30 1996 and continues to operate at the present time. BeppoSAX is primarily a hard x-ray satellite. The BeppoSAX Low Energy Concentrator Spectrometer (LECS) has a energy range of 0.1–10 keV with an energy resolution of 9% and spatial resolution of $2'$ at 6.0 keV. The three Medium Energy Concentrator Spectrometer (MECS) cover an energy range of 1.3-10 keV and have an energy resolution of 8% at 6.0 keV.

2.3 The Basics of Spectral Fitting

The number of counts, C, observed in spectrum channel I for a source with flux $F(E)$ can be expressed:

$$C(I) = \int_0^\infty R(E,I)F(E)A(E)\,dE \approx \sum_i R(E_i,I)F(E_i)A(E_i)\Delta E_i \qquad (2.1)$$

where the sum is over the number of detector channels. $R(E,I)$ is the probability of observing a photon with energy E in channel I. Basically, it relates output pulse height to input photon energy. $A(E)$ contains the total effective area for the given extraction region. This includes various effects such as the effective area of the XRT as a function of energy and off-axis angle, transmission of the detector window, and quantum efficiency of the detector at a specified position.

$R(E,I)$ is independent of position on the detector. The integral of $R(E,I)$ over all the channels is normalized to the quantum efficiency of the detector at that energy. For analysis, this information is contained in the redistribution matrix file (RMF). For ASCA, the RMFs of both the GIS2 and GIS3 are identical. Therefore, the same RMF can be used for all GIS observations. In contrast, every SIS chip has a different RMF which has to be calculated for each observation due to the degradation of the CCDs.

The effective area information in $A(E)$ is contained in the ancillary response file (ARF). For ASCA, ARFs are more complicated to calculate than the RMFs since the effective area depends on position on the detector and source photons are spread out by the PSF. For extended sources, like clusters, the spatial extent of the source must also be taken into account. The proper way to do this is to use ray tracing assuming a spatial distribution of the source (i.e., the surface brightness profile from ROSAT observations of the cluster). However, for the clusters in this thesis, the spatial profile is not generally known, so another approach is used. We calculated a weighted-average effective area with the weighting factor being the number of events at each pixel position. No attempt is made to correct for the spatial response.

Ideally, Equation 2.1 would be inverted to recover F(E). However, the instrument spectral and spatial responses are not well enough known and the signal-to-noise is usually too low to make this feasible. Such inversions tend to be non-unique and sensitive to small changes in C(I). Therefore, a "forward-fitting" approach is generally used. A spectral model in terms of a few parameters is chosen, convolved with the instrument responses, and the parameters varied until the model fits the observed spectrum. The goodness of fit (whether the model is an adequate representation of the data) is judged using the χ^2-squared fit statistic:

$$\chi^2 = \sum \frac{(C(I) - C_p(I))^2}{\sigma(I)^2} \tag{2.2}$$

where C_p(I) is the predicted spectrum and σ(I) is the uncertainty in channel I, usually $\sim \sqrt{C(I)}$.

A fit is usually judged to be acceptable if $\chi^2/\nu \approx 1$, where ν is the number of degrees of freedom in the fit. The number of degrees of freedom is equal to the number of channels minus the number of parameters fit. This fit statistic is usually referred to as the "reduced" χ^2 value or χ^2_r. If $\chi^2_r \gg 1$, the model is not a good representation of the data. On the other hand, $\chi^2_r \ll 1$ usually indicates that the errors are overestimated. The range of values over which one can be confident the true parameters lie can be calculated, assuming the best fit value for the current observation is the true value of the parameter. The "confidence intervals" are computed by varying the parameters until χ^2 increases by a set amount $\Delta\chi^2$ above the best fit values. The 90% confidence limit for one parameter corresponds to $\Delta\chi^2 = 2.71$.

Chapter 3

The ASCA Cluster Catalog

3.1 Introduction

For this thesis, we will be mainly concerned with a few global x-ray properties of clusters: their luminosity, temperature, and metal abundance. For our investigation of scaling laws, we would like as large a sample of clusters as possible with these properties accurately measured as well as one that covers a wide range of masses, from clusters to groups. While such samples can be compiled by diligently searching through the literature (e.g., Xue & Wu 2000), they suffer from the heterogeneity introduced by using data from different missions, data analyzed with different techniques, and by the different goals of the authors of individual studies. A homogeneous sample can only be created by analyzing the data from scratch and applying the same analysis techniques to all the clusters. This approach is more time consuming and involved but is also well suited to x-ray cluster data since all the observations are (eventually) available in public archives. Some of these observations may also never be published without such an effort.

In the last decade, several samples of x-ray observed clusters have been published. Edge & Stewart (1991a,b) used a sample of 36 clusters with EXOSAT luminosities and temperatures (and metal abundances for a smaller number) to measure various optical and x-ray correlations, such as the velocity dispersion – temperature relation (σ–T) and x-ray luminosity – temperature relation ($L_{\rm x} - T_{\rm x}$). David et al. (1993) constructed a sample of 84 clusters observed with the Einstein MPC and added additional clusters from the literature to obtain a sample of 104 clusters. This sample was then used to study the $L_{\rm x} - T_{\rm x}$ relation and is still an often referenced source for cluster temperatures. More recently, White et al. (1997) published a deprojection analysis of 207 clusters observed with Einstein to study cooling flows, baryon fractions, and other clusters properties. White (2000) subsequently published a sample of 106 clusters observed by ASCA (using only the ASCA GIS data) attempting to constrain the temperature and metallicity profiles

of clusters.

To improve on these studies, we have begun a project at Goddard to compile and analyze the large number of cluster observations available in the ROSAT and ASCA public archives. Here we present the analysis of clusters in the ASCA public archives. ASCA gives us the ability to accurately measure temperatures, metal abundances, and luminosities for a large number of clusters which we can then use to probe x-ray scaling laws and cluster properties. This sample will be subsequently referred to as the ASCA Cluster Catalog (ACC) to distinguish it from other ASCA compiled samples of clusters.

Since the number of clusters observed by ASCA is large (several hundred), reducing the data and processing each individual observation by hand would be impractical. Therefore, we have written a number of scripts in the Practical Extraction and Report Language (PERL) to automate many procedures. These scripts tie together the x-ray analysis tools of the `FTOOLS 5.0.1` package and `XSPEC`, the spectral fitting program of the High Energy Astrophysics Science Archive Research Center (HEASARC). This also makes it easy to update the catalog when new observations enter the archive.

The ACC contains measured luminosities, average temperatures, and metal abundances for 273 clusters and groups, including as many low mass systems, i.e., poor clusters and groups, as possible instead of concentrating solely on rich clusters. This is the largest such sample yet created, has superior spectral data compared to previous samples, and will form a baseline for future studies with improved instruments like Chandra and XMM-Newton.

This chapter describes the creation of the ACC, reduction of the data, and a number of issues affecting the results. Additional information, including images and spectra for each cluster, is available on the World Wide Web[1].

3.2 Constructing the Cluster Sample

The first goal in creating the ACC was to find all the known clusters and groups that were observed by ASCA, either as a target or serendipitously. Therefore, we cross correlated all publicly available ASCA observations (as of January 22, 2001) in the HEASARC archive with the NASA/IPAC Extragalactic Database (NED). NED contains optical catalogs of clusters, like Abell's and Zwicky's, as well as x-ray catalogs like the EMSS. We also checked previous catalogs and compilations of clusters (David et al. 1993; Edge & Stewart 1991b; De Grandi et al. 1999a; Böhringer et al. 2000; Ebeling et al. 1998) and groups (Helsdon & Ponman 2000b; Davis et al. 1999; White et al. 1999) in the literature to look for misclassifications

[1] `http://lheawww.gsfc.nasa.gov/user/horner/asca`

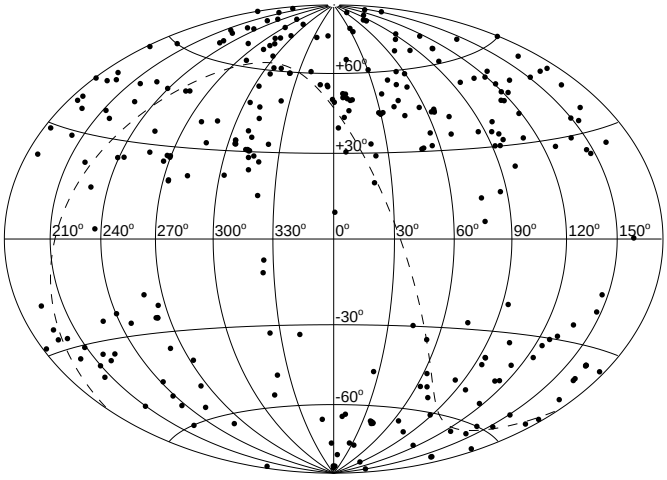

Figure 3.1: The distribution on the sky of the cluster sample in galactic longitude and latitude. The dashed line indicates the celestial equator.

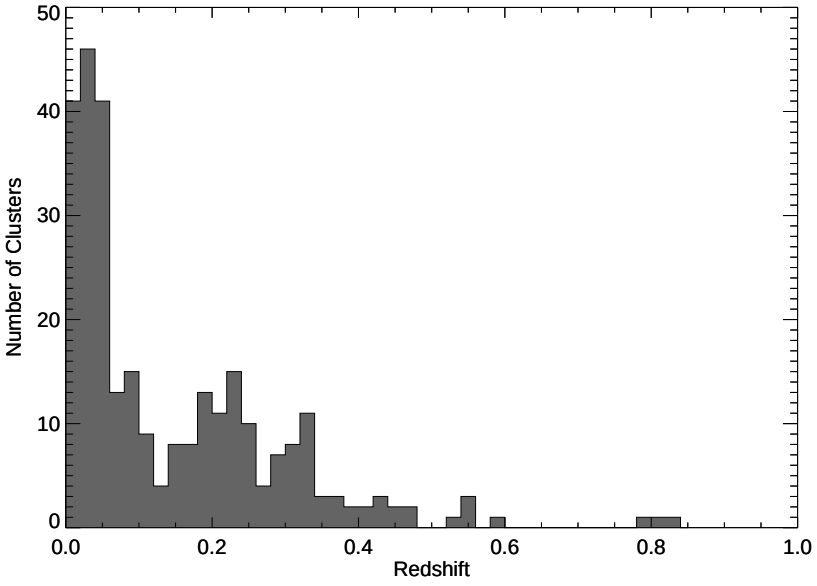

Figure 3.2: The redshift distribution of the cluster sample.

and incompleteness in NED. This added sources like Cygnus A which is classified as a galaxy pair in NED but is also a bright cluster. We limited the search to within $15'$ of the nominal GIS field center because the point spread function becomes very distorted further off axis and calibration uncertainties increase. We excluded the Coma, Virgo, and Perseus clusters from the sample since they are much larger than the field of view of ASCA and require different analysis techniques.

The preliminary cluster list included 434 clusters in 564 ASCA observations. We then pared this list down. Table A.1 in Appendix A.1 contains a list of 156 clusters in 222 ASCA observations that were removed from the sample for the following reasons: Since we are primarily interested in clusters with enough photons to obtain a spectrum, we examined the GIS and SIS images to screen out clusters that were not detected in a visual inspection of the field or detected only faintly. Many of these are distant clusters from the CfA 160 deg^2 survey of Vikhlinin et al. (1998) or the HST Medium Deep Survey (Ostrander et al. 1998) that were serendipitously in the GIS field of view. Observations of several well known and bright clusters were also removed from the sample because the cluster was too far off axis, causing much of the emission to go outside the GIS field-of-view. Usually, these observations were intentionally offset from these clusters, and the cluster was included in the ACC in other observations so we lose little by excluding the offset observations. We also screened out clusters that appeared as point sources in the SIS image, especially if they contained known AGN (e.g., 3C 215) since the AGN is likely to dominate the emission. Groups which seemed to be dominated by emission from a single elliptical galaxy were also excluded. A few sources were excluded for other reasons detailed in Appendix B. Images of all the ASCA fields containing the sources in Appendix A.1 are available at the WWW page.

We then split double clusters (e.g., ABELL 1750) into two separate components and consider them different clusters for the purposes of analysis. The final ACC sample contains a total of 273 different clusters in 337 ASCA observations (see Appendix A.2 for the list). Many clusters are known by several different names in the literature. We have tried to use the most common name (usually an Abell designation) but also one that is known by NED if possible. About 60% of the clusters are in the Abell catalog. Only about 20% of the clusters were first detected in x-ray catalogs, but these are the bulk of the sample at $z \gtrsim 0.2$. Only about 25% of the clusters in the sample could be considered poor clusters or groups, showing the observational bias towards richer systems.

Figure 3.1 shows the sky distribution of the sample. Only a few clusters fall in the zone of avoidance (13 at $|b| < 20^\circ$), and 60% are in the northern hemisphere. Figure 3.2 shows the distribution in redshift of the sample. We have 125 clusters at $z > 0.1$ and 41 at $z > 0.3$. From a search through the literature, we estimate that approximately 30% of these clusters have no previously reported ASCA results.

3.3 Extraction Region Selection

The first step in obtaining a spectrum for a cluster is to pick the area from which to take the photons. Our main goal in choosing the extraction region was to get as many cluster counts as possible while keeping a high signal-to-noise for the spectral fitting (i.e., not including a large amount of background photons). We chose the extraction regions based on an exposure corrected, combined GIS2 and GIS3 image. Reference sky coordinates from the literature were used as input to a centroid routine to determine the cluster center. A visual inspection of each field was used to mask out any other sources in the GIS field–of–view (a list of these sources is given in Appendix A.3), and a radial emission profile was constructed from this position. Note that this radial profile does not reflect the true cluster profile given the complicated PSF of the ASCA mirrors and the GIS detector. The extraction region was chosen to be the radius at which the radial profile reached 5σ above the background level. The background and the σ level were iteratively determined using a three sigma clipping algorithm. We set a minimum value of $6'$ on this extraction radius.

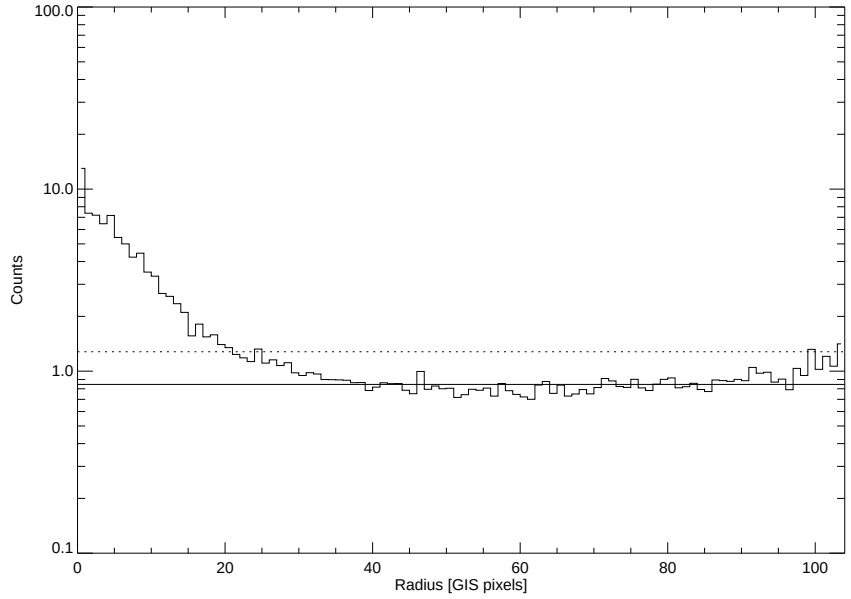

Figure 3.3: The GIS radial profile for Abell 483. The solid line is the background level while the dotted line is the 5σ level. One GIS pixel corresponds to about $0.25'$.

The SIS has a smaller PSF than the GIS, so the GIS derived extraction regions are too large for the SIS. However, given the gaps between chips and smaller field-

of-view of the SIS, determining the extraction region independently for the SIS data is difficult. Therefore, we used a dozen fields taken in 4-CCD mode to extract radial profiles and determine an extraction region for the SIS data as we did for the GIS. On average, the SIS extraction radius was 0.62 of the GIS radius with a 1σ scatter of 0.1 around this mean. Therefore, we used a conservative radius of 0.72 times the GIS radius to extract all the SIS data to ensure an extraction region with a similar signal–to–noise as the GIS for nearly all observations.

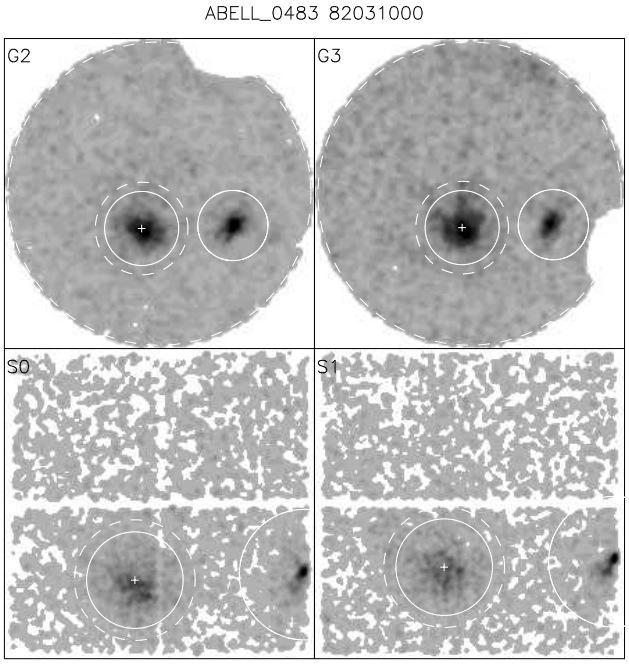

Figure 3.4: The detector images for each ASCA instrument for Abell 483. The cross marks the ASCA centroid while the solid circle denotes the region chosen for extraction. The background spectrum was extracted from rest of the field minus the region with the dashed circle (enclosing the cluster) and the region enclosing a nearby QSO.

All of the regions were then visually inspected. For a few clusters, mostly the double clusters, the regions were adjusted by hand to try to minimize contamination. Images showing the extraction region for each instrument (for each cluster and ASCA field) are available on the WWW page. As an example, the radial profile for Abell 483 is shown here in Figure 3.3 and the extracted regions in Figure 3.4.

During standard HEASARC processing, a transformation was applied to each photon to map its position on the detector to a position on the sky. Because the satellite drifts during the observations, converting between sky coordinates and

detector coordinates is not trivial. The procedure used above gives the cluster center in sky coordinates, i.e., right ascension and declination. The actual extraction of spectra should be done in detector coordinates, especially for the SIS where chip gaps need to be excluded. We converted the sky coordinates to detector coordinates by extracting a small region from the event files for photons near the sky coordinates. We then averaged the detector x and y values of these photons to get the appropriate center coordinates for the region file. We used empirically determined offsets between the detectors to convert the GIS2 position to detector positions appropriate for each instrument.

The centroid detector coordinates and the extraction radius (in detector pixels) were then put into a region file to be used by the extraction routine. Added to this were the regions excluded because of other sources in the field. Non-detector regions (e.g., the SIS chip gaps, the GIS calibration source) were also excluded. Otherwise, calculations requiring the region area, such as the background subtraction, would be incorrect.

3.4 Reduction of the GIS Data

Using the region files as described above, we extracted GIS events from the standard screened events files provided by the HEASARC using the latest GIS gain correction information as of April 10, 2001. Low bit rate data were excluded, and the high and medium bit rate events files combined. Spectra were extracted with `XSELECT` and grouped to a minimum of 25 counts per channel in order to use χ^2 statistics. The standard redistribution matrix files (RMFs) for the GIS provided by HEASARC were used (released March 6, 1995). A dead time correction was then applied to get the correct flux (this is only a small effect), and ancillary response files (ARFs) were generated.

Local backgrounds were extracted by masking out the cluster region (using a radius 1.25 $\times$ the extraction radius) and any other bright sources in the field. We also created background spectra at the cluster position using blank sky observations provided by HEASARC. Local backgrounds have the advantage of seeing a similar region of sky as the source under the same observing conditions. Blank sky backgrounds have the advantage of using the same detector region (since instrument performance often varies across the face of the detector) and a larger number of counts. In practice, we found little difference between the spectral fits using either type of background but have preferred the blank sky backgrounds since they have better signal-to-noise. The only exception is for clusters at low galactic latitudes ($|b| < 20^\circ$) where the background is higher and more variable. In these cases, we have used the local backgrounds if possible.

3.5 Reduction of the SIS Data

For the SIS reduction, we excluded the BRIGHT2 and low bit rate events and combined the rest of the standard screened events files. The spectrum channels were binned by 2 and then grouped to a minimum of 25 counts per channel. Due to the time evolution of the SIS response, RMFs were generated for each observation with the latest available calibration file released on March 30, 2001. If the cluster emission was spread over two or more chips, each chip was extracted separately and RMFs created for each chip because of their different responses. The RMFs were then combined weighting by the number of counts on each chip. The combined RMF was then used to generate an ARF for the total spectrum.

We extracted local backgrounds from source free areas of the chips, excluding an area of 1.25 times the extraction radius around the cluster. Since the SIS calibration has degraded with time, we used local backgrounds if the background spectrum had at least 500 counts. However, due to the smaller field of view of the SIS, especially in 1-CCD mode, nearly a quarter of the clusters had few or no counts that could be considered background (i.e., the cluster filled the SIS field of view). In these cases, we used blank sky background fields provided by the HEASARC that were taken at various times during ASCA's lifetime. We used the blank background matching the observation mode (1-CCD, 2-CCD, or 4-CCD) taken closest in time to the cluster observation.

3.6 Combining Spectrum Files

The ACC contains 57 clusters that were observed multiple times by ASCA. In addition to fitting the individual spectra, we also added together the spectra for each detector to increase the signal-to-noise. The HEASARC provided software tool `addascaspec` was used for this purpose. It runs several other `FTOOLS` to add the spectrum files with proper weights for the region sizes and exposure times. The resulting spectrum files can then be treated just like the individual observations.

3.7 Spectral Fitting

Using `XSPEC V11.0.1`, we fit the processed spectra to a single temperature MEKAL spectral model (see Section 1.2.2 and Mewe et al. 1995) over the energy range 0.8–10 keV for the GIS and 0.6–10 keV for the SIS. For data taken during and after 1998, a lower limit of 0.8 keV was used for the SIS data. Spectrum files were only included in the fit if they contained over 250 counts and all the spectra had to have at least a total of 1000 counts.

The spectra from each instrument were fit simultaneously, allowing the relative normalizations to vary as necessary. Since the effective area for the GIS drops rapidly below 1 keV, it is not very sensitive to the Galactic hydrogen column density, and we fixed the absorption at the Galactic value of Dickey & Lockman (1990). For the SIS, we left the column density as a free parameter since one effect of the radiation damage to the SIS CCDs manifests itself as spuriously high column densities. Therefore, we do not consider the fitted SIS column density values trustworthy.

All GIS3 data taken between February 10, 1994 and April 8, 1994 suffered from an on-board software related problem. GIS3 science files were binned to 128 channels, as opposed to 1024, effectively losing spectral resolution. This is termed the "GIS3 bit problem". We have excluded these GIS3 observations from the analysis since we found affected GIS3 spectra to be a poor match to the GIS2 observations.

The results of the spectral fitting are presented in Table A.2. In several cases, the fit to a source was modified (e.g., the energy range restricted or another component added to the fit), usually because of a large χ^2 value. These sources are noted in the table and discussed in Appendix B.

For five clusters (Abell 560, Abell 2537, Abell S0520, CL 1938.3+5409, and RX J0138.0−2156), we could find no optical redshift in the literature. Except for Abell 560, ASCA proposal abstracts indicate that these clusters are at $z \sim 0.3$. Abell 560 was serendipitously detected in an observation of a nearby QSO. Based on the magnitude of the tenth brightest cluster galaxy (m_{10}) given in Abell (1958) and $m_{10} - z$ relation given in Ebeling et al. (1996), we estimate that Abell 560 is at $z \approx 0.15$. In the spectral fits, we therefore used an estimated redshift of $z = 0.3$ (or $z = 0.15$ for Abell 560) and then allowed the redshift to be a free parameter in the fit. The fitted redshifts are flagged in Table A.2.

Figure 3.5 shows the distribution of reduced χ^2 for the fits as a function of temperature. In general, the fits are fairly good with $\chi^2 \sim 1$, except for groups which typically have higher χ^2 values. This is probably due to additional x-ray emission not from the IGM, e.g., from galaxies within the group and the non-solar abundance ratios of the elements in the gas. A few with large values of χ^2 are discussed in Appendix B.

3.8 Luminosity Correction

The bolometric luminosities (effectively the 0.01 to 50 keV band) listed in Table A.2 are based on the GIS2 spectrum and measured within the extraction radius R_{ext}. For many clusters this will be smaller than the total luminosity due to flux lost outside the extraction region or below the background, but it should be near to

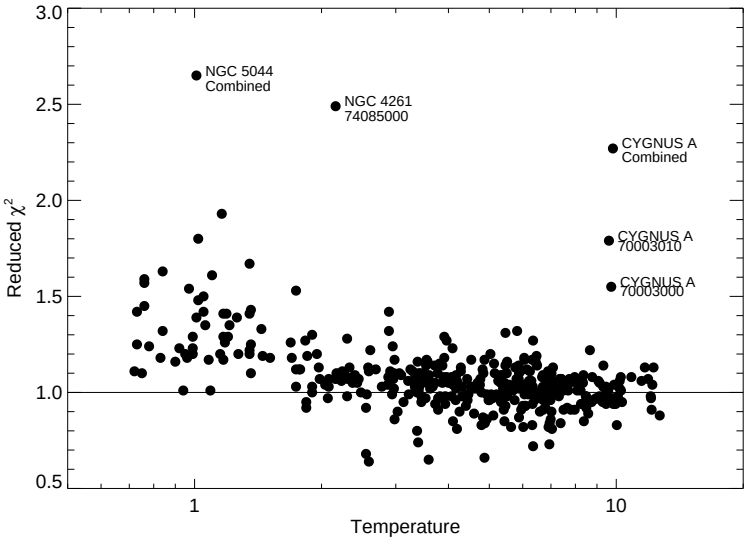

Figure 3.5: The reduced χ^2 values of fits versus temperature. The marked outliers are discussed in Appendix B.

the total cluster luminosity since we have chosen our extraction regions to contain nearly all of the cluster flux and most of the luminosity is produced by the dense gas in the central regions ($L_x \propto \rho^2$). Groups are more of a concern since we usually see emission from a smaller fraction of their virial radius and they have more diffuse surface brightness profiles, and thus, lower signal-to-noise with respect to the background.

We can extrapolate the bolometric luminosity from one radius to another if we know the surface brightness profile of the cluster emission. For the standard β-model profile (Equation 1.8), we need only the slope (β) and the core radius. We can then define a correction factor, l_{corr}, as the ratio of the luminosity within the chosen outer limit of integration (e.g., infinity) to the luminosity within the extraction radius. However, measuring spatial profile information with ASCA is difficult due to its complicated PSF, and while surface brightness profiles have been published in the literature for some clusters in the ACC, we do not have these measurements for many others. An alternative approach is to estimate β and r_c based on cluster properties that we do know. Correlations of β and r_c to x-ray temperature and luminosity have been reported by some authors (e.g., Neumann & Arnaud 1999), but the reality of these correlations has also been contested (Komatsu & Seljak 2001). For example, the correlation of β with temperature may just be an artifact of the outer limit of emission to which the β-model is fit.

Therefore, we have adopted a simple procedure to correct our luminosities that is similar to several ROSAT surveys (e.g., Scharf et al. 1997; Böhringer et al. 2000) where the counts are too few to accurately measure the surface brightness parameters. We fixed β at 0.67, the canonical value for clusters, and adopted a scaling of core radius based on the luminosity ($r_c \propto L_x^{0.28}$) from Böhringer et al. (2000). We also neglect any effects due to ASCA's PSF.

We then need to choose an outer limit of integration. Some authors have used infinity (Ebeling et al. 1998) while others have used multiples of the core radius (Böhringer et al. 2000) or some fixed radius (e.g., 1 Mpc; David et al. 1999). However, the most physically meaningful measure is the virial radius of the cluster since cluster flux does not truly extend to infinity and other radii are ad-hoc. We estimated the virial radius based on simulations of Evrard et al. (1996) who find a scaling between r_{vir} and temperature. This value corresponds to an overdensity $\delta = 200$ (see Chapter 7). We corrected the luminosities for "Combined" observations using an average for the individual observations weighted by the number of counts in each observation.

The correction factor is usually small for rich clusters ($\lesssim 10\%$) but can increase to a factor of two or more for lowest temperature groups in our sample. For $\approx$10% of the clusters, the correction factor is less than one. These are mostly nearby rich clusters where we are seeing all the emission. The correction factor for each cluster is listed Table A.2. We will test the effectiveness of this correction in Section 4.3. In the rest of this thesis, when we refer to luminosity we usually mean the corrected bolometric luminosity unless otherwise stated.

3.9 Consistency Checks

To asses the quality of our measurements, we performed several internal consistency checks, looking at multiple observations of the same cluster, the agreement of the GIS and SIS, and other effects.

3.9.1 Multiple Observations

Figure 3.6 shows a comparison of temperatures fitted to the individual observations to those from a fit to the combined observations. The temperatures all agree with the combined value to within the 90% confidence limits. A similar plot for metal abundances (see Figure 3.7) shows more scatter. The clusters that do not agree within the 90% confidence limits usually fall into a few classes: Some have small formal errors (e.g., 2A 0335+096, NGC 5044) so the actual difference are fairly small while other have very large formal errors (e.g., RX J1320.1+3308, HCG 062)

so the value are probably not completely reliable. NGC 507 and NGC 499 effectively form a double systems, so the spectra of each is contaminated by emission from the other which probably explains the discrepancy in their measurements.

3.9.2 GIS versus SIS

We checked for systematic biases (which are especially a concern for the SIS data given its calibration uncertainties) by comparing the results of fits using only the GIS or SIS data. Of course, the statistics are poorer since each has approximately half the photons, but we are able to distinguish trends, especially for the brighter clusters. In Figure 3.8, we show the ratio of the fitted SIS to GIS temperature as a function of the total number of counts in the GIS spectrum files. The temperatures usually agree within the 90% confidence limits, but the GIS temperatures are systematically slightly higher (by about 6%) than the SIS temperatures.

Among the bright clusters with discrepant temperature values are Ophiuchus, Abell 478, Abell 3627, and Abell 2147. For these clusters, the GIS and SIS (with its smaller field-of-view) see different regions of the cluster which may explain the difference in temperature. In Figure 3.9, we show the ratio of the GIS to SIS fitted abundances as a function of the GIS counts. As with temperature, the GIS and SIS abundances generally agree within the 90% confidence limits, but the GIS abundances are higher by about 10%.

We also checked for any variations between the GIS and SIS results as a function of time which could indicate calibration issues due to the degradation of the SIS CCDs. Figure 3.10 shows the ratio of the SIS to GIS temperatures as a function of the date of the observation. We have only plotted clusters with more than a total of 10^4 GIS counts to reduce the scatter. No significant trend exists in the difference between the GIS and SIS (temperatures or abundances) with time.

Overall, the agreement between the GIS and SIS is fairly good and is excellent for clusters with a large number of counts. For most clusters uncertainties due to photon statistics dominate. In any case, the differences are small enough that they do not have a large effect on the results in later chapters.

3.9.3 MEKAL versus Raymond-Smith models

The results presented in Table A.2 are for a single temperature MEKAL model. Cluster spectra are also commonly fit with the Raymond-Smith plasma code (Raymond & Smith 1977). These codes use a different treatment of the Fe-L complex. To see how these differences affect temperature and abundance determinations, we fitted the clusters in the ACC to a Raymond-Smith model and compare the results for temperature and metal abundance in Figure 3.11 and Figure 3.12.

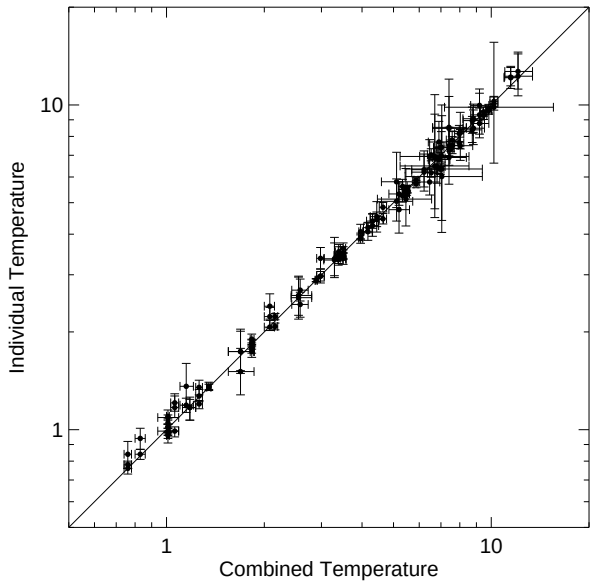

Figure 3.6: Comparison of the temperatures derived from the combined spectra to those from fits to the individual observations.

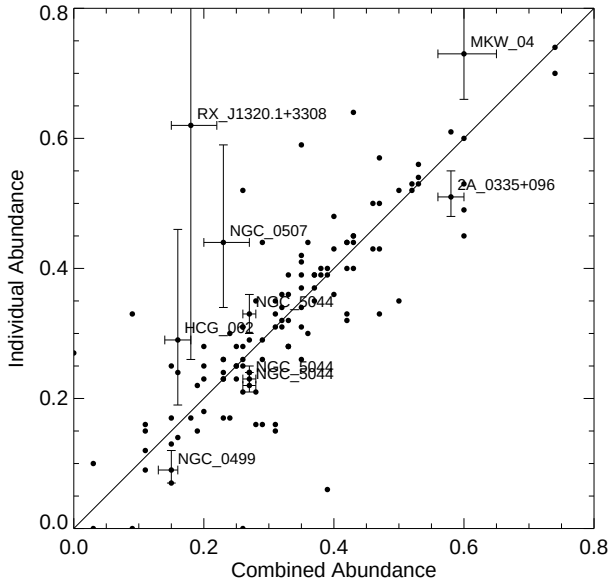

Figure 3.7: Comparison of the abundances derived from the combined spectra to those from fits to the individual observations. Error bars have only been plotted for clusters that were not consistent within the 90% confidence limits.

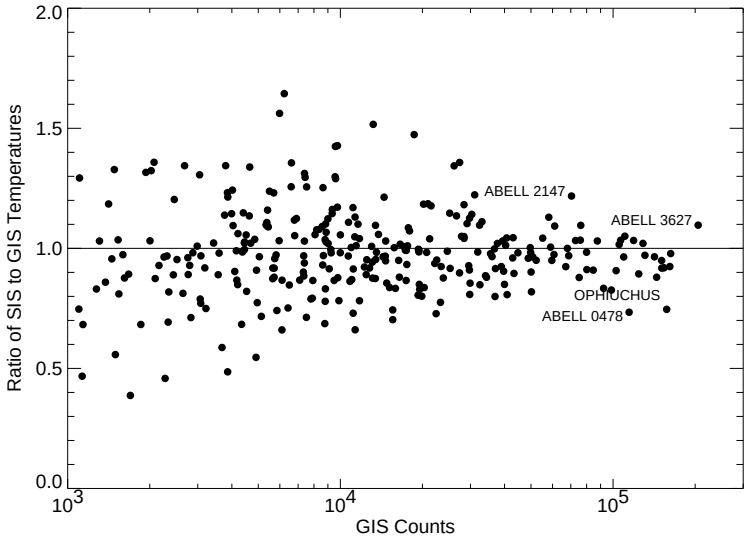

Figure 3.8: Ratio of the SIS to GIS fitted temperatures as a function of the total number of GIS counts. For clarity, error bars are not plotted but the temperatures are usually consistent. The marked outliers are discussed in the text.

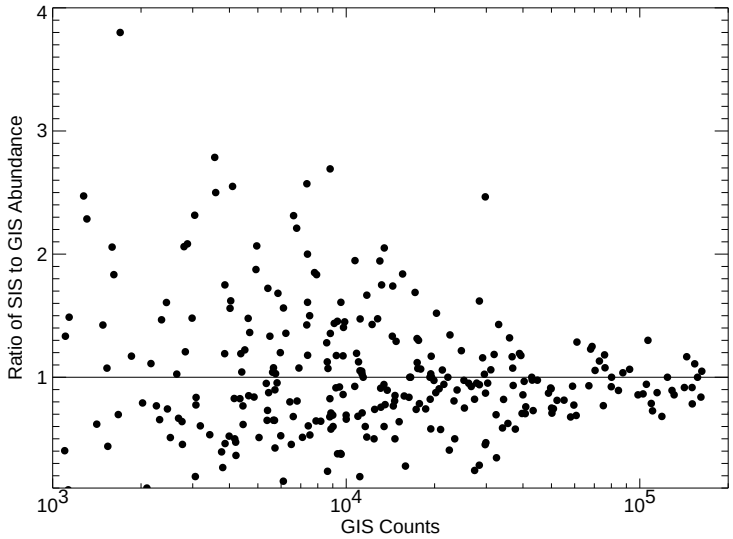

Figure 3.9: Ratio of the SIS to GIS fitted metal abundances as a function of the total number of GIS counts. For clarity, error bars are not plotted but the abundances are usually consistent.

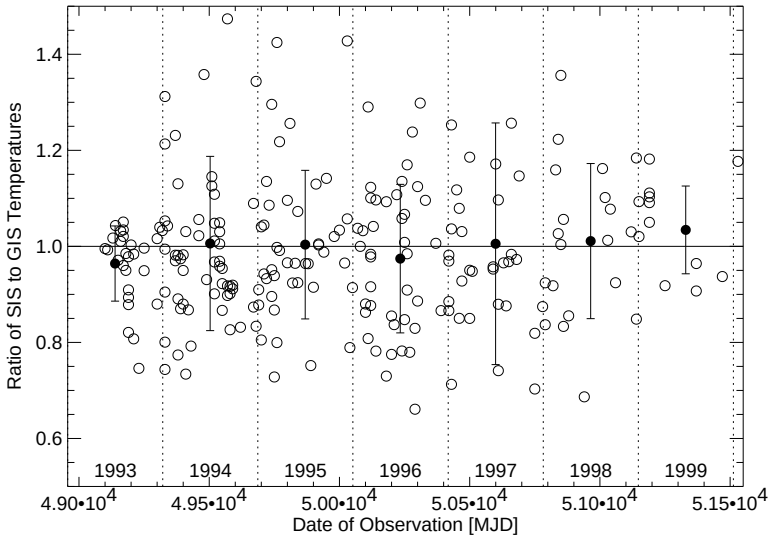

Figure 3.10: Ratio of the SIS to GIS fitted temperatures as a function of the Julian date of the observation. Open circles are individual clusters. Only clusters with greater than 10^4 GIS counts have been plotted. The filled circles represent the average (and standard deviation) for a given year. The dotted lines indicate the boundaries of each year.

The choice of model has little effect on temperature measurements. Although the distribution has a noticeable shape, the difference in the fitted temperature between the MEKAL and Raymond-Smith models are $\lesssim 10\%$, usually within the 90% confidence limits. Similarly, the abundance measurements are also usually consistent within the 90% confidence limits, but with a systematic trend for Raymond-Smith abundances to be lower at hotter temperatures by $\sim$10% and higher by $\sim$ 40% for temperatures $\sim$1 keV. This needs to be kept in mind when comparing abundance measurements between the two models, especially at low temperatures.

3.10 Conclusions

We have created the largest catalog yet assembled of temperatures, metal abundances, and luminosities for galaxy clusters and groups. Although the reduction of ASCA data is necessarily rather complex, our semi-automated reduction procedure seems quite robust. ASCA reduction procedures and tools have been tested and validated by a large number of users over the eight years lifetime of the mission. While calibration issues remain, especially for the SIS, they are small enough that they do not have a large effect on our results. For example, the measured temper-

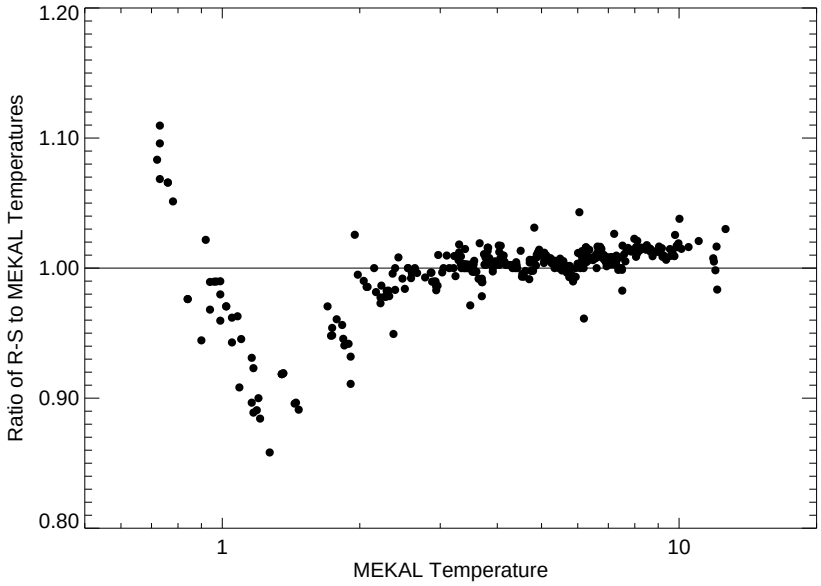

Figure 3.11: Ratio of temperatures from the Raymond-Smith model and the MEKAL model as a function of the MEKAL model temperature.

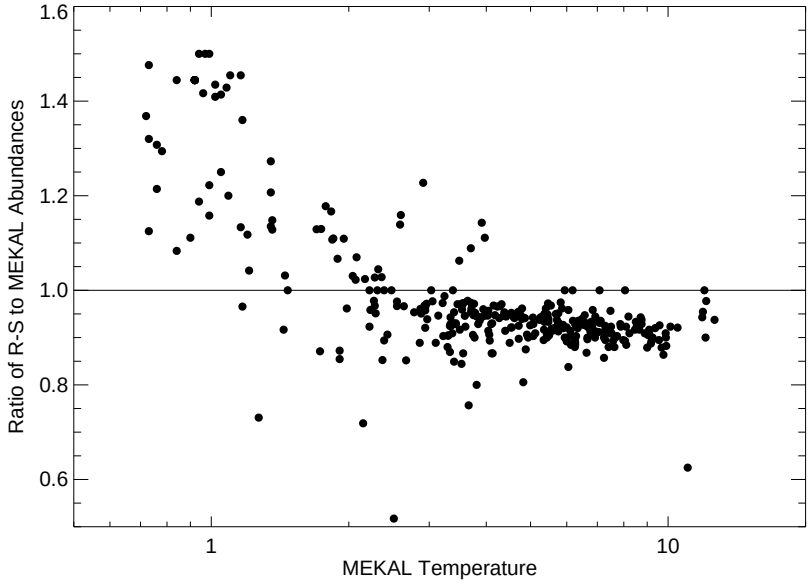

Figure 3.12: Comparison of Raymond-Smith to MEKAL model abundances as a function of the MEKAL model temperature.

atures and abundances for clusters observed multiple times agree quite well, and the difference between the GIS and SIS are also small. The uncertainties in our measurements are therefore dominated by photon statistics and any instrumental biases in ASCA, which will be explored in the next chapter.

Chapter 4

Comparison to Other Catalogs

We have checked the quality of our ASCA fits by comparing with previous literature results where available. This should reveal any systematic or instrumental biases in our measurements (or in those of others) and illuminate issues that affect the science results derived from such samples. In this chapter, we use the combined value of the fit for clusters with more than one observation.

4.1 X-ray Temperature

The results of the comparison of our ACC temperatures to others in the literature are summarized in Table 4.1 which shows the average ratio of our ASCA temperature to the temperature from the given reference sample, the standard deviation of that average, and the number of clusters used in the comparison.

4.1.1 Previous ASCA Results

4.1.1.1 White (2000)

Figure 4.1a shows the comparison of our ASCA temperatures to those of White (2000), previously the largest sample of temperatures in the literature. The White study was an attempt to measure the temperature and metallicity profiles for 106 clusters. He also provided single temperature MEKAL fits to the cluster spectra (in the 1–9 keV range) based only on the GIS data (since the SIS data had too small a field-of-view to be useful for his study). In principle, the ACC should completely subsume his catalog and improve on his measurements since we also use the SIS data. However, only 100 of the 106 clusters in his sample are in ours.

Three of the clusters in the White sample are Coma, Virgo, and Perseus which we excluded due to their large angular size. The other clusters in White's sample but not the ACC are Abell 1774, Abell 1772, and Abell 3221. Abell 1774 was

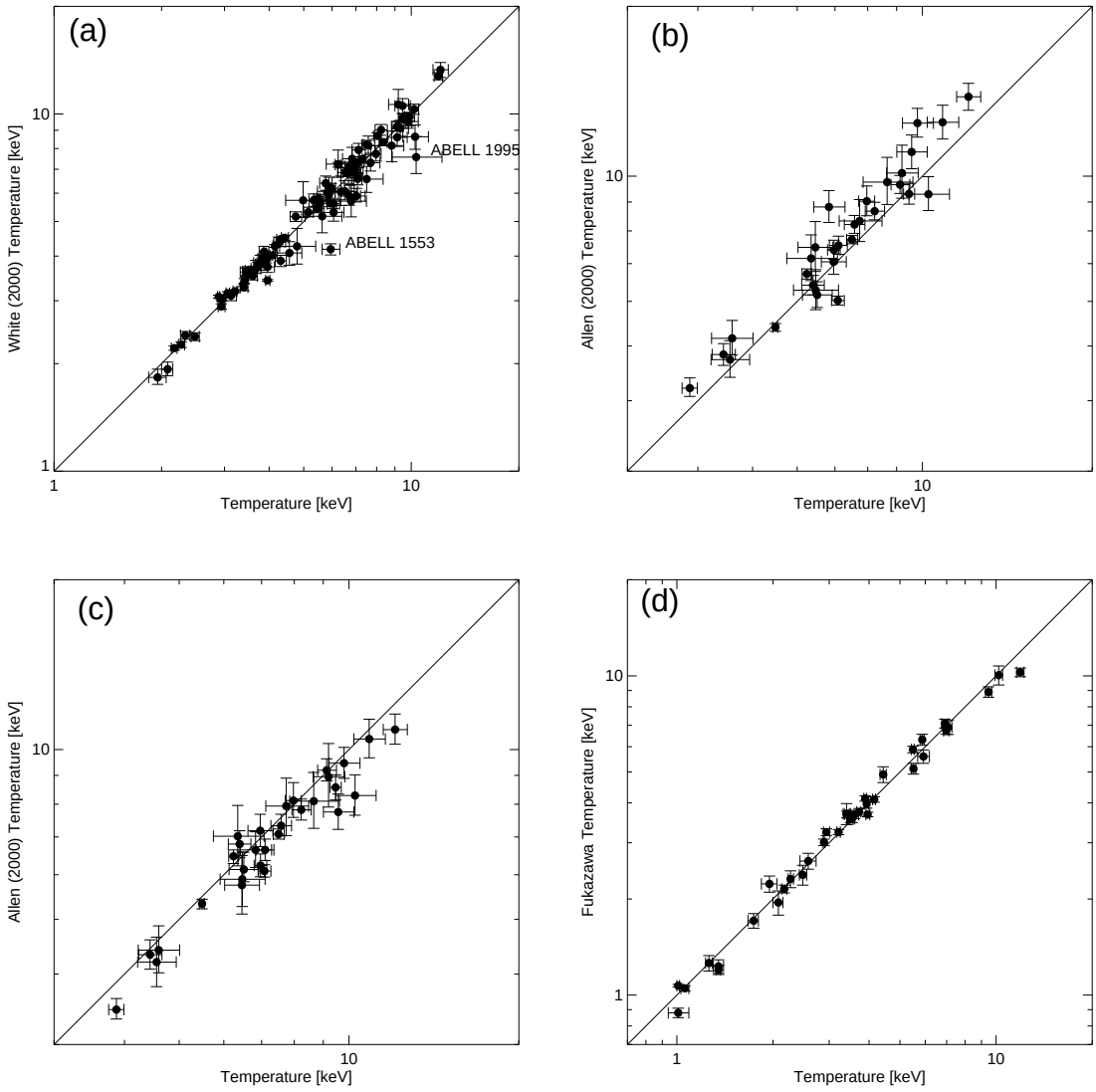

Figure 4.1: Comparison of ACC fitted temperatures to (a) White (2000) (b) Allen (2000), Model A (c) Allen (2000), Model B (d) Fukazawa et al. (1998). Error bars are 90% confidence limits except for White which are 1σ. The marked outliers are discussed in the text.

Table 4.1: Results of Temperature Comparisons

Comparison Sample	$\left\langle \frac{T_{\rm ACC}}{T_{REF}} \right\rangle$	1σ	N	Comments
White (2000)	1.01	0.09	100	
Allen (2000)	0.94	0.09	30	Model A
Allen (2000)	1.06	0.08	30	Model B
Fukazawa et al. (1998)	1.04	0.07	37	excluding center
Markevitch (1998)	0.99	0.06	29	
Markevitch (1998)	0.95	0.11	29	excluding center
Mushotzky & Scharf (1997)	0.94	0.10	38	
Henry (2000)	1.01	0.14	15	
Irwin & Bregman (2000)	1.07	0.03	11	1.65–10.0 keV
Irwin & Bregman (2000)	0.94	0.05	12	3.0–10.0 keV
White et al. (1997)	1.03	0.27	83	
David et al. (1993)	0.96	0.19	55	
Edge & Stewart (1991a)	1.01	0.15	28	
Davis et al. (1999)	1.01	0.11	15	
Hwang et al. (1999)	1.06	0.11	5	
Mulchaey & Zabludoff (1998)	1.28	0.24	8	
Helsdon & Ponman (2000b)	1.06	0.05	5	$T_{\rm x} \leq 1$ keV
Helsdon & Ponman (2000b)	1.23	0.19	6	$T_{\rm x} > 1$ keV

excluded from the ACC because it contains a QSO (B3 1338+402) which dominates the emission. Note that this is one of the handful of clusters in White's sample where he found a significant systematic decline in the temperature profile with radius. Abell 1772 in White's sample is, in fact, Abell 1722 (which is in the ACC). Besides the wrong name, White also used the wrong redshift. Abell 1722 is at $z = 0.3275$ and not 0.3058, the redshift of Abell 1772. Similarly, White's Abell 3221 should be Abell 3921 at a redshift of $z = 0.0936$, not $z = 0.1044$. I have left these clusters out of the comparison although the redshifts White used are close enough that it has little effect on the temperature measurement. With the 100 clusters in common we find very good agreement with White's temperature estimates (see Figure 4.1 and Table 4.1).

The two largest outliers evident in the plot are Abell 1553 and Abell 1995. White finds a strongly declining temperature profile for Abell 1553 and uses a much larger extraction radius ($19.4'$ versus $6.8'$) which might explain his lower temperature (4.18 keV versus 6.00 keV). We tested this possibility by re-extracting the data with a $19.4'$ radius (effectively the whole GIS field) and fitting only the GIS data, similar to White. This lowered the fitted temperature to ≈ 4 keV consistent with White's measurement. However, using such a large aperture introduces much larger systematic uncertainties with respect to the background since the Abell 1553 cluster spectrum has only $\sim 5,000$ total GIS counts. White's extraction radius is

also much larger than the extent of cluster emission and nearly 5 Mpc at the cluster redshift.

The other outlier, Abell 1995, is fairly distant (z=0.3186) also with $\sim 5,000$ GIS counts in the spectrum, making it only a moderately bright cluster for our sample. Temperature estimates for this cluster cover a wide range of values in the literature: $7.57^{+1.07}_{-0.76}$ keV from White, $8.6^{+0.86}_{-0.67}$ keV from Patel et al. (2000), $10.7^{+1.8}_{-2.5}$ keV from Mushotzky & Scharf (1997). The ACC temperature is $10.32^{+1.87}_{-1.47}$ keV. A contaminating source is located about $6'$ from the cluster. It seems likely that the treatment of this source may be a large factor in this discrepancy.

4.1.1.2 Allen (2000), Fukazawa et al. (1997), and Markevitch (1998)

Allen (2000) investigated the properties of a sample of 30 luminous, cooling flow clusters. All of these clusters are in the ACC. Allen fit a number of models to the spectra, using both the GIS and SIS spectra. The first, "Model A" is a single temperature MEKAL fit with hydrogen column density fixed at the Galactic value. The second, "Model B" is the same but with the column density left as a free parameter. Neither exactly reproduces our MEKAL model fits. We left the GIS column density fixed at the Galactic value since the GIS is insensitive below 1 keV, but left the SIS column density as a free parameter since radiation damage to the SIS CCDs can manifest itself as spuriously high column densities.

Figure 4.1b shows the comparison of our temperatures to his "Model A" temperatures. The ACC temperatures are generally lower than Allen's. If his "Model B" temperatures are used (Figure 4.1c), the opposite is observed. The ACC temperatures effectively fall in between these models. This shows that column density can change the fitted temperature by $\sim$10%. We feel that our approach to dealing with the column density is the best compromise.

A catalog of 40 clusters observed with ASCA was published by Fukazawa et al. (1998) (based on thesis work in Fukazawa (1997)). His data is mostly drawn from performance verification and other early ASCA observations. Three of his clusters (Coma, Perseus, and Virgo) are not in our ASCA sample. Fukazawa excluded the central regions of clusters, extracting an annular region for each cluster approximately $3'$ to $9'$ in radius (corresponding to about 0.15–0.4 Mpc). He then fit the GIS data in the 1–10 keV and the SIS data in the 0.65–9 keV band with a Raymond-Smith model. However, the temperature agreement is still very good (see Figure 4.1c). All the temperatures agree to within 15%.

Markevitch (1998) published ASCA temperatures for 31 clusters as part of a study of the x-ray luminosity – temperature relation and temperature function of clusters. One cluster in Markevitch's sample, Abell 3395, has been split into two clusters in our catalog. We do not include it in the comparison. Except for Cygnus

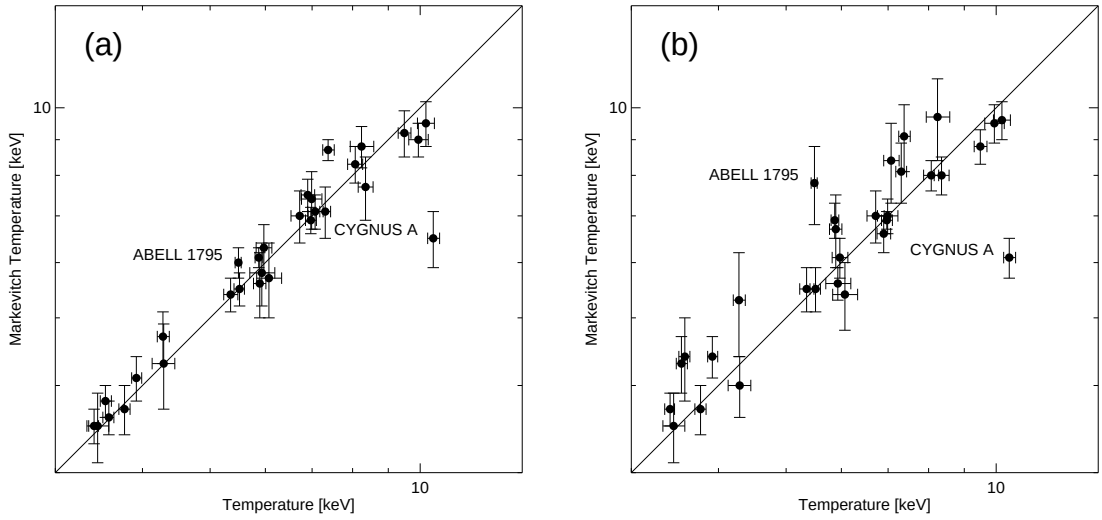

Figure 4.2: Comparison of ACC fitted temperatures to (a) Markevitch (1998) fit to the whole cluster (b) Markevitch (1998) fit excluding cluster center. Error bars are 90% confidence limits. The marked outliers are discussed in the text.

A which is an unusual cluster (see Appendix B), all temperatures agree to within 15%.

In addition to average temperature for the whole cluster (see Figure 4.2a) which agree very well with our measurements, Markevitch attempted to minimize the effects of cooling flows on his measurements by excluding a region of 100 h_{50}^{-1} kpc radius at the center of each cluster. Figure 4.2b shows the comparison of our temperatures to Markevitch's "corrected" temperatures. The agreement is still good although the dispersion has increased. Given the good agree of our temperatures with Fukazawa's and Markevitch's "corrected" temperatures, we can conclude that excluding the central parts of clusters has little effect on the fitted temperatures.

4.1.1.3 Higher Redshift Samples

The previous ASCA samples consist mostly of low redshift clusters. The maximum redshift of clusters in the Fukazawa sample is $z = 0.088$ while White has only three clusters at $z > 0.3$. Allen's sample is a mix of both high and low redshift clusters. Specific studies of high redshift clusters were carried out by Mushotzky & Scharf (1997) to study the luminosity–temperature relation and Henry (2000) to study the temperature function. Mushotzky & Scharf (1997) analyzed 38 clusters

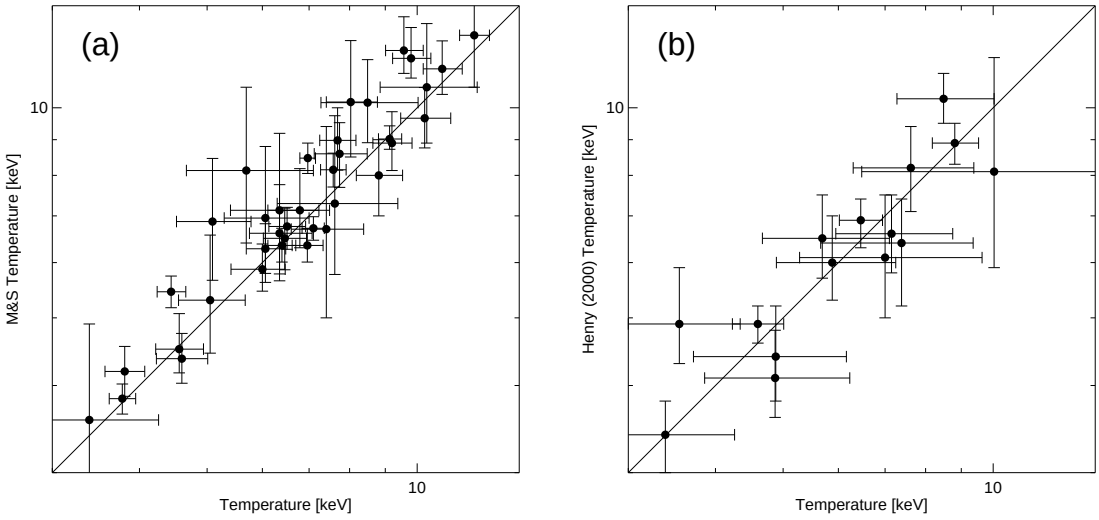

Figure 4.3: Comparison of ACC temperatures to (a) Mushotzky & Scharf (1997) (b) Henry (2000). Errors bars are 1σ errors for Henry's temperatures and 90% confidence limits otherwise.

with redshifts $z > 0.14$ which showed no strong substructure and had temperature uncertainties of $\delta T/T \lesssim 0.3$. Henry (2000) analyzed 15 clusters observed by ASCA in the redshift range 0.30–0.55 taken mostly from the EMSS. The temperature comparisons with the ACC are shown in Figure 4.3. Given the poorer photon statistics for most higher redshift clusters, the agreement is quite good.

4.1.2 Non-ASCA Temperatures

Irwin & Bregman (2000) published a sample of 11 clusters observed with BeppoSAX as part of a study of the radial temperature profiles of clusters. In a follow-up (Irwin & Bregman 2001), they examined metal abundance profiles for the same 11 clusters plus Abell 3562. Irwin & Bregman (2000) give two global temperatures for each cluster. The first is fit in the 1.65–10.5 keV energy range while the second uses just the 3.0–10.5 keV band. Irwin & Bregman (2001) only give the Abell 3562 temperature in the 3.0–10.5 keV band. In both cases, they fit an isothermal MEKAL model with the column density fixed at the Galactic value. As can be seen in Figure 4.4a, these two temperature estimates effectively straddle the ASCA estimates although the 1.65–10.5 keV estimates, which better match the ASCA fitted range, are closer to the actual ASCA temperatures. Most of the

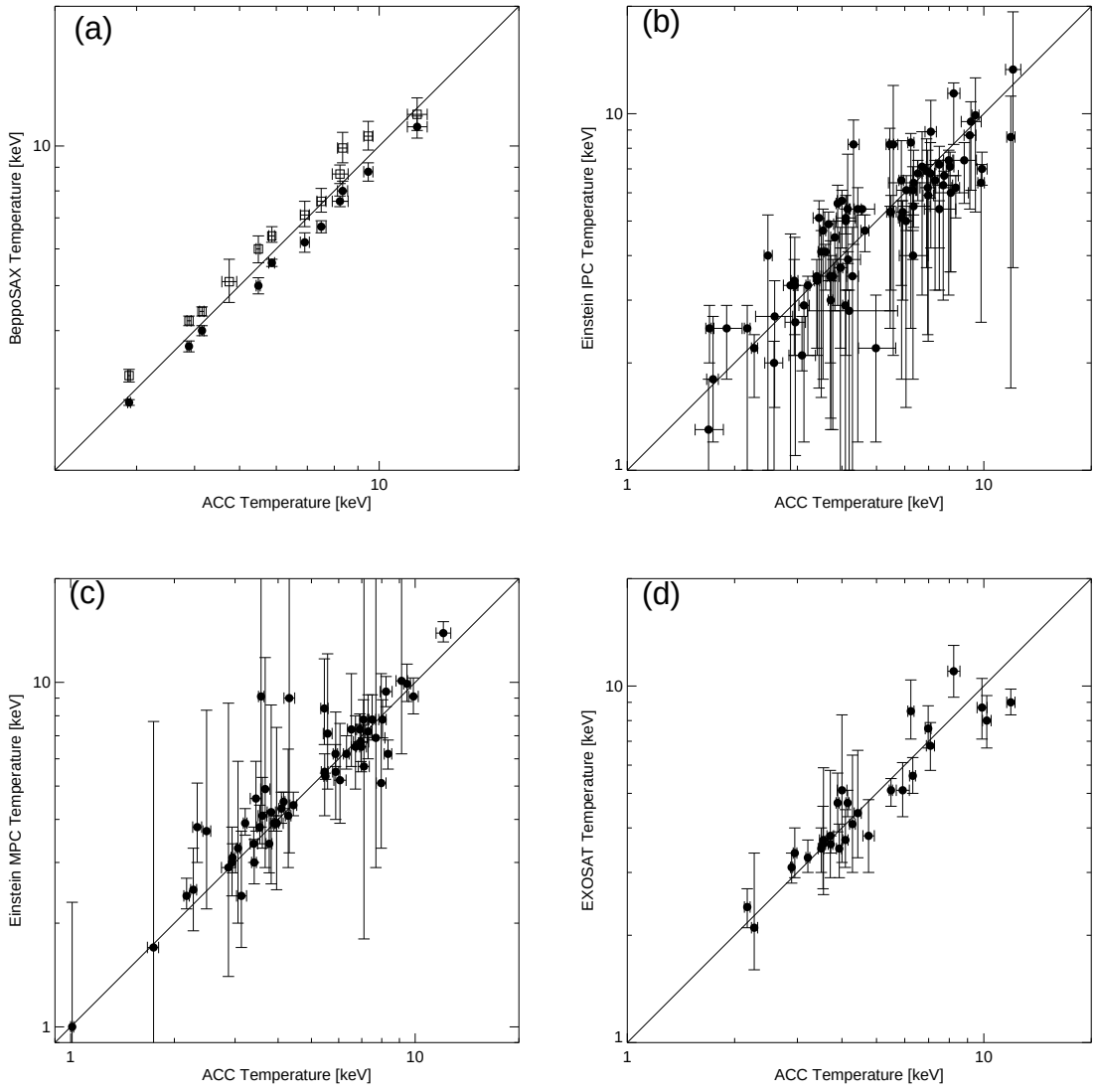

Figure 4.4: Comparison of ACC fitted temperatures to (a) BeppoSAX temperatures from Irwin & Bregman (2000) and Irwin & Bregman (2001). The solid circles are BeppoSAX temperatures fit in the 1.65–10.5 keV band while the open boxes were fit in the 3.0–10.5 keV band. (b) Einstein IPC temperatures from White et al. (1997). (c) Einstein MPC temperatures from David et al. (1993). (d) EXOSAT temperatures from Edge & Stewart (1991a). All errors bars are 90% confidence limits.

Irwin and Bregman clusters have strong cooling flows, so the higher temperatures in the 3.0–10.5 band may be a result of excluding the cooler gas from the global fit.

In Figure 4.4b, we compare our temperatures to the White et al. (1997) catalog of Einstein IPC temperatures. The agreement is still quite good on average, but the low quality of the Einstein data produces a scatter that is almost three times larger than for the White (2000) GIS data. In Figure 4.4c, we compare our temperatures to the Einstein MPC temperatures of David et al. (1993). Figure 4.4d shows a comparison of our temperatures to EXOSAT temperatures in Edge & Stewart (1991b). Both show similar agreement and scatter somewhat larger than for the White (2000) data.

4.1.3 Groups

The analysis of x-ray emission from groups is more complicated than for clusters. Groups are usually fainter, meaning that photon statistics are poorer and background subtraction becomes more important. They are also complicated by the possibility of contamination by x-ray emission from galaxies within the group. The reduced χ^2 values for fits to groups are usually higher than for clusters as was seen in Figure 3.5.

Several studies of groups have been published in recent years. Davis et al. (1999) fit ASCA spectra for a sample of 17 groups while Hwang et al. (1999) studied a smaller sample of five groups with ASCA. These comparison of temperatures are shown in Figure 4.5a and Figure 4.5b. The agreement is fairly good. The discrepancies can be accounted for by model and region difference. For example, the ACC temperature of PCC S49-140 is decreased if a Raymond-Smith model is used and is decreased even more (to a temperature consistent with Hwang) if a larger region is used.

Mulchaey & Zabludoff (1998) (hereafter MZ) studied a sample of groups observed with the ROSAT PSPC. They separate the x-ray emission into a central component from the dominant galaxy and an extended component from the diffuse gas in the IGM and fit the spectra from these two components separately and together. Since we cannot readily distinguish between these two components with the spatial resolution of ASCA, we use their "central+extended values" for the MEKAL model. Helsdon & Ponman (2000b) (hereafter HP) studied a larger sample of groups with the PSPC. However, Figure 4.5c and Figure 4.5d shows no consistent trend between the two samples. The ACC temperatures are usually higher than the MZ temperatures while a definite trend is seen with the HP data. At low temperatures, the ACC and HP temperatures agree very well, but at $T_{\rm x} > 1$ keV, the HP temperatures are systematically cooler by about 20%. We

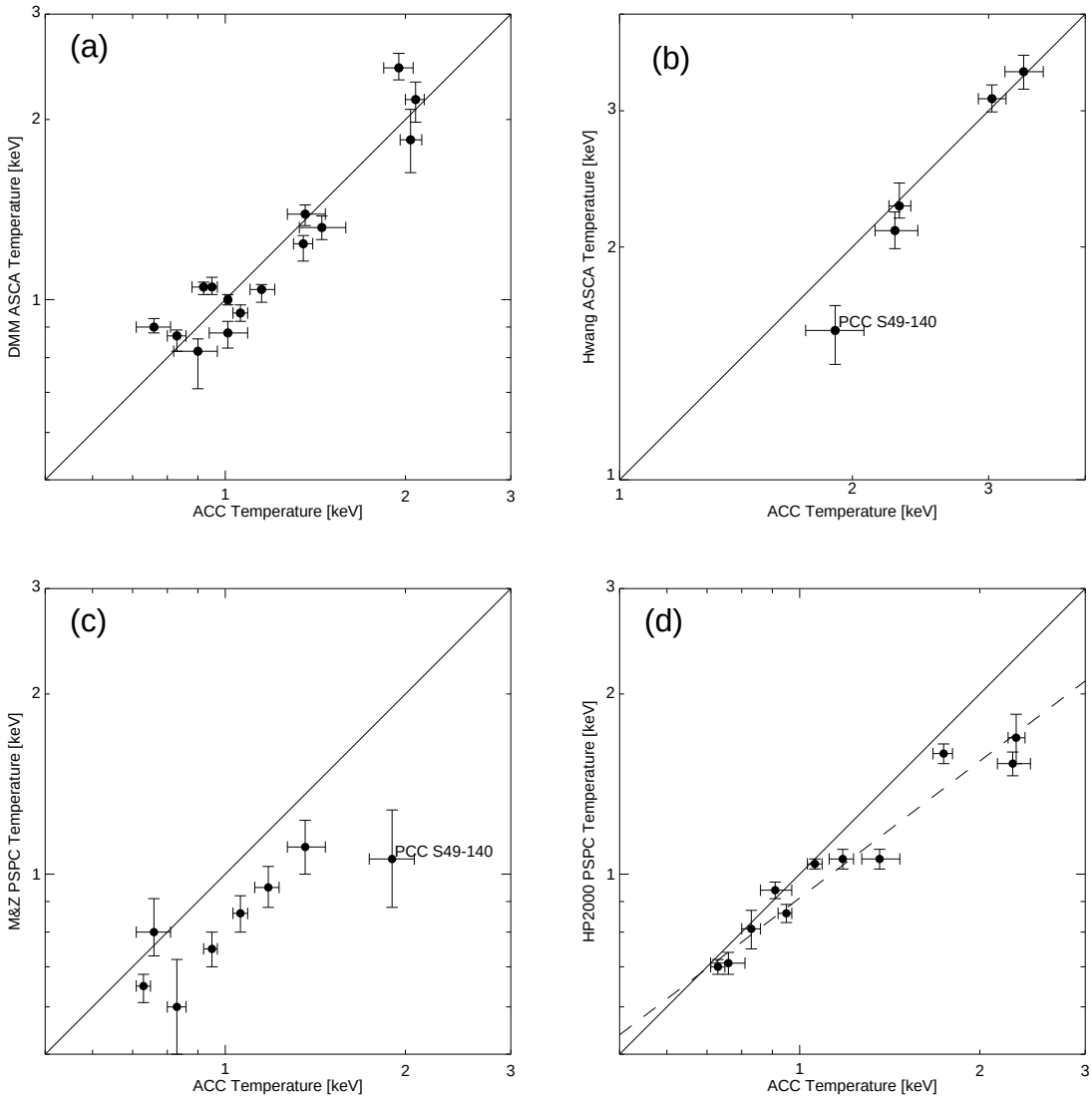

Figure 4.5: Comparison of ACC fitted temperatures to (a) ASCA temperatures from Davis et al. (1999). (b) ASCA temperatures from Hwang et al. (1999). (c) ROSAT PSPC temperatures from Mulchaey & Zabludoff (1998). (d) ROSAT PSPC temperatures from Helsdon & Ponman (2000b). The dashed line is the best fit. All errors are 90% confidence limits, except for the Helsdon & Ponman data which are 1σ. The marked outliers are discussed in the text.

fit this relationship and find that:

$$T_{\rm ACC} = (1.13 \pm 0.03)\, T_{\rm HP}^{1.32\pm0.11} \tag{4.1}$$

We will use this relationship later in Chapter 5.

A discrepancy between ASCA and PSPC temperatures similar to that seen with the HP data was also reported by Hwang et al. (1999). This difference is probably due to the superior spectral resolution and larger energy range of ASCA doing a better job fitting the continuum for higher temperature groups, which determines the fitted temperature in that regime. At low temperatures, the fit is dominated by the spectral lines and both ASCA and ROSAT can accurately estimate the temperatures. This does not explain the discrepancy between the MZ and HP samples. MZ usually used larger apertures which may explain some of the discrepancy. This problem will be taken up again in Section 4.2.3.

4.2 Metal Abundance

Several of the catalogs mentioned in the previous section also give estimates of the metal abundance of clusters. The results are summarized in Table 4.2 which shows the average ratio of our ASCA abundance to the abundance from the given reference sample, the standard deviation of that average, and the number of clusters used in the comparison.

Table 4.2: Results of Abundance Comparisons

Comparison Sample	$\left\langle \frac{Z_{\rm ACC}}{Z_{REF}} \right\rangle$	1σ	N	Comments
White (2000)	1.14	0.17	40	$> 10^5$ counts
Allen (2000)	1.05	0.19	30	Model B
Mushotzky & Loewenstein (1997)	1.19	0.28	21	
Fukazawa et al. (1998)	1.42	0.29	37	
Irwin & Bregman (2001)	1.09	0.18	12	
Edge & Stewart (1991a)	1.15	0.41	16	
Davis et al. (1999)	1.10	0.56	15	
Hwang et al. (1999)	1.10	0.26	5	
Mulchaey & Zabludoff (1998)	2.07	1.16	8	
Helsdon & Ponman (2000b)	1.07	2.10	11	

4.2.1 Previous ASCA Results

In Figure 4.6a we show the comparison of our ACC abundances to the ASCA GIS abundances of White (2000). Since the scatter is larger for abundances than for

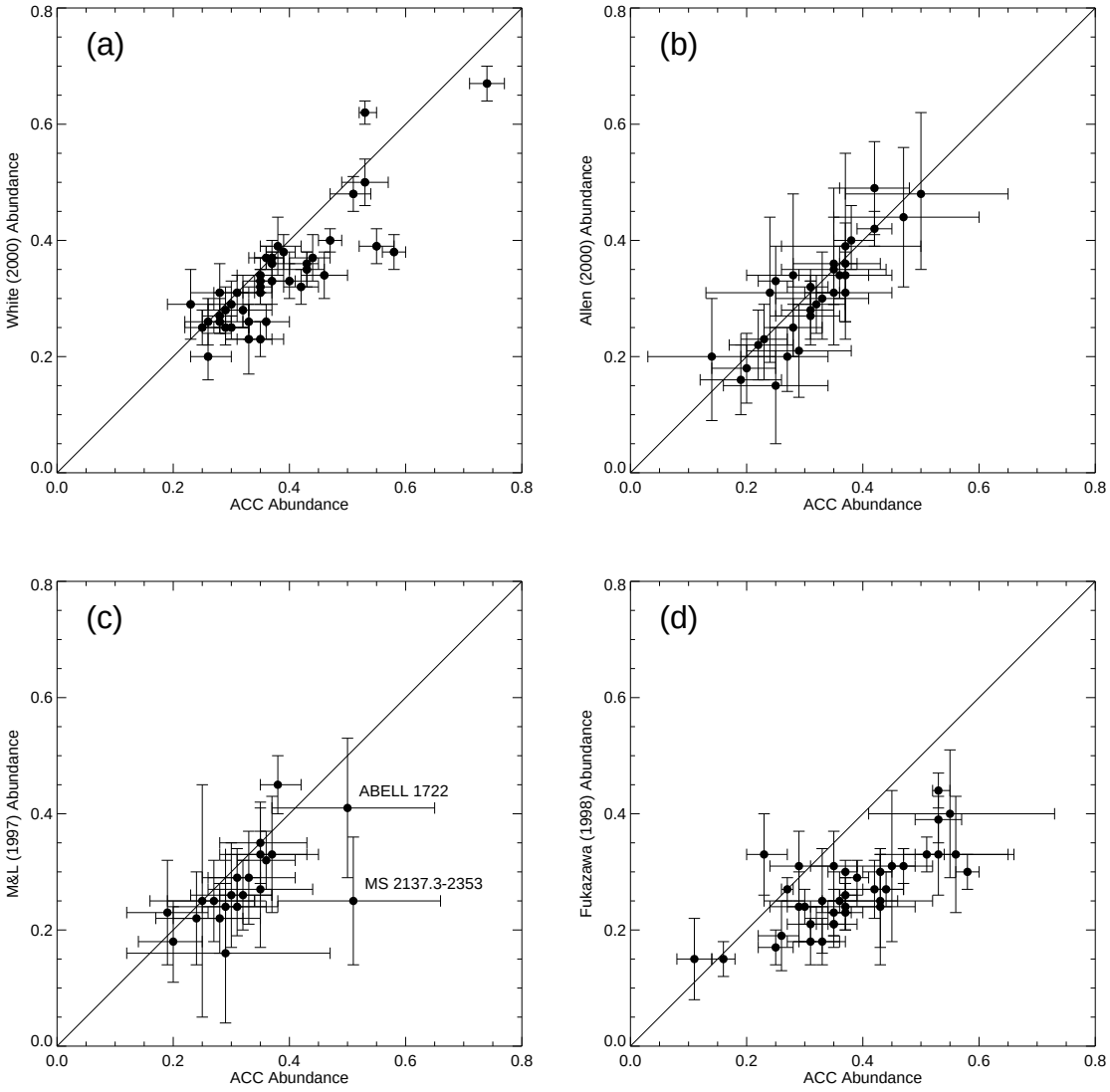

Figure 4.6: Comparison of ACC fitted abundances to (a) White (2000) (b) Allen (2000), Model B (c) Mushotzky & Loewenstein (1997) (d) Fukazawa et al. (1998). Error bars are 90% confidence limits except for White which are 1σ. The marked outliers are discussed in the text.

temperatures, we have only plotted those clusters which had more than 10^5 counts in the ACC (GIS+SIS). Although many of the abundance values agree within their 90% confidence limits, the ACC abundances are higher by about 15%. The origin of this offset is unclear. We attempted to replicate the White results with our data by fitting the GIS data between the 1–9 keV with the column densities fixed at the Galactic value, as White did. However, we still see a similar offset.

Unlike temperature, virtually no difference exists between Allen (2000) Model A and Model B abundances (Model B abundances are used in Figure 4.6b). The ACC abundances are slightly, but not significantly, higher. At higher redshifts, Mushotzky & Loewenstein (1997) (hereafter ML) complements the Mushotzky & Scharf (1997) study by giving abundance measurements for 21 clusters. Like the White sample, the ACC abundances are systematically higher (see Figure 4.6c) However, ML fit a Raymond-Smith model to the spectrum. As we saw in Section 3.9.3, MEKAL abundances are higher than Raymond-Smith abundances for hotter clusters. If we fit a Raymond-Smith model to our data, the difference between the ACC abundances and the ML abundances decrease to a level very similar to that of the ACC and Allen data.

Although the ACC temperatures agreed very well with those of Fukazawa et al. (1998), a clear systematic trend is visible in the comparison with the abundances (see Figure 4.6d). The main difference between Fukazawa's and our reduction methods is that Fukazawa excluded the central regions of the clusters. If extraction regions are the difference between the ASCA results, we should be able to reproduce Fukazawa's results by using the same regions as he did. Using the regions given in Fukazawa (1997), we re-extracted the data for Fukazawa cluster's and then fit a Raymond-Smith model to the results. The strong trend disappears but the ACC abundances are still about 25% higher than Fukazawa's on average. The origin of this discrepancy is not clear.

4.2.2 Non-ASCA Abundances

The Irwin & Bregman (2001) BeppoSAX abundances, with a few exceptions, agree fairly well with our ASCA abundances (see Figure 4.7a). The outlier, 2A 0335+096, can be brought into agreement with the BeppoSAX results if we fit only the 3.0–10.0 keV energy band similar to Irwin & Bregman. This cluster has a strong cooling flow component which dominates the spectra at low energies. The EXOSAT abundances of Edge & Stewart (1991b) also show general agreement with our ASCA abundances but with a very large scatter (see Figure 4.7b).

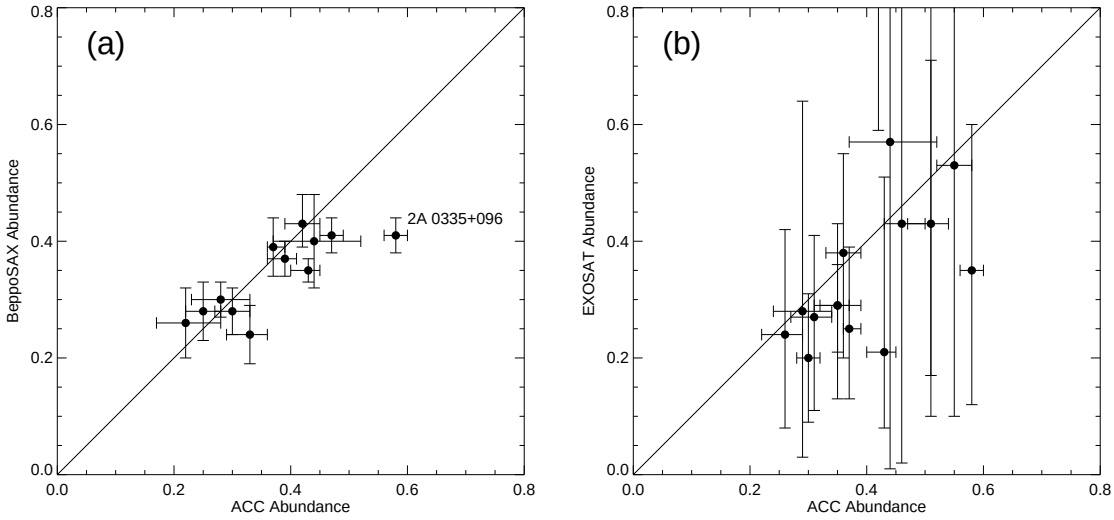

Figure 4.7: Comparison of ACC fitted abundances to (a) BeppoSAX abundances from Irwin & Bregman (2000). (d) EXOSAT abundances from Edge & Stewart (1991a). All errors bars are 90% confidence limits.

4.2.3 Groups

Figure 4.8 shows the comparison of our ACC abundances with the groups samples of Davis et al. (1999), Hwang et al. (1999), Mulchaey & Zabludoff (1998), and Helsdon & Ponman (2000b). The ASCA results are again consistent (with a few exceptions).

The inconsistency in the ROSAT PSPC results noted in the temperature comparison are even more apparent here. The MZ abundances are nearly all lower than ours while the HP abundances are nearly all higher. Because of its low spectral resolution, the PSPC lumps all the emission from the Fe–L region, the dominant feature for cool systems, into one spectral feature. With its superior spectral resolution and wider energy band, ASCA should be able to better constrain the abundance of the gas. Bauer & Bregman (1996) have already raised questions about the accuracy of PSPC determined abundances for stellar corona.

Buote (2000) has also noticed the discrepancy between the MZ and HP samples. He concludes that MZ did not correct their background spectra for vignetting and takes the HP abundances as the correct ones. He also argues that the bias is in the ASCA data, caused by trying to fit an isothermal model to a multi-temperature plasma. The PSPC is not as affected in his scenario since it reaches lower energy ($\sim$ 0.2–0.5 keV) where it can better determine the continuum. The resolution

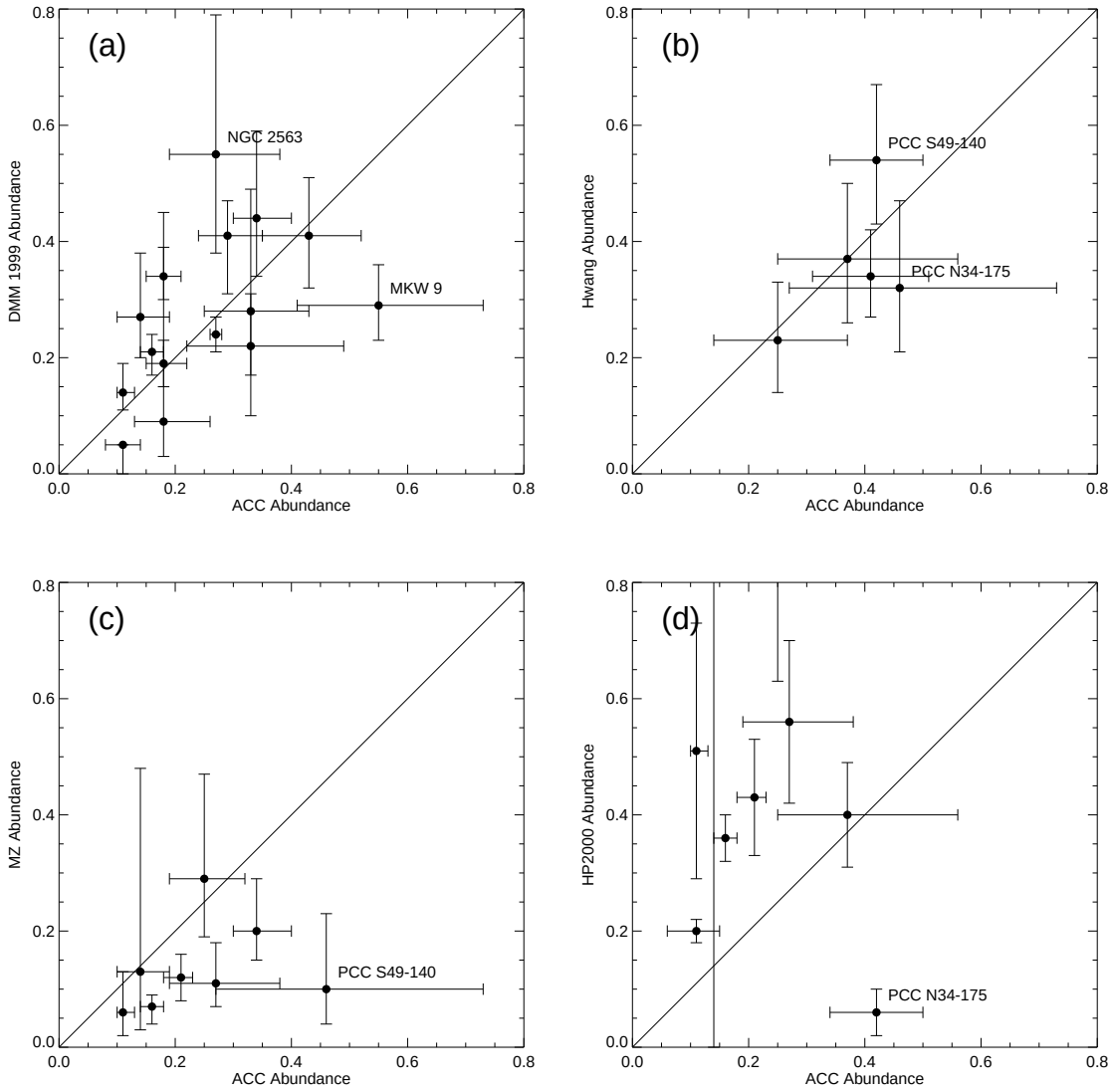

Figure 4.8: Comparison of ACC fitted abundances to (a) ASCA abundances from Davis et al. (1999). (b) ASCA abundances from Hwang et al. (1999). (c) ROSAT PSPC abundances from Mulchaey & Zabludoff (1998). (d) ROSAT PSPC abundances from Helsdon & Ponman (2000b). All errors are 90% confidence limits, except for the Helsdon & Ponman data which are 1σ.

of group abundance measurements will probably have to wait until Chandra and XMM results. However, preliminary XMM results for the NGC 4325 group are in excellent agreement with the ASCA values (Mushotzky, private communication).

4.3 Bolometric Luminosity

We have compared our corrected ASCA bolometric luminosities (i.e., $L(< R_{ext}) \times l_{corr}$) to bolometric luminosities from: the ROSAT All-Sky Survey (Figure 4.9a); EXOSAT (Edge & Stewart 1991a) (Figure 4.9b); Einstein MPC (David et al. 1993) (Figure 4.9c); ASCA (Henry 2000) (Figure 4.9c); ROSAT groups from Mulchaey & Zabludoff (1998) (Figure 4.10a); and ROSAT groups from Helsdon & Ponman (2000b) (Figure 4.10b).

The results are summarized in Table 4.3 which shows the average ratio of the luminosities, the standard deviation of that average, and the number of clusters used in the comparison.

Table 4.3: Results of Luminosity Comparisons

Reference	$\left\langle \frac{L_{ACC}}{L_{REF}} \right\rangle$	1σ	N	Comments
RASS (various authors)	1.04	0.27	173	
Edge & Stewart (1991a)	1.29	0.30	28	
David et al. (1993)	1.23	0.20	58	
Henry (2000)	1.05	0.19	15	high z
Mulchaey & Zabludoff (1998)	1.16	0.46	8	
Helsdon & Ponman (2000b)	0.91	0.32	11	$R = R_{ext}$
Helsdon & Ponman (2000b)	0.71	0.30	11	$R = R_{vir}$

4.3.1 Clusters

By far the largest number of cluster luminosity measurements available in the literature are from RASS based catalogs: NORAS (Böhringer et al. 2000); BCS (Ebeling et al. 1998); XBACS (Ebeling et al. 1996); and RASS1 (De Grandi et al. 1999b). Since NORAS is the largest of these available, we have preferentially used their luminosities. Although x-ray luminosity mostly depends on the flux (actually the count rate in the detector's energy band), it also has a dependence on the x-ray temperature and metal abundance. ROSAT luminosities also have a strong dependence on the hydrogen column density since the ROSAT has a low energy bandpass (0.1–2.4 keV).

RASS bolometric luminosities are usually calculated by assuming a form for the x-ray luminosity–temperature relation of clusters and a metal abundance of

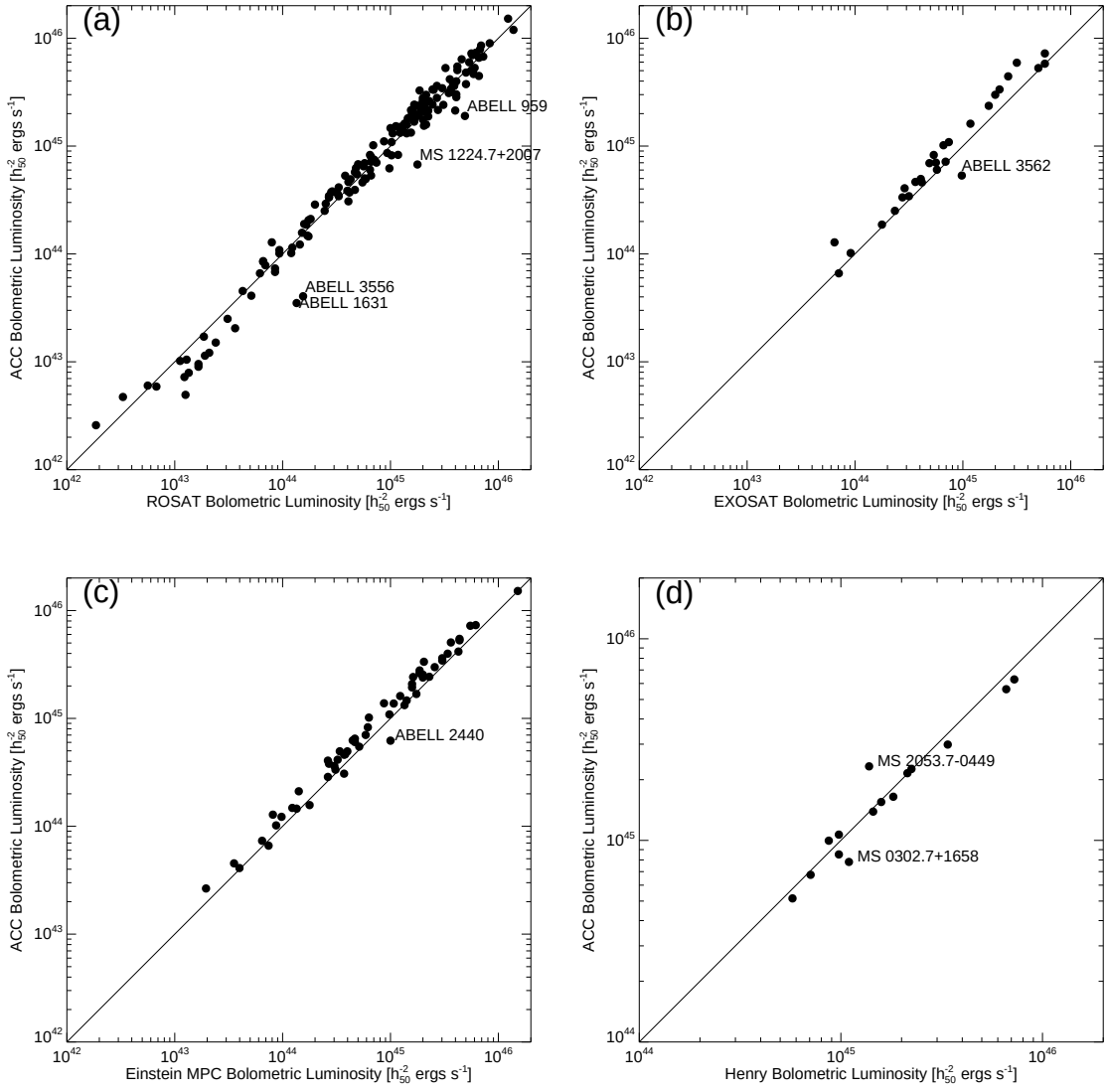

Figure 4.9: Comparison of ACC bolometric luminosity to (a) ROSAT bolometric luminosity (b) EXOSAT bolometric luminosity (c) Einstein MPC bolometric luminosity. (d) ASCA bolometric luminosity from the high redshift sample of Henry (2000).

$0.3Z_{\odot}$, since temperatures and abundances are not generally known. We have recalculated the RASS bolometric luminosities using our ASCA temperatures and metal abundances. For the EXOSAT and Einstein luminosities, we used those given by the authors, corrected to the same cosmology. For the Henry (2000) ASCA data, we converted his 2–10 keV luminosities to bolometric luminosities using the temperatures given in his paper and an abundance of $0.3Z_{\odot}$.

If we had not applied the correction factor to the ACC luminosities, the comparisons would have a slope roughly $\propto L_{REF}^{1.1}$, with a noticeable decrease at lower luminosities. Therefore, our simple method for correcting the luminosities improves our results. A slight systematic trend for the ACC luminosities to be lower than the RASS at lower luminosities (i.e., for groups) is evident, but these are usually low flux systems where the RASS luminosities are based on relatively few counts. We will discuss the situation for groups in more detail below.

On average, the ACC luminosities are ≈5% higher than the Henry and RASS luminosities. If we consider only luminosities $\gtrsim 10^{44}$erg s^{-1}, this increases to ≈10% for the RASS luminosities. However, the EXOSAT and Einstein luminosities are about 20% lower that our ACC luminosities over the whole range. This may indicate calibration issues between the instruments. Disagreement between Einstein and ROSAT fluxes for EMSS clusters has been noticed by others (e.g., Jones et al. 1998; Henry 2000). Resolving this issue will take a more detailed study of calibration and systematic issues beyond the scope of this thesis. Normalization differences will not substantially change our science results.

Figure 4.9a shows that Abell 959, Abell 1631, Abell 3556, and MS 1224.7+2007 have much higher RASS luminosities. Abell 959 and MS 1224.7+2007 have other x-ray sources nearby which may be contaminating the RASS measurement. The emission from Abell 3556 and Abell 1631 is diffuse and complex. The luminosity for these clusters is therefore more difficult to quantify. A ROSAT HRI observation also shows that Abell 1631 contains a point source.

The EXOSAT luminosity for Abell 3562 and Einstein luminosity for Abell 2240 may be contaminated by extra emission from other sources in the field-of-view. Although our agreement with Henry's high redshift sample is quite good overall, two clusters, MS 2053.7-0449 and MS 0302.7+1658, are different by ≈50%. These are the two faintest clusters in the Henry sample ($f_x(0.5-2.0\text{keV}) \lesssim 3 \times 10^{-13}$ erg cm^{-2} s^{-1}). We have not been able to understand the exact cause of the discrepancy. Henry used local backgrounds and treated the clusters as point sources for computing ARFs, but this hardly affects the luminosities. However, since we are concerned about the global properties of clusters rather than the detailed properties of individual objects, the disagreement is not of great concern to us. In fact, the generally good agreement for these faint, high redshift objects is encouraging.

Most of the clusters in the ACC have a large number of counts, so the luminosity errors are dominated by the systematics, such like the luminosity correction and calibration uncertainties. The dispersion in the comparison with other samples is fairly uniform around ≈20% which we take a rough estimate of the non-systematic error in our luminosities.

4.3.2 Groups

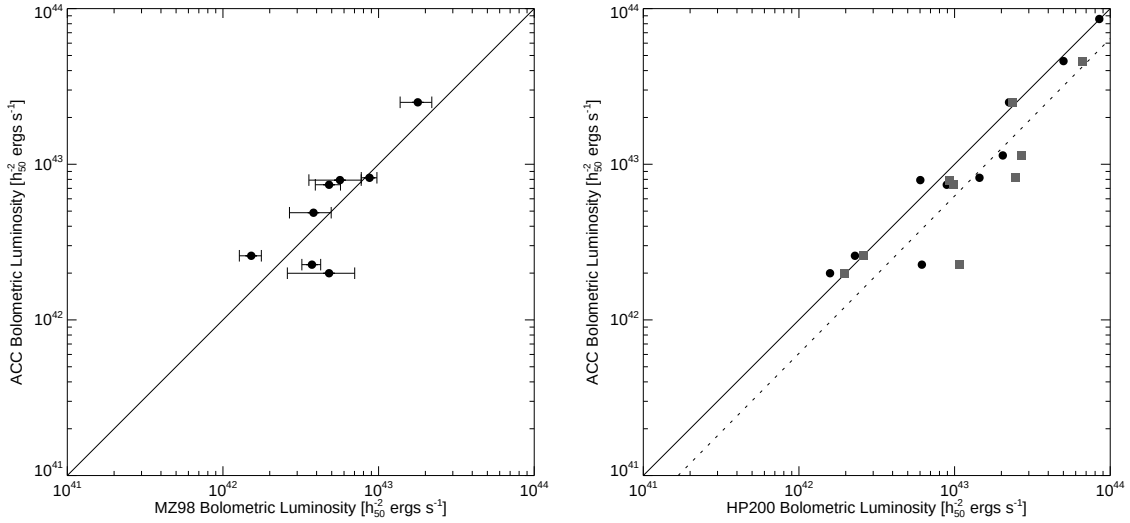

Figure 4.10: Comparison of ACC bolometric luminosity to (left) ROSAT PSPC bolometric luminosity from Mulchaey & Zabludoff (1998) (right) ROSAT PSPC bolometric luminosity from Helsdon & Ponman (2000b) for their corrected (gray boxes) and uncorrected luminosities (solid circles) (see text).

A number of problems are inherent in estimating the x-ray luminosity of groups. Group emission is generally fainter and seen out to a smaller fraction of the virial radius than for clusters. The luminosity corrections are corresponding larger for groups. Groups are also more likely have diffuse emission significantly contaminated by unrelated sources. The fraction of emission associated with the diffuse gas versus individual galaxies is not always clear. ASCA brings additional problems compared to studies like MZ and HP which use the ROSAT PSPC. ASCA is less sensitive to the soft x-ray emission from groups and our extraction radii are 2–4 times smaller in many cases. ROSAT studies can also mask out other x-ray sources in the group and estimate the missing flux from the masked out regions

using a surface brightness profile. ASCA's PSF makes it difficult to mask out any sources.

In Figure 4.10, we compare our luminosities to the MZ and HP samples (for MZ we use their "central+extended" values). Given the small number of clusters in common the agreement is fairly good but with a great deal of scatter. However, the MZ and HP values are only luminosity within their extraction radius for each group. Although larger than ours, their extraction radii are still only $\sim$1/2 the virial radius of the groups.

HP also give a corrected luminosity based on their fits to the surface brightness, which they modeled as a double–β profile. This is the sum of two β profiles, one for the center of the group (i.e., the central dominant galaxy) and one for the extended emission. This leads to shallower β values for the extended emission and therefore a larger correction than for single β fits. Comparing their corrected luminosities to ours improves the agreement in some cases while in others their luminosities become much larger. Given the low surface brightness of groups, the amount of flux that is actually being missed by either ASCA or the PSPC is difficult to estimate. Resolving this issue will be left to improved instruments like XMM.

4.4 Conclusions

We have seen in this chapter that our ASCA measurements agree well with previous ones. Differences in method and models are not a large factor in determining x-ray temperatures to $\sim$20% or better for ASCA data. Our ACC temperatures also agree just as well, or even better, with BeppoSAX temperatures than they do with other ASCA measurements. The ROSAT PSPC, however, shows a systematic bias at $T_{\rm x} \gtrsim 1$ keV, giving lower temperatures than ASCA. Metal abundance seems to be more dependent on the regions used, the reduction methods, and the instrument used to measure it. In particular, ROSAT PSPC abundances should be interpreted with caution. Our x-ray luminosities agree well with ROSAT and other ASCA luminosities, but we find systematically higher luminosities than both EXOSAT and the Einstein MPC. Group luminosities need to be interpreted with caution as we may be missing a significant fraction of flux from some groups.

Overall, we have shown that our ASCA cluster catalog is a high quality source of x-ray information on clusters and groups. In the following chapters, we discuss some of the science results that can be obtained with the ACC.

Chapter 5

The X-ray Luminosity – Temperature Relation

5.1 Introduction

The x-ray luminosities and temperatures of galaxy clusters have long been known to be strongly correlated, roughly as $L_{\rm bol} \propto {T_{\rm x}}^3$ (e.g., Mushotzky 1984; Edge & Stewart 1991b; David et al. 1993) although with a large amount of scatter. The $L_{\rm x} - T_{\rm x}$ relationship is an important diagnostic of the state of the gas in clusters. The average x-ray temperature primarily reflects the depth of the (dark matter) potential well in which the gas resides and is closely tied to the total cluster mass. On the other hand, the x-ray luminosity depends not only on the amount of x-ray gas but also on how it is distributed within the cluster. The distribution of the gas can be modified by heating (e.g., by supernovae or AGN) or cooling (e.g., galaxy formation) of the gas that may happen during cluster evolution.

The $L_{\rm x}-T_{\rm x}$ is usually parameterized by a power law ($L_{\rm bol} \propto {T_{\rm x}}^{\alpha}$). The observed relationship is steeper than the expected $\alpha = 2$ for gas that has fallen into the potential well of clusters and heated up through shocks. It also has a great deal of intrinsic dispersion (i.e., not due to measurement errors). Attempting to explain the observed slope and dispersion has motivated a large number of theoretical and observational investigations.

In this chapter, we examine the $L_{\rm x}-T_{\rm x}$ relationship using data from our ASCA cluster catalog. Our $L_{\rm x} - T_{\rm x}$ is the first homogeneous sample to be well populated on all scales, so we can consider the properties of the population as a whole rather than concentrating solely on rich clusters or groups, as has often been the case. In Section 5.2 and Section 5.3, we review the theoretical underpinning of the $L_{\rm x} - T_{\rm x}$, the results of numerical simulations, and previous observational results regarding the $L_{\rm x} - T_{\rm x}$. In Section 5.4, we discuss the slope of the $L_{\rm x} - T_{\rm x}$. In Section 5.5, we examine the dispersion in the $L_{\rm x} - T_{\rm x}$ relationship and how it correlates with other cluster properties. In Section 5.6, we examine of evolution of the $L_{\rm x} - T_{\rm x}$ relationship with redshift. Lastly, in Section 5.7 we summarize our results and

discuss what they tell us about the nature of clusters of galaxies.

5.2 Theory

The x-ray luminosity of clusters can be represented as (e.g., Arnaud & Evrard 1999):

$$L_{\rm bol} \propto f_{gas}^2 \, M(T_{\rm x}) \, \langle \rho \rangle \; \Lambda(T_{\rm x}) \, Q(T_{\rm x}) \tag{5.1}$$

where f_{gas} is the gas mass fraction (i.e., the baryon fraction of the cluster since most of the baryons are in the gas), M is the total mass of the cluster, $\langle \rho \rangle$ is the average density of the cluster, Λ is the radiative cooling function, and Q is a form factor which depends on the shape of the gas density distribution (i.e., β and r_c for a β-model parameterization, see Equation 1.8).

The standard theoretical expectation for the $L_{\rm x} - T_{\rm x}$ relies on a number of assumptions. Gas fractions are assumed to be constant because clusters are thought to be "fair samples" of the universe. For bremsstrahlung emission, $\Lambda \propto {T_{\rm x}}^{1/2}$, and for clusters in virial equilibrium $M \propto {T_{\rm x}}^{3/2}$. Spherical collapse models and numerical simulations suggest that the average cluster density is about 200 times the background density at the virial radius (i.e., this is the threshold necessary for collapse to occur). Q is expected to be constant since the gas density is expected to trace the underlying dark matter distribution, and in the hierarchical model of structure formation, clusters are believed to have similar gravitational potentials when scaled to their virial radii (see e.g., Navarro et al. 1996). This leads to a predicted scaling between luminosity and temperature of $L_{\rm bol} \propto {T_{\rm x}}^2$. This scaling is also found by hydrodynamical simulations (e.g., Evrard et al. 1996; Bryan & Norman 1998) of cluster formation and evolution.

The fact that the observed slope is significantly steeper implies that at least one of these assumptions is wrong. However, virial equilibrium ($M \propto {T_{\rm x}}^{3/2}$ or close to it) is supported by numerical simulations and observations (the M–T relationship is covered in detail in Chapter 7), as is assumption that $\langle \rho \rangle$ is approximately constant. Variations in the cooling function are unlikely to be a significant effect, at least for $T_{\rm x} \gtrsim 2$ keV. At lower temperatures, line emission can be a significant fraction of the flux (for metal abundances on the order of solar), but the effect of the additional line emission is to increase x-ray luminosity for a given temperature which would tend to flatten the relationship, not steepen it.

One possibility is a systematic change in the gas fraction with mass. However, the gas has fallen into the cluster from large distances (∼20 Mpc) and should represent the general properties of matter in the universe. Various theories have attempted to find a mechanism that would change the gas fraction as a function of mass (e.g., David & Blumenthal 1992; Bryan 2000) usually by inhomogeneous

cooling and star formation, which would remove gas from the ICM. However, observational evidence points to no systematic changes in the gas fractions of clusters, at least for clusters with $T_{\rm x} \gtrsim 5$ keV (e.g., Mohr et al. 1999; Ettori & Fabian 1999; Roussel et al. 2000; Grego et al. 2001). Some authors have reported lower gas fractions for cooler clusters (Mohr et al. 1999; Arnaud & Evrard 1999), but this has been disputed Roussel et al. (2000).

If clusters are in virial equilibrium and the gas fractions are constant, all that is left is a change in the gas density distribution, which requires some non-gravitational mechanism that can modify the gas distribution. Many theories have focused on nongravitational heating of the gas by winds from supernovae or active galactic nuclei (e.g., Cavaliere et al. 1997; Balogh et al. 1999; Loewenstein 2000; Wu et al. 2000; Bower et al. 2001). In basic terms, the energy injected into the ICM decreases the gas density at the cluster center and depresses the x-ray luminosity. This process has a progressively larger effect on lower mass (hence lower temperature) systems because of the lower pressures in smaller clusters and groups. The effect can also be viewed in terms of entropy. The heating raises the entropy of the gas to a fixed, minimum level creating an apparent entropy "floor" in the centers of groups and clusters. Some observational evidence exists supporting the presence of such a floor (Ponman et al. 1999).

When and where the excess energy was injected are still uncertain, as is the source of the energy. Models can generally be divided into two classes: external heating (or preheating) scenarios in which the gas was heated at high redshift before collapsing into the cluster (e.g., Cavaliere et al. 1997; Balogh et al. 1999; Tozzi et al. 2000; Tozzi & Norman 2001) and internal heating where the gas is heated after some or most of it is already in the cluster (e.g., Loewenstein 2000; Brighenti & Mathews 2001). Both scenarios are able to reproduce, at least roughly, the observed $L_{\rm x}-T_{\rm x}$ although the energy requirements are still uncertain. For example, most theories assumed that the energy source is supernovae, and significant energy injection to the gas could have been made when the gas was enriched with heavy elements. However, supernovae heating may be insufficient, and some or most of the heating could be due to other sources, such as QSOs (Valageas & Silk 1999; Kravtsov & Yepes 2000; Fujita 2001).

5.3 Observations

A great deal of work has recently focused on reducing the dispersion in the $L_{\rm x}-T_{\rm x}$ and/or determining the "intrinsic" slope, usually by attempting to remove the effects of cooling flows. Fabian et al. (1994) first suggested that the scatter in the $L_{\rm x}-T_{\rm x}$ is due to cooling flows in clusters (see Section 1.2.5 for a review of cooling flows) with cooling flow clusters being more luminous than non-cooling

flow clusters for a given mean temperature. They found that the residuals in the $L_{\rm x} - T_{\rm x}$ relation were correlated with the mass deposition rate ($\dot{M}$) such that $L_{bol} \propto \dot{M}^{0.4} {T_{\rm x}}^{3.3}$. Allen & Fabian (1998a) applied a multiphase model to explicitly account for the cooling flow to a sample of 24 rich, luminous clusters. They derived "corrected" luminosities and temperatures for cooling flows clusters and found that the dispersion in the relationship was reduced and that the slope of the $L_{\rm x} - T_{\rm x}$ flattened to $\alpha \approx 2$, similar to theoretical expectations.

Markevitch (1998) used a sample of 35 rich clusters with ROSAT luminosities and ASCA temperatures to study the $L_{\rm x} - T_{\rm x}$ and temperature function of clusters. Markevitch derived his temperatures and luminosities from the ASCA and ROSAT data, respectively, by excluding the central $100 h_{50}^{-1}$ Mpc. He found that the scatter was greatly reduced ($\sigma_{log\,L} = 0.10$) and a slope of $\alpha = 2.64 \pm 0.16$. Arnaud & Evrard (1999) found $\alpha = 2.88 \pm 0.15$ for 24 "weak" cooling flow clusters ($\dot{M} \leq 100 M_{\odot}$ yr^{-1}) with temperatures ($T_{\rm x} \geq 2$ keV) measured primarily by the GINGA satellite.

At the other end of the mass scale, Mulchaey & Zabludoff (1998) found that the $L_{\rm x} - T_{\rm x}$ for their sample of poor groups was consistent with an extrapolation of the rich cluster $L_{\rm x} - T_{\rm x}$ ($\alpha \approx 3$). However, Ponman et al. (1996) reported that Hickson's Compact Groups (HCGs) follow a steeper relation $\alpha \sim 8$. Subsequently, Helsdon & Ponman (2000b) have found a steepening of the $L_{\rm x} - T_{\rm x}$ at group scales to $\alpha \approx 5$ for both poor and compact groups. These results have stimulated a great deal of theoretical work to explain this additional steepening (e.g., Cavaliere et al. 1997; Balogh et al. 1999; Bryan 2000).

Several studies have also looked at the evolution of the $L_{\rm x} - T_{\rm x}$ with redshift. So far, observations have excluded significant evolution to $z \sim 0.5$ (Mushotzky & Scharf 1997; Fairley et al. 2000), and observations of individual high redshift clusters ($z \gtrsim 0.8$) usually find that they are consistent with the low redshift $L_{\rm x} - T_{\rm x}$ (e.g., Donahue et al. 1999). The expected evolution of the $L_{\rm x} - T_{\rm x}$ is dependent on the details of the cosmological model. In a closed universe, where gravity dominates the evolution of the gas and dark matter, the relationship between luminosity and temperature should change as a function of redshift. The lack of evolution of the $L_{\rm x} - T_{\rm x}$ is expected in low Ω models where clusters formed early. However, heating of the ICM can also make the redshift evolution of the $L_{\rm x} - T_{\rm x}$ relation slower or absent (Evrard & Henry 1991), so for a given cosmology, the observed evolution also constrains theories of nongravitational heating.

5.4 The Slope of the $L_{\rm x} - T_{\rm x}$ Relation

Figure 5.1 shows the $L_{\rm x} - T_{\rm x}$ relationship based on our ACC data. The correlation is obvious and extends over four orders of magnitude in luminosity. However, the large dispersion in both luminosity and temperature is also quite evident. We only

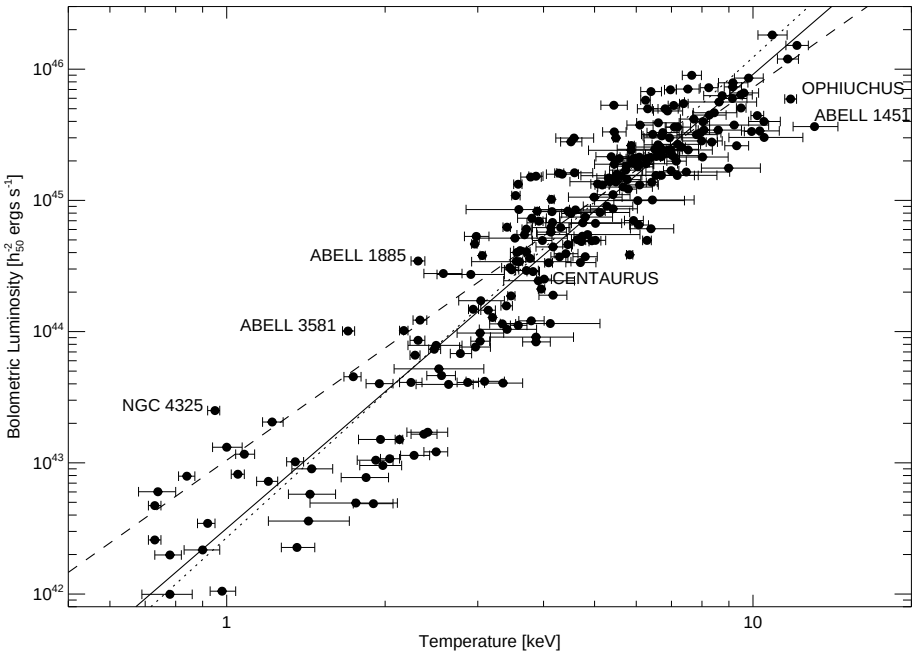

Figure 5.1: The Bolometric Luminosity – Temperature Relation. The solid line is the best fit line to the entire sample. The dashed line is a fit to clusters with $L_{\rm bol} > 2 \times 10^{44}$ erg s^{-1}. The dotted line is a fit to clusters with $L_{\rm bol} \leq 2 \times 10^{44}$ erg s^{-1}. Error bars on the temperatures are 90% confidence limits.

consider those clusters with temperature errors ($\Delta T/T$ for the 90% confidence limits) less than 25% and reduced χ^2 values of less than 1.5, leaving a total of 246 clusters in the sample. The bias towards observing richer clusters is evident, only 66 clusters have luminosities $L_{\rm bol} \leq 2 \times 10^{44}$ erg s^{-1}.

To fit the relationship, we have adopted the Bivariate Correlated Errors and Scatter (BCES) bisector method of Akritas & Bershady (1996) which takes into account the errors in both variables and the possibility of intrinsic scatter. The best fit to all temperatures is:

$$L_{\rm bol} = 10^{42.50 \pm 0.07} \, T_{\rm x}^{\,3.49 \pm 0.10} \, h_{50}^{-2} \text{ ergs s}^{-1}. \tag{5.2}$$

This result does not greatly depend on the fitting method we use. At the extreme, an unweighted ordinary least squares fit gives a shallower fit $\alpha = 3.3$. The error in luminosity has been assumed to be 20% but is not a large factor in changing the fit.

The relationship does seem to change at lower luminosities ($\lesssim 10^{44}$ erg s^{-1}) and the scatter increases. As we commented in Section 4.3, where we compared our

luminosities to others in the literature, we may be underestimating the luminosity of groups because we are missing flux, but this is unlikely to have a large effect. If we limit our fit to the 179 clusters with $L_{\rm bol} > 2 \times 10^{44}$ erg s^{-1}, we find that the relationship flattens to:

$$L_{\rm bol} = 10^{43.02\pm0.10} {T_{\rm x}}^{2.84\pm0.13} h_{50}^{-2} \text{ ergs s}^{-1}. \quad (5.3)$$

This is consistent with several earlier studies (e.g., David et al. 1993; Arnaud & Evrard 1999; Xue & Wu 2000) which found $\alpha \approx 3$ but were limited to luminous clusters. It is also very close to the value of Arnaud & Evrard (1999) even though we made no attempt to account for cooling flows.

A fit to just the poor clusters and groups ($L_{\rm bol} \leq 2 \times 10^{44}$ erg s^{-1} and $T_{\rm x} \leq 4$ keV) gives a fit similar to the fit to the whole sample $\alpha = 3.66 \pm 0.24$. Helsdon & Ponman (2000b) (hereafter HP) updated the work of Ponman et al. (1996) which found a steepening of the $L_{\rm x} - T_{\rm x}$ for groups. The HP sample consisted of 24 groups observed with the ROSAT PSPC. They reported a slope of $\alpha = 4.9 \pm 0.8$ or $\alpha = 4.2 \pm 0.7$ if they corrected their luminosities to their estimated virial radius (see the discussion in Section 4.3.2). This is steeper than our fits to lower temperature systems. As a check, we fit the HP data using our method and find a slope of $\alpha = 4.80 \pm 0.40$ and $\alpha = 4.60 \pm 0.50$ for their uncorrected and corrected luminosities. This agrees with the HP fit well within the large errors, so the fitting technique is not the source of the discrepancy.

In Figure 5.2, we show the tail end of our $L_{\rm x} - T_{\rm x}$ along with the data from HP. We have only plotted HP's virial luminosities. The HP sample extends to lower luminosities and temperatures than our sample, but it is interesting to note that several of HP's lowest luminosity groups lie quite nicely on an extrapolation of our best fit to the whole ACC sample ($\alpha = 3.5$). In contrast, at higher temperature and luminosities HP's groups nearly all lie above our best fit. At $L_{\rm bol} \sim 10^{43}$ erg s^{-1}, we have groups with temperatures between ≈ 0.7–2.5 keV while HP's groups are all cooler than $\lesssim 1$ keV.

For example, Abell 194 has a temperature of $T_{\rm x} = 2.5$ keV and a luminosity $L_{\rm bol} \approx 10^{43}$ erg s^{-1}. The luminosity from the ROSAT All Sky Survey is 50% higher (Ebeling et al. 1996), but even then it is still lower than that of NGC 4325 which has a temperature of $T_{\rm x} \approx 1$ keV. The temperature and luminosity of NGC 4325 are consistent between the ROSAT PSPC and ASCA. XMM also finds similar values (Mushotzky, private communication). Many of the hotter clusters at $L_{\rm bol} \approx 10^{43}$ erg s^{-1} are classified optically as poor clusters, e.g., from Abell's supplemental catalog or the WBL catalog of poor clusters (White et al. 1999). In contrast, HP's sample are selected from groups optically defined as compact (e.g., Hickson's Compact Groups) or "loose". This seems to point to a bias in the selection of HP's sample which can explain a great deal of the steepening they find.

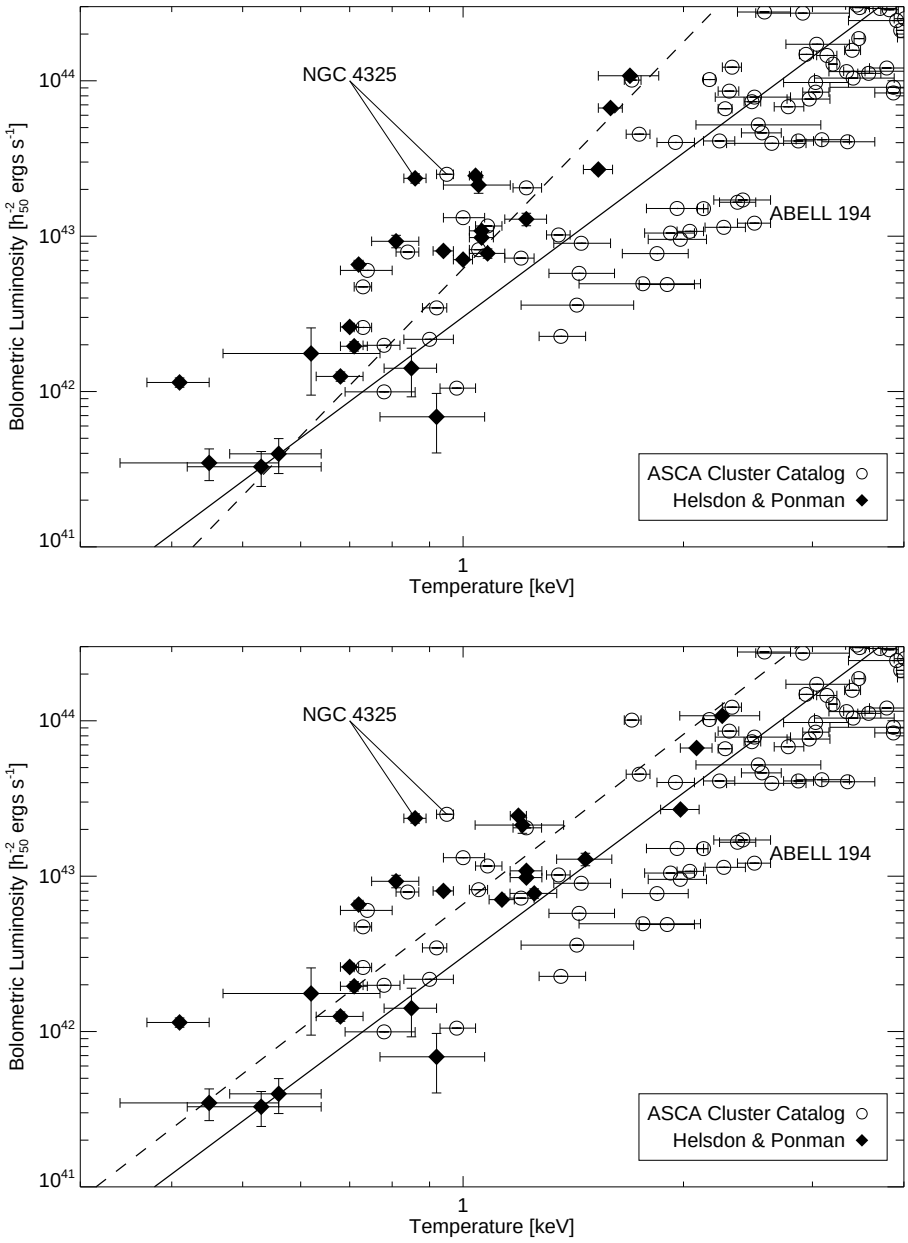

Figure 5.2: The $L_{\rm x} - T_{\rm x}$ for groups. In both panels, the open circles are our ACC data as in Figure 5.1, and the solid line is the best fit to the whole ACC sample given in Equation 5.2 ($\alpha = 3.5$). The diamonds are Helsdon & Ponman (2000b) PSPC temperatures and virial luminosities. The dashed line is a fit the their data. The bottom panel is the same as the top but with a correction to the PSPC temperatures above 1 keV (see text).

The HP results are also biased by the PSPC temperature estimates for the hotter groups in their sample. In Section 4.1.3, we compared our ASCA temperatures with HP's and found that their ROSAT PSPC temperatures were systematically cooler than ASCA's for $T_{\rm x} \gtrsim 1$ keV (see Figure 4.5). If we apply the fit between ASCA and PSPC temperatures given in Equation 4.1 to "correct" HP's PSPC temperatures above 1 keV, we find that this shifts the HP groups over toward our best fit line (see the bottom panel of Figure 5.2). Fitting the temperature corrected HP data, we obtain $\alpha = 3.52 \pm 0.42$ for their virial luminosities. These are consistent within the errors to our fit to the whole sample or the groups sample.

5.5 Dispersion in the $L_{\rm X} - T_{\rm X}$ Relationship

Figure 5.3 shows the residuals of the fit for both luminosity and temperature (i.e., L_{bol}/L_{fit}, the ratio of the luminosity/temperature to the "model" value predicted using Equation 5.2 or Equation 5.3). As can be seen, Equation 5.2 is not the best fit at the upper end of the $L_{\rm x}-T_{\rm x}$ where clusters generally have lower luminosities than would be predicted. Equation 5.3 is a better match. However, the 1σ dispersion in the residuals are not greatly affected by this (see Table 5.1 and Table 5.2).

The dispersion in both temperature and luminosity increases at lower luminosity/temperatures. The dispersion in temperature at a fixed luminosity is relatively constant for luminosities above a few $\times 10^{43}$ at about 20% (see Table 5.2 and Figure 5.3). At lower luminosities, the dispersion doubles to roughly 40%. Furthermore, the nature of the dispersion changes. At $L_{\rm bol} \gtrsim 10^{44}$ erg s^{-1}, the distribution of the clusters around the best fit is reasonably well characterized by a Gaussian while at lower luminosities the distribution around the best fit is fairly flat.

To gain some insight into the origin of the scatter, we now look at other cluster properties to determine if or how they are correlated with the scatter. This will require additional data from the literature (primarily from ROSAT PSPC observations) which are listed in Table A.4 and effectively limit the discussion to richer, most luminous clusters since these are the ones best studied. Therefore, we will consider Equation 5.3 ($\alpha = 2.8$) as our $L_{\rm x} - T_{\rm x}$ relationship.

5.5.1 Cooling Flows

Fabian et al. (1994) found that the mass deposition rate ($\dot{M}$) was correlated with the luminosity residuals such that $L_{bol} \propto \dot{M}^{0.4} {T_{\rm x}}^{3.3}$. They obtained their cooling flow parameters from published EXOSAT and Einstein observations (Edge et al. 1990, 1992; David et al. 1993). We have used cooling flow data from Peres et al. (1998) and Allen & Fabian (1998b) which were determined from deprojection of

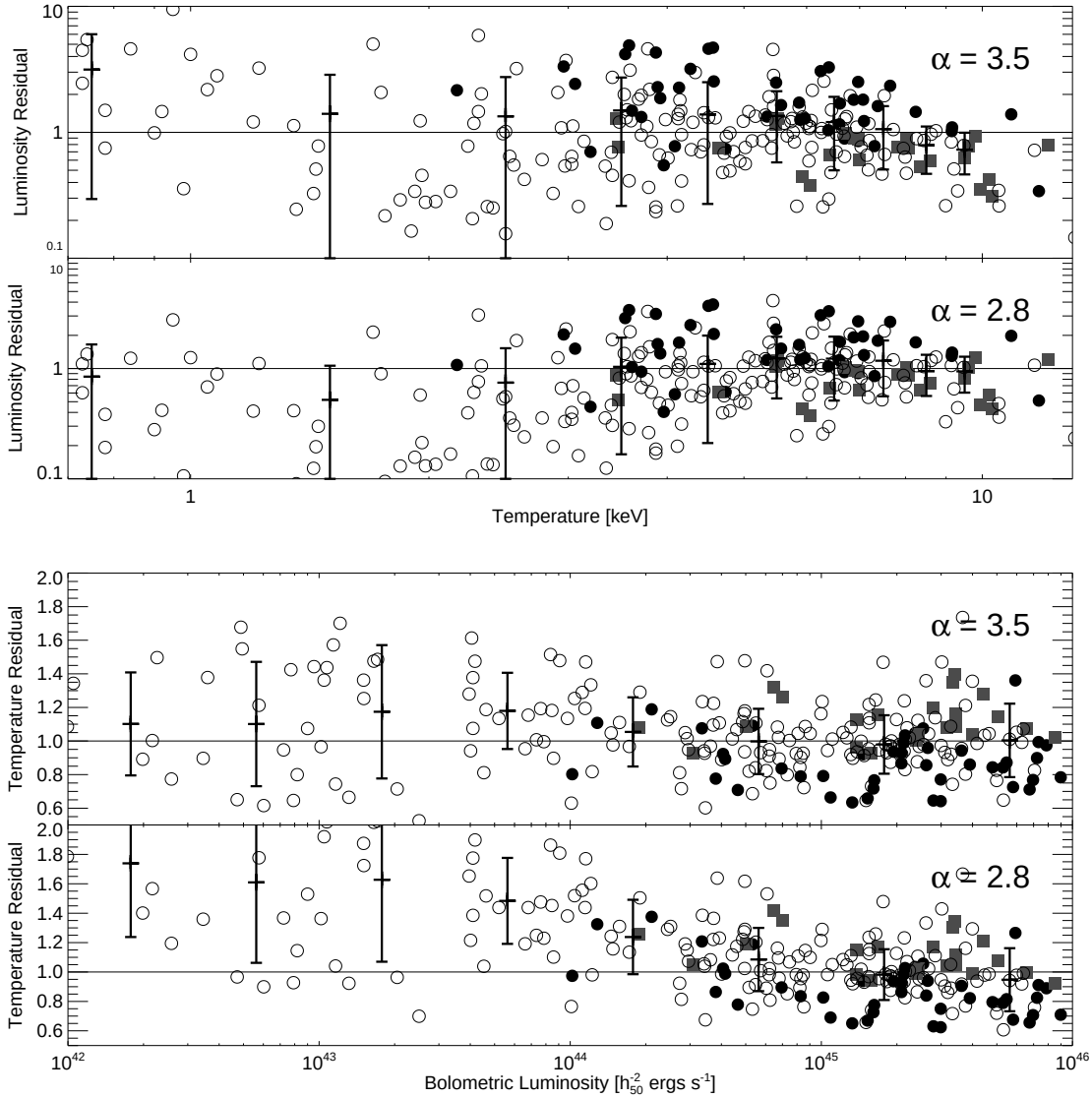

Figure 5.3: (top) The ratio of the luminosity to the best fit luminosity as a function of temperature for $\alpha = 3.5$ and $\alpha = 2.8$. Open circles are individual clusters. Solid circles are known cooling flow clusters. Gray boxes are known non-cooling flow clusters. The error bars represent the 1σ standard deviations of the average residual in 1 keV bins. See Table 5.1. (bottom) The same but showing the ratio of the best fit temperature for a given luminosity to the measured temperature. Bins are $\Delta log(L_{\rm bol}) = 0.5$. See Table 5.2.

Table 5.1: Luminosity Dispersion in the $L_{\rm x} - T_{\rm x}$ Relationship

$T_{\rm x}$ [keV]	$\left\langle \frac{L_{\rm bol}}{L_{\rm fit}} \right\rangle$	1σ	$\left\langle \frac{L_{\rm bol}}{L_{\rm fit}} \right\rangle$	1σ	N
	$\alpha = 3.5$		$\alpha = 2.8$		
0.5–1.5	3.15	2.85	0.84	0.81	10
1.0–2.0	1.40	1.46	0.52	0.54	19
2.0–3.0	1.34	1.40	0.75	0.78	25
3.0–4.0	1.49	1.23	1.04	0.87	41
4.0–5.0	1.38	1.11	1.10	0.89	32
5.0–6.0	1.35	0.77	1.24	0.70	33
6.0–7.0	1.21	0.71	1.23	0.72	39
7.0–8.0	1.06	0.55	1.18	0.62	17
8.0–9.0	0.79	0.32	0.95	0.39	11
9.0–10.0	0.73	0.26	0.94	0.34	10

Table 5.2: Temperature Dispersion in the $L_{\rm x} - T_{\rm x}$ Relationship

$\log(L_{bol})$	$\left\langle \frac{T_{\rm x}}{T_{\rm fit}} \right\rangle$	1σ	$\left\langle \frac{T_{\rm x}}{T_{\rm fit}} \right\rangle$	1σ	N
	$\alpha = 3.5$		$\alpha = 2.8$		
42.0–42.5	1.10	0.31	1.74	0.50	5
42.5–43.0	1.10	0.37	1.61	0.55	13
43.0–43.5	1.17	0.40	1.63	0.56	13
43.5–44.0	1.18	0.23	1.48	0.29	19
44.0–44.5	1.05	0.21	1.24	0.25	24
44.5–45.0	1.00	0.19	1.08	0.22	52
45.0–45.5	0.98	0.17	0.98	0.17	73
45.5–46.0	1.00	0.22	0.95	0.21	43

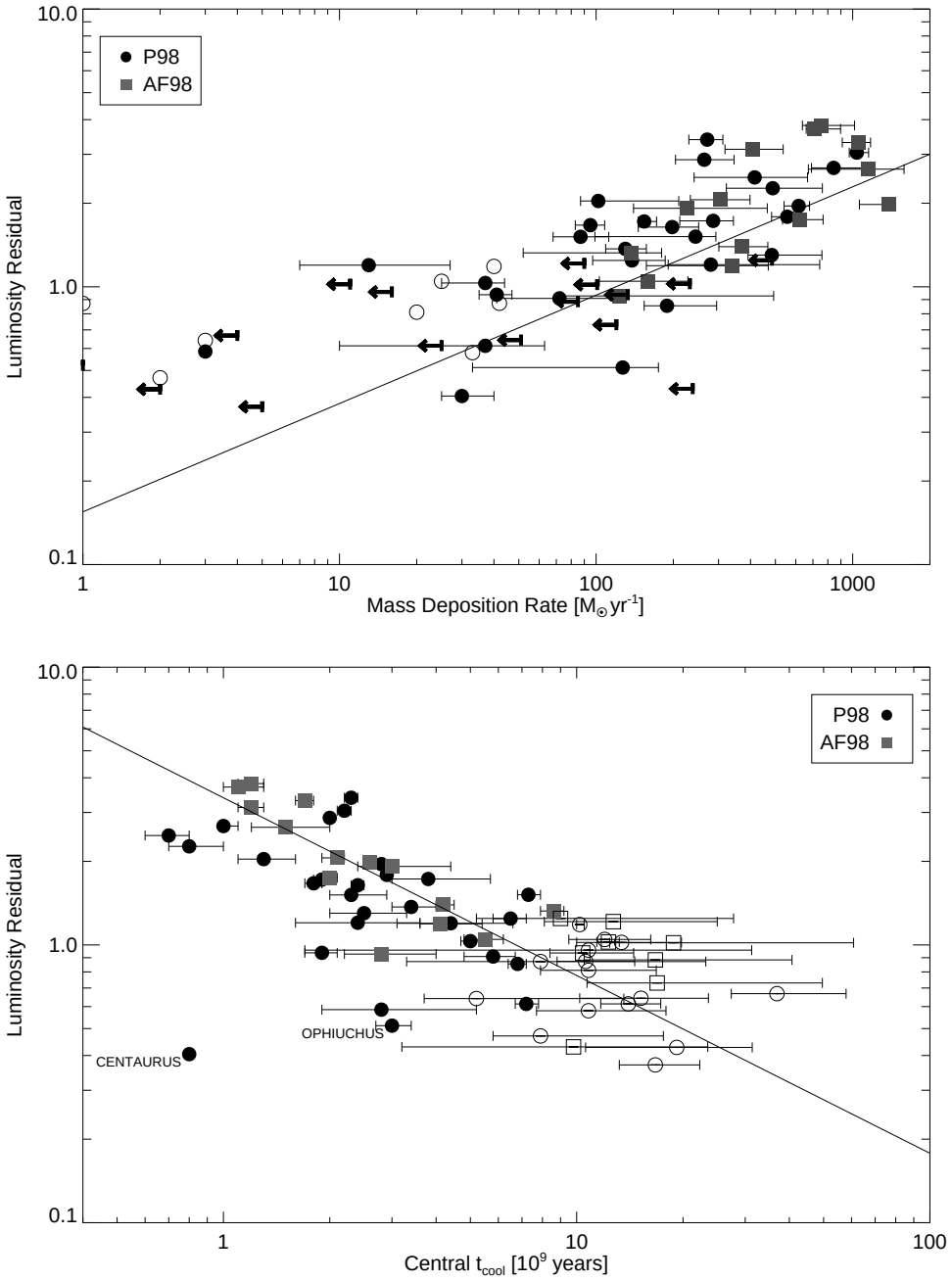

Figure 5.4: The luminosity residuals versus the mass deposition rate (top) and central cooling time (bottom). Circles are data from Peres et al. (1998) while boxes are data from Allen & Fabian (1998a). Filled symbols are cooling flow clusters. Open symbols are non-cooling flow clusters. The arrows are upper limits on $\dot{M}$ for non-cooling flow clusters.

ROSAT PSPC and HRI data. There are 68 clusters in common with our sample, 44 of which are considered cooling flow clusters. We follow the definition of Allen & Fabian (1998b) who consider a cooling flow cluster as one for which the upper 90% confidence limit on the central cooling time is less than 10 Gyr (i.e., a Hubble time).

Like Fabian et al. (1994), we find that cooling flow clusters generally have higher luminosities for a given temperature or cooler temperatures for a given luminosity (see Figure 5.3). In Figure 5.4, we show the correlation between our luminosity residuals and mass deposition rate for the 44 cooling flow clusters. We also plot the upper limits on $\dot{M}$ given for the 24 non-cooling flow clusters. We performed a more general power law fit between $L_{\rm bol}$, $\dot{M}$, and $T_{\rm x}$ using the orthogonal distance regression package (ODRPACK, Boggs et al. 1989) which gives a best fit:

$$L_{\rm bol} = 10^{42.68\pm0.10}\, \dot{M}^{0.38\pm0.04}\, {T_{\rm x}}^{2.35\pm0.15}\, h_{50}^{-2}\ {\rm ergs\ s^{-1}}. \tag{5.4}$$

The 1σ dispersion in the residuals for this fit is 0.32 compared to 0.90 for the same sample using just Equation 5.3. The temperature dependence of the relationship is also much flatter than just a simple fit between $L_{\rm x}$ and $T_{\rm x}$. This difference will be discussed more thoroughly in Section 5.7.

We also find a correlation with the central cooling time. Figure 5.4 shows the luminosity residuals versus central cool time for the 68 cooling flow and non-cooling flow clusters. Cooling flow and non-cooling flow clusters form a fairly continuous population with no breaks or flattening evident. A three parameter fit excluding the outlier Centaurus gives:

$$L_{\rm bol} = 10^{42.90\pm0.14}\, t_{\rm cool}^{-0.51\pm0.07}\, {T_{\rm x}}^{3.52\pm0.19}\, h_{50}^{-2}\ {\rm ergs\ s^{-1}}. \tag{5.5}$$

The 1σ dispersion in the residuals is 0.45, somewhat larger than for the mass deposition rate. The temperature dependence is steeper than Equation 5.3.

5.5.2 Metal Abundance

Scharf & Mushotzky (1997) argued that the dispersion in the $L_{\rm x} - T_{\rm x}$ is linked to the metal (iron) abundance with more metal rich clusters being more luminous for a given temperature. In Figure 5.5, we show the correlation between our luminosity residuals and metal abundance for the ACC. We have limited the comparison to clusters with abundance errors ($\Delta Z/Z$) less than 30%, a total of 120 clusters. We show the $T_{\rm x} > 5$ keV and $T_{\rm x} \leq 5$ keV clusters separately since the abundance and temperature are correlated for cooler clusters in our sample (see Chapter 6 for details). A rough correlation is seen ($L_{bol}/L_{fit} \propto Z^{2.03\pm0.28}$), similar to that of Scharf & Mushotzky (1997), especially for more luminous clusters, but the correlation is not very strong.

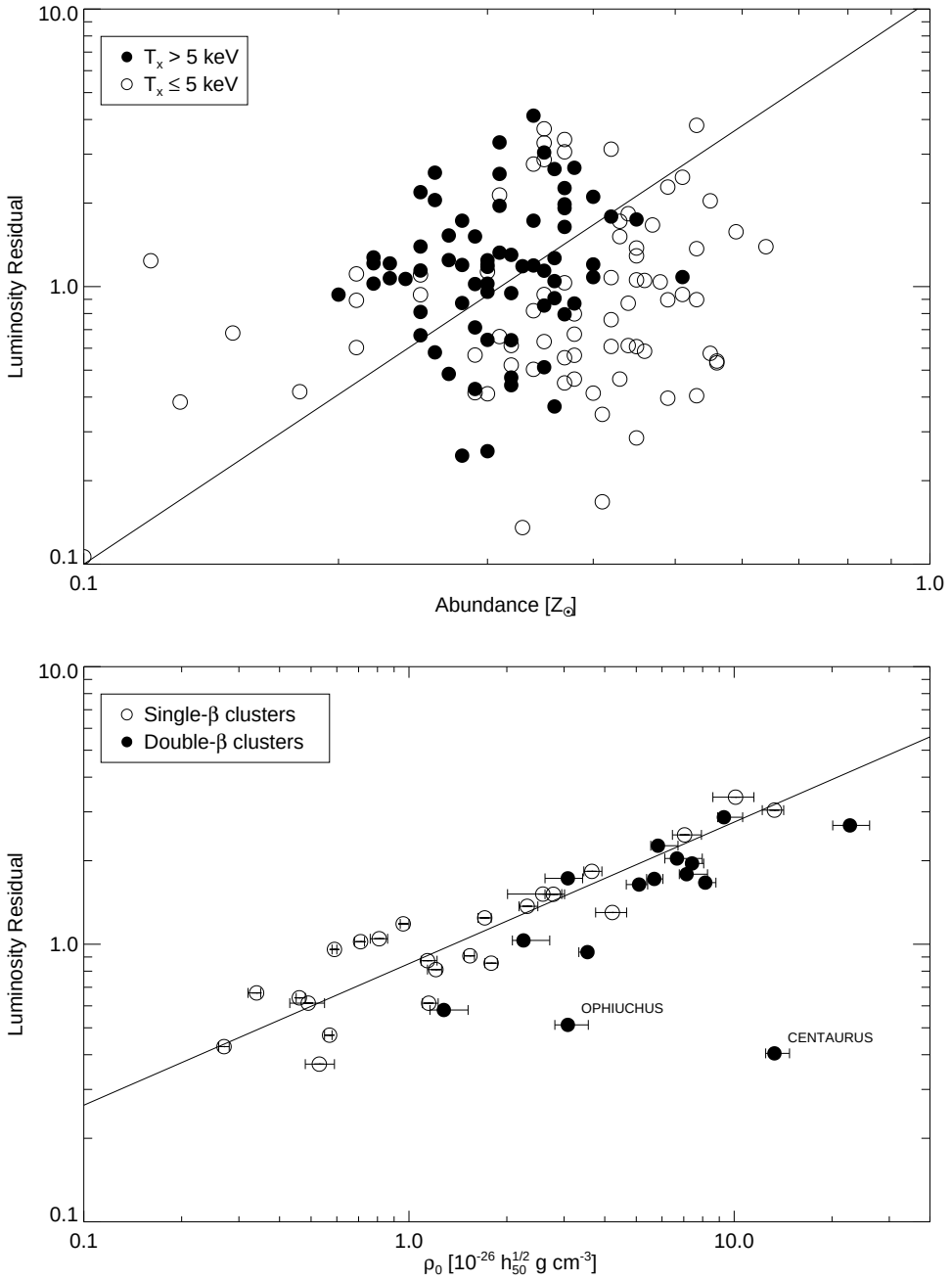

Figure 5.5: (top) The luminosity residuals versus metal abundance. Solid circle are clusters with temperatures > 5 keV. Open circles are clusters with temperatures ≤ 5 keV. Error bars on abundance have been excluded for clarity. (bottom) The luminosity residuals versus central density. Open (solid) circles are clusters fit with a single (double) β model (see text). Error bars are 90% confidence limits.

5.5.3 Central Density

The central cooling time is directly related to the central gas density of the clusters ($t_{cool} \propto \rho_0^{-1}$). The central density cannot be measured directly from x-ray observations but can be inferred from the surface brightness distribution of the gas. Effectively it is defined as the best fit parameter to a β-profile fit to the surface brightness distribution (see Equation 1.8). Note that this is a mass density (i.e., in units of g cm^{-3}) not the number density.

Many authors have fit surface brightness profiles of clusters using ROSAT data (e.g., Mohr et al. 1999; Vikhlinin et al. 1999; Ettori & Fabian 1999; Neumann & Arnaud 1999; Finoguenov et al. 2001) or Einstein data (Jones & Forman 1999). However, most authors only give the spatial parameters, β and core radius, for their fits. We found central densities for 42 clusters in our sample in Mohr et al. (1999) (hereafter MME), who fit β-profiles to PSPC data. The MME sample has the advantage of being a homogeneous sample using an instrument with better spatial characteristics than ASCA or Einstein. We have listed the central densities in Table A.4.

MME added a second β model component to their fits for clusters where they find a central excess that is not well fitted by a single β model to the entire surface brightness profile, e.g., cooling flow clusters. In these "double-β" fits, they constrain the β parameter for both of the central and outer components to be the same while fitting the normalization and core radii separately for each component. Although cooling flow clusters are usually distinguished by a central excess of emission, the correspondence between cooling flow clusters and MME's single versus double β fits is not exact. MME used a single-β fit for 11 of the 27 clusters in their sample considered cooling flows by the criteria of Section 5.5.1.

Figure 5.5 also shows the correlation of the luminosity residuals directly with central density. The clusters fitted with double-β models generally have higher central densities, but no systematic differences are evident in the relationship between the two populations. We excluded Centaurus and Ophiuchus and performed a three parameter fit to find:

$$L_{\rm bol} = 10^{42.76\pm0.12}\, \rho_0^{0.46\pm0.05}\, {T_{\rm x}}^{3.07\pm0.14}\, h_{50}^{-2}\ {\rm ergs\ s^{-1}}. \tag{5.6}$$

The residuals of this fit have a 1σ dispersion of 0.29, similar to those for the mass deposition rate. The temperature dependence is similar to Equation 5.3.

5.5.4 Spatial Distribution

We also looked for correlations with the spatial properties of clusters using the MME sample. No correlation is evident between the residuals and the outer slope

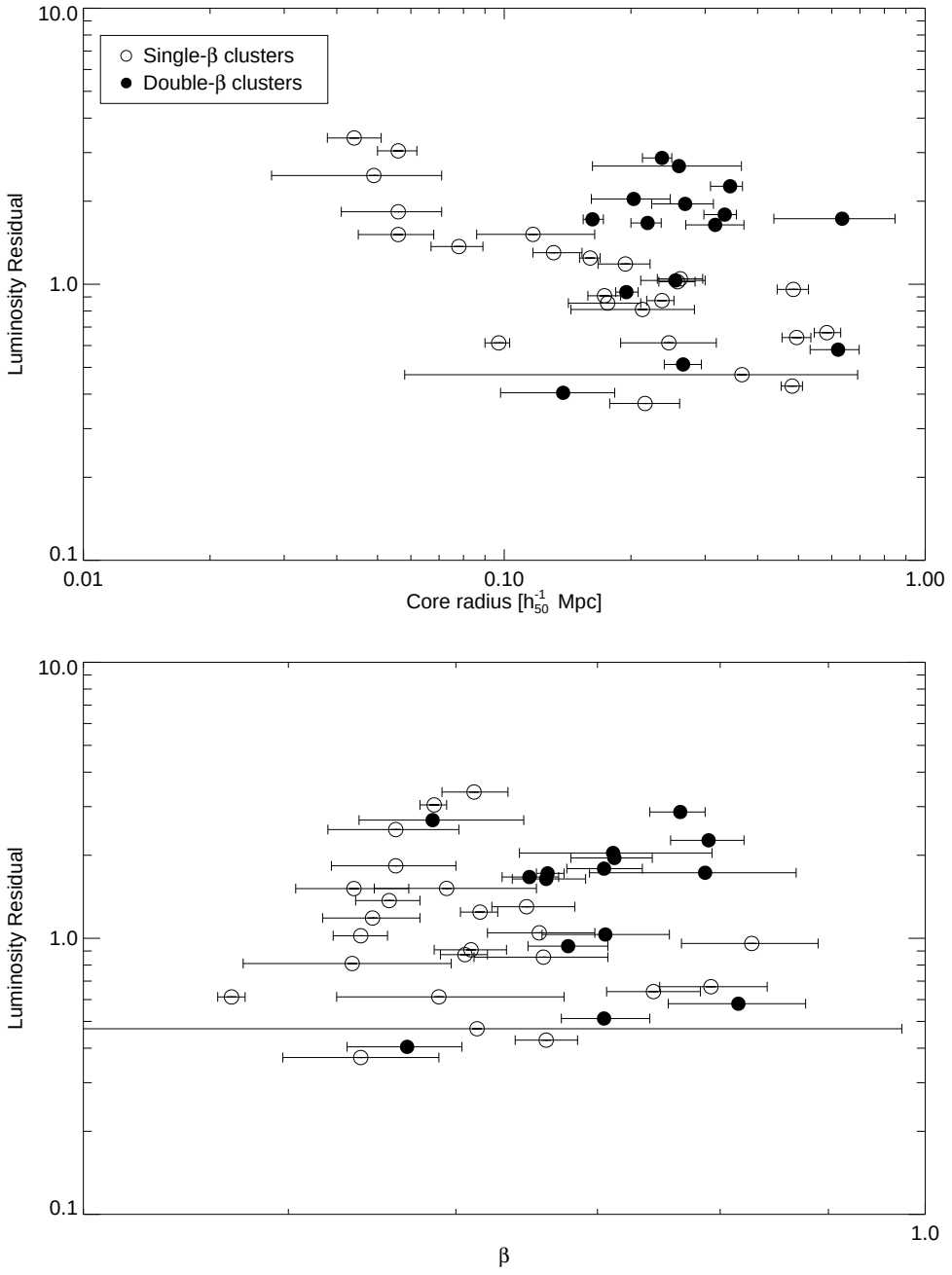

Figure 5.6: (top) The luminosity residuals versus core radius. (bottom) The luminosity residuals versus β. Clusters fitted with a double (single) β-model are filled (open) circles.

parameter β (see Figure 5.6). The core radius for single-β fits does show a correlation with the residuals, but neither the inner nor outer core radius from double-β fits do. However, the MME r_c values are correlated with the ρ_0 values for the single-β clusters, so this may just be an artifact of their fitting procedure.

We also checked other studies which give spatial parameters for clusters (Finoguenov et al. 2001; Vikhlinin et al. 1999; Neumann & Arnaud 1999). Unlike MME, these studies simply excluded the central parts of clusters considered to be cooling flows and just fit the outer parts. None of these samples show a correlation of β with the luminosity residuals and perhaps only weakly see a correlation of r_c with the residuals. However, the fitting method can make a large difference in the derived core radii. In general, the core radii derived by these studies are only consistent for fairly large values ($r_c \gtrsim 0.2$ Mpc).

5.6 Redshift Evolution

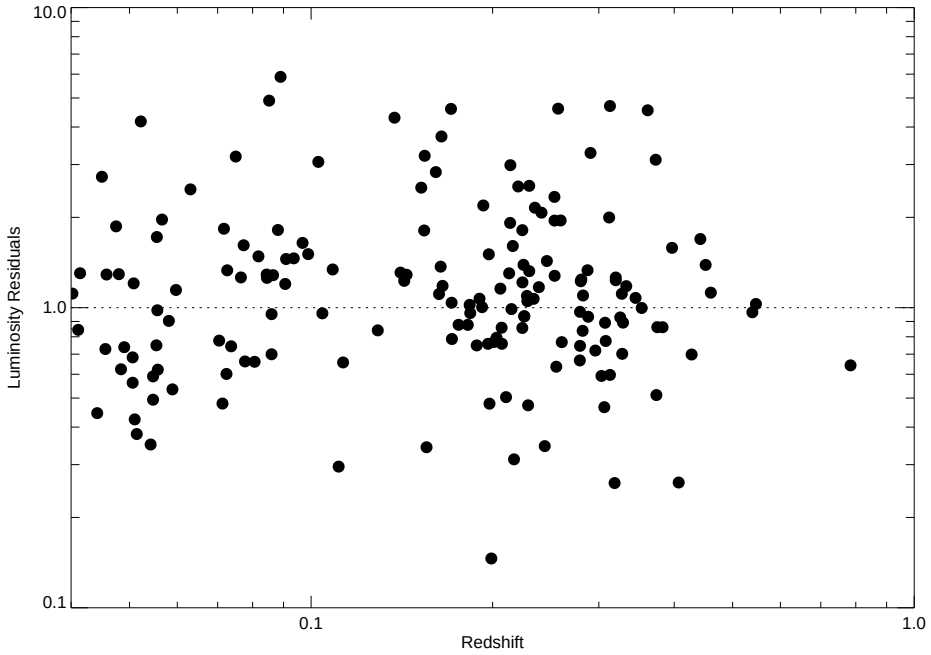

Figure 5.7: Luminosity residuals as a function of redshift.

Now we look at the evolution of the $L_{\rm x}$–$T_{\rm x}$ relationship with redshift. Figure 5.7 shows the luminosity residuals as a function of redshift for clusters with $L_{\rm bol} >$

2×10^{44} erg s^{-1}. No obvious evolution is evident similar to the results of Mushotzky & Scharf (1997). We fit the relation between luminosity, temperature, and redshift and find that:

$$L_{\rm bol} = 10^{43.94\pm0.02} {T_{\rm x}}^{2.98\pm0.14} (1+z)^{0.02\pm0.16} \tag{5.7}$$

which is consistent with no evolution. Note that the dispersion is also fairly constant across all redshifts. The lack of any change in the $L_{\rm x} - T_{\rm x}$ would indicate that the formation redshift of clusters must be high or that the heating of the gas has suppressed any evolution.

5.7 Discussion and Conclusions

In summary, we find that the $L_{\rm x} - T_{\rm x}$ relationship steepens somewhat from $\alpha = 2.8$ at cluster scales to $\alpha \approx 3.6$ at group scales. However, these changes are fairly small and a simple power law with $\alpha = 3.5$ fits fairly well over four orders of magnitude in luminosity. Our slope for rich clusters agrees with other recent estimates (e.g., Arnaud & Evrard 1999; Xue & Wu 2000) even though we have not attempted to minimize the dispersion through cluster selection. We do not see the large steepening to $\alpha \sim 5$ for group reported by Helsdon & Ponman (2000b). We conclude that this is due to selection biases towards optically poor objects in their small sample and to a bias in ROSAT PSPC calibration which gives systematically cooler temperatures for $T_{\rm x} \gtrsim 1$ keV.

The $L_{\rm x} - T_{\rm x}$ relation has a large intrinsic dispersion. We looked for correlations with mass deposition rate, central cooling time, metal abundance, central density, core radius, and outer profile slope β. The dispersion is only weakly correlated with metal abundance and not correlated with β. We quantified these correlations by performing multi-variable fits between $L_{\rm x}$, $T_{\rm x}$, and other clusters properties. In particular, we find that $L_{\rm bol} \propto \dot{M}^{0.38} {T_{\rm x}}^{2.35}$ (Equation 5.4), $L_{\rm bol} \propto t_{\rm cool}^{-0.51} {T_{\rm x}}^{3.52}$ (Equation 5.5), and $L_{\rm bol} \propto \rho_0^{0.46\pm0.05} {T_{\rm x}}^{3.07}$ (Equation 5.6).

However, these relationship are not independent of each other. The central cooling time can be directly related to the central density and temperature, $t_{cool} \propto \Lambda(T_{\rm x})/\rho_0$. For thermal bremsstrahlung, this is then $t_{cool} \propto {T_{\rm x}}^{1/2}/\rho_0$. Substituting this in Equation 5.5 gives a similar relationship to Equation 5.6. The dependence of mass deposition rate on density and temperature is more complicated. The mass deposition rate can be written $\dot{M} \propto L_{cool}/T_{\rm x}$. L_{cool} is the luminosity within the cooling radius, r_{cool}, the radius at which the cooling time is equal to the cluster age. L_{cool} depends on the central density and temperature (e.g, similarly to Equation 5.1).

These dependencies explain why the relationships in Equation 5.4 and Equation 5.5 are flatter and steeper, respectively, than a simple fit between $L_{\rm x}$ and

$T_{\rm x}$. Since $\dot{M}$ and t_{cool} have fairly direct density and temperature dependences, the correlation with the central density would seem to be the primary one. Following Fabian et al. (1994), the dispersion in the $L_{\rm x} - T_{\rm x}$ has usually been assumed to be linked to cooling flows. However, as they point out, the luminosity related to the increased density of the cooling gas is not enough to account for the dispersion by itself. There must be some other underlying difference between cooling flow and non-cooling flow clusters to account for the dispersion. In addition, reasons to doubt the standard cooling flow picture of clusters have come from recent XMM and Chandra observations (Peterson et al. 2001; Kaastra et al. 2001; Tamura et al. 2001) which have failed to find evidence for very cool gas ($T_{\rm x} \lesssim 2$ keV) at the centers of clusters. This implies that our understanding of cooling flows is not well founded and any results predicated on this model (e.g., the mass deposition rate) need to be reexamined (Fabian et al. 2001; Molendi & Pizzolato 2001).

Similar evidence can be found in several previous studies of cooling flow clusters. A cooling flow creates an excess of emission at the cluster center which should come out at soft x-ray energies. Ikebe et al. (1999) found that the central excess emission in Centaurus, interpreted as a cooling flow, was also present over the entire ASCA energy band, although the excess fraction was lower at higher energies. The cooling-flow model, either with or without excess central absorption, did not give acceptable fits to the spectra. Although Centaurus is an outlier in many of our correlations, Xu et al. (1998) saw a similar effect in Abell 1795, which is not.

We can perform a similar, albeit cruder, check with our data. Since ROSAT samples only the soft band (0.1–2.4 keV), bolometric luminosities measurements based on the ROSAT flux for cooling flows should be higher than those based, like ASCA, on a wider band pass. However, we find good agreement between the ASCA and ROSAT luminosities for cooling flow clusters. As a further check, we refit our clusters using only the 3–10 keV band of ASCA, which should not contain much cooling flow emission. We find good agreement between the 0.5–2.0 keV luminosity estimated from the 3–10 keV spectrum and that measured by ROSAT with no systematic difference between cooling flow and non-cooling flow clusters.

Therefore, any interpretation of the scatter in the $L_{\rm x} - T_{\rm x}$ in terms of cooling flows should be done with caution. As we have seen, more luminous clusters for a given temperature have higher central gas densities and smaller core radii. This may indicate that the shape of the gravitational potential in clusters becomes deeper than a King-type profile toward the cluster center. If so, simply excluding the cluster center in fitting surface brightness profiles as done by many authors may not give meaningful results.

This technique was employed by Markevitch (1998) in a study of the $L_{\rm x} - T_{\rm x}$ and temperature function of clusters. Markevitch attempted to minimize the effects of cooling flows on his measurements by excluding a region of 100 h_{50}^{-1}

kpc radius at the center of each cluster. Markevitch used ASCA to measure the temperatures of his clusters. As we showed in Section 4.1, the agreement between our ASCA temperatures and Markevitch's temperatures is quite good on average, even for his "corrected" temperatures. Markevitch used ROSAT data to measure the luminosities for his clusters within 2 h_{50}^{-1} Mpc of the cluster center. He corrected for the flux lost due to the excluded central region by assuming a β-profile with $\beta = 0.6$ and $r_c = 250\ h_{50}^{-1}$ kpc for all clusters. He considers this "corrected" luminosity to be representative of the main cluster gas and finds that the scatter in the $L_{\rm x} - T_{\rm x}$ relationship decreases by about a factor of two.

However, this reduction in scatter should not come as a large surprise. Cooling flow clusters have long been associated with large peaks in the surface brightness profile. If you exclude the central regions and assume that clusters are self-similar (i.e., follow the same density profile in the outer parts, as Markevitch does) then clusters without a large peak will not be greatly affected while clusters with a large peak will have their luminosity greatly decreased. Markevitch's procedure effectively decreases the scatter by construction by getting rid of "extra" luminosity but does not offer any insight into the reasons for the scatter (c.f., Neumann & Arnaud 1999).

The variations with central density may mean that the dispersion in the $L_{\rm x} - T_{\rm x}$ relation reflects a range in cluster formation epoch. In a hierarchical universe, dark matter halos collapse when they achieve a particular overdensity above the background $\delta = \langle\rho\rangle / \rho_c$, where ρ_c is the critical density of the universe, which is a function of redshift $\delta \propto (1+z)^3$. Therefore, clusters which form earlier must be denser because the mean density of the universe is higher at earlier times. Numerical simulations show that the density and density profile of the original halo remains relatively unchanged (e.g., Eke et al. 1998; Bullock et al. 2001) while accreting dark matter forms an extended envelope around it. The original halo is only disrupted in the case of a major merger. This picture is supported by the recent theoretical studies using a modified Press-Schechter formalism (Enoki et al. 2001). Although these arguments are for the dark matter halo, we might expect the gas would follow a similar track. Indeed, Eke et al. (1998) find that the gas density and dark matter profiles of simulated clusters remain proportional to each other regardless of cluster mass or redshift. Therefore, higher central gas densities probably reflect the formation epoch although we are not aware of any simulations or theoretical models which directly show this.

Of course, explaining the dispersion in the $L_{\rm x} - T_{\rm x}$ relationship in terms of central density is only valid if the central densities we use are physically meaningful parameters. These densities are not actually measured at the cluster core but only inferred based on a model relating the surface brightness to the gas density. If the model is seriously in error then the central densities may not reflect the

true conditions of the gas in the cluster core. However, we can rule out obvious problems. For example, the central densities from Mohr et al. (1999) are based on ROSAT PSPC observations of low redshift clusters ($z \approx 0.02 - -0.1$). At these distances, the PSF of the ROSAT PSPC ($\approx 30'$) ranges from about 17 to 75 kpc. However, there is no correlation of the measured central density with redshift, so the resolution of the instrument does not appear to create a bias in the measured densities. The Mohr et al. (1999) central densities are also not obviously correlated with x-ray temperature or luminosity. However, these issues cannot really be addressed with the present data. It will take Chandra or XMM observations to reliably understand the conditions in cluster cores.

Chapter 6

The Metal Abundances of Clusters of Galaxies

6.1 Introduction

The detection of iron lines in the x-ray spectra of clusters (Mitchell et al. 1976; Serlemitsos et al. 1977) provided the best evidence of the thermal origin of the x-ray emission. Today, the metal abundances of clusters (which are primarily driven by the iron abundance) are studied for the clues they provide about several important phenomena, like past star formation and supernovae activity. The presence of metals in the gas provides direct evidence that ICM has been enriched by material lost by galaxies in the course of their evolution. The favored mechanism for ejecting metals from galaxies is supernovae driven galactic winds (e.g., David et al. 1991; Metzler & Evrard 1994), although ram pressure stripping has also been proposed (e.g., Gunn & Gott 1972; Gaetz et al. 1987).

Hatsukade (1989) first suggested that the abundance decreases slightly with increasing temperature. Arnaud et al. (1992) fitted the relationship with a power law for 24 clusters with EXOSAT and GINGA abundances and found that the abundance $Z = (0.61 \pm 0.06)\, {T_{\rm x}}^{-0.37\pm0.06}$. These studies were mainly limited to richer clusters. Renzini (1997) found, for a sample of clusters and groups drawn from the literature, that clusters with temperature $T_{\rm x} \gtrsim 2.5$ keV have similar abundances ($Z \sim 0.3 Z_{\odot}$) with small dispersion while cooler clusters showed an increase in abundance to nearly solar before dropping precipitously to very low values ($Z \lesssim 0.1 Z_{\odot}$) below 1 keV. Similarly, Davis et al. (1999), in their sample of groups observed with ASCA, found that abundance had a steep dependence on temperature below 1.5 keV with $Z \propto {T_{\rm x}}^{2.5\pm0.94}$. They used the anomalously low group abundances to argue for a wind model where gas is expelled from relatively shallow potential well of groups.

Allen & Fabian (1998b) (hereafter AF98) showed that clusters with cooling flows have a higher mean abundances than those without cooling flows. For their sample of 21 cooling flow (CF) and 9 non-cooling flow (NCF) clusters, they find

$Z = 0.34Z_\odot$ for CFs and $Z = 0.21Z_\odot$ for NCFs. Irwin & Bregman (2001) find a similar result for BeppoSAX observations with $Z = 0.37Z_\odot$ for eight CF clusters and and $Z = 0.27Z_\odot$ for four NCF clusters.

ASCA has allowed us to construct a large sample of clusters to study the metal abundances. Our ASCA Cluster Catalog is the largest compilation of cluster and group abundances currently available. In this chapter, we will revisit the correlations of metal abundance with temperature and other cluster properties with our much larger sample. In Section 6.2, we discuss the relationship between metal abundance and x-ray temperature. In Section 6.3 and Section 6.4, we look for correlations between metal abundance and other cluster properties, such as cooling flows and central density. In Section 6.5, we examine the evolution of cluster metal abundances with redshift. Lastly, we summarize our results and draw some conclusions in Section 6.6.

Since abundance is more difficult to measure than x-ray temperature, the errors are corresponding larger. For this chapter, we use only those clusters with abundance errors ($\Delta Z/Z$) less than 25% (using the 90% confidence limits) and reduced χ^2 values of less than 1.5, leaving a total of 119 clusters in the sample.

6.2 Abundance – Temperature Correlation

Table 6.1: Dispersion in Metal Abundance as a Function of Temperature

T_x [keV]	$\langle$Fe$\rangle$ $Z_\odot$	1σ	N
0– 1	0.20	0.09	6
1– 2	0.28	0.13	6
2– 3	0.44	0.08	10
3– 4	0.44	0.08	25
4– 5	0.39	0.06	17
5– 6	0.32	0.05	16
6– 7	0.33	0.05	17
7– 8	0.32	0.05	8
8– 9	0.27	0.04	4
9–10	0.30	0.03	5

In Figure 6.1, we plot metal abundance as a function of x-ray temperature. Abundances are relatively uniform for hotter clusters ($T_x \gtrsim 5$ keV) with an average of 0.31 ± 0.06 but steadily increase to a maximum of $\approx$0.6 around 3 keV before dropping sharply to $\lesssim 0.2$ below 1 keV. This is similar to the relationship reported by Davis et al. (1999) and Renzini (1997) although we see the trend much more

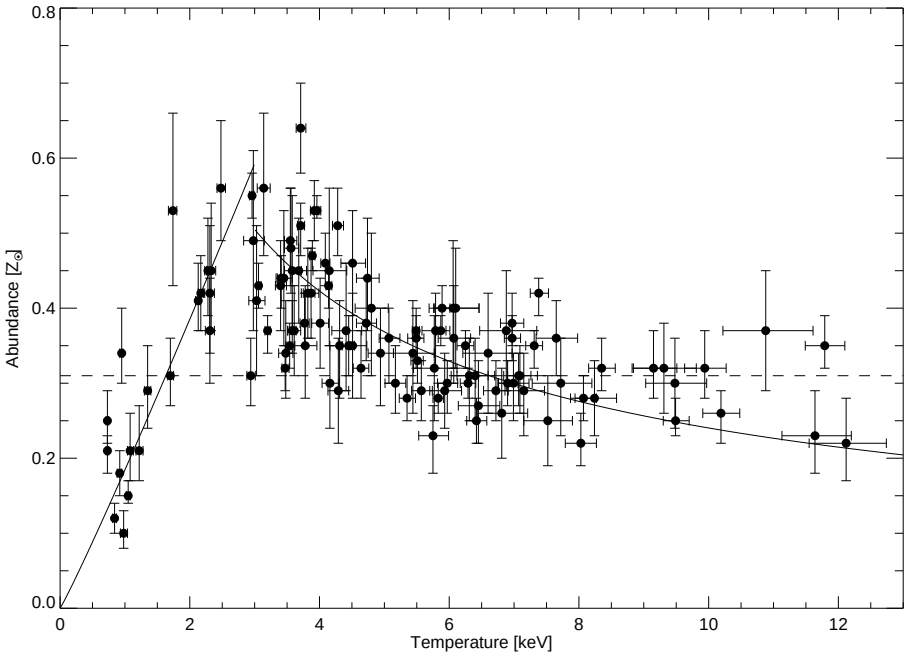

Figure 6.1: Metal abundances as a function of temperature. The solid lines are best fit power laws for $T_{\rm x} > 3$ keV and $T_{\rm x} \leq 3$ keV. The dashed line is the average abundance for clusters with $T_{\rm x} > 5$ keV. Error bars are 90% confidence limits.

clearly. We can also see that the dispersion, the spread in abundances for a given temperature, also increases for cooler clusters and groups (see Table 6.1).

We parameterized the relation by fitting two power laws to the data above and below 3 keV.

$$Z = (0.99 \pm 0.08)\, {T_{\rm x}}^{-0.62\pm0.05}\, Z_\odot \qquad T_{\rm x} > 3\,{\rm keV} \tag{6.1}$$

$$Z = (0.18 \pm 0.02)\, {T_{\rm x}}^{1.06\pm0.13}\, Z_\odot \qquad T_{\rm x} \leq 3\,{\rm keV} \tag{6.2}$$

These are somewhat different than the $Z \propto {T_{\rm x}}^{-0.37\pm0.06}$ for clusters (Arnaud et al. 1992) and $Z \propto {T_{\rm x}}^{2.5\pm0.94}$ (Davis et al. 1999) for groups, but we sample this distribution better than either.

6.3 Cooling Flows

Figure 6.2 shows a histogram of the metal abundances of the clusters in our sample. The average abundance (and the standard deviation) for the whole sample is 0.35 ± 0.09 $Z_\odot$. Figure 6.2 also shows the distribution of abundance for clusters classified as cooling flow and non-cooling clusters. As in Chapter 5, we use the cooling flow data of Peres et al. (1998) along with the data of AF98 (see Table A.4). This gives us 68 clusters in the ACC with cooling flow measurements, 56 of which meet our criteria for $\Delta Z/Z \leq$25%. The NCF clusters have lower average abundances (0.30 ± 0.05 for 18 clusters) compared to the cooling flow clusters (0.39 ± 0.07 for 38 clusters). Our results agree better with Irwin & Bregman (2001) than with AF98. However, if we consider only the AF98 sample we get averages similar to theirs.

The reason for the disagreement with AF98 is that the population of CF and NCF clusters are not truly distinct but form a continuous population with respect to abundance and the cooling time (t_{cool}). AF98 found that their abundances are correlated with the central cooling time, but we see this correlation better with our much larger number of clusters (Figure 6.3). The average abundances of CF versus NCF clusters depends on how you sample the population.

We find that for a power law fit using the BCES method:

$$Z = 10^{-0.31\pm0.02} t_{cool}^{-0.23\pm0.03} Z_\odot. \tag{6.3}$$

The 1σ dispersion of the abundances around the best fit is $\approx$ 18%.

The correlation of abundance with mass deposition rate is not nearly as strong as for the cooling time (Figure 6.3). We find that for a power law fit using the BCES method:

$$Z = 10^{-0.36\pm1.31} \dot{M}^{-0.04\pm0.59} Z_\odot \tag{6.4}$$

which is consistent with no dependence of abundance on the mass deposition rate.

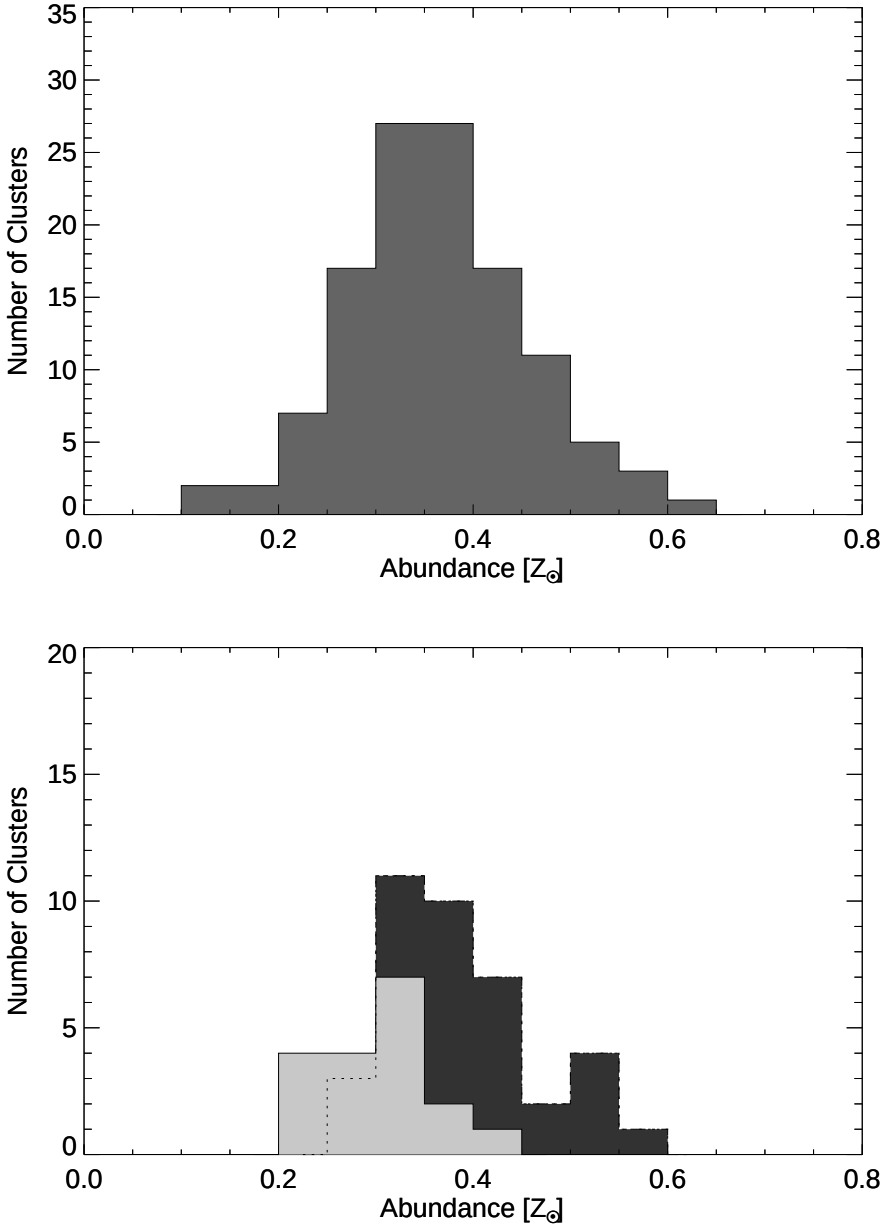

Figure 6.2: (top) The abundance distribution of the sample. (bottom) The darker gray histogram represents cooling flow clusters while the lighter gray histogram represents non-cooling flow clusters.

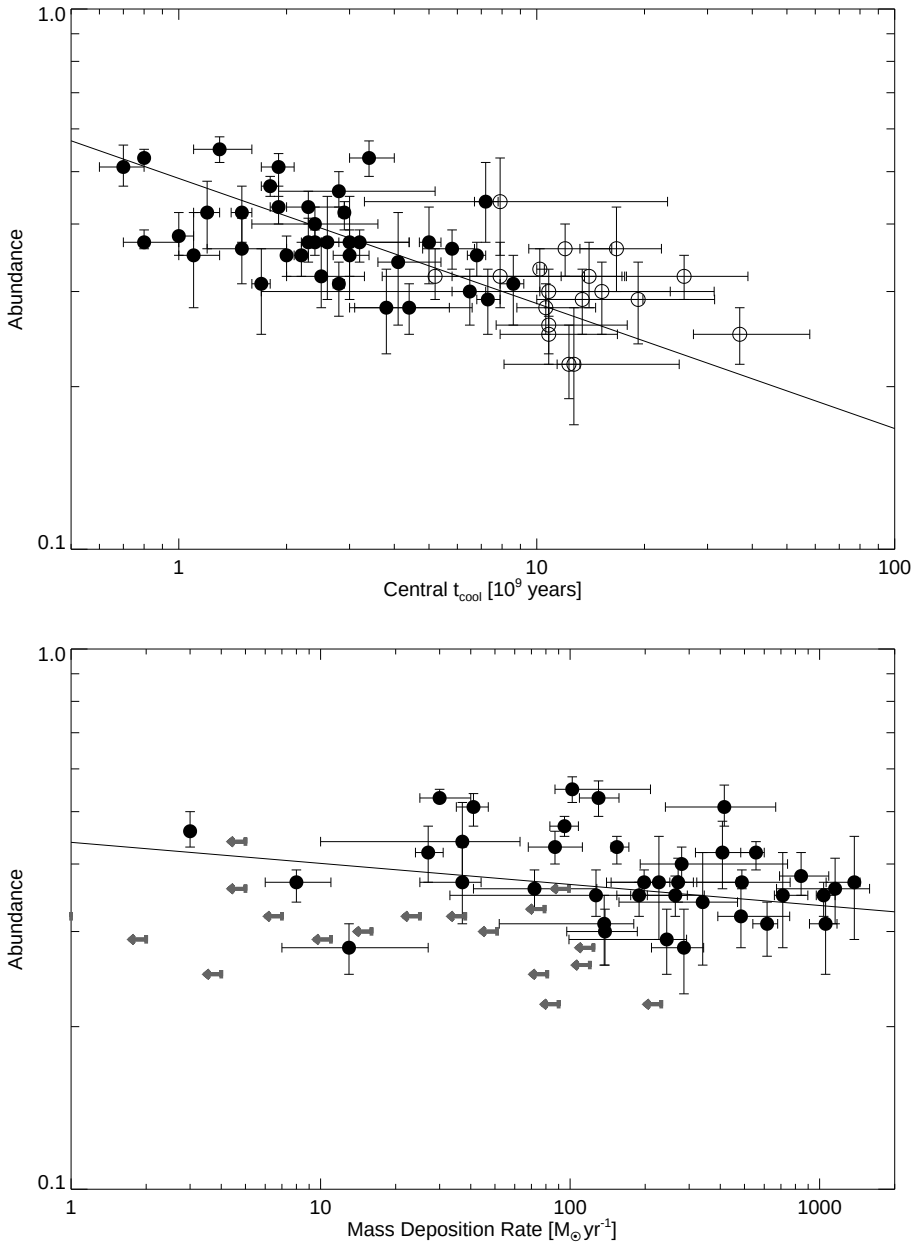

Figure 6.3: (top) The metal abundance as a function of the central cooling time. Solid circles are cooling flow clusters. Open circles are non-cooling flow clusters. The line is a best fit power law. Error bars are 90% confidence limits. (bottom) The metal abundance as a function of the mass deposition rate. The arrows are upper limits on $\dot{M}$ for non-cooling flow clusters. The line is a best fit power law to the cooling flow clusters.

6.4 Central Density and Core Radius

As in Section 5.5.3, we use central densities and spatial properties from Mohr et al. (1999) (hereafter MME). Figure 6.4 shows the correlation between central density and abundance. We find that for a power law fit using the BCES method:

$$Z = 10^{-0.51\pm0.02}\rho_0^{0.19\pm0.03}Z_\odot. \tag{6.5}$$

The 1σ dispersion of the abundances around the best fit is $\approx 21\%$.

There is no obvious correlation of the abundance with the outer slope parameter β. The correlation with core radius is more complicated. As in Chapter 5, clusters fit with a single-β model and double-β model show distinct differences. However, we also see a correlation similar to the single-β relationship for core radii from other data sets (Finoguenov et al. 2001; Vikhlinin et al. 1999; Neumann & Arnaud 1999). We fit the relationship between the single-β core radii and abundance to find:

$$Z = 10^{-0.66\pm0.03}r_c^{-0.24\pm0.04}Z_\odot. \tag{6.6}$$

The 1σ dispersion of the abundances around the best fit is $\approx 15\%$.

We also attempted a three parameter fit similar to those done in Chapter 5 between abundance, central density, and temperature. We find that:

$$Z = 10^{-0.22\pm0.05}\rho_0^{0.07\pm0.02}{T_{\rm x}}^{-0.33\pm0.06}Z_\odot. \tag{6.7}$$

The 1σ dispersion of the abundance around the best fit is 19%, slightly better but not a significant improvement over only fitting the central density by itself.

6.5 Evolution

In Figure 6.5, we have plotted abundance versus redshift. For clarity, we have only shown clusters with $T_{\rm x} > 5$ keV since these are the only ones seen at a large distances ($z \gtrsim 0.1$), and they do not show the systematically higher abundances of cooler clusters seen in Section 6.2. The mean abundance (and standard deviation) is 0.31 ± 0.06 for 69 clusters. We find no strong evidence of evolution of the metal abundance with redshift in agreement with Mushotzky & Loewenstein (1997).

To quantify any possible evolution, we fit the relationship with the standard parameterization of evolution as $(1+z)^\alpha$. We find

$$Z = 0.32 \pm 0.03(1+z)^{-0.25\pm0.76}Z_\odot \tag{6.8}$$

which is consistent with no evolution within the 1σ uncertainties.

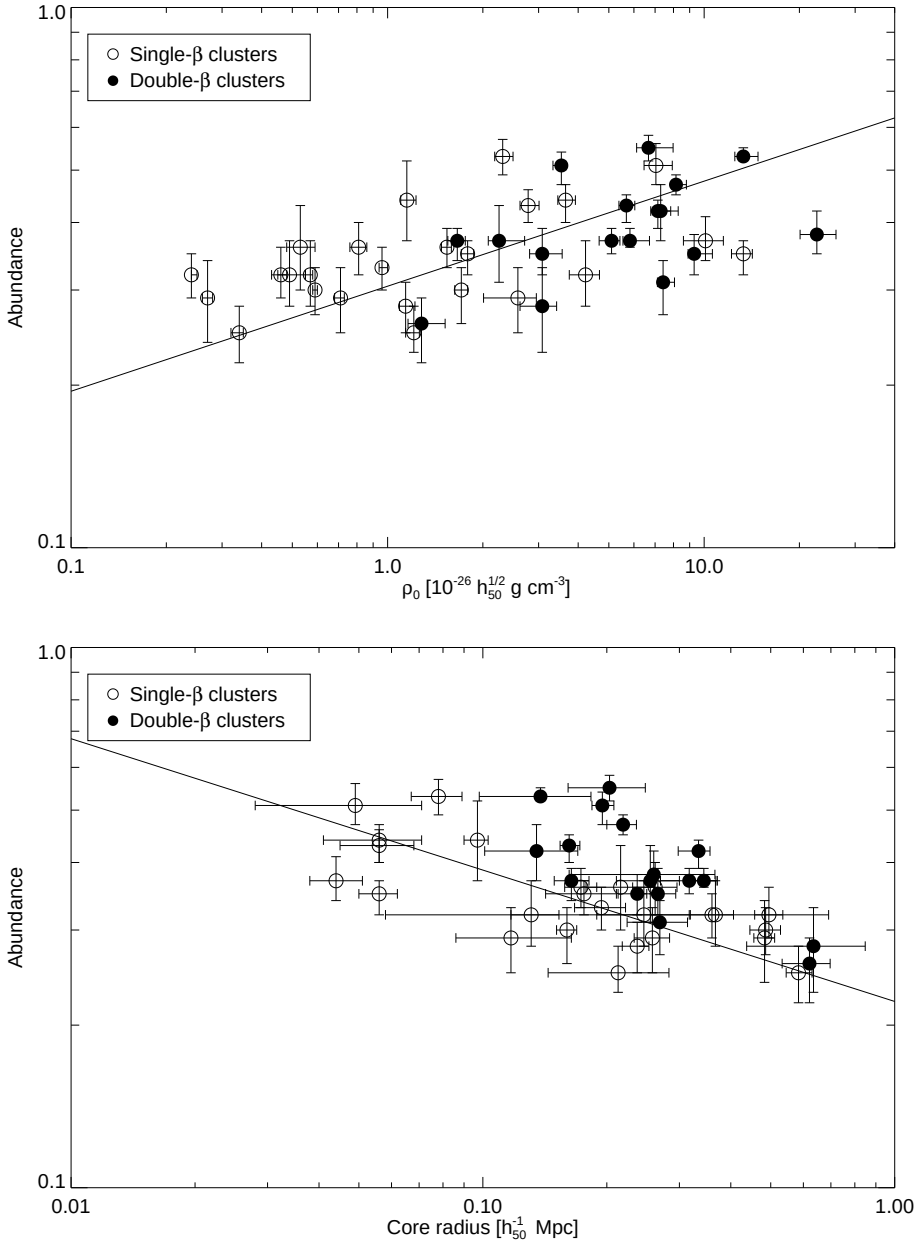

Figure 6.4: (top) Metal abundance versus central density. (bottom) Metal abundance versus core radius. Clusters fitted with a single β-model are open circle. Clusters fitted with a double β-model are filled circles. Error bars are 90% confidence limits.

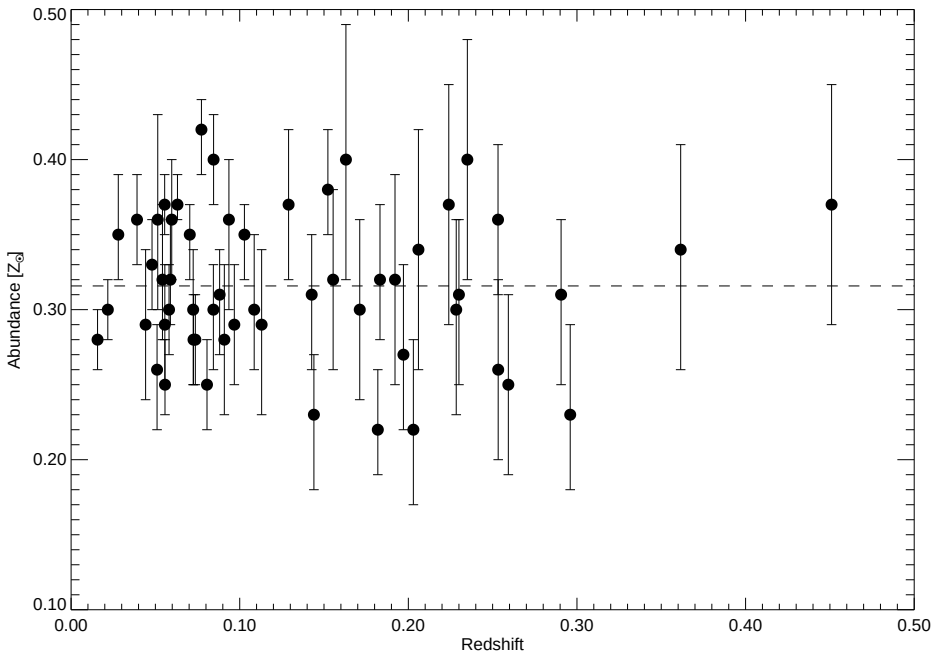

Figure 6.5: Abundance versus redshift for clusters with temperatures greater than 5 keV. The dashed line is the average for the sample. Error bars are 90% confidence limits.

The general interpretation of the lack of evolution of metal abundance is that the ICM was enriched relatively early at epochs $z > 1$. If the metals seen in the ICM were produced by the same population that produced the stars seen today in elliptical galaxies, then star formation in cluster ellipticals must have stopped about 2 Gyr before $z \sim 0.4$ since the ellipticals in rich clusters have shown only passive evolution since then (e.g., Bender et al. 1996).

6.6 Discussion and Conclusions

In summary, we find that the metal abundances of clusters are relatively constant for hotter clusters but then rise for cooler systems until falling sharply at group scales. We have also seen that abundance is correlated with cooling flow properties, such as central cooling time; and with the spatial properties, like central density and core radius. The average abundance of clusters is also relatively constant with redshift.

These relationships can be explained in two general ways. Either they reflect physical differences in cooler clusters and groups or they are the result of an ob-

servational bias in the measurement of the abundance. In the latter scenario, the rise in abundance seen at temperatures $\approx$ 2–5 keV is caused by radial abundance gradients in clusters. ASCA and BeppoSAX observations (Sarazin et al. 1998; Finoguenov et al. 2000; White 2000; Irwin & Bregman 2001) have suggested that radial abundance gradients are a common feature in clusters. In some clusters the metal abundance declines from $\approx 0.5 Z_{\odot}$ at the center to $\approx 0.2 Z_{\odot}$ at 0.5 Mpc. Known cooling flow clusters also seem to harbor stronger gradients than non-cooling flow clusters (De Grandi & Molendi 2001; Irwin & Bregman 2001).

Since the abundance we measure is weighted by the emission, the additional luminosity due to the denser central gas would bias the abundance measurement to the higher central values. Allen & Fabian (1998b) suggest a similar argument for why their cooling flow clusters have higher average abundances. Also, ASCA sees out to a smaller fraction of the virial radius in cooler clusters since these clusters are usually dimmer (hence lower surface brightness) than hotter clusters at comparable distance. This would increase the bias towards the higher central values for cooler clusters.

The very low metal abundances observed at $T_{\rm x} \lesssim 1$ keV may simply indicate problems in the spectral models. At high temperatures, the metal abundance is determined by the Fe-K shell lines (hydrogen and helium-like ions). At cooler temperatures ($T_{\rm x} \lesssim 3$ keV), the abundance is determined primarily by more complex Fe-L shell lines. The handling of the Fe-L lines can make a large difference in the fitted abundance, but the understanding of these more complex transitions is much poorer than for Fe-K. As we saw in Section 3.9.3, MEKAL model abundance can be higher than Raymond-Smith abundances by 20%-50% for temperatures $\lesssim$1 keV. Hwang et al. (1997) showed that abundances of groups at temperatures of a few keV determined separately through K and L shell lines were consistent. However, this is no guarantee that the same is true at much cooler temperatures $\lesssim$ 1 keV. The drop in abundance may simply reflect faults in the models at low energies.

If the variations in abundance are due to a physical effect, the rise in abundance could reflect a change in the gas fraction of cooler clusters. The metal abundance can be related to the gas fraction and the optical mass–to–light ratio such that:

$$Z = \frac{M_{Fe}}{M_{gas}} = \frac{M_{Fe}}{f_{gas} M} \propto \frac{L_{opt}/M}{f_{gas}} \tag{6.9}$$

where M_{Fe} is the mass in iron, M_{gas} is the gas mass, M is the total mass, f_{gas} is the gas fraction, and L_{opt} is the total optical luminosity. The last proportionality in Equation 6.9 assumes that the mass in iron is directly proportional to the mass in stars, and hence the total optical luminosity, which is supported by observations (Arnaud et al. 1992). The mass–to–light ratio is probably constant or nearly so for clusters (see Section 8.3 for a discussion of the mass–to–light ratio). While the gas

fractions of hotter clusters ($T_{\rm x} \gtrsim 5$ keV) seem to be relatively constant, although with some scatter (Mohr et al. 1999; Ettori & Fabian 1999; Roussel et al. 2000; Grego et al. 2001), Mohr et al. (1999) and Arnaud & Evrard (1999) find that the gas fractions for cooler clusters are lower. However, Roussel et al. (2000) do not see this effect, so the evidence for lower gas fractions is not yet firmly established. The lower gas fraction would tend to increase the observed metal abundance.

The steep drop in abundances at $T_{\rm x} \lesssim 2$ keV could be a sign of mass loss by groups (Davis et al. 1999). Early supernovae (e.g., during a starburst) can drive winds out of galaxies at speeds of up to ~ 1000 km s^{-1} (Heckman 2001). For systems with masses $\lesssim 10^{14}$ M$_\odot$ (corresponding to a few keV in temperature), the wind will not be bound to the system, and the gas can be expelled from the relatively shallow potential well of groups. Since these winds are coming from supernovae and stars (where the metals must originate), they would be enriched in metals compared to the primordial gas. If the winds can escape the group, this would lead to a preferential loss of metal enriched gas leading to a lower observed abundance. However, there are no detailed calculations regarding how the winds interact with the primordial gas (e.g., how important is mixing?), so mass loss scenarios can only be regarded as preliminary.

Without higher resolution spectral imaging and more complete plasma codes, we cannot give an unambiguous explanation for the variations of metal abundances seen in cooler clusters. Higher quality observations by XMM and Chandra will be necessary to determine the distribution of abundances and gas fraction within clusters.

Chapter 7

Mass – Temperature Relation

In this chapter, we investigate the relationship between the mass and x-ray temperature of clusters of galaxies. Much of the work in this chapter has been published in Horner et al. (1999) (hereafter HMS) as one of the first investigations of the mass–temperature relationship. Subsequently, many additional studies have been published (Neumann & Arnaud 1999; Ettori & Fabian 1999; Nevalainen et al. 2000; Finoguenov et al. 2001; Xu et al. 2001). For this chapter, we have updated the HMS study using temperatures from our ASCA cluster catalog in Section 7.3 but have otherwise left it much the same. We will discuss subsequent results and changes to the conclusions of HMS in Section 7.5.

7.1 Introduction

The relationship between the mass and x-ray temperature of galaxy clusters is a necessary bridge between theoretical Press-Schechter models, which give the mass function (MF) of clusters, and the observed x-ray temperature function (TF) (e.g., Edge et al. 1990; Henry & Arnaud 1991; Henry 1997; Markevitch 1998; Henry 2000). Theoretical arguments suggest that the virial mass of a galaxy cluster is simply related to its x-ray temperature as $M \propto T_{\rm x}^{3/2}$. These arguments are supported by simulations which show a tight correlation between mass and temperature (e.g., Evrard et al. 1996; Bryan & Norman 1998; Eke et al. 1998). This suggests that the M–T relationship may be a relatively accurate and easy way to estimate cluster mass. However, the M–T relationship first needs to be calibrated using masses estimated by some other means.

The oldest method of measuring cluster mass is the virial mass estimate based on dynamical analysis of the observed velocity dispersion of the cluster galaxies. The existence of the x-ray emitting ICM of galaxy clusters allows an independent mass estimate but requires knowledge or assumptions about both the x-ray temperature and surface brightness profiles. More recently, strong and weak gravitational

lensing by clusters has provided a third independent mass estimate. If clusters are dynamically relaxed and relatively unaffected by non-gravitational process, these three methods should give the same results.

The M–T relationship has only been tackled observationally quite recently. Hjorth et al. (1998) used strong and weak lensing derived masses to conclude that the M–T was consistent with the numerical simulations of Evrard et al. (1996). Horner et al. (1999), in an earlier version of this chapter, found that the M–T derived from optical virial masses seemed consistent with the Evrard et al. (1996) simulations, but x-ray estimates led to a steeper slope or lower normalization for the M–T. Subsequent studies have confirmed or expanded on these results (Ettori & Fabian 1999; Nevalainen et al. 2000; Xu et al. 2001; Finoguenov et al. 2001). These results have stimulated theoretical studies concentrating on understanding the M–T relationship, either through semi-analytic methods (Voit & Donahue 1998; Loewenstein 2000; Voit 2000; Afshordi & Cen 2001) or numerical simulations (Muanwong et al. 2001; Thomas et al. 2001).

In Section 7.2, we discuss the theoretical basis of the M–T relation and the results of cluster simulations. We then compare this relation with those using masses based on galaxy velocity dispersions (Section 7.3), x-ray mass estimates of clusters with spatially resolved x-ray temperature profiles (Section 7.4.1), and isothermal x-ray mass estimates (β-model estimates in Section 7.4.2 and surface brightness deprojection in Section 7.4.3). In Section 7.6, we discuss the results and present conclusions.

Table 7.1: Fitting Results $M_{200} = 10^{\gamma} \times T_{\rm x}^{\alpha}\ h_{50}^{-1} M_{\odot}$

Sample	γ	α	N	Comments
EMN simulation	13.95 ± 0.06	1.5	...	
Virial Masses	13.80 ± 0.12	1.76 ± 0.19	38	all clusters
Virial Masses	13.80 ± 0.85	1.73 ± 0.14	32	excluding mergers
Non-isothermal Temperatures	13.74 ± 0.08	1.48 ± 0.12	12	
Isothermal β-model	13.66 ± 0.03	1.77 ± 0.05	38	
Deprojection	13.61 ± 0.06	2.06 ± 0.10	83	

Notes: M_{200} is the mass inside a radius where the density is 200 times the critical density.

7.2 Theory and Simulations

For gas that shock heats on collapse to the virial temperature of the gravitational potential, the average x-ray temperature is:

$$T_{\rm x} \propto \frac{M_{\rm vir}}{r_{\rm vir}} \propto M_{\rm vir}^{2/3} \tag{7.1}$$

where $r_{\rm vir}$ is the virial radius, the boundary separating the material which is close to hydrostatic equilibrium from the matter which is still infalling. The coefficient of this relationship is a complicated function of cosmological model and density profile of the cluster (see e.g., Lilje 1992). However, because the infall occurs on a gravitational timescale $t_{\rm grav} \propto \rho^{-1/2}$, the virial radius should occur at a fixed value of the density contrast, defined as:

$$\delta = \frac{\overline{\rho(r)}}{\rho_c(z)} = \frac{M(<r)}{\frac{4}{3}\pi\rho_c(z)r^3} \tag{7.2}$$

where $\rho_c(z)$ is the critical density. For an $\Omega_0 = 1$ universe, $\delta_{\rm vir} = 18\pi^2 \approx 178$ but drops to lower density contrasts for lower values of Ω_0 (e.g., Lacey & Cole 1993). Since we do not have *a priori* knowledge of the actual value of $\delta_{\rm vir}$, we scale all of our results to $\delta = 200$, which should contain only virialized material, and has been used previously by other authors (e.g., Carlberg et al. 1996; Navarro et al. 1995). Using other overdensities should only change the normalization, not the slope, of the M–T relation.

Evrard et al. (1996) (hereafter EMN) present a theoretical M–T relation which seems to describe well simulated clusters in six different cosmological models (two $\Omega_0 = 0.2$ and four $\Omega_0 = 1$ models, see their Table 1 for details). EMN assume that $M \propto T_{\rm x}^{3/2}$ and then fit the coefficient of the relationship at various density contrasts. For $\delta \approx 200$, the coefficient depends only weakly on Ω_0, with a difference of $\approx 5\%$ between the $\Omega_0 = 0.2$ and $\Omega_0 = 1$ models while the difference rises to $\approx 40\%$ at $\delta = 2500$.

From EMN's Equation 9 and fitting the normalization using their Table 5 (excluding the $\delta = 2500$ values but including both $\Omega_0 = 0.2$ and $\Omega_0 = 1$ points), the expression for mass as a function of temperature and density contrast is:

$$M(\delta, T_{\rm x}) = (3.62 \pm 0.46) \times 10^{14} \delta^{-0.266\pm0.022} \left(\frac{T_{\rm x}}{\rm keV}\right)^{3/2} \; h_{50}^{-1} \; {\rm M}_\odot \tag{7.3}$$

where h_{50} is the Hubble constant in units of 50 km s^{-1} Mpc^{-1}. Note that Equation 7.3 shows that clusters in the EMN simulations are consistent with a dark matter density profiles $\rho(r) \propto r^{-2.4}$ in accordance with the effective slope of the universal density profile of Navarro et al. (1996) in the relevant range of radii.

Other simulations using different cosmological models and codes generally give normalizations similar to Equation 7.3 to within $\lesssim 20\%$. Eke et al. (1998) give masses and gas temperatures at a density contrast of 100 for their simulations of an $\Omega_0 = 0.3$ and $\Omega_\Lambda = 0.7$ model which are well described by Equation 7.3. Bryan & Norman (1998) give the M–T at $\delta = 250$ for simulations using a variety of cosmological models. Like EMN they find that the normalization is fairly insensitive to the model used although their normalizations are about 20% higher. We will use the EMN simulations as a baseline to which we will compare our results.

A redshift dependence is introduced into the normalization of the M–T relation by the definition of density contrast since the critical density is a function of Ω and the redshift of formation (e.g., Lilje 1992; Eke et al. 1996; Voit & Donahue 1998). This should not substantially affect our results as the samples considered consist mainly of low redshift ($z \lesssim 0.1$) objects and/or have scatter in their mass estimates considerably greater than the effect introduced by the redshift dependence.

Since we have restricted ourselves to low density contrasts and redshifts, we will not discuss gravitational lensing mass estimates. Lensing estimates are usually limited to high density contrasts $\delta \geq 3000$ (even for weak lensing) and to moderate-to-high redshifts. However, Hjorth et al. (1998) have reported good agreement between the EMN relation and their sample of eight lensing clusters. They assume $M \propto T_{\rm x}^{3/2}$ and an $\Omega_0 = 1$ cosmology. Their best fit normalization is 0.82 ± 0.38 (rms dispersion) times the EMN normalization.

7.3 Virial Theorem Mass Estimates

Girardi et al. (1998a) (hereafter G98) have derived virial masses for 170 nearby clusters ($z \leq 0.15$) using data compiled from the literature and the ENACS data set (Katgert et al. 1998). They define the virial radius to be $r_{vir} = 0.004\sigma_r \; h_{50}^{-1}$ Mpc where σ_r is measured in km s^{-1} and consider only galaxies within this radius in the mass estimation. Their quoted masses are generally smaller than previous estimates by $\lesssim 40\%$ which they attribute to stronger rejection of interlopers and a correction factor of $\sim 19\%$ accounting for the surface term (see Section 1.1.4 in Chapter 1).

We have cross-correlated the G98 catalog with the ACC and found 48 clusters in common. Table A.5 lists clusters in the sample along with their G98 virial radius, and virial mass, and number of redshifts used to estimated the mass. From this we derive a subsample 38 clusters with at least 30 redshifts within r_{vir} (the reasoning behind this cut will be discussed in Section 7.3.1).

The assumption that $r_{vir} = 0.004\sigma_r$ is quite approximate, and the actual relation between r_{vir} and σ_r depends on the cosmological model. The density contrast of the G98 virial masses ($= M_{vir}/(4/3\pi r_{vir}^3 \rho_c)$) is generally less than 200 with

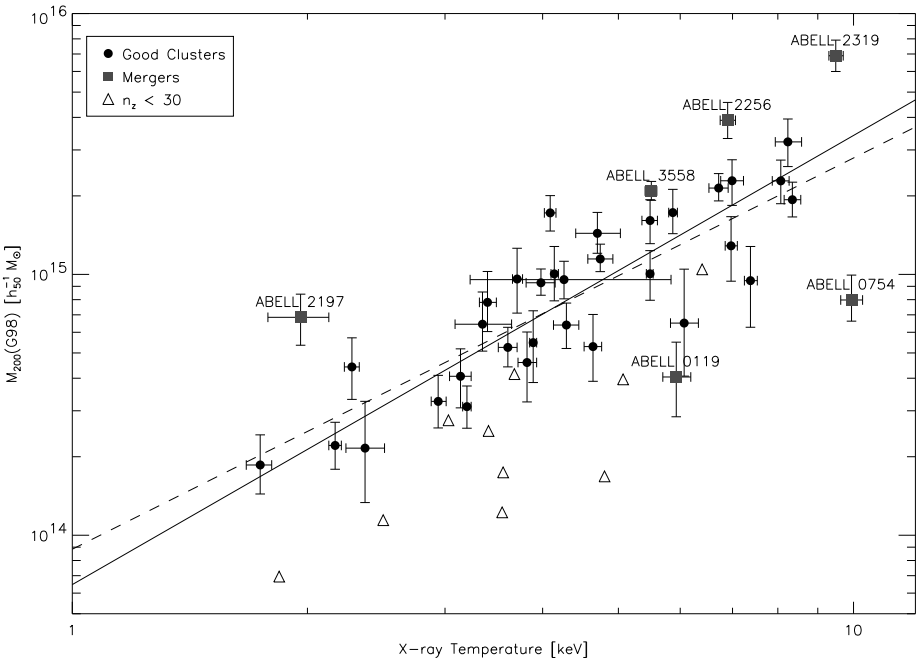

Figure 7.1: Virial Mass-Temperature Relation. The dashed line is the theoretical EMN relation while the solid line is a fit to the G98 virial masses (rescaled to a density contrast of 200) and ASCA temperatures. The error bars represent the 90% confidence intervals for temperature and 68% confidence for mass. The boxes indicate known mergers (named in the plot). Triangles are clusters with less than 30 redshifts used to calculate the mass.

a mean (and standard deviation) of 97 ± 23. Assuming a dark matter density $\rho(r) \propto r^{-2.4}$ in the outer parts of the clusters, which both the EMN simulations and Girardi data (at least the galaxy distribution) seem to follow, we have rescaled their masses to $\delta = 200$. Effectively this is just a change of normalization such that the rescaled masses are smaller than M_{vir} by about 15% (with a standard deviation of about 5%).

Figure 7.1 shows the distribution of rescaled virial masses versus temperature for this subsample. A power law fit using the BCES bisector method of Akritas & Bershady (1996), which takes into account the errors in both variables and the possibility of intrinsic scatter, gives $M \propto T_{\rm x}^{1.76\pm0.19}$ (all quoted errors are 1σ unless otherwise stated), marginally inconsistent with the EMN relation. The six most severe of the outliers in this plot are A119, A754, A2197, A2256, A2319, and A3558. All are known to contain complex velocity or temperature structure. We have marked these clusters in Figure 7.1. However, excluding them hardly changes the fit (see Table 7.1). Given the relatively large scatter, more clusters with

well measured temperatures, especially cooler/less massive clusters, are needed to further constrain the relationship between virial mass and x-ray temperature.

7.3.1 Scatter in Virial Mass Estimator

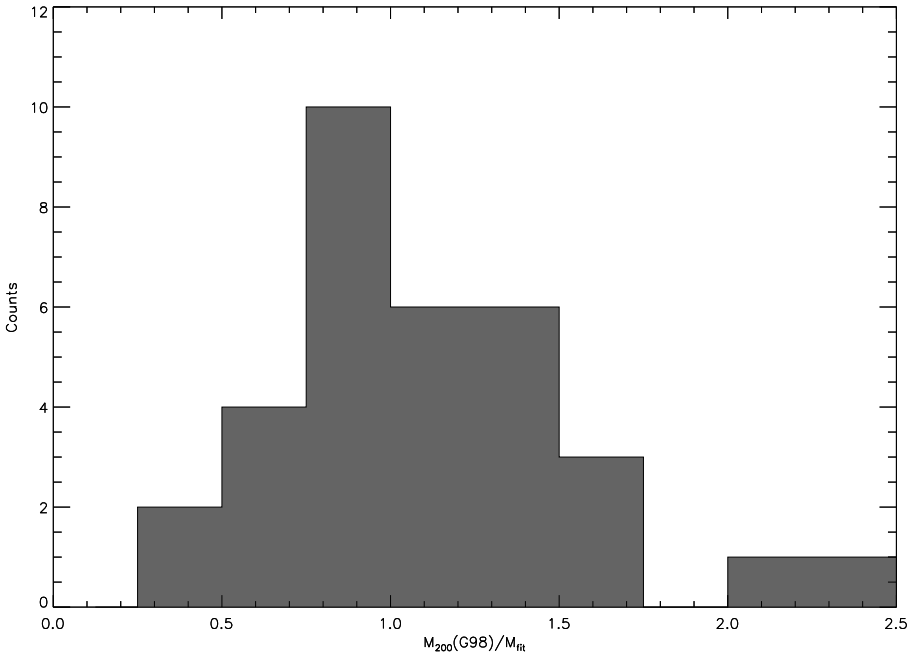

Figure 7.2: Histogram of virial to best fit masses excluding mergers.

The scatter in the virial mass estimator is expected to be quite large because of shot noise due to the finite number of galaxies in a cluster and projection effects due to contamination by background and foreground galaxies. The scatter in the observed virial mass–temperature relation is then a combination of the dispersion in the virial mass estimator (with respect to the true cluster mass) and any intrinsic dispersion in the M–T relation.

Figure 7.2 shows a histogram of the ratio of the rescaled virial masses ($M_{200}(G98)$) to the mass expected from the best fit relation (M_{fit}). The mean (or median) is approximately 1.0 with a standard deviation of 0.40. Figure 7.2 excludes the six outliers, including these clusters increases the standard deviation to 0.62. The expected scatter in the virial mass estimator has not been widely reported in the literature, but Fernley & Bhavsar (1984) find that in their simulations of galaxy clusters the ratio of the virial mass to true mass is 0.97 ± 0.36 (1σ standard deviation) after removing contaminating background and foreground galaxies. This

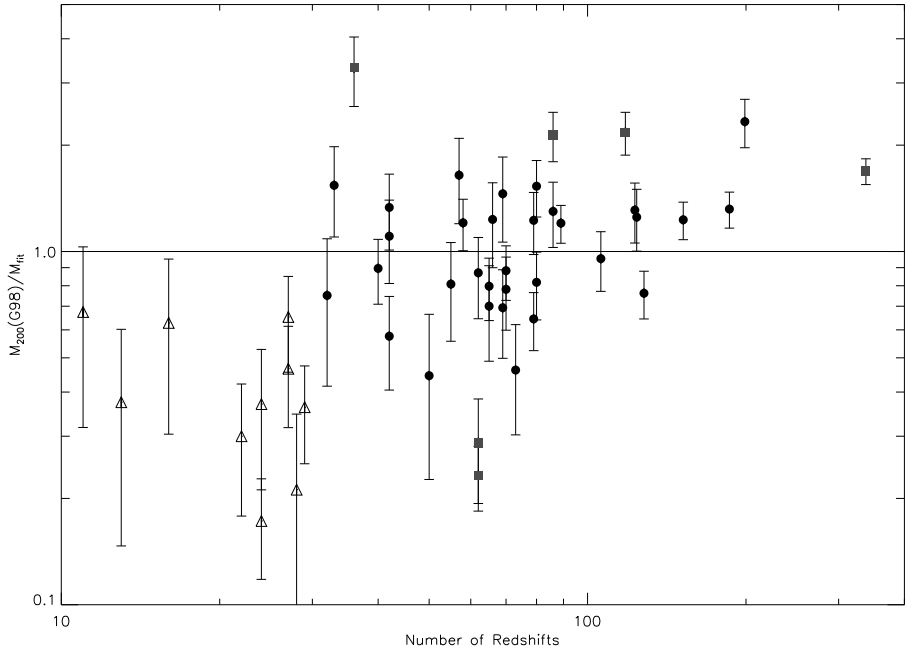

Figure 7.3: Ratio of virial to best fit masses as function of number of redshifts used to calculate virial mass. The symbols are the same as in Figure 7.1.

predicted scatter is close to the observed scatter around the fit and suggests that the dispersion in the virial mass – temperature relationship is primarily due to the scatter in the virial mass estimator.

This supposition is further supported by the distribution of $M_{200}(G98)/M_{fit}$ as a function of the number of redshifts (n_z) used to calculate the virial mass (see Figure 7.3 which also includes clusters with less than 30 redshifts). The scatter is about a factor of 2 lower for clusters with $n_z \geq 80$. This result is not surprising as a larger number of redshifts increases the accuracy of the virial mass estimator by decreasing the shot noise. Together with the results in Figure 7.2, this further indicates that the M-T relation must have very small intrinsic scatter, at least over the range of masses and temperatures covered by our data.

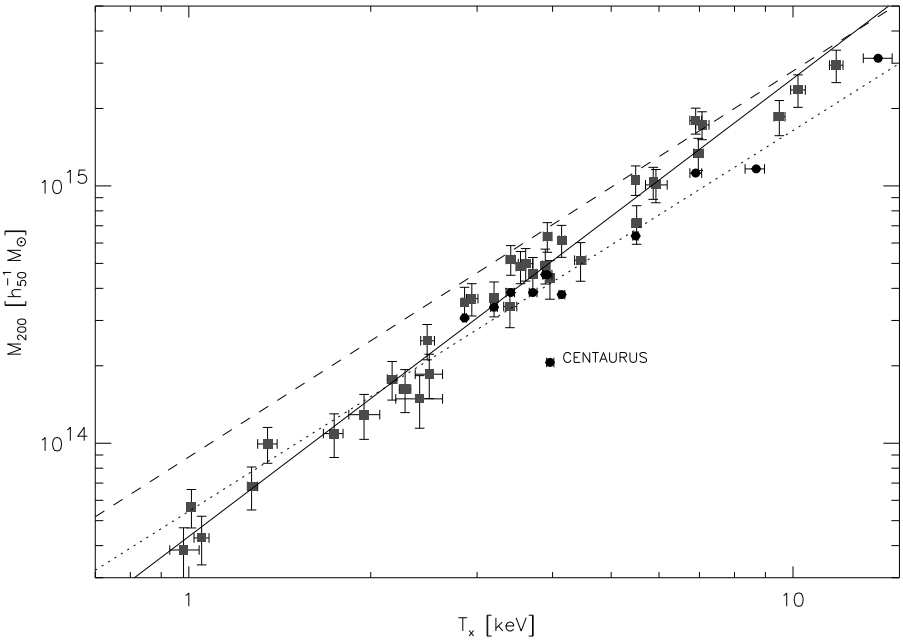

Figure 7.4: X-ray Mass–Temperature Relation. Solid circles are clusters with masses measured using spatially resolved temperature profiles rescaled to a density contrast of 200. The dotted line is a fit to these data. Gray boxes are isothermal β-model masses within an overdensity of 200. The solid line is the corresponding fit. The dashed line is the theoretical EMN relation. Error bars are 90% confidence limits.

7.4 X-ray Mass Estimates

7.4.1 Mass Estimates with Spatially Resolved Temperature Profiles

No large catalog of clusters with masses measured using spatially resolved temperature profiles has been published. Therefore, we have searched the literature (including conference proceedings) to obtain a sample of 12 clusters with masses measured using known temperature profiles. These clusters are presented in Table A.5 with the largest radius in which the mass was given, the mass within that radius, and the reference from which the data was taken. If given, we have used global temperature values given by the respective authors. Otherwise, we have taken them from our ASCA catalog. The formal errors on these mass estimates are small as they are well constrained by the density and temperature profiles. However, the systematic uncertainties (i.e., uncertainties in the ASCA PSF and effective area) are much more difficult to quantify. For fitting purposes, we have

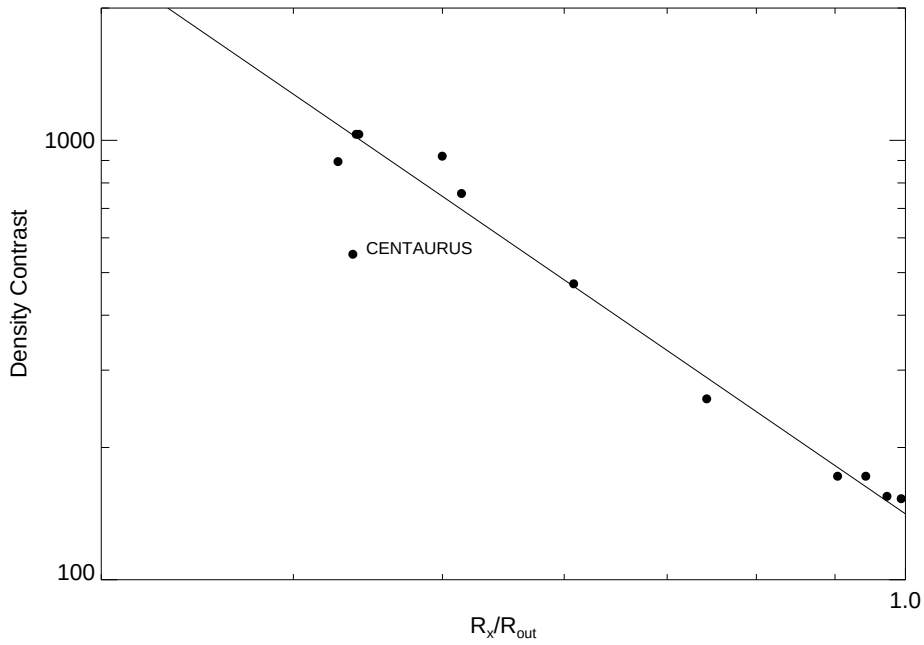

Figure 7.5: Density profiles of clusters with resolved temperature profiles as a function of radius, normalized to the EMN's r_{200}. The solid line represents a fit to the data, $\delta \propto (r/r_{200})^{-2.4\pm0.1}$.

chosen not to weight the fit with any mass errors, only with the errors in temperature.

Several of the clusters used warrant some comments. The masses for A496 and A2199 from Mushotzky et al. (1994) were derived without ASCA PSF corrections. However, the corrections are not large for these clusters as they are relatively cool and only the central field-of-view of the telescope was used. A2256 is a known merger, but Markevitch & Vikhlinin (1997) argue that the subcluster is physically well separated along the line of sight and has not disturbed the bulk of the primary cluster's gas. Although this cluster was considered a merger in the virial mass fit, this classification can be attributed due to contamination of the optical velocity dispersion measurement.

As with the virial masses, we have rescaled the masses to a density contrast of 200 assuming the dark matter density profile $\rho(r) \propto r^{-2.4}$. On average, the effect of rescaling is to increase the masses by an average of 20% with a standard deviation of $\approx$25%. There is some support for using this profile. Markevitch et al. (1996) and Markevitch & Vikhlinin (1997) report similar profiles for A2163 and A2256. While other authors in Table A.5 do not give density profiles, some (e.g., Ohashi

1997; Sarazin et al. 1998) contain plots of the mass as a function of radius which are consistent with the $\rho(r) \propto r^{-2.4}$ profile. Lastly, the clusters themselves seem to obey this profile. Figure 7.5 show the density contrast (effectively the average density) as a function of radius. We normalize the radius to EMN's r_{200}, the radius at which the density contrast is 200, so that we are comparing similar scales in different clusters but this makes little difference. An unweighted fit indicates that $\rho(r) \propto r^{-2.4\pm0.1}$.

In Figure 7.4, we plot the rescaled masses versus temperature. Excluding Centaurus (A3526), the best fit is $M \propto T_{\rm x}^{1.48\pm0.12}$ but with a normalization about 40% lower than that of the EMN relation. Given the heterogeneous nature of the sample, the dispersion around this fit is surprisingly small ($\lesssim 10\%$ in mass) indicating that the intrinsic correlation between temperature and mass is quite tight. Using a different density profile to extrapolate the mass to a density contrast of 200 has the tendency to increase the dispersion in this fit (i.e., about 25% for $\rho(r) \propto r^{-2}$) but does not have much effect on the power law index or normalization of the fit.

The lower normalization than that found using the EMN relation or virial masses may reflect systematics in the masses derived using the temperature profiles, or it could be a problem with the simulations and systematics in the virial mass determinations. Aceves & Perea (1998) have found that the virial mass estimate can either overestimate or underestimate the mass depending on the aperture of the region sampled. However, a direct comparison of the virial mass and x-ray masses for the 9 clusters with temperature profiles masses ($M_{200}(T(r))$) and G98 virial masses ($M_{200}(G98)$) (Figure 7.6) shows no clear trend. Further simulations and future observations of clusters with temperature profiles and virial masses are needed to explore this issue further.

7.4.2 The Isothermal β-model

The β-model mass can be written in terms of density contrast (Equation 7.2) as:

$$M(\delta, \beta, T_{\rm x}) = 1.1 \times 10^{15} \delta^{-1/2} \beta^{3/2} \left(\frac{T_{\rm x}}{\rm keV}\right)^{3/2} \left(1 - 0.01 \frac{\delta r_c^2}{\beta T_{\rm x}}\right)^{3/2} h^{-1} M_\odot \qquad (7.4)$$

We derive β-model masses using the data of Fukazawa (1997) (hereafter F97). In his study of the metal abundances and enrichment in the ICM, F97 presents a catalog of 38 clusters with temperatures, core radii, and β parameters derived from ASCA data (see Table A.5). F97 estimated the β parameter from the ASCA GIS data using a Monte-Carlo method to take into account the spatial and energy dependence of the GIS PSF and estimated temperatures by excluding the central region of the x-ray emission to minimize cooling flow biases.

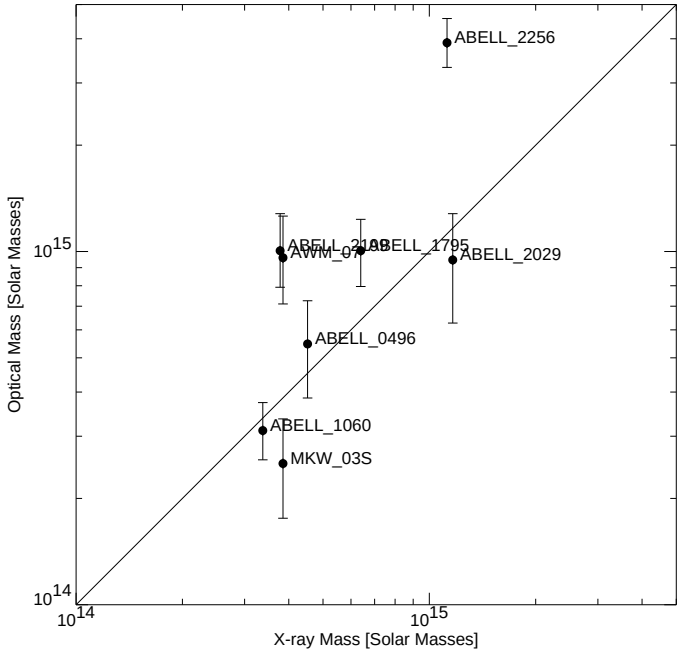

Figure 7.6: Comparison of virial and temperature resolved mass estimates.

The F97 data has the advantage of being a homogeneous sample which covers a wide range of temperatures ($\approx$ 1–12 keV), although ASCA is not the best instrument for surface brightness fitting due to its complicated PSF. However, the ASCA GIS β-model fits are rather insensitive to the presence of cooling flows due to the high energy bandpass of the GIS. The clusters are also at low redshifts and so subtend a large area of the detector minimizing the effect of the poor resolution of the GIS. We compared the F97 β values with those of derived from ROSAT studies (primarily using the PSPC) of David et al. (1995), Cirimele et al. (1997), and various others taken from the literature via the compilation of Arnaud & Evrard (1999) (see Figure 7.7). In general, they agree fairly well although ROSAT β values are higher by an average of about 5%.

In Figure 7.4, we plot the estimated β-model mass at $\delta = 200$ (using Equation 7.4) versus x-ray temperature. The relationship ($M \propto T_{\rm x}^{1.78\pm0.05}$) is steeper than that seen using the EMN simulations or temperature profile masses. In addition, the relative normalization with respect to the other mass estimators is a function of density contrast. Increasing the density contrast shifts the β-model masses lower with respect to the EMN relation and closer to the temperature profile masses while decreasing the density contrast has the opposite effect.

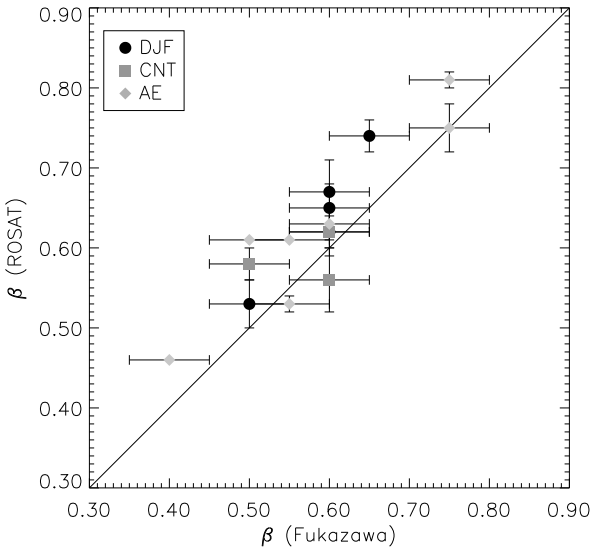

Figure 7.7: Comparison F97 ASCA GIS β values to ROSAT β values. The circles are taken from David et al. (1995). The squares are from Cirimele et al. (1997), and the diamonds are taken from references listed in Arnaud & Evrard (1999).

Equation 7.2 shows that the scaling $M \propto (\beta T_{\rm x})^{3/2}$ is built in to the β-model mass. The steepening of the M–T can be attributed to a dependence of β on temperature. The EMN relation is basically a β-model with $\beta = 0.68$ for all clusters (depending on density contrast) regardless of x-ray temperature. However, the F97 data show a definite correlation of β with $T_{\rm x}$ (see Figure 7.8). This indicates that the gas profile becomes shallower at lower masses.

The variation of β with $T_{\rm x}$ is unlikely to be an artifact of the F97 fitting procedure. As we noted in the previous section the F97 β values generally agree with ROSAT values. The correlation of β and $T_{\rm x}$ has also been noted previously in Einstein data by David et al. (1991), and, more recently, Mohr & Evrard (1997) have found a similar trend for β defined in a non-parametric and non-azimuthally averaged fashion using PSPC data. Arnaud & Evrard (1999) also note the behavior of β with $T_{\rm x}$ and the discrepancy between the β-model and the expected EMN masses in their sample of clusters compiled from the literature. In fact, redoing the preceding analysis with their sample gives virtually identical results.

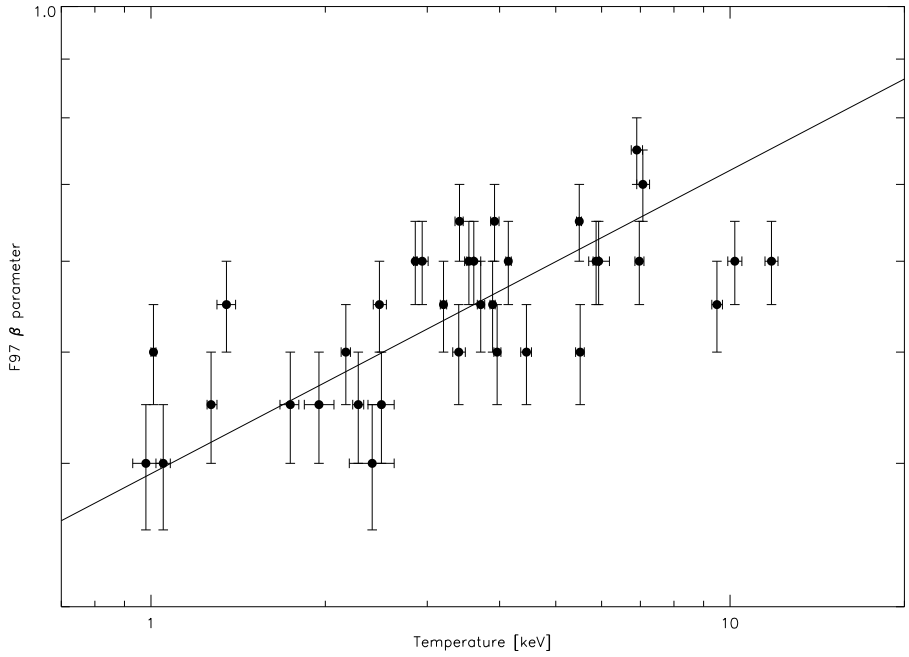

Figure 7.8: Relation between β and $T_{\rm x}$ for F97 data. The line is a fit to the data ($\beta \propto T^{0.26\pm0.03}$).

7.4.3 Surface Brightness Deprojection

Another method for determining the mass of a cluster is x-ray image deprojection. The constraint of the observed surface brightness profile means that the profiles for the variables in Equation 1.11 & 1.12 can be determined by specifying one of them. The usual procedure is to divide the surface brightness emission into annuli. The outer pressure must be set in the outermost annuli (assumed to be due to gas not detected because its surface brightness is too low). The observed emissivity in the outer shell determines the temperature and hence the density. This procedure is then stepped inward and repeated. For more detailed discussion see Arnaud (1988), White et al. (1997) (hereafter WJF) and references therein.

WJF present an analysis of 207 clusters using an x-ray image deprojection analysis of Einstein IPC and HRI data to estimate the masses of clusters. WJF choose the functional form of the gravitational potential as two isothermal spheres, representing the central galaxy and general cluster potentials. These are parameterized by a velocity dispersion and core radius. For the central galaxy, these are fixed at 350 km s^{-1} and 2 h_{50}^{-1} kpc. The velocity dispersion of the cluster potential is taken from the literature or interpolated from the x-ray temperature or luminosity using an empirical relation. The core radius is a free parameter in the analysis

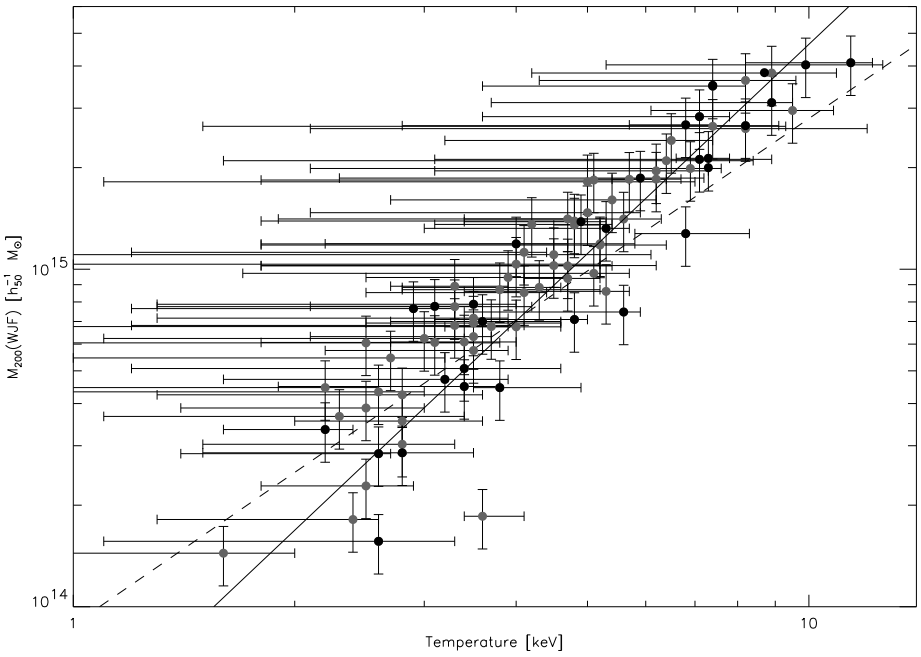

Figure 7.9: Mass–Temperature relation for WJF clusters using clusters with data for $\delta \leq 2000$. The solid circles are clusters which did not have any interpolated input data. The dashed line is the theoretical EMN relation. The solid line is a fit to the data. The error bars represent the 90% confidence intervals.

which, with the outer pressure, is constrained to produce a flat temperature profile. Therefore, the derived gravitational mass depends on the velocity dispersion, x-ray surface brightness distribution, and temperature.

WJF determine the mass within the radius for which they have x-ray data, which may be fairly small, while the EMN relation is only valid in the outer parts of the cluster (i.e., low values of density contrast). As with the G98 clusters, we can rescale the mass to a $\delta = 200$, at least for the WJF clusters which have data in the outer parts of the cluster. We have rescaled the clusters with data at density contrasts ($= M_{WJF}/(4/3\pi r_{WJF}^3 \rho_c)$) less than 2000 to $\delta = 200$ assuming $\rho(r) \propto r^{-2}$ as is the case for an isothermal sphere.

In Figure 7.9, we show the resulting M_{200} versus $T_{\rm x}$ relation. Although the lower $T_{\rm x}$ error bars are quite large, allowing the points to be statistically consistent with the EMN relation, the relation is obviously steeper. Fitting this relation using the BCES method gives a $M \propto T_{\rm x}^{2.06\pm0.10}$ somewhat steeper than than found from the F97 data. The scatter in mass around this relation is also larger, about 50%.

Although WJF interpolated σ or $T_{\rm x}$ for many clusters, using only the 45 clusters

with data at $\delta < 2000$ which did not have interpolated data does not alter our results. Also, the results reported using a subsample of 19 clusters with better determined parameters by White & Fabian (1995) are consistent with the WJF results. Furthermore, a recent deprojection analysis by Peres et al. (1998) of 45 clusters with ROSAT PSPC or HRI data gives a similar relationship as the WJF data, although the Peres et al. data are generally at higher density contrasts ($\gtrsim 3000$) making the extrapolation to $\delta = 200$ even more uncertain.

Interpretation of the deprojection results is difficult as the derived gravitational masses are a combination of optical (the velocity dispersion) and x-ray data (the core radius and temperature). The large scatter is probably due to the use of the velocity dispersion to set the depth of the potential well and the relatively poor quality of the Einstein data.

7.5 Updated Results

Since HMS was published there have been several additional studies of the M–T relationship (Neumann & Arnaud 1999; Ettori & Fabian 1999; Nevalainen et al. 2000; Finoguenov et al. 2001; Xu et al. 2001). In particular, Nevalainen et al. (2000) used temperature profile information for 6 clusters using ASCA and 3 groups using the PSPC. Finoguenov et al. (2001) (hereafter FRB) used a sample of 39 clusters with temperature profiles determined by ASCA. Below, we summarize how various sections of this chapter are affected by newer data and results.

7.5.1 Virial Theorem Mass Estimates

Using G98 virial masses and ASCA temperatures, we find a slope that is steeper ($\alpha = 1.7$) than the EMN relationship whether or not we include merger clusters. This result differs somewhat from the one originally given in HMS. They found that removing the known mergers flattened the relationship such that it was consistent with the EMN relationship. We now have eight more clusters in the sample, including several at lower temperatures. With the updated temperatures, this is enough to steepen the relationship. Unfortunately, the still relatively small number of clusters and the large scatter in the relationship make definitive statements about the M–T slope based on virial masses questionable.

The offset between the normalization of the relationships found with virial masses and those with x-ray determined masses is puzzling. We found no clear trend between the two mass estimators. However, Lewis et al. (1999) found good agreement and no systematic difference between x-ray (β-model) and optical virial masses for 14 higher redshift clusters from the CNOC sample (Yee et al. 1996). FRB compared their x-ray masses to G98 masses and find a similar result to ours.

However, they find better agreement with clusters characterized by G98 as having decreasing velocity dispersion profiles with radius (as opposed to ones with flat or increasing profile) and suggest this is the origin of the bias.

7.5.2 The Isothermal β-model

We showed that the steepening of the β model mass estimates is driven by the variation of β with x-ray temperature. However, Vikhlinin et al. (1999) (hereafter VFJ) find no (or only a weak) correlation of β and $T_{\rm x}$ in their study of 33 clusters observed with the ROSAT PSPC. They excluded the central parts of the cluster with a radius estimated to be twice the cooling radius. They ascribe the correlations found in other samples to incomplete exclusions of the central cool regions. Using the VFJ β values in our analysis leads to a slope of $\alpha = 1.64 \pm 0.04$.

Xu et al. (2001) and FRB report a similar slope for β-model masses. However, Xu et al. (2001) claim a break in the relationship such that the M–T for lower temperature systems ($T_{\rm x} < 3.5$ keV) is steeper while the upper end is consistent with $\alpha = 1.5$. We need better measurements of the surface brightness profiles of clusters and especially groups out to larger radii to come to any definitive conclusions about the β-model. For instance, if the gas near the centers of clusters follows a density profile steeper at small radii than the β-profile (e.g, an NFW profile (Navarro et al. 1996)) then masses found by excluding the central parts will be biased.

7.5.3 Mass Estimates with Spatially Resolved Temperature Profiles

Our sample of clusters with masses using resolved temperature profiles is a very heterogeneous one. Nevalainen et al. (2000) derived temperature profile information for 6 clusters using ASCA and 3 groups using the PSPC and found a steep M–T with $\alpha = 1.78 \pm 0.14$. However, we find that fitting only their ASCA clusters (without the groups) gives a slope of $\alpha = 1.46 \pm 0.53$, consistent with ours. Finoguenov et al. (2001) (hereafter FRB) investigated whether a break exists in the M–T using a sample of 39 clusters with temperature profiles determined by ASCA. They find $\alpha = 1.79 \pm 0.14$ for their whole sample, but a flatter slope ($\alpha \approx 1.5$) if they limited their data to higher temperatures or masses. FRB also find that the scatter increases at lower temperatures.

7.6 Conclusions

We have examined the relationship between various galaxy cluster mass estimators and x-ray gas temperature. The normalizations of the resulting relationships generally agree to within $\lesssim 40\%$ in mass but with systematic offsets between different types of mass estimators. Our x-ray mass estimates using spatially resolved temperature profiles scale similarly to the EMN relationship ($M \propto {T_{\rm x}}^{3/2}$) but with a normalization about 40% lower than the EMN or virial mass M–T's. The virial mass M–T and isothermal β-model mass estimates give slopes $\alpha \approx 1.8$ that are steeper than the EMN relationship.

This difference in slopes and normalization is not an artifact of the $\rho(r) \propto r^{-2.4}$ dark matter density profile that we used to extrapolate the virial mass and x-ray mass estimates to $\delta = 200$. The isothermal β-model implicitly assumes a dark matter density profile of $\rho(r) \propto r^{-2}$ in the outer parts of clusters. Using this profile in the extrapolation has little effect of our results. In the case of the virial mass estimates, they already extend to the Girardi's estimated virial radius and any changes are therefore small. The correction is larger in the case of the x-ray masses but still produce only a small change in the fitted M–T. The slope of the best fit is only slightly steepened, to $\alpha = 1.55 \pm 0.18$, and the normalization is about 20% higher. This is still not enough to reconcile the x-ray and optical mass estimates. Since δ only appear in the coefficient of the M–T relation (e.g., see Equation 7.2), using a different δ only effects the absolute normalization of the M–T relation fits.

As with the $L_{\rm x} - T_{\rm x}$ relation, a slope steeper than the canonical $M \propto {T_{\rm x}}^{3/2}$ is usually taken as evidence of some non-gravitational mechanism affected the gas. For example, if heating of the ICM (due to supernovae or AGN) releases a similar amount of energy per unit gas mass in clusters and groups, groups would be affected to a greater degree and exhibit a stronger shift towards higher temperatures than more massive clusters. That is, the observed cluster temperature does not accurately reflect the true virial temperature of the systems (which is still $T_{virial} \propto M^{2/3}$). Theoretical studies and numerical simulation have managed to reproduce M–T relations similar to those observed (e.g., Mohr & Evrard 1997; Loewenstein 2000) using various heating scenarios. However, other non-gravitational mechanisms, such as radiative cooling (Muanwong et al. 2001), may also be able explain the steepening the slope of the M–T.

Another idea was presented by the theoretical study of Afshordi & Cen (2001). They find that the measured steepening in the M–T is due to increased and asymmetric scatter in the low mass M–T relationship such that groups are scattered preferentially toward higher temperatures. The amount of scatter is dependent on cosmology. They find that the FRB results are consistent with a ΛCDM cosmology.

They also argue that the scatter is due to the initial conditions not the formation time as argued by FRB. As we have seen in Chapter 5, the luminosity–temperature relation also indicates that such effects are important.

Cluster mass generally seems to be well correlated with temperature at least for $T_{\rm x} \gtrsim 3$ keV. The scatter in the virial mass – temperature relation is consistent with most of the scatter being due to the dispersion in the virial mass estimator. The small scatter of the masses of clusters with spatially resolved temperature profiles also indicates that the dispersion in the M–T relation is probably $\lesssim 10\%$.

In the future, more optical virial mass estimates for cooler clusters (and a better understanding of the biases in virial mass estimates) and larger samples of clusters with resolved temperature profiles will enable better constraints on the M–T relation. Better x-ray data will allow the effect of energy injection on the apparent temperature and the spatial distribution of the ICM to be disentangled. X-ray observations with Chandra and XMM will produce both the gas density and temperature maps of clusters and allow maps of the gas entropy to be constructed which should produce new constraints on energy injection histories and entropy variations within the cluster population. Such entropy maps can then be compared with those produced from simulations and theory.

Chapter 8

Optical to X-ray Scaling Laws

8.1 Introduction

So far, we have been mainly concerned with the relationship between the x-ray properties of clusters or the relationship of the x-ray properties to global properties like mass. Now we investigate the relationships between the optical and x-ray properties of clusters. The x-ray properties of a cluster have long been known to be correlated with some of the optical properties of clusters (e.g., Abramopoulos & Ku 1983). In this chapter, we will discuss the optical velocity dispersion, luminosity, and richness (see Section 1.1 for a review of these properties). These properties are tied to the cluster mass and should complement our previous results, especially for the M–T relation.

No large uniform sample of the optical properties of clusters exists in the literature for comparison to our ASCA sample. In many ways, optical properties are harder to accurately quantify than the properties of the x-ray gas since they depend on the summed or ensemble properties of the individual galaxies. We have searched the literature for compilations of optical properties to compare with our x-ray results, trying to keep the optical samples as homogeneous as possible. Table A.6 lists the optical data we have compiled for clusters from the literature. The references from which the data are taken are described in more detail in the sections that follow. The number of clusters with optical data is much smaller than the number of clusters in the ACC which limits the results we can obtain. A summary of the fitted scaling laws is given in Table 8.1.

8.2 Optical Velocity Dispersion

In Section 7.3, we examined the relationship between optical virial mass ($M_{\rm vir}$), which is based on the optical velocity dispersion (σ_r), and x-ray temperature. To first order, $M_{vir} \propto \sigma_r^3$ since $M_{vir} \propto \sigma_r^2 r_{vir}$ and $r_{vir} \propto \sigma_r$. Therefore, the

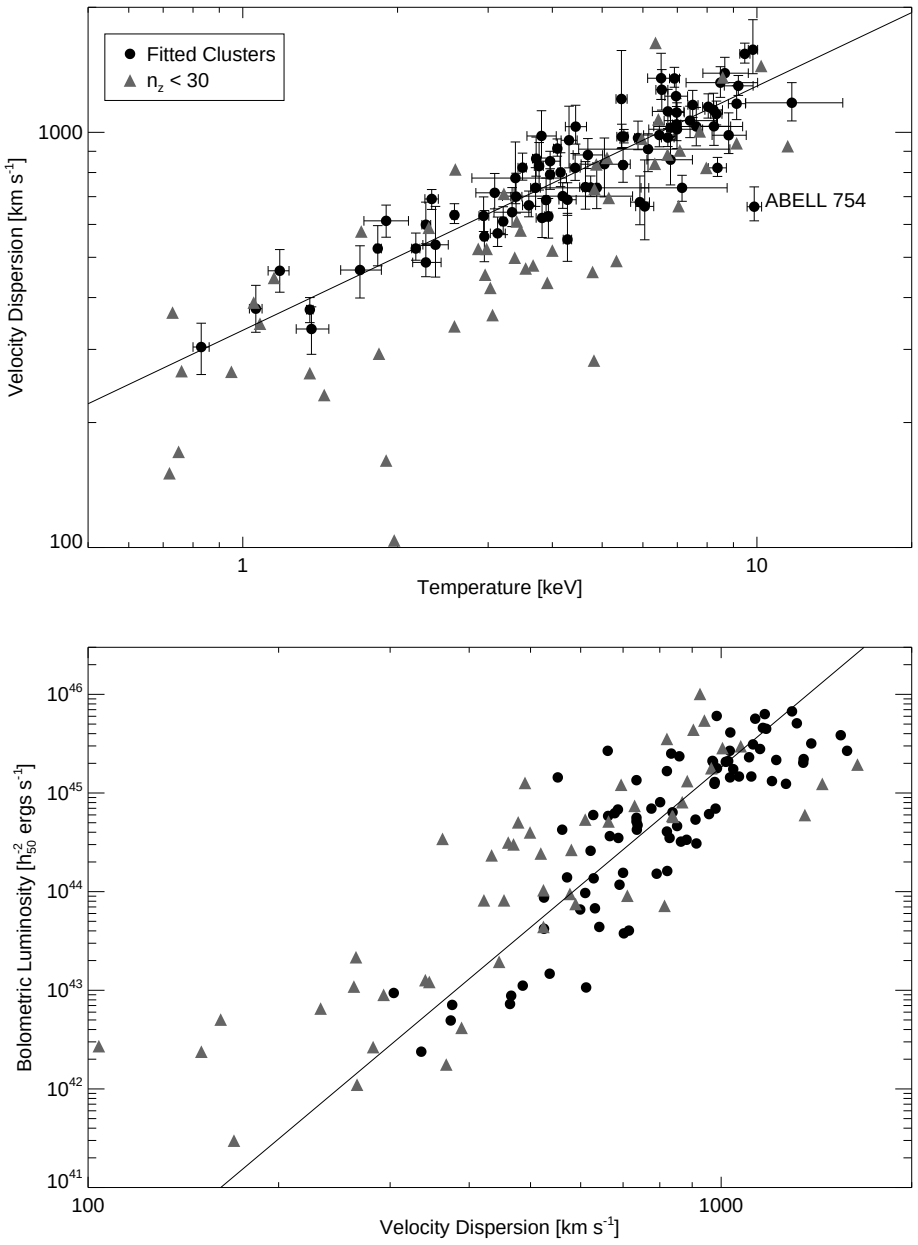

Figure 8.1: Optical velocity dispersion versus x-ray temperature (top) and luminosity (bottom). Error bars are 1σ for velocity dispersion and 90% confidence limits for temperature. The solid line is a fit to the data excluding the clusters marked by triangles which used less than 30 redshifts to calculate the dispersion (see text).

Table 8.1: Correlations Between X-ray and Optical Properties: $Y = 10^{\gamma} \times X^{\alpha}$ for N clusters.

Correlation (Y–X)	γ	α	N	Comments
σ_r–$T_{\rm x}$	2.53 ± 0.02	0.59 ± 0.03	81	...
$L_{\rm bol}$ –σ_r	20.09 ± 0.87	5.39 ± 0.30	81	...
$L_{\rm opt}$ –$T_{\rm x}$	11.55 ± 0.18	1.89 ± 0.27	23	...
$L_{\rm bol}$ –$L_{\rm opt}$	12.16 ± 6.17	2.53 ± 0.48	23	...
N_A–$T_{\rm x}$	1.12 ± 0.05	1.08 ± 0.06	155	...
$L_{\rm bol}$ –N_A	40.49 ± 0.51	2.36 ± 0.26	155	...
$N_{\rm B}$ –$T_{\rm x}$	0.49 ± 0.09	1.18 ± 0.13	28	...
$L_{\rm bol}$ –$N_{\rm B}$	40.68 ± 0.33	3.26 ± 0.33	28	...
$B_{\rm gg}$ –$T_{\rm x}$	2.45 ± 0.08	0.99 ± 0.12	42	YL+AO
$B_{\rm gg}$ –$T_{\rm x}$	2.30 ± 0.14	1.12 ± 0.18	21	YL only
$B_{\rm gg}$ –$T_{\rm x}$	2.38 ± 0.14	1.29 ± 0.30	21	AO only
$L_{\rm bol}$ –$B_{\rm gg}$	28.46 ± 1.60	3.95 ± 0.52	40	YL+AO
$L_{\rm bol}$ –$B_{\rm gg}$	36.74 ± 2.25	2.67 ± 0.70	20	YL only
$L_{\rm bol}$ –$B_{\rm gg}$	34.28 ± 2.29	3.24 ± 0.79	20	AO only

Notes: The units used are $L_{\rm bol}$ in erg s^{-1}, $L_{\rm opt}$ in $L_{\odot}$, $T_{\rm x}$ in keV, and σ_r in km s^{-1}. YL and A0 refer to the Yee & López-Cruz (1999) and Andersen & Owen (1994) data used in Section 8.4.3.

mass–temperature relation is related to the more extensively discussed velocity dispersion–temperature (σ_r–$T_{\rm x}$) relation (e.g., Lubin & Bahcall (1993); Bird et al. (1995); Wu et al. (1998) and references therein). The velocity dispersion is easier to measure, and more clusters have velocity dispersions than virial masses available in the literature. Similarly to the M–T, if galaxies and gas are both in equilibrium with the cluster potential and gravity is the only source of energy, $\sigma_r \propto T_{\rm x}^{1/2}$ (e.g., Bird et al. 1995). However, based on the results of Chapter 7, we might expect the σ_r–$T_{\rm x}$ relation to be steeper than this. For $M \propto {T_{\rm x}}^{1.8}$, we should see $\sigma_r \propto {T_{\rm x}}^{0.6}$.

We searched the literature to compile velocity dispersion estimates for 134 clusters in our sample. These are listed in Table A.6 along with the number of redshifts used to calculate the velocity dispersion. As we saw in Section 7.3.1, a low number of velocities can create a systematic bias in the results.

8.2.1 The Velocity Dispersion – Temperature Relation

Figure 8.1 shows the relationship between velocity dispersion and x-ray temperature. We fit the relationship using the BCES method. If we fit all the data, we find a steep relationship, $\sigma_r \propto {T_{\rm x}}^{0.74 \pm 0.06}$. However, the number of redshifts (n_z) used to calculate the velocity dispersion varies from 5 to 338 for the clusters in our sample. Restricting the fit to clusters with velocity dispersion based on more than 10 redshifts flattens the relationship to $\sigma_r \propto {T_{\rm x}}^{0.66 \pm 0.04}$. Further restricting the fit

to $n_z > 20$ flattens it even further to $\sigma_r \propto T_{\rm x}^{0.61\pm0.03}$. Increasing n_z even more has little effect on the fit. We derive $\sigma_r \propto T_{\rm x}^{0.59\pm0.03}$ for $n_z > 30$ and $\sigma_r \propto T_{\rm x}^{0.60\pm0.04}$ for $n_z > 40$.

As one can easily see in Figure 8.1, the clusters with $n_z < 30$ are usually extreme outliers. The relationship we give in Table 8.1 is for $n_z > 30$ and is what we discuss in the rest of this section. The fitted relationship is steeper than expected from simple theory but consistent with a steepened M–T relationship. Unlike the M_{vir}–$T_{\rm x}$ relation, we have not excluded any outliers (e.g., known mergers). Since there are so many more clusters in the relationship, they do not affect the fit very much and with the exception of Abell 754 are not large outliers.

The fitted $\sigma_r - T_{\rm x}$ relationship is also consistent with previous estimates (e.g., 0.61 ± 0.13 from Bird et al. (1995); 0.62 ± 0.04 Girardi et al. (1998a)), although not as steep as others (0.65 ± 0.03 Wu et al. (1999)). As we saw above, a steeper relationship may result from the inclusion of velocity dispersions with a low number of redshifts. Helsdon & Ponman (2000b) report a steepening of the $\sigma_r - T_{\rm x}$ relation at low temperatures to $\sigma_r \propto T_{\rm x}^{1.1\pm0.2}$, but their dispersions are based on a small number of redshifts. There is no steepening evident at low temperatures in our data, but the number of poor groups in our sample ($T_{\rm x} \lesssim 1$ keV) with a large number of redshifts is small.

The residuals of the fit (the ratio of the observed velocity dispersion to the expected from the fit, σ_r/σ_{fit}) are shown in Figure 8.2. Clusters with $n_z \lesssim 30$ generally have lower observed velocity dispersions than expected based on their temperature. To accurately determine the velocity dispersion, a large number of clusters are need to sample the tail of the galaxy velocity distribution. Based on our results this number seems to be around 30 redshifts. Similarly, Zabludoff & Mulchaey (1998) found that velocity dispersions calculated using only a few bright galaxies are significantly underestimated.

The residuals have a standard deviation of 0.15 for clusters with $n_z > 30$ and a somewhat lower dispersion of 0.11 for clusters $n_z > 60$. Given that the average 1σ errors on the velocity dispersion are ≈ 0.11 ($n_z > 30$) and ≈ 0.08 ($n_z > 60$), the intrinsic variance in the $\sigma_r - T_{\rm x}$ relationship is quite small, unlike the $L_{\rm x} - T_{\rm x}$ relationship, suggesting that σ_r and $T_{\rm x}$ are measuring the same thing.

8.2.2 The Velocity Dispersion – X-ray Luminosity Relation

Since x-ray luminosity is easier to obtain than temperature, several recent papers have studied the relationship between x-ray luminosity and velocity dispersion, especially for groups. Dell'Antonio et al. (1995) and Mahdavi et al. (1999) suggest that the relation flattens for lower luminosity groups as the galaxy luminosities begin to dominate over that of the intragroup gas. This would seem inconsistent

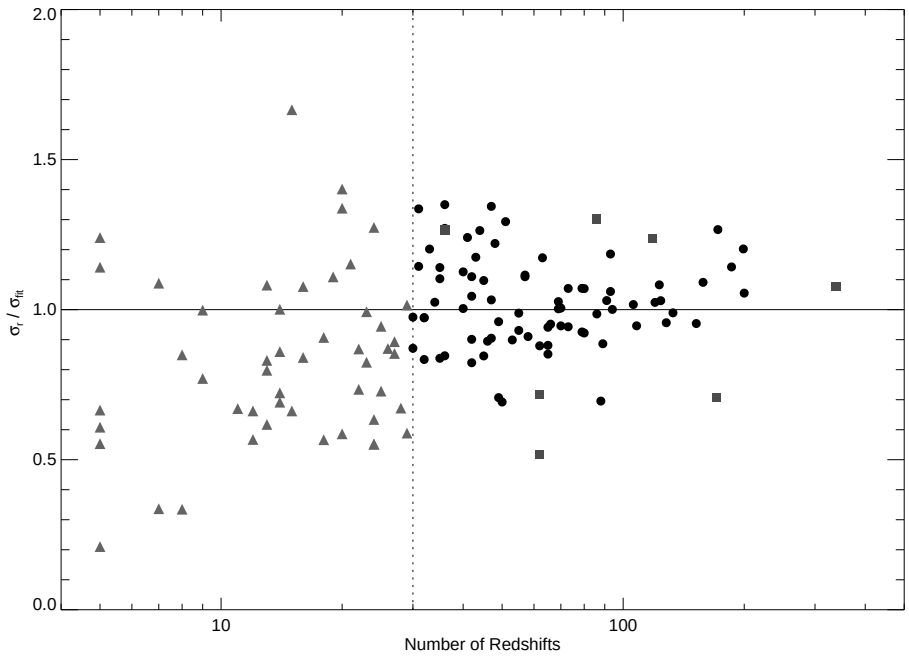

Figure 8.2: Ratio of the observed velocity dispersion (σ_r) to best fit velocity dispersion (σ_{fit}) based on the temperature as a function of the number of galaxies used to determine σ_r. Symbols are as in Figure 8.1.

with the behavior of the σ_r–$T_{\rm x}$ relation which may steepen at group scales.

Figure 8.1 shows the relationship between velocity dispersion and bolometric x-ray luminosity for our sample. There does seem to be some flattening at low luminosity, but this is only for a few clusters with $n_z < 30$. As we saw in the last section, we should be wary of conclusions based on such clusters. The Mahdavi et al. (1999) results are based on velocity dispersions with $\lesssim 10$ redshifts and may therefore be misleading.

8.3 Optical Luminosity

The total optical luminosity of a cluster is another measure of the total galaxy population in a cluster. The goal of much of the work in measuring optical luminosities is to determine the mass-to-light ratio (M/L) of clusters. The mass-to-light ratio is thought to increase from galaxy to cluster scales and then reach an asymptotic value of $\sim 150 M_\odot/L_\odot$ at large scales (e.g., Bahcall et al. 1995). If so, then the optical light on large scales can be used to measure the mass density of the universe

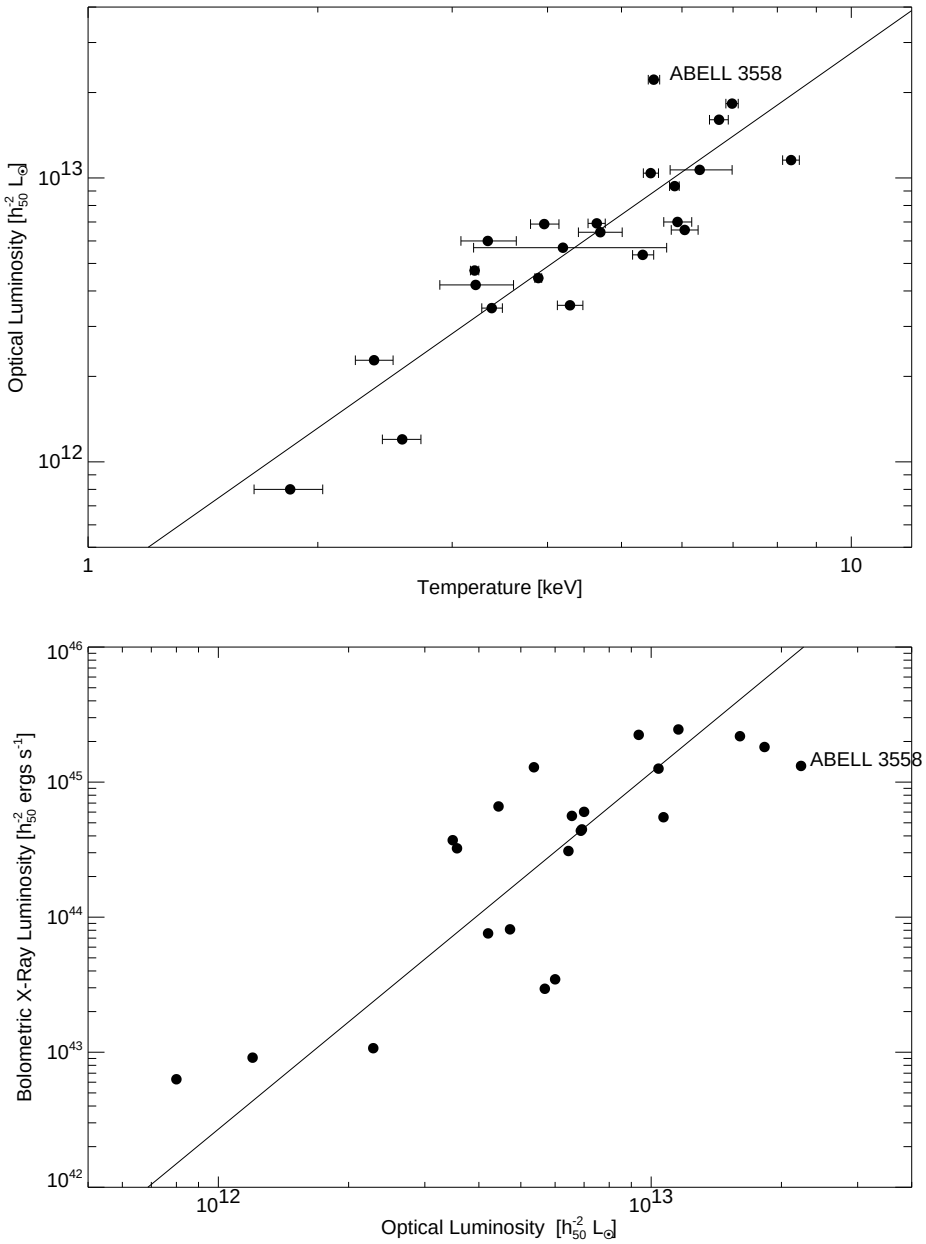

Figure 8.3: X-ray temperature (top) and bolometric x-ray luminosity (bottom) versus optical luminosity (L_{B_j}) from Girardi et al. (2000). Error bars on the temperatures are 90% confidence limits. The lines are a best fits.

Ω_0 (Bahcall et al. 2000).

Of course, measuring the M/L ratio requires some measure of the mass, introducing additional sources of possible errors and biases. Observational difficulties make it difficult to build a large sample of clusters where both masses and luminosities are computed in a homogeneous way. Some of the difficulties in measuring mass were discussed in Chapter 7. The determination of cluster luminosities includes uncertainties in: the quality, calibration and completeness of the photometric data; corrections and conversions of the galaxy magnitudes (e.g., K-corrections, isophotal to total magnitudes); corrections for background/foreground galaxy contamination; extrapolation of the sum of measured luminosities to include the contribution from faint objects below the completeness of the data; extrapolation to outer parts of the cluster beyond the region studied.

Here we directly compare two observable quantities, the optical luminosity and x-ray temperature (or luminosity). If M/L is constant for clusters than the optical luminosity should be related to the x-ray temperature just as the mass is. A different slope in the $L_{\rm opt} - T_{\rm x}$ relation would suggest a systematic variation of M/L with mass. The intrinsic dispersion in the $L_{\rm opt} - T_{\rm x}$ relationship would also indicate that M/L varies from object to object.

Girardi et al. (2000) derived the total optical luminosities for a homogeneous sample of 89 clusters (called the "C sample" in their paper to distinguish it from heterogeneous samples they use) based on B_j magnitudes and positions available from the COSMOS catalog (Yentis et al. 1992). They computed the optical luminosity within various radii for two different background estimators. We have used the values for L_{B_j} within their estimated virial radius and local background subtraction, which give a better relation than using a global mean background subtraction. Unfortunately, there are only 23 clusters in common between our samples.

There are several other sample of optical luminosities available in the literature, but these are smaller samples and usually also have other factors, e.g., measured at smaller radii (Hradecky et al. 2000) or limited to higher temperature clusters (Carlberg et al. 1997), that make them less suitable for our purposes than the Girardi data. In addition, the heterogeneity of optical luminosity samples, e.g., using different optical bands (e.g., L_B or L_V), makes it difficult to combine such catalogs to obtain a larger sample.

Figure 8.3 shows the relationship of the optical luminosity from Girardi to x-ray temperature and luminosity, respectively. $L_{\rm opt}$ and $T_{\rm x}$ are correlated but with a great deal of scatter. After considering a number of sources of systematic and random error, Girardi et al. (2000) estimate that their optical luminosities have errors of 20–30% although they do not give individual errors. Therefore, we fit the relationship using the BCES method assuming 30% errors for the optical

luminosities. Increase or decreasing the errors by ±20% only changes the slope by ±0.1 which is well within the errors of the fit. Using an unweighted fit also has little effect on the fitted parameters.

The fitted relationship ($L_{\rm opt} \propto {T_{\rm x}}^{1.9\pm0.3}$) agrees with the steeper M–T relation found in Chapter 7 and may be consistent with a constant M/L ratio for clusters, but the error is large enough that a weak dependence of $L_{\rm opt}$ on mass cannot be ruled out. Mohr et al. (1999) found that the gas mass of the ICM followed the relation $M_{gas} \propto {T_{\rm x}}^{1.98\pm0.18}$. Since the optical luminosity should be proportional to the mass in stars, these relationships would imply that the ratio of M_{stars}/M_{gas} is constant. This would argue against models which try to explain the steepening of the x-ray luminosity – temperature relationship (see Chapter 5) through more efficient star formation in lower mass systems depleting the x-ray gas (e.g., David & Blumenthal 1992; Bryan 2000).

The 1σ scatter around this best fit is ±45% for optical luminosity and ±20% for temperature. This is somewhat larger than Girardi's estimated errors on the luminosities and also larger than the temperature errors ($\sim$ 12%). However, like the slope of the fit, the statistics are currently too poor to make any definitive statements about whether M/L varies from object to object.

The $L_{\rm bol} - L_{\rm opt}$ relationship has a much larger scatter than the $L_{\rm opt} - T_{\rm x}$ relationship. The 1σ scatter around the best fit is ±60% for optical luminosity and about a factor of 1.5 for x-ray luminosity. This makes predicting the x-ray luminosity or flux from the optical luminosity (or vice-versa) difficult (see e.g., Donahue et al. 2001).

Neither the optical luminosity nor the dispersion around the best fit appears to be correlated with metal abundance or the cooling flow properties of the clusters. Unlike the $L_{\rm x} - T_{\rm x}$ relationship, cooling flow clusters are not more likely to have higher x-ray luminosity for a given optical luminosity. Abell 3558 has a higher optical luminosity than would be expected given its temperature or x-ray luminosity; however, it is located in the central region of the Shapley Supercluster, so the background may have been underestimated in determining $L_{\rm opt}$.

8.4 Optical Richness

Assuming clusters have similar mass-to-light ratios and galaxy luminosity functions, the number of galaxies in the cluster, measured by the richness, should be closely related to cluster mass. In this section, we check how well various richness estimators are correlated with x-ray temperature and luminosity.

Richness has always been a difficult attribute to quantify. Membership of a galaxy to a cluster cannot be individually assigned due to contamination by background and foreground galaxies, especially using only photometry and projected

positions. Usually, the richness is defined by the number of galaxies within some projected radius above some luminosity level.

Equation 1.2, the King model for the surface density profile of galaxies, can be integrated to get the number of galaxies within a projected radius (b) from the cluster center:

$$N(b) = 2\pi r_c^3 n_0 \ln\left[1 + \left(\frac{b}{r_c}\right)^2\right], \tag{8.1}$$

where r_c is the core radius and n_0 is the central galaxy density.

The core radius can be written in term of other cluster properties using the Poisson equation (see Sarazin 1988):

$$r_c^2 = \frac{9\sigma_r^2}{4\pi G n_0 m} \tag{8.2}$$

where m is the average galaxy mass.

For $r_c < b \ll r_{vir}$ and a constant mass-to-light ratio, a rough correlation can be established, $N(b) \propto \sigma^2$. Therefore, richness is expected to scale as $N \propto {T_{\rm x}}^{1.2}$ for the $\sigma_r - T_{\rm x}$ relation found earlier. However, the exact dependence is a function of the counting radius used.

8.4.1 Abell Richness

Abell (1958) offered the first quantified measure of cluster richness which he defined as the number of galaxies within 3 Mpc of the cluster center within 2 magnitudes of the third brightest galaxy. Abell et al. (1989) (hereafter ACO), in their addition of southern clusters to the Abell catalog, used essentially this measure but with a global instead of local correction to estimate background contamination. This systematic difference does not effect the results in this section, but we will comment on the shortcomings of the ACO technique for a few cases.

The Abell richnesses (N_A) for 155 clusters (119 from Abell (1958) and 36 from ACO) are given in Table A.6. Figure 8.4 shows N_A versus x-ray temperature and luminosity. As can be seen, Abell richness is not well correlated with either although there is a general trend for higher temperature/luminosity clusters to have higher Abell richnesses. This is only apparent by looking at the overall distribution. At low or higher temperatures, it is practically a scatter plot. Abell considered $N_A = 50$ to be the lower limit for inclusion in his statistical sample, but even for these clusters the correlation is rather poor.

We quantify the relationship by fitting a power law to the data. Since the temperature errors are small in comparison to the scatter, and the richness errors are unknown, we fit the relationship with a unweighted least squares bisector fit

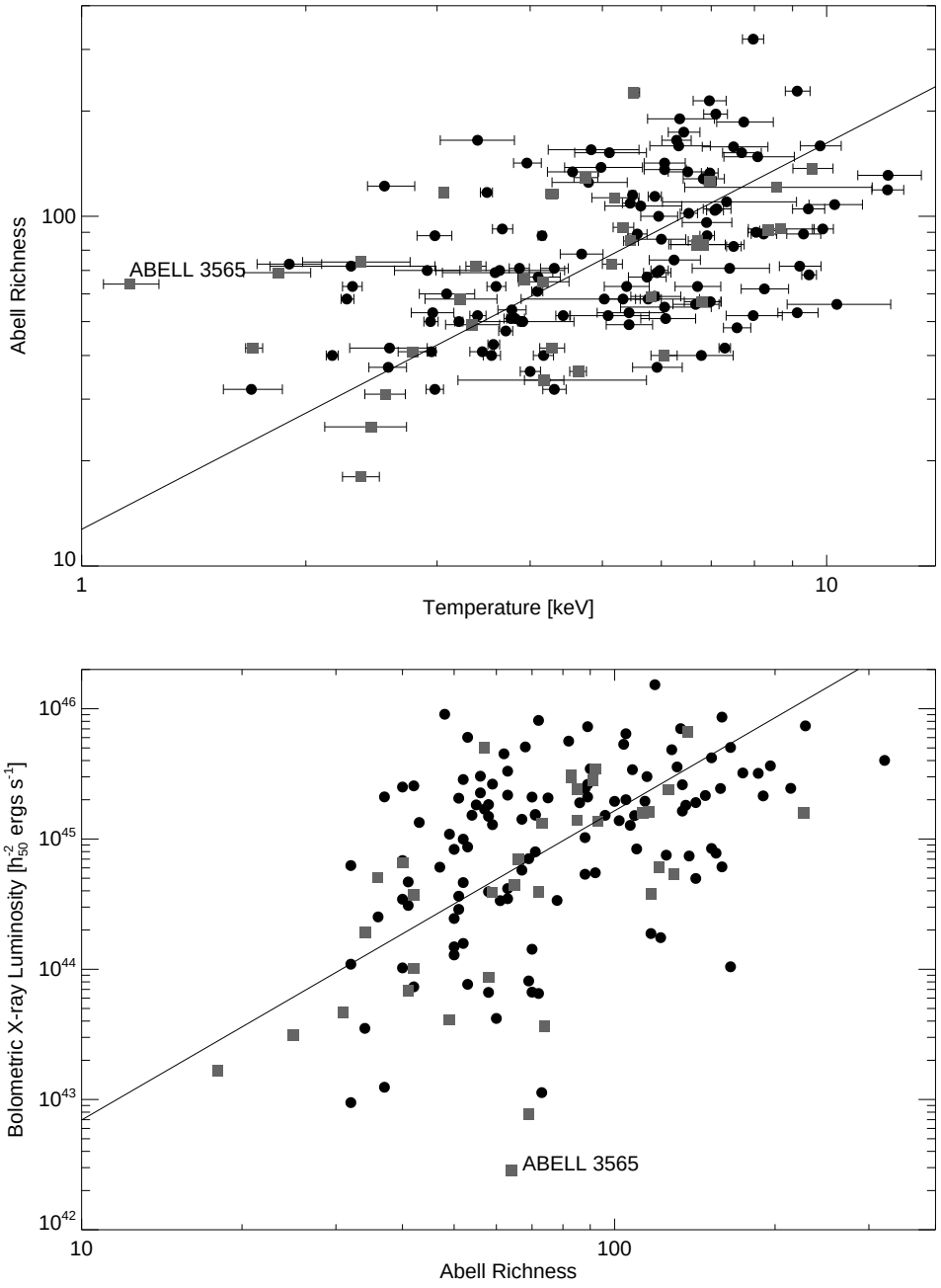

Figure 8.4: Abell richness versus x-ray temperature (top) and bolometric luminosity (bottom). Solid circles are richnesses from Abell (1958) while gray boxes are from Abell et al. (1989). Error bars on the temperatures are 90% confidence limits. The solid line is a best fit to the data.

(Isobe et al. 1990) and use bootstrap resampling to estimate the errors. We find that Abell richness is nearly linearly related to temperatures $N_A \propto {T_{\rm x}}^{1.1}$ (see Table 8.1), roughly what would be expected for the relation between richness and temperature. The scatter (1σ) around this best fit is $\pm 60\%$ in temperature or richness.

The lowest temperature cluster in the sample, Abell 3565, has a very high richness for its x-ray temperature. This discrepancy is probably because it is located in the Shapley Supercluster and the ACO global background underestimates the local galaxy density. The lowest richness cluster, Abell S0636 (the Antlia group) from the ACO supplemental catalog, has a unrealistic richness of 1 and is not even in the plotted range. Again, this is probably due to ACO's use of a global background estimate.

The relation between x-ray luminosity and richness has been studied by Edge & Stewart (1991a), Burg et al. (1994), and David et al. (1999). Edge & Stewart (1991a) also showed a correlation between x-ray temperature/luminosity and Abell richness but with only 18 clusters in the sample did not attempt to fit the relationship. Burg et al. (1994) showed that the x-ray luminosity function of galaxy clusters was similar for each Abell richness class but that the characteristic luminosity L_* increased for each class. David et al. (1999) created a sample of 150 Abell clusters observed by the ROSAT PSPC. Their plot of x-ray luminosity (in the 0.5–2.0 keV band within 1 Mpc of the cluster center) looks similar to ours. They do not fit the relationship but report a correlation between Abell richness and x-ray luminosity based on Kendall's τ statistical test.

While Abell richness and x-ray properties are correlated in a statistical sense, they are not in a predictive sense. For example, a 6 keV cluster can have a richness anywhere between about 40 to 200, covering practically the whole range of Abell's richness classes. The x-ray luminosity of nearly any given Abell richness can span at least two orders of magnitude. Abell richnesses are related to the mass of a cluster only in the broadest sense and are not useful for estimating the mass or other x-ray properties of clusters.

Several other richness measures similar to Abell's have been used for catalogs which cover of a portion of the southern sky survey (Dalton et al. 1997; Mazure et al. 1996; Lumsden et al. 1992). Abell's richness counts were done by eye. These surveys attempt to improve on Abell's method by using machine based algorithms. However, the overlap between these catalogs and the ACC is poor (6–17 clusters depending on the catalog). In general, these measures seem to perform no better than Abell's original richness measure.

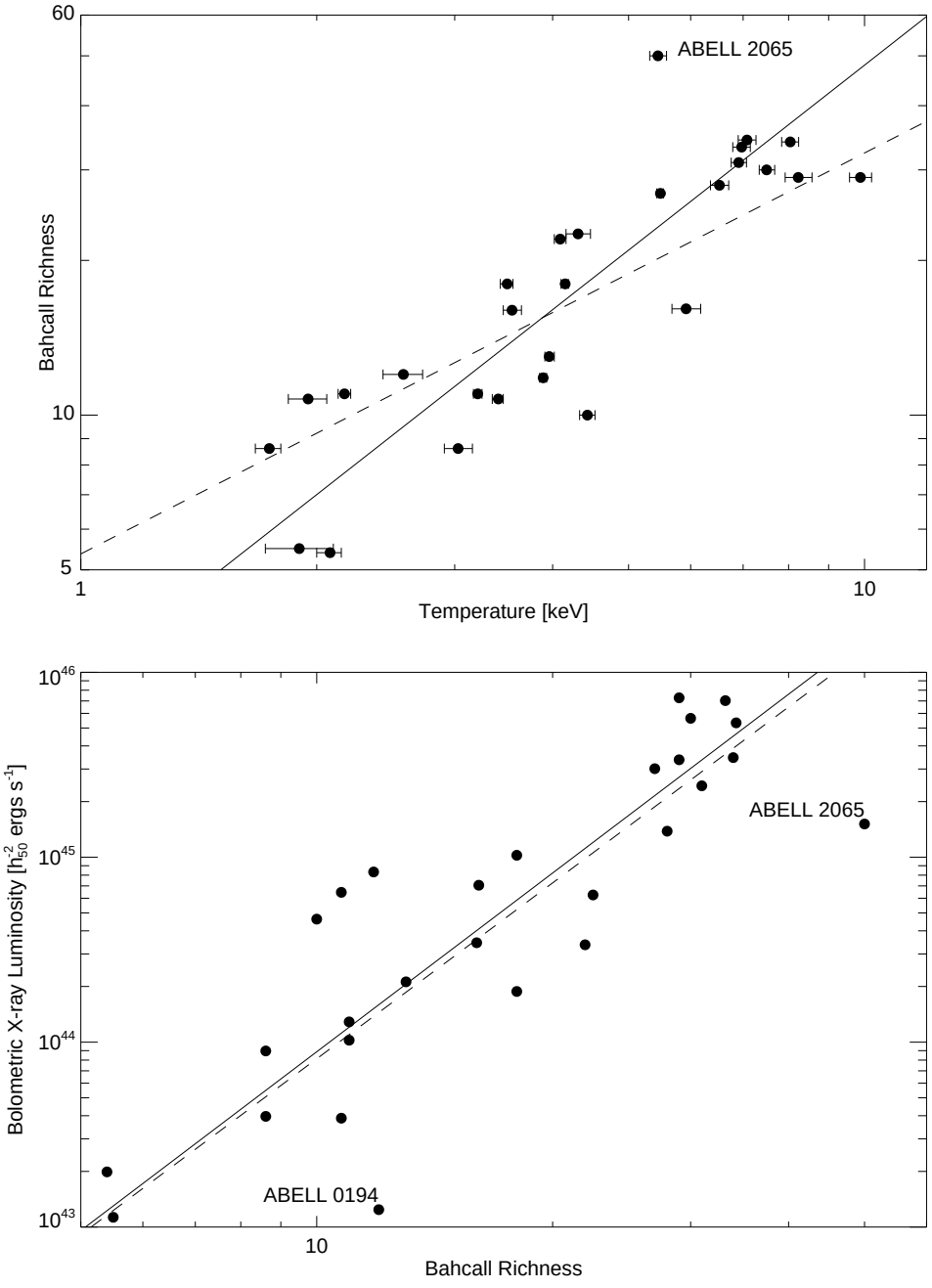

Figure 8.5: X-ray temperature (top) and bolometric x-ray luminosity (bottom) versus Bahcall Richness. The dotted lines are the fits given in Edge & Stewart (1991a).

8.4.2 Bahcall Richness

Another measure of richness was developed by Bahcall (1977). The Bahcall richness is essentially the Abell richness but with a smaller aperture, 0.5 Mpc rather than 3 Mpc. This minimizes the contamination due to field galaxies. Bahcall (1981) later introduced a correction factor to try to obtain the number of galaxies within a fixed part of the cluster luminosity function based on a relation between the magnitude of the third brightest cluster member and the richness. We will use these corrected richnesses here.

The Bahcall richnesses (N_B) for 28 clusters and groups were taken from Bahcall (1977, 1980, 1981). Figure 8.5 shows the correlation of N_B with temperature and luminosity, respectively. Unlike Abell richness, N_B is obviously correlated with both x-ray luminosity and temperature. We fit the data using an unweighted fit, as we did with Abell richness, and find that N_B scales as $N_B \propto {T_{\rm x}}^{1.2\pm0.1}$, which, as we showed earlier, is exactly what we would expect for a constant M/L ratio for clusters. Note that our fit is steeper than that given in Edge & Stewart (1991a) (for 18 clusters), but consistent within their large errors (0.78 ± 0.47).

The 1σ scatter around the best fit is about 30% for both temperature and richness. Bahcall estimates errors in the N_B determinations of about 30–50% so all the scatter may be due to measurement errors. The largest outlier on the plot is Abell 2065, which has a high richness for its temperature. This cluster is probably in the late stages of a merger (Markevitch et al. 1999) and has two central galaxies, which probably accounts for the discrepancy.

8.4.3 Two Point Correlation Function

A more sophisticated approach to determine the richness of a cluster uses the two-point correlation function ($\xi(r)$), defined by the relation:

$$n(r)\,dV = n_0\,[1 + \xi(r)]\,dV, \tag{8.3}$$

where $n(r)$ is the number of galaxies within a volume dV at a distance r from the counting center and n_0 is the average density of galaxies. This equation can be integrated to give the number of galaxies within the volume. Groth & Peebles (1977) determined that the distribution of galaxies was well fitted by a power law such that

$$\xi(r) = B_{gg} r^{-\gamma}, \tag{8.4}$$

where $\gamma \approx 1.77$. B_{gg} is called the spatial two-point correlation coefficient and represents a measure of the degree of clustering of a system. For a galaxy cluster, B_{gg} can be estimated using the two dimensional distribution of galaxies around the cluster center but requires a knowledge of the luminosity function of the galaxies

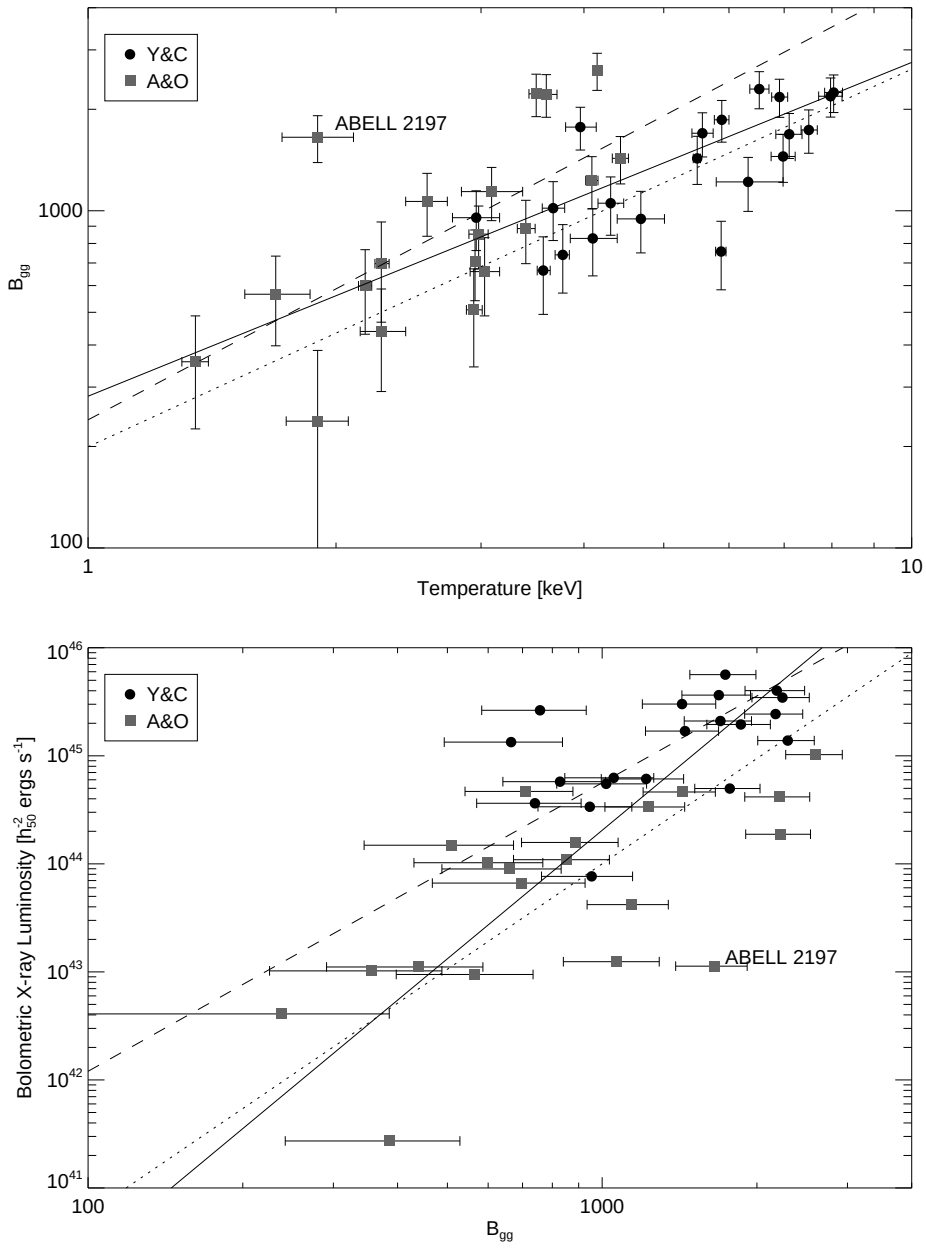

Figure 8.6: X-ray temperature (top) and bolometric x-ray luminosity (bottom) versus the spatial two point correlation function (B_{gg}). The filled circles are from Yee & López-Cruz (1999) while the squares are from Andersen & Owen (1994). The solid, dashed, and dotted lines are best fits to all the data, the YL data, and the AO data, respectively. Error bars are 1σ for the B_{gg} values.

in the cluster (for normalization) and background galaxy distribution. See Yee & López-Cruz (1999) and references therein for more information.

We use two samples of the B_{gg} values. Andersen & Owen (1994) (hereafter AO) measured the correlation function for a sample of clusters and groups using POSS data. Yee & López-Cruz (1999) (hereafter YL) used CCD data for a sample of Abell clusters. However, systematic differences exist between the derived values since each study assumed a different luminosity function. Following Miller et al. (1999) we multiply the AO values by a factor of 2 to account for the systematic differences although this may not entirely eliminate them (more below). There are 40 clusters in common between the two optical samples and the ACC (20 each) with no clusters in common between the YL and A0 samples.

Figure 8.6 shows the two-point correlation function for each sample against x-ray temperature and bolometric luminosity. Since individual errors are given on the B_{gg} estimate, we fit the data using the BCES method (although an unweighted fit gives similar results). We fit all the data and separately fit only the YL or AO data (see Table 8.1). All the fits yield slopes $\approx$1, similar to the Abell richness.

Although the fits are consistent within the 1σ uncertainties, there do seem to be systematic differences between the two B_{gg} samples. The YL data show significantly less scatter for a given temperature, $\approx$30%, compared to $\approx$50% for the AO data. This probably reflects differences in the data quality used (CCD data for YL versus photographic for AO).

The error bars on the B_{gg} values are about $\pm$20% for the YL data and $\pm$25% for the AO data. For the YL data, this is about the same size as the dispersion seen in both temperature and richness around the best fit. The AO dispersion is larger but may simply reflect the poorer quality data. Therefore, the scatter may be all due to measurement errors.

The largest outlier in both plots is Abell 2197 which has a high richness for its temperature (or alternatively low temperature for its richness). This cluster was also an outlier in the M_{vir}–$T_{\rm x}$ relation in the same sense, a high $M_{\rm vir}$ or low $T_{\rm x}$. It is a merging cluster with a great deal of substructure which probably explains the rather poor correlation.

8.5 Conclusions

The $\sigma_r - T_{\rm x}$ and $L_{\rm opt} - T_{\rm x}$ relationships are steepened in ways which imply that non-gravitational mechanisms have affected the x-ray emission. We also see that the M/L ratio of clusters and groups is consistent with a constant value based on the $L_{\rm opt}$ –$T_{\rm x}$ and $N_{\rm B}$ –$T_{\rm x}$ relationship. The scatter in all these relationship can be explained by measurement error and no intrinsic dispersion is required.

However, we need better and large optical samples with a larger overlap with x-ray samples. The number of clusters well observed in both the optical and x-ray is fairly small given the larger number of clusters known. More lower mass systems (i.e., groups) are also needed to better constrain the relationship and overcome scatter in the measurements. For example, the sample used for the $L_{\rm opt}$ –$T_{\rm x}$ relation contains only three clusters with temperatures below 3 keV. Without these three clusters, the correlation becomes much worse. Besides being larger, optical samples also need to achieve a degree of homogeneity as has our ASCA catalog. This may soon be possible to some degree with the Sloan Digital Sky Survey.

Chapter 9

Summary and Conclusions

For this thesis, we have obtained x-ray temperatures, metal abundances, and luminosities for a catalog of 273 clusters and groups observed with the ASCA x-ray satellite. We have used these data, in combination with additional data from the literature, to examine correlations (scaling laws) between the properties of clusters. We have then drawn a number of conclusions about the physics and evolution of clusters of galaxies. Our data reduction and results are summarized and discussed below.

9.1 Summary of Data Reduction and Analysis

To construct the cluster catalog, we searched the literature for galaxy clusters that were observed by ASCA, either targeted or serendipitously, and available in the HEASARC public archives. We then removed clusters which were too faint, seriously contaminated by AGN, or otherwise not useful (see Table A.1 in Appendix A.1) to obtain a sample of 273 clusters and groups of galaxies. This is our ASCA Cluster Catalog (ACC) which is the largest catalog of cluster data created to date.

We then used a series of semi-automated scripts to tie together the x-ray analysis tools of the `FTOOLS 5.0.1` package and `XSPEC`, the spectral fitting program. We extracted spectra from the GIS and SIS observations from a circular region with a radius chosen so that the ASCA surface brightness was roughly 5σ times the background level. We then fit a single temperature MEKAL spectral model to the spectra to obtain x-ray temperatures, metal abundances, and luminosities. Table A.2 lists the ACC sample and the results of the fitting procedure.

To test our reduction procedures, we compared our results to those previously published in the literature. Our x-ray temperatures agree to within 10% on average with other ASCA measurements of the same clusters. We find similarly good agreement to BeppoSAX derived temperatures. The agreement is also good with

earlier Einstein and EXOSAT temperatures although with a large dispersion. However, we find poorer agreement between ASCA and ROSAT PSPC temperatures. In particular, the PSPC temperatures for a sample of groups (Helsdon & Ponman 2000b) agree well with our temperatures for $T_{\rm x} \lesssim 1$ keV but are systematically cooler than the ASCA temperatures for higher temperatures. This seems to be due to the poor energy resolution and small bandpass of the ROSAT PSPC. Therefore, PSPC temperatures for systems above 1 keV should be interpreted with caution.

We find good agreement with other ASCA abundance measurements, although ours are consistently slightly higher ($\sim 10\%$) on average, except for the ASCA abundances of Fukazawa et al. (1998). However, Fukazawa et al. (1998) excluded the central regions of clusters. If we follow a similar reduction procedure, the discrepancy is greatly reduced. In comparing our ASCA abundances to those from other instruments, we find agreement with BeppoSAX and EXOSAT abundances although the latter have a large dispersion. At group scales, ROSAT PSPC abundance agree poorly with the ASCA derived abundances for most groups. Unlike the ASCA abundances, the PSPC abundances for the same groups differ greatly between different authors. Therefore, we conclude that ROSAT abundances are not reliable in general.

Our derived luminosities agree well with those based on the ROSAT All-Sky Survey but are $\sim 25\%$ higher than those from Einstein and EXOSAT, pointing to calibration issues between the instruments. Overall, the average 1σ dispersion between our ASCA luminosities and other cluster luminosities is about 30%. At groups scales, we may be missing a substantial amount of flux below the background for some groups, depending on the surface brightness distribution of the gas. Comparing with ROSAT PSPC luminosities of Helsdon & Ponman (2000b), we find that some agree quite well while for others our ASCA luminosities are up to 5 times lower.

9.2 Summary of Science Results

The significant new results discovered in the course of this thesis research are:

- The dispersion of the $L_{\rm x} - T_{\rm x}$ relationship is correlated with the mass deposition rate, central cooling time, and central density. These correlations may reflect the deeper central potentials in some clusters due to age differences.

- The average metal abundance of clusters varies as a function of temperature. The abundance is relatively constant at $\approx 0.3\ Z_{\odot}$ for temperatures $T_{\rm x} \gtrsim 5$ keV, then rises to $\approx 0.5\ Z_{\odot}$ between 2–5 keV before falling to ≈ 0.2 for $T_{\rm x} \approx 1$ keV.

- The metal abundance is correlated with cooling time and central density (but not mass deposition rate).

- Different mass estimators give different slopes of the mass – temperature relationship. For optical virial masses and isothermal β-model estimates, we find that $M \propto {T_{\rm x}}^{1.8}$ although the normalization of the viral mass M–T is about 40% higher. For x-ray mass estimates which include temperature profile information, we find that $M \propto {T_{\rm x}}^{1.5}$, although our sample only contains clusters hotter than $T_{\rm x} \gtrsim 3$ keV. The origin of these discrepancies is unclear.

- Unlike the $L_{\rm x} - T_{\rm x}$ relation, the intrinsic dispersion in the M–T is probably quite small. The virial mass estimator shows a large scatter but this is probably due to inherent noise in the virial mass measurement.

- The number of redshifts used to determine the velocity dispersion can affect the fitted relationships between velocity dispersion and x-ray temperature or luminosities. We find that velocity dispersions are systematically underestimated if $\lesssim 30$ redshifts are used to calculate the dispersion.

In addition to the new results, we have also shown the following:

- The x-ray luminosity – temperature relationship is $L_{\rm bol} \propto {T_{\rm x}}^{2.8}$ for clusters but steepens ($\alpha \approx 3.6$) for groups.

- The $L_{\rm x} - T_{\rm x}$ relationship does not evolve with redshift out to at least $z \sim 0.5$.

- The average metal abundance of clusters (with $T_{\rm x} > 5$ keV) does not evolve out to at least $z \sim 0.3$.

- The optical velocity velocity dispersion is related to the x-ray temperature as $\sigma_r \propto {T_{\rm x}}^{0.6}$, slightly steeper than if only gravitational physics were important. We do not see any intrinsic dispersion.

- The optical luminosity is correlated with x-ray temperature such that $L_{\rm opt} \propto {T_{\rm x}}^{1.9}$. This may indicate a change in the mass–to–light ratio in clusters depending on the M–T relation.

- The optical richness is correlated with the x-ray temperature roughly as $N \propto {T_{\rm x}}^{1.0}$, depending slightly on how richness is measured. Abell richness is only loosely correlated with x-ray temperature or luminosities. The Bahcall richness and the two point correlation coefficient show a tighter relationship but are still affected by large uncertainties in measuring the richnesses.

Our results should not be greatly affected by the heterogeneous nature of the sample. We only require that the clusters in the catalog be representative of the general population. Clusters are in the sample because they were picked to be targets of ASCA observations. This means that the bulk of the sample is comprised of nearby clusters and groups, since they are the brightest (highest flux) objects. In general, they were not observed because they had a particular temperature, abundance, luminosity, or velocity dispersion. Therefore, our scaling laws should be relatively free of biases.

9.3 Discussion

In this thesis, one of the main themes we have seen is that clusters are not completely self similar, contrary to early theoretical expectations (e.g. Kaiser 1986). That is, less massive systems are not just scaled down versions of more massive clusters. This can be seen in the steepened slope of the $L_{\rm x} - T_{\rm x}$, M-T, and σ-$T_{\rm x}$ relations relative to what would be expected in simple models. Assuming the trends seen between abundances and temperatures are real, they also indicate that different physics operates in smaller systems. This physics could be changing gas fractions, which might explain the slope of the $L_{\rm x} - T_{\rm x}$ and the rise in abundance at lower temperatures, or energy injection by supernovae or possibly the effects of cooling. The present data is not good enough to distinguish between such scenarios.

We have also seen that there can be a great deal of variation between otherwise similar clusters. For example, clusters with similar temperatures and abundances can have very different luminosities. This may be a sign of age differences between such clusters. However, we have also seen a great deal of evidence that clusters are old systems. The $L_{\rm x} - T_{\rm x}$ and abundance of clusters is relatively constant out to $z \sim 0.5$, meaning that clusters must have formed long before that.

Comprehensive simulation and theoretical investigations will be needed to try to tie all of our observations together to come to a better understanding of the formation and evolution of clusters in the universe.

As we have seen, homogeneous samples with well understood errors (and known quality control) provide important insight in cluster physics. The ASCA Cluster Catalog is a first step towards building such large samples and will provide a baseline for future work. For example, we are currently working on a similar catalog for clusters observed by ROSAT. With the better spatial resolution of ROSAT, we will fit the surface brightness of clusters to better explore the scatter in the $L_{\rm x}-T_{\rm x}$ relationship and obtain gas masses. Combined with the ACC, we can obtain cluster masses as well. With the gas mass and abundance, we can obtain the total iron mass which is known to be correlated with the optical luminosities

(Arnaud et al. 1992) and may be important in understanding the relation between metal abundance and other properties. It will take a long time for Chandra and XMM to build such a large database of cluster observations.

Appendix A

Data Tables

A.1 Clusters Not Included in the ASCA Sample

Table A.1 lists cluster and groups that were not included in the final catalog (see Table A.2). See the discussion in Section 3.2. Images of these fields are available on the World Wide Web[1].

The columns in Table A.1 are as follows:

1. Cluster name.
2. The ASCA sequence number of the observation.
3. The nominal right ascension (J2000) of the cluster from the literature.
4. The nominal declination (J2000) of the cluster.
5. The off–axis distance of the cluster from the GIS field center. Only clusters $< 15'$ were included.
6. The ASCA field name assigned to the observation, usually the intended target of the observation.
7. A flag indicating the reason the source was excluded from further analysis. The meanings of the flags are as follows:

   AGN The cluster appears to be a point source in the SIS image, so all or most of the emission likely comes from an AGN located in the cluster.

   bright source nearby The cluster is close to a bright source which severely contaminates the emission.

[1] `http://lheawww.gsfc.nasa.gov/user/horner/asca`

galaxy emission The emission appears to be dominated by a single elliptical galaxy.

not detected No emission was evident at the cluster coordinates.

offset The cluster is too far off–axis causing much of the emission to go outside the GIS field-of-view. These observations were usually intentionally offset from a bright cluster that is included in the catalog in another observation.

see notes A more detailed explanation is required. See Appendix B for further information about this source.

too faint Emission is seen at the cluster coordinates but is too faint to obtain a spectrum.

Table A.1: Clusters Not Included in ASCA Sample.

Cluster	Sequence	α [arcmin.]	δ [deg.]	Off-Axis [deg.]	Field Name	Flag
1RXS J031413.7−223533	20021000	48.5538	-22.5947	7.21	EF ERI	AGN
3C 215	83041000	136.6329	16.7698	5.43	3C215	AGN
4C +37.67	22007000	343.4819	38.1745	9.13	SW LAC	not detected
ABELL 0496	86069000	68.4045	-13.2462	13.31	A496	offset
	86069010	68.4045	-13.2462	13.72	A496	offset
ABELL 0745	66006000	136.7070	4.7818	8.10	IRASF09039+0503	not detected
ABELL 1030	83063000	157.7267	31.0570	1.56	B2 1028+313/A1030	AGN
	83063010	157.6555	30.9932	1.51	B2_1028+313_N2	AGN
ABELL 1396	73037000	177.8081	54.8553	12.94	PG 1148+549	not detected
ABELL 1588	74017000	190.3946	-4.7908	6.70	3C275	not detected
	75023000	190.3946	-4.7908	14.41	NGC 4593	not detected
ABELL 1593	76069000	190.5081	33.3094	4.19	IRAS 12397+3333	AGN
ABELL 1635	86008010	193.5755	-8.9377	7.66	HCG62	not detected
ABELL 1714	93006150	200.1529	33.4549	12.96	CENT.	not detected
	93007030	200.1529	33.4549	3.27	P1	not detected
	93007070	200.1529	33.4549	12.65	P1	not detected
ABELL 1716	93007050	200.2266	33.9050	11.89	P1	too faint
ABELL 1774	83049000	205.2914	40.0144	6.85	ABELL 1774	AGN
ABELL 2199	86068010	247.1540	39.5243	13.53	A2199	offset
ABELL 2235	74004000	253.7413	40.0211	14.88	MKN501	not detected
	74004010	253.7413	40.0211	14.68	MKN501	not detected
ABELL 2256	10004010	255.9314	78.7174	13.14	A2256	offset
	10004020	255.9314	78.7174	6.00	A2256	offset
ABELL 2536	84014000	346.9425	-22.4291	5.47	A2534-A2536	not detected
ABELL 2541	86045000	347.5170	-22.9618	12.17	SCC100_7	not detected
ABELL 2546	86044000	347.6913	-22.6616	11.34	SCC100_6	not detected
	86045000	347.6913	-22.6616	13.37	SCC100_7	not detected
ABELL 2634:SM98 02	83002000	354.4837	27.1920	11.18	A2634	bright source nearby
ABELL 2791	73062000	8.5248	-21.5744	3.22	IRAS 00317-2142	not detected
ABELL 2804	84004000	9.9111	-28.8893	5.71	A2811-OFFEST	not detected
ABELL 2843	83027000	14.1557	-27.5130	14.99	J1888.16CL	not detected
	92005000	14.1557	-27.5130	13.35	GSGP4	not detected
ABELL 3002	73021000	34.5525	-50.0367	10.19	QSO 0215-504	not detected
ABELL 3526B	80033000	192.5168	-41.3836	4.41	CEN CL (SUBCLUSTER)	bright source nearby
ABELL 3571	85064000	206.8706	-32.8658	13.94	A3571	offset
	85064010	206.8706	-32.8658	14.58	A3571	offset
ABELL 3574	70005000	207.2890	-30.2983	1.16	IC4329A	AGN
	75047000	207.2890	-30.2983	3.83	IC4329A	AGN
	75047010	207.2890	-30.2983	3.97	IC4329A	AGN
	75047020	207.2890	-30.2983	4.02	IC4329A	AGN
	75047030	207.2890	-30.2983	4.06	IC4329A	AGN
ABELL 3755	76042000	318.8659	-43.3749	4.80	LBQS 2111-4335	not detected
ABELL S0549	70006000	87.6649	-32.2708	4.57	PKS 0548-322	AGN
	74006000	87.6649	-32.2708	5.55	PKS 0548-322	AGN
ABELL S0636	85011000	157.5146	-35.3234	14.67	NGC 3268	offset
ABELL S0822	34012000	294.4083	-46.3703	9.44	QS TEL	not detected
ABELL S0911	63010000	314.6521	-42.9557	14.19	IRAS 20551-4250	not detected
ABELL S1071	71035000	343.4915	-17.6335	1.89	MR2251-178	AGN

Cluster	Sequence	α [arcmin.]	δ [deg.]	Off-Axis [deg.]	Field Name	Flag
	71035010	343.4915	-17.6335	2.47	MR2251-178	AGN
	71035020	343.4915	-17.6335	2.16	MR2251-178	AGN
	71035040	343.4915	-17.6335	2.15	MR2251-178	AGN
	71035050	343.4915	-17.6335	2.23	MR2251-178	AGN
	71035060	343.4915	-17.6335	2.10	MR2251-178	AGN
	74028000	343.4915	-17.6335	8.96	MR 2251-178	AGN
	74028010	343.4915	-17.6335	9.03	MR 2251-178	AGN
	74028020	343.4915	-17.6335	2.07	MR 2251-178	AGN
	74028030	343.4915	-17.6335	2.13	MR 2251-178	AGN
APMCC 103	84004000	10.2493	-28.9427	13.85	A2811-OFFEST	not detected
APMCC 412	72005000	53.5635	-40.1773	7.63	PKS0332-403	AGN
APMCC 878	72042000	349.4444	-42.3732	13.78	NGC_7582	not detected
	74026000	349.4444	-42.3732	7.63	NGC7582	AGN
APM 045231.0−182236	86017000	73.6813	-18.2971	4.57	RXJ0454.8-1806	not detected
AX J2019+112	82027000	304.8250	11.4528	3.48	MG 2016+112	see notes
CEN 45	80034000	192.2048	-41.0419	1.76	CEN CL (OFFSET)	not detected
CL 0107+31	85038000	17.3667	31.8225	11.07	CL0107+31	AGN
	85038010	17.3667	31.8225	6.00	CL0107+31_S1	AGN
CL 0303+1706	84028000	46.5778	17.3009	8.98	MS0302.7+1658	too faint
CRSS J1406.9+2834	86064000	211.7262	28.5706	5.08	WARPJ1406.9+2834	too faint
ClG J0848+4453	90009010	132.1425	44.8931	7.38	Lynx Field	not detected
	90009020	132.1425	44.8931	7.35	Lynx Field	not detected
	90009030	132.1425	44.8931	7.31	Lynx Field	not detected
Cl 0302+1658	87055010	46.3913	17.1683	14.96	MS0302+1717_S1	too faint
EDCC 015	45010000	325.0914	-22.8703	13.61	NGC 7099	not detected
EDCC 067	72012000	329.6197	-29.9199	14.79	PKS2155-304	not detected
	78003004	329.6197	-29.9199	14.98	PKS2155-304	not detected
EDCC 504	74081000	14.2276	-22.2722	8.01	TON S 180	too faint
ESO 161−IG 006	85043000	96.5219	-54.0343	5.56	CLUSTER LINK REGION	too faint
F1835.22CR	93008000	161.7568	-0.4473	12.01	BJS855	too faint
GHO 0317+1521	83028000	50.0096	15.5302	5.20	CL0317+1521	not detected
GHO 1311+3200	74048010	198.4243	31.7355	11.84	LSS1988+317	not detected
	92001050	198.4243	31.7355	8.85	LSS_LineD-P9	not detected
	92002060	198.4243	31.7355	5.56	LSS_LineC-P8	not detected
GHO 1311+3218	92001050	198.3697	32.0437	9.90	LSS_LineD-P9	not detected
	93006060	198.3697	32.0437	11.62	CENT.	not detected
GHO 1313+3224	92001040	199.0259	32.1397	9.85	LSS_LineB-P9	not detected
	93006000	199.0259	32.1397	8.98	CENT.	not detected
	93006140	199.0259	32.1397	8.34	CENT.	not detected
	93006190	199.0259	32.1397	11.74	CENT.	not detected
GHO 1316+3227	93007190	199.7570	32.1942	13.61	P1	not detected
GHO 1322+3114	81006000	201.2015	30.9833	3.50	CL132229+30274	too faint
HCG 004	73062000	8.5667	-21.4467	4.91	IRAS 00317-2142	AGN
HCG 016	74001000	32.3888	-10.1630	7.45	HCG16	see notes
HCG 048	83024000	159.4402	-27.0805	3.61	HCG48	see notes
	83024010	159.4402	-27.0805	3.22	HCG48_N2	see notes
HCG 090	74091000	330.5017	-31.8659	10.89	NGC 7172	AGN
HCG 092	62002000	339.0021	33.9658	6.12	NGC7320	see notes
HST J051909−45493	74066000	79.7875	-45.8223	12.13	PICTOR A	not detected
HST J051910−45510	74066000	79.7948	-45.8516	12.14	PICTOR A	not detected
HST J072049+71089	71006000	110.2066	71.1492	9.70	0716+714	not detected
	71006010	110.2066	71.1492	9.68	0716+714	not detected

Cluster	Sequence	α [arcmin.]	δ [deg.]	Off-Axis [deg.]	Field Name	Flag
	71006020	110.2066	71.1492	9.91	0716+714	not detected
HST J075047+14412	32000000	117.6985	14.6877	12.88	RE0751+14	not detected
HST J111744+44177	74072000	169.4365	44.2960	13.18	PG 1114+445	not detected
HST J121111+39273	70000000	182.7982	39.4561	8.75	NGC4151	not detected
	70000010	182.7982	39.4561	4.45	NGC4151	not detected
	71019000	182.7982	39.4561	2.96	NGC 4151	not detected
	71019010	182.7982	39.4561	2.94	NGC 4151	not detected
	71019020	182.7982	39.4561	2.99	NGC 4151	not detected
	71019030	182.7982	39.4561	2.98	NGC 4151	not detected
	73019000	182.7982	39.4561	13.33	NGC4151	not detected
	78001000	182.7982	39.4561	13.28	NGC4151	not detected
	78001001	182.7982	39.4561	13.26	NGC4151	not detected
	78001002	182.7982	39.4561	13.27	NGC4151	not detected
	78001003	182.7982	39.4561	13.30	NGC4151	not detected
	78001004	182.7982	39.4561	13.28	NGC4151	not detected
	78001005	182.7982	39.4561	13.27	NGC4151	not detected
HST J122332+15518	55044000	185.8870	15.8649	4.20	SN1979C NGC4321	not detected
HST J122355+15495	55044000	185.9810	15.8256	9.64	SN1979C NGC4321	not detected
HST J123155+14163	75031000	187.9812	14.2731	7.77	NGC4501	not detected
HST J141653+52210	86056000	214.2221	52.3511	14.52	CFRS1415+52	not detected
HST J141727+52267	86056000	214.3653	52.4458	6.80	CFRS1415+52	not detected
HST J150620+01448	61012000	226.5852	1.7470	9.24	NGC 5846	not detected
HST J150621+01431	61012000	226.5910	1.7187	7.59	NGC 5846	not detected
HST J193928−46139	34012000	294.8690	-46.2333	11.37	QS TEL	not detected
HST J214823−34530	74016000	327.0975	-34.8848	9.38	NGC7130	not detected
HST J225657−36342	60005000	344.2386	-36.5709	7.76	IC1459	not detected
J1556.15BL	80038000	54.8574	-35.4888	14.10	NGC1399/FORNAX	not detected
	80039000	54.8574	-35.4888	4.79	WEST OF NGC1399	not detected
J1836.10RC	74047000	206.0750	-0.1713	13.60	RD J13434+0001	not detected
	96009000	206.0750	-0.1713	9.24	BJS864	not detected
J1836.23TR	74047000	205.7755	-0.0231	9.27	RD J13434+0001	not detected
J1888.16CL	83027000	14.2370	-27.6750	5.31	J1888.16CL	not detected
	92005000	14.2370	-27.6750	7.94	GSGP4	not detected
MS 0354.6−3650	82042000	59.1192	-36.6944	12.56	MS0353.6-3642	not detected
MS 0407.2−7123	33008000	61.7230	-71.2655	8.89	VW HYI	not detected
MS 0419.0−3848	87052000	65.1893	-38.6970	10.40	MS0418.3-3844	not detected
MS 0451.6−0305	77042000	72.9192	-3.0990	11.64	NGC 1685	not detected
MS 0537.1−2834	71005000	84.7759	-28.5503	13.09	PKS0537-286	not detected
MS 0623.6−5238	24022000	96.1909	-52.6789	2.57	HD45348	too faint
MS 1208.7+3928	70000010	182.8145	39.2016	11.96	NGC4151	not detected
	71019000	182.8145	39.2016	13.80	NGC 4151	not detected
	71019010	182.8145	39.2016	13.90	NGC 4151	not detected
	71019020	182.8145	39.2016	14.04	NGC 4151	not detected
	71019030	182.8145	39.2016	13.97	NGC 4151	not detected
MS 1209.0+3917	73019000	182.2625	39.2993	13.30	NGC4151	not detected
	78001000	182.2625	39.2993	13.32	NGC4151	not detected
	78001001	182.2625	39.2993	13.35	NGC4151	not detected
	78001002	182.2625	39.2993	13.33	NGC4151	not detected
	78001003	182.2625	39.2993	13.30	NGC4151	not detected
	78001004	182.2625	39.2993	13.32	NGC4151	not detected
	78001005	182.2625	39.2993	13.32	NGC4151	not detected
MS 1219.9+7542	63025000	185.5292	75.4381	7.85	NGC 4291	not detected

Cluster	Sequence	α [arcmin.]	δ [deg.]	Off-Axis [deg.]	Field Name	Flag
	72045000	185.5292	75.4381	7.54	MKN 205	not detected
	75011000	185.5292	75.4381	6.75	MKN 205	not detected
MS 1409.9−0255	75033000	213.1441	-3.1525	13.96	NGC 5506	not detected
MS 1610.4+6616	83042000	242.6991	66.1448	8.96	3C330	not detected
NGC 0315	74000000	14.4550	30.3366	6.39	NGC315	galaxy emission
NGC 1407	63021000	55.0492	-18.5799	5.37	NGC 1407	galaxy emission
	66002000	55.0492	-18.5799	5.33	NGC 1407	galaxy emission
NGC 1600	63029000	67.9162	-5.0862	6.88	NGC 1600	galaxy emission
NGC 2300	85005010	113.0812	85.7092	12.00	NGC2300 GROUP	offset
NGC 3923	66001000	177.7588	-28.8065	5.16	NGC 3923	galaxy emission
	66001010	177.7588	-28.8065	4.99	NGC_3923_N2	galaxy emission
	82016000	177.7588	-28.8065	5.27	NGC3923/HG28	galaxy emission
NGC 4151	70000000	182.6312	39.4052	0.89	NGC4151	AGN
NGC 4278	76008000	185.0279	29.2726	5.06	NGC4278	galaxy emission
NGC 4321	55044000	185.7333	15.8229	5.04	SN1979C NGC4321	galaxy emission
NGC 4365	60031000	186.1121	7.3230	0.69	NGC4365	galaxy emission
NGC 4472	60029000	187.4457	8.0021	3.28	NGC 4472 NW3.5	galaxy emission
	60030000	187.4457	8.0021	8.44	NGC 4472 NW8.5	galaxy emission
NGC 4631	62004000	190.5667	32.5475	7.10	NGC4631	galaxy emission
NGC 4636	60032000	190.7071	2.6884	13.51	NGC4636	galaxy emission
	64008000	190.7071	2.6884	12.18	NGC 4636	galaxy emission
NGC 4649	61005000	190.9182	11.5502	3.56	NGC4649	galaxy emission
OPHIUCHUS CLUSTER	80028000	258.1082	-23.3759	13.99	OPH_CL OFF_1	offset
RSCG 75	77077000	221.7775	11.5914	13.28	RXS J144701.1+114536	not detected
RX J0018.8+1602	93005000	4.6896	16.0281	12.53	SA68B	not detected
RX J0336.3+0035	22017000	54.0754	0.5933	10.50	HR1099	not detected
RX J0337.2+0033	22017000	54.3204	0.5511	8.72	HR1099	not detected
RX J1053.7+5735	95001000	163.4308	57.5892	7.06	LOCKMAN HOLE #1	not detected
	95001010	163.4308	57.5892	7.07	LOCKMAN_HOLE_N2	not detected
RX J1236.2+2554	62005000	189.0676	25.9049	5.58	NGC4565	not detected
RX J1236.8+2550	62005000	189.2110	25.8344	14.32	NGC4565	not detected
RX J1506.0+0641	84024000	226.5221	6.6975	12.30	SC2028/2029	too faint
RX J1555.0+1105	73049000	238.7527	11.0735	7.52	PG 1553+11	not detected
RX J1730.4+7423	26040000	262.6200	74.3861	12.72	29 DR DRA	not detected
	26040010	262.6200	74.3861	12.40	29 DR DRA	not detected
	26040020	262.6200	74.3861	11.14	29 DR DRA	not detected
SCL 060	84073000	72.2418	-20.4138	11.07	ABELL 514	not detected
SCL 196	81033000	335.7443	-1.6468	11.23	A2440	not detected
SC 1327−312	83058000	202.4458	-31.6081	14.29	SHAP_ICM1	offset
TW Hya X08	25027000	165.2083	-34.7238	7.67	TW HYA	not detected
WBL 088	80037000	43.6342	41.5861	12.98	AWM7 - WEST	offset
	81011030	43.6342	41.5861	10.38	AWM7#4	offset
WBL 280	74007000	160.4013	6.2716	3.82	4C06.41	not detected
	74007010	160.4013	6.2716	3.86	4C06.41_N2	not detected
ZWCL 1114.1+1824	64003000	169.2332	18.0602	3.63	NGC3607/3608	galaxy emission
ZwCl 1201.5+0205	52027000	181.1065	1.7451	8.60	MKW4	not detected
	82014000	181.1065	1.7451	8.68	MKW4 SW	not detected
	82015000	181.1065	1.7451	6.41	MKW4 SE	not detected
ZwCl 1305.4+2941	91001010	196.9583	29.4289	12.72	SA57#1	too faint
	91001020	196.9583	29.4289	14.33	SA57#4	too faint
	91003030	196.9583	29.4289	12.91	POINT_B_N4	too faint
	91005030	196.9583	29.4289	10.85	POINT_D_N4	too faint

Cluster	Sequence	α [arcmin.]	δ [deg.]	Off-Axis [deg.]	Field Name	Flag
ZwCl 1454.8+2233	82053000	224.0778	22.3569	9.06	E1455_PT1	too faint
	82053010	224.0778	22.3569	9.01	E1455_PT2	too faint
ZwCl 1555.3+4529	75034000	239.0842	45.2559	2.65	MS 1555.1+4522	not detected
KSD98 16	92001090	197.5104	30.9221	13.46	LSS_LineD-P5	not detected
	96002020	197.5104	30.9221	11.53	CENT	not detected
KSD98 18	91003000	197.7329	30.6299	9.43	POINT B.	not detected
	91004000	197.7329	30.6299	10.18	POINT C.	not detected
	92001090	197.7329	30.6299	7.98	LSS_LineD-P5	not detected
	92002090	197.7329	30.6299	11.68	LSS_LineC-P5	not detected
	96002010	197.7329	30.6299	14.24	CENT	not detected
LP96 Cl1044+0006	93008000	161.5902	-0.1673	10.26	BJS855	not detected
LP96 Cl1044−0004	93008000	161.5307	-0.3336	3.51	BJS855	not detected
LP96 Cl1341+0005	74047000	205.9337	-0.1727	10.44	RD J13434+0001	not detected
	96009000	205.9337	-0.1727	5.21	BJS864	not detected
LP96 Cl1341+0015	74047000	206.0021	-0.0004	4.45	RD J13434+0001	not detected
LP96 Cl1341−0006	96009000	205.8870	-0.3539	6.80	BJS864	not detected
LP96 Cl1342+0009	74047000	206.1169	-0.1071	13.06	RD J13434+0001	not detected
	96009000	206.1169	-0.1071	13.61	BJS864	not detected
TGN97 J132543.5−294	73071000	201.4312	-29.7428	5.60	NGC 5135	not detected
VMF98 004	96008000	13.5117	-28.3994	14.39	SGP3	not detected
VMF98 009	75084000	17.9025	-38.1867	11.32	TOL0109-383	not detected
VMF98 022	31002000	31.5975	15.1878	4.98	TT ARI	not detected
VMF98 026	76043000	37.0550	-10.0944	7.54	0226-104	too faint
VMF98 034	75070000	55.4879	-45.0031	6.02	QSF1	not detected
VMF98 037	61011000	68.5654	-8.5214	10.17	NGC1614	not detected
VMF98 040	73015000	80.2946	-25.5122	5.34	IRAS05189-2524	not detected
VMF98 041	73055000	80.5592	-36.4178	11.49	PKS0521-365	not detected
	73055010	80.5592	-36.4178	12.41	PKS0521-365	not detected
VMF98 042	33013000	82.1679	-32.8606	7.38	TV COL	not detected
VMF98 057	72002010	130.4308	70.7814	9.38	S5_0836+715	not detected
VMF98 058	75067000	130.7200	50.3878	13.60	NGC 2639	not detected
VMF98 059	76059000	131.7971	34.8211	6.69	PG 0844+349	too faint
VMF98 070	71042000	140.3058	45.4806	9.52	3C219	not detected
	71042010	140.3058	45.4806	13.51	3C219[SUPP]	not detected
	71042020	140.3058	45.4806	10.60	3C219	not detected
VMF98 071	76058000	141.6525	12.7156	5.06	MRK 705	not detected
VMF98 072	76058000	141.6900	12.5686	13.74	MRK 705	not detected
VMF98 093	90010000	163.3267	57.3464	10.73	LOCKMAN HOLE P1	not detected
	90010010	163.3267	57.3464	9.35	LOCKMAN HOLE P2	not detected
	90010020	163.3267	57.3464	9.59	LOCKMAN HOLE P2	not detected
	95001000	163.3267	57.3464	11.31	LOCKMAN HOLE #1	not detected
	95001010	163.3267	57.3464	11.30	LOCKMAN_HOLE_N2	not detected
VMF98 105	36005000	174.6829	3.2606	9.62	T LEO	not detected
VMF98 109	71048000	179.5487	55.3625	8.79	NGC 3998	not detected
VMF98 122	73063000	189.3546	11.6908	5.54	NGC 4579	not detected
VMF98 124	20020000	193.0225	-29.3461	4.31	EX HYA	not detected
VMF98 125	20020000	193.0471	-29.2497	4.28	EX HYA	not detected
VMF98 131	74094000	197.4817	32.3753	3.76	B2 1308+326	not detected
	74094010	197.4817	32.3753	3.69	B2_1308+326_N2	not detected
VMF98 134	77058000	201.3121	65.8414	14.85	PG 1322+659	not detected
VMF98 152	72028000	208.7046	69.2889	4.23	MRK 279	not detected
VMF98 159	70018000	214.6296	25.1806	8.39	NGC5548	not detected

Cluster	Sequence	α [arcmin.]	δ [deg.]	Off-Axis [deg.]	Field Name	Flag
	74038000	214.6296	25.1806	12.92	NGC5548	not detected
	74038010	214.6296	25.1806	12.81	NGC5548	not detected
	74038020	214.6296	25.1806	12.75	NGC5548	not detected
	74038030	214.6296	25.1806	12.69	NGC5548	not detected
	74038040	214.6296	25.1806	12.88	NGC5548	not detected
	76029000	214.6296	25.1806	11.16	NGC5548	not detected
	76029010	214.6296	25.1806	11.27	NGC5548	not detected
	76029020	214.6296	25.1806	11.20	NGC5548	not detected
	76029030	214.6296	25.1806	11.28	NGC5548	not detected
	76029040	214.6296	25.1806	3.66	NGC5548	not detected
VMF98 163	71044000	217.4087	42.5736	12.80	H 1426+428	not detected
VMF98 164	22012000	219.7312	64.3956	5.88	HD 129333	not detected
VMF98 216	74026000	349.5200	-42.5917	8.49	NGC7582	not detected

A.2 ASCA Cluster Catalog

This is the final catalog of clusters that comprise the ASCA cluster catalog along with the results of a single temperature MEKAL plasma model fit to the spectra. See Chapter 3 and Section 3.7. This catalog is available on the World Wide Web[2] along with images and spectra for these clusters.

The columns in Table A.2 are as follows:

1. The assigned cluster name. We tried to use a conventional name but also one that would be recognized by NED, if possible.

2. The ASCA sequence number of the observation. A value of "Combined" means that the spectra from the previously listed sequences were summed for each instrument and then fit.

3. The ASCA instruments include in the fit: G2, G3, S0, and S1 for the GIS2, GIS3, SIS0, and SIS1 instruments, respectively.

4. The right ascension (J2000) of the cluster GIS centroid, in degrees, corrected for systematic pointing error using the offsets of Gotthelf et al. (2000).

5. The declination (J2000) of the cluster GIS centroid, in degrees, corrected for systematic pointing error using the offsets of Gotthelf et al. (2000).

6. The extraction radius used for the spectrum file, in arc minutes.

7. The hydrogen column density from Dickey & Lockman (1990), in units of 10^{20} cm^{-2}.

8. The x-ray temperature with 90% confidence limits, in keV.

9. The metal abundance with 90% confidence limits with respect to the solar abundance of Anders & Grevesse (1989).

10. The cluster redshift.

11. The log of the unabsorbed flux within R_{ext} in the 0.5–2.0 keV band, in units of ergs cm^{-2} s^{-1}, from the fit to the GIS2 spectrum.

12. The log of the bolometric x-ray luminosity within R_{ext} for $H_0 = 50$ km s^{-1} Mpc^{-1} and $q_0 = 0.5$, in units of ergs s^{-1}, from the fit to the GIS2 spectrum.

[2] `http://lheawww.gsfc.nasa.gov/user/horner/asca`

13. Estimated factor to correct the observed bolometric luminosity within R_{ext} in column 12 to the bolometric luminosity within the virial radius. See Section 3.8.

14. The reduced χ^2 value which gives a measure of the quality of the fit.

15. The number of degrees of freedom of the fit.

16. Flags. A "z" means that the redshift is estimated from a fit from the x-ray spectrum. An "N" means that a note exists in Appendix B about the source. A "g" indicates an observation affected by the GIS3 bit problem (see Section 3.7).

Table A.2: Cluster Sample and Fitting Results

Cluster (1)	Sequence (2)	Instr. (3)	α (4)	δ (5)	R_{ext} (6)	N_H (7)	T_X (8)	Z (9)	z (10)	f_X (11)	L_{bol} (12)	l_{vir} (13)	χ^2 (14)	d.o.f (15)	Flags (16)
2A 0335+096	82029000	G2G3S0S1	54.6695	9.9712	14.36	17.80	$2.88^{+0.04}_{-0.03}$	$0.51^{+0.04}_{-0.03}$	0.0349	-10.34	44.77	1.24	1.08	1467	
	82040000	G2G3S0S1	54.6702	9.9743	15.34	17.80	$2.89^{+0.02}_{-0.03}$	$0.61^{+0.03}_{-0.02}$	0.0349	-10.34	44.77	1.21	1.32	1782	
	Combined	G2G3S0S1	54.6655	9.9710	...	17.80	$2.86^{+0.02}_{-0.02}$	$0.58^{+0.02}_{-0.01}$	0.0349	-10.33	44.77	1.22	1.58	1958	
3C 129	86050000	G2G3S0S1	72.5086	45.0630	18.54	70.80	$6.29^{+0.12}_{-0.12}$	$0.30^{+0.02}_{-0.02}$	0.0218	-10.59	44.60	1.25	1.23	1831	N
3C 295	71003000	G2G3S0S1	212.8408	52.2033	6.00	1.33	$6.51^{+1.37}_{-0.99}$	$0.36^{+0.22}_{-0.20}$	0.4600	-12.12	45.39	1.00	1.05	195	
ABELL 0068	86061000	G2G3S0S1	9.2793	9.1646	6.51	4.94	$7.99^{+0.75}_{-0.64}$	$0.26^{+0.09}_{-0.10}$	0.2550	-11.62	45.44	1.03	1.08	532	
ABELL 0085	81024000	G2G3S0S1	10.4550	-9.3108	14.85	3.44	$5.90^{+0.10}_{-0.10}$	$0.38^{+0.03}_{-0.02}$	0.0555	-10.31	45.35	1.16	1.09	1866	
	81024010	G2G3S0S1	10.4533	-9.2984	14.12	3.45	$5.73^{+0.15}_{-0.14}$	$0.40^{+0.04}_{-0.04}$	0.0555	-10.32	45.33	1.18	1.03	1360	
	Combined	G2G3S0S1	10.4372	-9.3110	...	3.45	$5.87^{+0.08}_{-0.07}$	$0.37^{+0.02}_{-0.02}$	0.0555	-10.31	45.35	1.17	1.18	2003	
ABELL 0115	82034000	G2G3S0S1	13.9680	26.4175	9.70	5.45	$6.45^{+0.33}_{-0.31}$	$0.27^{+0.06}_{-0.05}$	0.1971	-11.27	45.51	0.98	1.17	886	
ABELL 0119	83045000	G2G3S0S1	14.0772	-1.2443	14.85	3.20	$5.93^{+0.26}_{-0.23}$	$0.29^{+0.05}_{-0.05}$	0.0442	-10.68	44.78	1.17	1.11	1087	N
ABELL 0133	85062000	G2G3S0S1	15.6731	-21.8948	12.40	1.53	$3.71^{+0.08}_{-0.07}$	$0.64^{+0.06}_{-0.06}$	0.0566	-10.82	44.73	1.12	1.16	1144	
ABELL 0194	81028000	G2G3S0S1	21.4882	-1.3741	9.21	3.78	$2.70^{+0.21}_{-0.21}$	$0.28^{+0.16}_{-0.14}$	0.0180	-11.50	42.98	1.37	1.12	315	
	81028010	G2G3S0S1	21.4892	-1.3874	9.45	3.78	$2.44^{+0.22}_{-0.21}$	$0.32^{+0.20}_{-0.15}$	0.0180	-11.52	42.93	1.35	1.05	283	
	Combined	G2G3S0S1	21.4881	-1.3786	...	3.78	$2.50^{+0.13}_{-0.13}$	$0.35^{+0.10}_{-0.10}$	0.0180	-11.50	42.95	1.36	1.07	561	
ABELL 0222	83069000	G2G3S0S1	24.3911	-12.9901	6.00	2.30	$4.60^{+0.62}_{-0.51}$	$0.40^{+0.25}_{-0.21}$	0.2130	-11.85	44.90	1.07	1.06	174	
ABELL 0223	83069000	G2G3	24.4811	-12.8170	6.00	2.20	$5.44^{+1.16}_{-0.85}$	$0.36^{+0.31}_{-0.27}$	0.2070	-11.82	44.95	1.06	1.03	90	
	83070000	G2G3S0S1	24.4814	-12.8099	6.00	2.20	$5.12^{+0.83}_{-0.66}$	$0.53^{+0.27}_{-0.23}$	0.2070	-11.84	44.92	1.06	1.21	166	
	Combined	G2G3S0S1	24.4770	-12.8145	...	2.20	$5.28^{+0.63}_{-0.52}$	$0.49^{+0.19}_{-0.17}$	0.2070	-11.83	44.93	1.06	0.93	247	
ABELL 0262	81031000	G2G3S0S1	28.1981	36.1535	15.59	5.37	$2.17^{+0.04}_{-0.04}$	$0.42^{+0.05}_{-0.05}$	0.0163	-10.48	43.86	1.41	1.10	928	
ABELL 0267	85048000	G2G3S0S1	28.1809	1.0135	8.47	2.80	$5.93^{+0.48}_{-0.42}$	$0.26^{+0.08}_{-0.09}$	0.2300	-11.55	45.33	0.98	1.11	613	
ABELL 0370	80010000	G2G3S0S1	39.9757	-1.5738	6.00	3.06	$7.20^{+0.75}_{-0.77}$	$0.39^{+0.16}_{-0.13}$	0.3750	-11.92	45.43	0.99	0.91	305	
ABELL 0376	85063000	G2G3S0S1	41.5195	36.9153	11.66	6.75	$4.01^{+0.13}_{-0.13}$	$0.38^{+0.06}_{-0.06}$	0.0484	-11.11	44.34	1.15	1.07	931	
ABELL 0399	82008000	G2G3S0S1	44.4740	13.0456	12.89	10.90	$6.99^{+0.24}_{-0.23}$	$0.30^{+0.04}_{-0.05}$	0.0724	-10.80	45.18	1.11	0.96	1449	
ABELL 0400	83037000	G2G3S0S1	44.4191	6.0259	13.38	9.47	$2.28^{+0.05}_{-0.05}$	$0.45^{+0.07}_{-0.06}$	0.0244	-10.97	43.73	1.23	1.11	1037	
ABELL 0401	82010000	G2G3S0S1	44.7441	13.5782	13.13	10.50	$8.07^{+0.20}_{-0.20}$	$0.28^{+0.03}_{-0.03}$	0.0737	-10.55	45.48	1.14	1.04	1844	
ABELL 0478	81015000	G2S0S1	63.3598	10.4649	13.87	15.10	$7.07^{+0.19}_{-0.17}$	$0.31^{+0.03}_{-0.04}$	0.0881	-10.48	45.69	1.08	1.13	1269	g
ABELL 0483	82031000	G2G3S0S1	64.0039	-11.5453	6.00	3.92	$4.99^{+0.65}_{-0.53}$	$0.19^{+0.15}_{-0.13}$	0.2800	-11.98	45.02	1.01	0.97	274	
ABELL 0496	80003000	G2G3S0S1	68.4096	-13.2584	15.83	4.59	$3.89^{+0.04}_{-0.04}$	$0.47^{+0.02}_{-0.02}$	0.0329	-10.28	44.82	1.25	1.07	1850	
ABELL 0514	84073000	G2G3S0S1	72.0651	-20.4740	11.17	3.14	$4.70^{+0.33}_{-0.29}$	$0.17^{+0.09}_{-0.09}$	0.0713	-11.31	44.49	1.09	1.04	623	
ABELL 0520	82041000	G2G3S0S1	73.5402	2.9286	8.22	7.79	$7.81^{+0.74}_{-0.64}$	$0.25^{+0.09}_{-0.09}$	0.2011	-11.38	45.49	1.03	1.08	540	
ABELL 0521	84071000	G2G3S0S1	73.5242	-10.2403	7.49	5.80	$6.74^{+0.50}_{-0.45}$	$0.19^{+0.07}_{-0.08}$	0.2873	-11.58	45.53	0.97	0.92	679	

Cluster (1)	Sequence (2)	Instr. (3)	α (4)	δ (5)	R_{ext} (6)	N_H (7)	T_X (8)	Z (9)	z (10)	f_X (11)	L_{bol} (12)	l_{vir} (13)	χ^2_r (14)	d.o.f (15)	Flags (16)
ABELL 0539	83003000	G2G3S0S1	79.1615	6.4513	12.64	12.60	$2.94^{+0.07}_{-0.06}$	$0.31^{+0.05}_{-0.04}$	0.0284	-10.85	44.07	1.26	0.99	1086	
ABELL 0548E	84034000	G2G3S0S1	87.1542	-25.4775	10.43	1.98	$3.14^{+0.10}_{-0.10}$	$0.56^{+0.10}_{-0.09}$	0.0397	-11.12	44.08	1.21	0.95	760	
ABELL 0560	74003000	G2G3S0S1	100.6876	67.8892	6.00	5.48	$4.12^{+1.00}_{-0.81}$	$0.47^{+0.59}_{-0.42}$	*0.1732*	-12.35	44.01	1.13	0.88	139	z
ABELL 0562	87001000	G2G3S0S1	103.3291	69.3315	6.00	5.11	$3.04^{+0.33}_{-0.28}$	$0.31^{+0.26}_{-0.21}$	0.1100	-11.91	44.17	1.16	1.09	221	
ABELL 0576	84001000	G2G3S0S1	110.3820	55.7543	13.38	5.71	$4.09^{+0.07}_{-0.07}$	$0.46^{+0.04}_{-0.03}$	0.0389	-10.81	44.45	1.19	1.23	1403	
ABELL 0586	81009010	G2S0S1	113.0847	31.6335	7.24	5.15	$6.39^{+0.72}_{-0.60}$	$0.24^{+0.12}_{-0.11}$	0.1710	-11.35	45.30	1.07	1.01	278	g
ABELL 0611	84063000	G2G3S0S1	120.2376	36.0601	6.26	4.99	$6.69^{+0.51}_{-0.44}$	$0.19^{+0.08}_{-0.07}$	0.2880	-11.76	45.35	1.00	1.08	619	
ABELL 0644	83022000	G2G3S0S1	124.3559	-7.5189	14.36	6.82	$7.31^{+0.13}_{-0.13}$	$0.35^{+0.02}_{-0.03}$	0.0704	-10.59	45.36	1.11	1.03	2000	
ABELL 0665	80035000	G2G3S0S1	127.7343	65.8444	7.98	4.24	$8.14^{+0.48}_{-0.44}$	$0.26^{+0.06}_{-0.07}$	0.1819	-11.20	45.57	1.06	1.02	897	
	85033000	G2G3S0S1	127.7465	65.8614	9.94	4.24	$7.69^{+0.31}_{-0.30}$	$0.23^{+0.04}_{-0.05}$	0.1819	-11.16	45.59	1.01	0.93	1433	
	Combined	G2G3S0S1	127.7466	65.8558	...	4.24	$8.03^{+0.24}_{-0.24}$	$0.22^{+0.04}_{-0.03}$	0.1819	-11.17	45.59	1.02	1.07	1616	
ABELL 0697	84031000	G2G3S0S1	130.7387	36.3641	8.96	3.41	$9.14^{+0.60}_{-0.54}$	$0.24^{+0.07}_{-0.07}$	0.2820	-11.38	45.79	0.97	1.04	1006	
ABELL 0744	83041000	G2G3	136.8275	16.6601	6.00	3.64	$2.50^{+0.30}_{-0.29}$	$0.43^{+0.46}_{-0.31}$	0.0729	-11.87	43.80	1.24	0.79	102	
ABELL 0750	83034000	G2G3S0S1	137.3002	10.9782	9.45	3.53	$6.06^{+0.40}_{-0.37}$	$0.40^{+0.09}_{-0.08}$	0.1630	-11.32	45.27	1.01	1.04	578	
ABELL 0754	82057000	G2G3S0S1	137.2945	-9.6798	16.82	4.37	$9.94^{+0.33}_{-0.31}$	$0.32^{+0.05}_{-0.04}$	0.0542	-10.33	45.46	1.16	1.06	1785	
ABELL 0773	82001000	G2G3S0S1	139.4741	51.7312	7.73	1.44	$10.30^{+0.92}_{-0.79}$	$0.29^{+0.09}_{-0.09}$	0.2170	-11.47	45.51	1.05	1.08	754	
ABELL 0779	63018000	G2G3S0S1	139.9407	33.7496	6.00	1.60	$1.49^{+0.25}_{-0.21}$	$0.27^{+0.26}_{-0.14}$	0.0229	-11.73	42.84	1.56	1.26	77	
	84018000	G2G3S0S1	139.9560	33.7402	6.00	1.59	$1.85^{+0.29}_{-0.23}$	$0.34^{+0.30}_{-0.16}$	0.0229	-11.76	42.85	1.55	1.48	152	
	84018010	G2G3S0S1	139.9309	33.7403	6.00	1.60	$1.79^{+0.23}_{-0.24}$	$0.58^{+0.47}_{-0.30}$	0.0229	-11.81	42.78	1.53	1.09	112	
	Combined	G2G3S0S1	139.9441	33.7424	...	1.60	$1.92^{+0.15}_{-0.15}$	$0.42^{+0.14}_{-0.12}$	0.0229	-11.78	42.83	1.55	1.37	314	
ABELL 0851	83068000	G2G3S0S1	145.7726	46.9926	6.00	1.25	$8.16^{+1.97}_{-1.42}$	$0.14^{+0.22}_{-0.14}$	0.4069	-12.24	45.21	1.00	1.00	230	
	84029000	G2G3S0S1	145.7201	46.9856	6.00	1.25	$9.45^{+4.06}_{-2.47}$	$0.07^{+0.37}_{-0.07}$	0.4069	-12.22	45.26	1.01	0.96	163	
	86035000	G2G3S0S1	145.7623	46.9942	6.00	1.25	$7.21^{+2.04}_{-1.34}$	$0.35^{+0.29}_{-0.27}$	0.4069	-12.22	45.21	1.01	1.05	205	
	Combined	G2G3S0S1	145.7463	46.9945	...	1.25	$8.99^{+1.34}_{-1.01}$	$0.36^{+0.14}_{-0.13}$	0.4069	-12.24	45.24	1.01	1.20	539	
ABELL 0854	83006000	G2G3S0S1	145.5167	8.9535	6.00	3.11	$6.09^{+0.52}_{-0.45}$	$0.26^{+0.10}_{-0.10}$	0.2072	-11.71	45.09	1.07	1.02	485	
ABELL 0959	82006000	G2G3S0S1	154.4230	59.5587	6.00	0.88	$6.26^{+0.93}_{-0.81}$	$0.04^{+0.15}_{-0.04}$	0.3533	-11.97	45.29	0.98	1.10	212	
ABELL 0963	80000000	G2G3S0S1	154.2640	39.0490	6.00	1.40	$6.60^{+0.37}_{-0.39}$	$0.34^{+0.08}_{-0.08}$	0.2060	-11.43	45.38	1.11	1.00	596	
ABELL 0990	84070000	G2G3S0S1	155.9210	49.1377	8.72	1.17	$5.75^{+0.24}_{-0.22}$	$0.23^{+0.04}_{-0.05}$	0.1440	-11.23	45.24	1.05	1.04	1116	
ABELL 1045	84023000	G2G3S0S1	158.7456	30.6979	7.24	1.84	$4.40^{+0.24}_{-0.22}$	$0.43^{+0.09}_{-0.09}$	0.1407	-11.50	44.88	1.06	0.98	569	
	84023010	G2G3S0S1	158.7562	30.6922	6.51	1.84	$4.26^{+0.35}_{-0.31}$	$0.57^{+0.17}_{-0.15}$	0.1407	-11.54	44.84	1.09	0.90	275	
	Combined	G2G3S0S1	158.7548	30.6941	...	1.84	$4.51^{+0.20}_{-0.18}$	$0.46^{+0.07}_{-0.07}$	0.1407	-11.52	44.87	1.07	1.10	743	
ABELL 1060	80004000	G2G3S0S1	159.1722	-27.5288	16.82	4.89	$3.20^{+0.04}_{-0.04}$	$0.37^{+0.02}_{-0.03}$	0.0126	-10.30	43.91	1.58	1.11	1659	
ABELL 1068	84064000	G2G3S0S1	160.1812	39.9561	7.00	0.98	$3.87^{+0.12}_{-0.12}$	$0.42^{+0.06}_{-0.06}$	0.1375	-11.19	45.15	1.08	1.05	825	
ABELL 1111	84036000	G2G3S0S1	162.6561	-2.6011	6.01	3.97	$2.98^{+0.17}_{-0.15}$	$0.49^{+0.12}_{-0.12}$	0.1645	-11.71	44.71	1.04	0.86	344	
ABELL 1204	82002000	G2G3S0S1	168.3329	17.5958	6.01	1.40	$3.78^{+0.18}_{-0.16}$	$0.35^{+0.08}_{-0.07}$	0.1706	-11.37	45.15	1.07	0.91	553	

Cluster (1)	Sequence (2)	Instr. (3)	α (4)	δ (5)	R_{ext} (6)	N_H (7)	T_X (8)	Z (9)	z (10)	f_X (11)	L_{bol} (12)	l_{vir} (13)	χ^2_r (14)	d.o.f (15)	Flags (16)
ABELL 1246	83007000	G2G3S0S1	170.9941	21.4833	8.22	1.39	$6.04^{+0.42}_{-0.37}$	$0.24^{+0.08}_{-0.07}$	0.1902	-11.47	45.25	1.01	0.99	705	
ABELL 1300	84067000	G2G3S0S1	172.9819	-19.9354	7.49	4.50	$8.26^{+0.63}_{-0.58}$	$0.18^{+0.08}_{-0.08}$	0.3072	-11.56	45.66	0.98	0.94	768	
ABELL 1367	81029000	G2G3S0S1	176.1868	19.7306	16.57	2.31	$3.61^{+0.14}_{-0.13}$	$0.39^{+0.09}_{-0.08}$	0.0220	-10.56	44.17	1.28	1.02	737	
	81029010	G2G3S0S1	176.1897	19.6946	16.08	2.31	$3.51^{+0.15}_{-0.14}$	$0.36^{+0.10}_{-0.09}$	0.0220	-10.58	44.14	1.29	1.10	663	
	81030000	G2G3S0S1	176.2298	19.6719	14.12	2.32	$3.36^{+0.15}_{-0.13}$	$0.28^{+0.08}_{-0.09}$	0.0220	-10.58	44.12	1.36	0.80	723	
	81030010	G2G3S0S1	176.2178	19.7297	13.87	2.32	$3.45^{+0.13}_{-0.11}$	$0.28^{+0.08}_{-0.07}$	0.0220	-10.58	44.13	1.37	0.94	779	
	Combined	G2G3S0S1	176.1977	19.7087	...	2.31	$3.47^{+0.06}_{-0.05}$	$0.32^{+0.03}_{-0.03}$	0.0220	-10.57	44.15	1.32	1.05	1383	
ABELL 1413	81008000	G2G3S0S1	178.8232	23.4078	11.42	2.19	$7.09^{+0.27}_{-0.25}$	$0.31^{+0.04}_{-0.05}$	0.1427	-10.97	45.55	1.02	1.01	1247	
ABELL 1423	85071000	G2G3S0S1	179.3233	33.6123	9.45	1.20	$5.38^{+0.39}_{-0.35}$	$0.34^{+0.09}_{-0.09}$	0.2138	-11.44	45.35	0.96	1.02	672	N
ABELL 1430	86059000	G2G3S0S1	179.8058	49.7923	7.24	2.04	$6.86^{+0.68}_{-0.62}$	$0.00^{+0.08}_{-0.00}$	0.2105	-11.63	45.20	1.03	1.04	406	
	86059010	G2G3S0S1	179.8114	49.7889	6.00	2.04	$7.57^{+1.16}_{-0.93}$	$0.10^{+0.14}_{-0.10}$	0.2105	-11.73	45.13	1.08	1.06	267	
	Combined	G2G3S0S1	179.8046	49.7952	...	2.04	$7.18^{+0.56}_{-0.53}$	$0.00^{+0.07}_{-0.00}$	0.2105	-11.67	45.17	1.05	1.12	642	
ABELL 1451	84038000	G2G3S0S1	180.8225	-21.5465	7.49	4.40	$12.82^{+1.89}_{-1.50}$	$0.16^{+0.15}_{-0.16}$	0.1990	-11.46	45.52	1.08	0.88	542	
	84038010	G2G3S0S1	180.8260	-21.5405	7.73	4.40	$12.18^{+2.03}_{-1.55}$	$0.44^{+0.18}_{-0.18}$	0.1990	-11.45	45.52	1.07	1.12	378	
	Combined	G2G3S0S1	180.8157	-21.5394	...	4.40	$13.09^{+1.41}_{-1.17}$	$0.34^{+0.12}_{-0.11}$	0.1990	-11.45	45.53	1.08	1.02	796	
ABELL 1466	85054000	G2G3S0S1	181.2520	22.6175	6.00	2.14	$4.87^{+1.49}_{-0.95}$	$0.85^{+0.69}_{-0.49}$	0.2519	-12.24	44.68	1.11	1.29	83	
ABELL 1553	84069000	G2G3S0S1	187.6961	10.5577	6.75	1.99	$5.99^{+0.36}_{-0.33}$	$0.25^{+0.07}_{-0.07}$	0.1652	-11.35	45.25	1.09	0.91	718	
ABELL 1576	83014000	G2G3S0S1	189.2399	63.1866	6.51	1.68	$7.53^{+0.84}_{-0.69}$	$0.25^{+0.11}_{-0.11}$	0.2790	-11.72	45.38	1.01	1.01	459	
ABELL 1631	85035000	G2G3S0S1	193.2147	-15.4089	7.24	3.93	$4.26^{+1.58}_{-1.03}$	$0.11^{+0.41}_{-0.11}$	0.0462	-11.94	43.47	1.19	0.85	99	
ABELL 1650	84021000	G2G3S0S1	194.6692	-1.7564	11.17	1.56	$5.89^{+0.12}_{-0.12}$	$0.40^{+0.03}_{-0.03}$	0.0845	-10.78	45.24	1.11	1.10	1630	
ABELL 1651	82036000	G2G3S0S1	194.8379	-4.1936	11.17	1.81	$5.97^{+0.16}_{-0.15}$	$0.30^{+0.03}_{-0.04}$	0.0844	-10.74	45.27	1.12	1.04	1422	
ABELL 1672	85042000	G2G3	196.1132	33.5901	6.75	1.04	$5.42^{+0.61}_{-0.51}$	$0.32^{+0.16}_{-0.15}$	0.1882	-11.77	44.92	1.04	0.84	215	
ABELL 1674	84026000	G2G3S0S1	195.9627	67.5116	7.00	1.85	$3.41^{+0.47}_{-0.39}$	$0.23^{+0.24}_{-0.20}$	0.1066	-12.09	43.99	1.06	1.05	266	
ABELL 1682	84075000	G2G3S0S1	196.7154	46.5564	7.24	1.35	$6.27^{+0.52}_{-0.47}$	$0.25^{+0.09}_{-0.09}$	0.2339	-11.60	45.31	1.00	1.05	573	
ABELL 1689	80005000	G2G3S0S1	197.8694	-1.3412	10.68	1.82	$9.15^{+0.36}_{-0.33}$	$0.32^{+0.05}_{-0.04}$	0.1832	-10.94	45.86	1.01	0.98	1387	
ABELL 1704	81007000	G2G3S0S1	198.6038	64.5796	6.01	1.77	$4.58^{+0.38}_{-0.34}$	$0.37^{+0.12}_{-0.11}$	0.2205	-11.58	45.20	1.02	1.02	308	
ABELL 1722	81013000	G2G3S0S1	200.0132	70.0743	6.51	1.51	$6.05^{+0.43}_{-0.61}$	$0.51^{+0.14}_{-0.14}$	0.3275	-11.91	45.29	0.97	0.94	370	
ABELL 1732	85070000	G2G3S0S1	201.2748	-20.2439	6.75	7.79	$5.77^{+0.35}_{-0.32}$	$0.32^{+0.07}_{-0.07}$	0.1921	-11.61	45.14	1.04	0.96	722	
ABELL 1736	83061000	G2G3S0S1	201.7375	-27.1934	10.92	5.34	$3.45^{+0.13}_{-0.12}$	$0.44^{+0.09}_{-0.09}$	0.0458	-10.94	44.41	1.20	0.98	751	
ABELL 1750N	81010000	G2G3S0S1	202.7922	-1.7312	7.98	2.37	$3.71^{+0.20}_{-0.17}$	$0.38^{+0.10}_{-0.10}$	0.0860	-11.49	44.42	1.11	0.94	540	
ABELL 1750S	81010000	G2G3S0S1	202.7118	-1.8568	8.72	2.39	$4.41^{+0.24}_{-0.22}$	$0.37^{+0.09}_{-0.08}$	0.0860	-11.40	44.55	1.11	0.93	651	
ABELL 1758N	83013000	G2G3S0S1	203.1970	50.5516	6.26	1.06	$8.28^{+1.19}_{-0.95}$	$0.18^{+0.14}_{-0.15}$	0.2792	-11.63	45.50	1.03	1.07	304	
	83013010	G2G3S0S1	203.1835	50.5339	7.00	1.06	$7.49^{+0.91}_{-0.74}$	$0.28^{+0.13}_{-0.13}$	0.2792	-11.60	45.50	1.00	1.06	310	
	Combined	G2G3S0S1	203.2045	50.5384	...	1.06	$7.95^{+0.74}_{-0.62}$	$0.20^{+0.09}_{-0.09}$	0.2792	-11.61	45.51	1.01	1.17	543	
ABELL 1758S	83013000	G2G3S0S1	203.1524	50.4169	6.00	1.06	$6.22^{+0.47}_{-0.78}$	$0.09^{+0.16}_{-0.09}$	0.2792	-11.75	45.30	1.03	0.92	208	

Cluster (1)	Sequence (2)	Instr. (3)	α (4)	δ (5)	R_{ext} (6)	N_H (7)	T_X (8)	Z (9)	z (10)	f_X (11)	L_{bol} (12)	l_{vir} (13)	χ^2_r (14)	d.o.f (15)	Flags (16)
	83013010	G2G3S0S1	203.1406	50.4051	6.51	1.06	$6.35^{+0.90}_{-0.73}$	$0.25^{+0.15}_{-0.15}$	0.2792	-11.72	45.35	0.99	0.84	241	
	Combined	G2G3S0S1	203.1608	50.4067	...	1.06	$6.55^{+0.65}_{-0.56}$	$0.18^{+0.09}_{-0.10}$	0.2792	-11.74	45.33	1.01	1.09	421	
ABELL 1763	83044000	G2G3S0S1	203.8269	41.0031	8.47	0.94	$7.72^{+0.48}_{-0.44}$	$0.30^{+0.06}_{-0.07}$	0.2284	-11.33	45.62	1.00	1.01	875	
ABELL 1775	85056000	G2G3S0S1	205.4682	26.3695	9.21	1.05	$3.68^{+0.12}_{-0.12}$	$0.45^{+0.07}_{-0.07}$	0.0717	-11.08	44.68	1.14	1.03	864	
ABELL 1795	15708000	G2G3S0S1	207.2178	26.5903	15.84	1.19	$5.38^{+0.10}_{-0.09}$	$0.35^{+0.03}_{-0.03}$	0.0631	-10.31	45.43	1.10	1.09	1654	
	80006000	G2G3S0S1	207.2103	26.5982	15.34	1.19	$5.51^{+0.08}_{-0.09}$	$0.39^{+0.03}_{-0.02}$	0.0631	-10.32	45.43	1.11	1.10	1946	
	Combined	G2G3S0S1	207.2098	26.5995	...	1.19	$5.49^{+0.05}_{-0.06}$	$0.37^{+0.02}_{-0.01}$	0.0631	-10.31	45.43	1.11	1.15	2103	
ABELL 1835	82052000	G2G3S0S1	210.2563	2.8733	8.96	2.32	$7.79^{+0.49}_{-0.45}$	$0.30^{+0.07}_{-0.06}$	0.2532	-11.08	45.96	0.97	0.91	768	
	82052010	G2G3S0S1	210.2584	2.8751	9.21	2.32	$7.54^{+0.48}_{-0.43}$	$0.44^{+0.08}_{-0.08}$	0.2532	-11.05	45.98	0.96	1.03	712	
	Combined	G2G3S0S1	210.2579	2.8763	...	2.32	$7.65^{+0.33}_{-0.31}$	$0.36^{+0.05}_{-0.05}$	0.2532	-11.06	45.97	0.96	1.05	1077	
ABELL 1851	82007000	G2G3S0S1	210.0364	72.1226	6.75	1.75	$4.80^{+0.61}_{-0.51}$	$0.39^{+0.20}_{-0.17}$	0.2149	-11.90	44.87	1.01	0.83	250	
ABELL 1885	85057000	G2G3S0	213.4261	43.6641	6.51	1.18	$2.31^{+0.07}_{-0.07}$	$0.37^{+0.07}_{-0.07}$	0.0890	-11.37	44.48	1.14	1.07	541	
ABELL 1895	83033000	G2G3S0S1	213.5075	71.3035	6.26	1.96	$5.67^{+0.77}_{-0.60}$	$0.34^{+0.16}_{-0.15}$	0.2257	-11.77	45.09	1.03	0.82	269	
ABELL 1913	86048000	G2G3S0S1	216.6473	16.7451	9.21	1.53	$2.97^{+0.20}_{-0.20}$	$0.64^{+0.24}_{-0.21}$	0.0528	-11.61	43.83	1.13	1.07	353	
ABELL 1914	84032000	G2G3S0S1	216.5035	37.8285	9.21	0.95	$9.48^{+0.49}_{-0.45}$	$0.30^{+0.06}_{-0.06}$	0.1712	-10.97	45.78	1.06	1.04	1200	
ABELL 1942	83000000	G2G3S0S1	219.5997	3.6669	6.00	2.61	$5.12^{+0.71}_{-0.56}$	$0.27^{+0.17}_{-0.15}$	0.2240	-11.92	44.89	1.04	0.91	303	
ABELL 1995	82005000	G2G3S0S1	223.2383	58.0436	6.26	1.42	$10.50^{+1.94}_{-1.50}$	$0.19^{+0.17}_{-0.18}$	0.3186	-11.83	45.47	1.02	0.96	302	
ABELL 2028	83040050	G2G3S0S1	227.3732	7.5720	7.00	2.45	$3.91^{+0.67}_{-0.55}$	$0.77^{+1.25}_{-0.61}$	0.0777	-11.53	44.32	1.17	1.29	134	
ABELL 2029	81023000	G2S0S1	227.7343	5.7472	15.83	3.05	$7.40^{+0.19}_{-0.18}$	$0.40^{+0.04}_{-0.04}$	0.0773	-10.30	45.71	1.09	0.85	1448	g
	83040010	G2G3S0S1	227.7324	5.7453	13.38	3.05	$7.30^{+0.40}_{-0.37}$	$0.44^{+0.09}_{-0.08}$	0.0773	-10.36	45.65	1.13	0.98	780	
	Combined	G2G3S0S1	227.7335	5.7472	...	3.05	$7.38^{+0.15}_{-0.13}$	$0.42^{+0.02}_{-0.03}$	0.0773	-10.31	45.70	1.09	1.09	1757	
ABELL 2033	83040000	G2G3S0S1	227.8613	6.3487	8.47	2.83	$4.09^{+0.26}_{-0.25}$	$0.32^{+0.14}_{-0.12}$	0.0818	-11.14	44.76	1.15	1.08	308	
	85058000	G2G3S0S1	227.8611	6.3533	9.21	2.82	$4.21^{+0.16}_{-0.15}$	$0.31^{+0.06}_{-0.06}$	0.0818	-11.11	44.79	1.12	1.08	877	
	Combined	G2G3S0S1	227.8594	6.3534	...	2.83	$4.16^{+0.14}_{-0.12}$	$0.30^{+0.05}_{-0.06}$	0.0818	-11.11	44.78	1.13	1.09	976	
ABELL 2034	84022000	G2G3S0S1	227.5458	33.5033	10.68	1.59	$7.15^{+0.32}_{-0.29}$	$0.29^{+0.05}_{-0.06}$	0.1130	-11.05	45.27	1.07	1.05	1156	
ABELL 2052	85061000	G2G3S0S1	229.1875	7.0210	16.08	2.71	$2.96^{+0.03}_{-0.04}$	$0.55^{+0.03}_{-0.03}$	0.0350	-10.47	44.60	1.17	1.23	1501	
ABELL 2063	81002000	G2S0S1	230.7758	8.6116	13.87	2.99	$3.61^{+0.10}_{-0.10}$	$0.37^{+0.06}_{-0.06}$	0.0353	-10.60	44.53	1.22	1.10	776	g
ABELL 2065	84054000	G2G3S0S1	230.6220	27.7096	11.66	2.96	$5.42^{+0.19}_{-0.18}$	$0.29^{+0.05}_{-0.04}$	0.0726	-10.75	45.11	1.13	1.05	1091	
	84054010	G2G3S0S1	230.6101	27.7145	12.89	2.96	$5.48^{+0.20}_{-0.18}$	$0.26^{+0.04}_{-0.04}$	0.0726	-10.73	45.14	1.10	1.05	1089	
	Combined	G2G3S0S1	230.6200	27.7103	...	2.96	$5.35^{+0.13}_{-0.12}$	$0.28^{+0.03}_{-0.03}$	0.0726	-10.74	45.12	1.11	1.06	1477	
ABELL 2104	84072000	G2G3S0S1	235.0326	-3.3034	10.19	8.70	$9.31^{+0.50}_{-0.47}$	$0.32^{+0.06}_{-0.06}$	0.1554	-11.30	45.40	1.04	1.03	1163	
ABELL 2107	85060000	G2G3S0S1	234.9224	21.7739	11.17	4.54	$3.82^{+0.11}_{-0.10}$	$0.42^{+0.06}_{-0.06}$	0.0411	-10.91	44.37	1.22	0.98	950	
ABELL 2111	85065000	G2G3S0S1	234.9224	34.4203	6.51	1.93	$8.02^{+0.95}_{-0.77}$	$0.13^{+0.13}_{-0.12}$	0.2290	-11.64	45.31	1.05	1.01	509	
ABELL 2142	81004000	G2S0S1	239.5868	27.2352	12.89	4.20	$8.24^{+0.34}_{-0.30}$	$0.28^{+0.05}_{-0.05}$	0.0909	-10.37	45.81	1.12	1.01	1077	g
ABELL 2147	83074000	G2G3S0S1	240.5548	15.9737	14.85	3.39	$4.45^{+0.09}_{-0.10}$	$0.35^{+0.04}_{-0.04}$	0.0350	-10.60	44.58	1.21	1.09	1493	

Cluster (1)	Sequence (2)	Instr. (3)	α (4)	δ (5)	R_{ext} (6)	N_H (7)	T_X (8)	Z (9)	z (10)	f_X (11)	L_{bol} (12)	l_{vir} (13)	χ^2_r (14)	d.o.f (15)	Flags (16)
ABELL 2152	83031000	G2G3S0S1	241.4104	16.4261	6.01	3.40	$3.09^{+0.28}_{-0.24}$	$0.27^{+0.19}_{-0.16}$	0.0410	-11.73	43.50	1.32	1.08	226	
ABELL 2163	80024000	G2G3S0S1	243.9302	-6.1487	11.66	12.10	$12.12^{+0.62}_{-0.57}$	$0.22^{+0.06}_{-0.05}$	0.2030	-10.85	46.18	1.00	0.98	1436	
ABELL 2187	86053000	G2G3S0S1	246.0549	41.2372	6.00	0.98	$5.42^{+0.42}_{-0.36}$	$0.38^{+0.11}_{-0.10}$	0.1836	-11.66	45.01	1.08	1.04	584	
ABELL 2197	85068000	G2G3S0S1	246.9275	40.9282	6.00	0.97	$1.96^{+0.17}_{-0.18}$	$0.59^{+0.32}_{-0.23}$	0.0308	-11.88	42.99	1.54	1.14	282	
ABELL 2199	80023000	G2G3S0S1	247.1519	39.5533	17.06	0.86	$4.14^{+0.05}_{-0.04}$	$0.43^{+0.02}_{-0.03}$	0.0299	-10.13	44.90	1.28	1.09	1877	
ABELL 2204	82045000	G2G3S0S1	248.1986	5.5718	9.94	5.67	$6.35^{+0.24}_{-0.23}$	$0.39^{+0.05}_{-0.05}$	0.1523	-10.76	45.80	1.03	1.03	1064	
	82045010	G2G3S0S1	248.1942	5.5701	10.68	5.67	$7.41^{+0.29}_{-0.26}$	$0.40^{+0.04}_{-0.05}$	0.1523	-10.76	45.84	1.03	1.02	1167	
	Combined	G2G3S0S1	248.1918	5.5743	...	5.67	$6.97^{+0.18}_{-0.18}$	$0.38^{+0.04}_{-0.03}$	0.1523	-10.76	45.83	1.03	1.08	1502	
ABELL 2218	80001000	G2G3S0S1	248.9543	66.2161	7.49	3.24	$6.97^{+0.37}_{-0.34}$	$0.20^{+0.05}_{-0.06}$	0.1756	-11.33	45.36	1.06	1.00	864	
ABELL 2219	82037000	G2G3S0S1	250.0795	46.7110	10.68	1.75	$9.81^{+0.65}_{-0.59}$	$0.27^{+0.07}_{-0.08}$	0.2256	-11.06	45.94	0.98	0.96	962	
ABELL 2244	86073000	G2G3S0S1	255.6659	34.0661	9.70	2.13	$5.57^{+0.17}_{-0.15}$	$0.29^{+0.04}_{-0.04}$	0.0968	-10.85	45.27	1.12	1.04	1237	
ABELL 2255	84012000	G2G3S0S1	258.2284	64.0570	12.40	2.59	$6.22^{+0.21}_{-0.19}$	$0.31^{+0.04}_{-0.05}$	0.0806	-10.90	45.09	1.09	1.00	1399	
	84012010	G2G3S0S1	258.1755	64.0624	12.40	2.59	$7.06^{+0.32}_{-0.29}$	$0.21^{+0.05}_{-0.06}$	0.0806	-10.91	45.11	1.10	0.95	1163	
	Combined	G2G3S0S1	258.1997	64.0600	...	2.59	$6.42^{+0.16}_{-0.15}$	$0.25^{+0.03}_{-0.03}$	0.0806	-10.90	45.10	1.09	1.16	1686	
ABELL 2256	80002000	G2G3S0S1	256.1307	78.6343	15.83	4.10	$6.90^{+0.16}_{-0.15}$	$0.30^{+0.03}_{-0.03}$	0.0581	-10.41	45.33	1.13	0.83	1803	
ABELL 2259	85053000	G2G3S0S1	260.0405	27.6662	7.49	3.70	$5.32^{+0.29}_{-0.27}$	$0.18^{+0.06}_{-0.06}$	0.1640	-11.42	45.15	1.05	0.95	767	
ABELL 2261	84062000	G2G3S0S1	260.6208	32.1355	8.96	3.28	$6.88^{+0.47}_{-0.41}$	$0.37^{+0.08}_{-0.08}$	0.2240	-11.21	45.69	0.98	1.07	673	
ABELL 2319	80041000	G2G3S0S1	290.2749	43.9644	17.06	7.94	$9.24^{+0.28}_{-0.28}$	$0.28^{+0.04}_{-0.04}$	0.0557	-10.19	45.63	1.16	0.95	1753	
	80041010	G2G3S0S1	290.2968	43.9429	15.10	7.96	$9.62^{+0.32}_{-0.31}$	$0.24^{+0.05}_{-0.04}$	0.0557	-10.20	45.62	1.21	0.99	1664	
	Combined	G2G3S0S1	290.2855	43.9671	...	7.95	$9.49^{+0.21}_{-0.19}$	$0.25^{+0.03}_{-0.02}$	0.0557	-10.19	45.63	1.19	1.05	2015	
ABELL 2390	82032000	G2G3S0S1	328.3943	17.7250	7.98	6.81	$9.91^{+1.17}_{-0.95}$	$0.17^{+0.12}_{-0.13}$	0.2280	-11.12	45.91	1.04	0.95	370	
	82032010	G2G3S0S1	328.4006	17.6948	7.73	6.81	$8.80^{+1.00}_{-0.84}$	$0.35^{+0.13}_{-0.13}$	0.2280	-11.15	45.86	1.03	1.08	352	
	82032020	G2G3S0S1	328.4218	17.6904	7.24	6.80	$9.32^{+1.55}_{-1.19}$	$0.21^{+0.16}_{-0.16}$	0.2280	-11.13	45.88	1.06	1.14	240	
	Combined	G2G3S0S1	328.4025	17.7043	...	6.81	$9.16^{+0.62}_{-0.56}$	$0.25^{+0.08}_{-0.07}$	0.2280	-11.13	45.88	1.04	1.09	810	
ABELL 2440	81033000	G2G3S0S1	335.9579	-1.6429	10.92	5.08	$4.31^{+0.16}_{-0.15}$	$0.35^{+0.06}_{-0.07}$	0.0906	-11.23	44.77	1.06	1.03	835	
ABELL 2534	84014000	G2G3S0S1	346.9068	-22.7180	6.00	2.19	$6.44^{+1.29}_{-1.00}$	$0.11^{+0.21}_{-0.11}$	0.1976	-11.82	44.94	1.16	0.95	206	
ABELL 2537	85047000	G2G3S0S1	347.0955	-2.1853	6.00	4.45	$6.08^{+0.59}_{-0.49}$	$0.26^{+0.12}_{-0.11}$	0.2806	-11.80	45.32	1.02	0.94	384	Nz
ABELL 2540	84015000	G2G3S0S1	347.3532	-22.1829	6.00	2.14	$3.87^{+0.69}_{-0.70}$	$0.65^{+0.65}_{-0.42}$	0.1297	-12.39	43.90	1.14	1.19	125	
ABELL 2550	84013000	G2G3S1	347.9033	-21.7507	6.00	2.10	$2.72^{+0.37}_{-0.33}$	$1.70^{+3.70}_{-0.76}$	0.1543	-12.02	44.33	1.27	0.94	92	
	86042000	G2G3	347.8967	-21.7516	6.00	2.10	$2.68^{+0.43}_{-0.33}$	$1.29^{+2.12}_{-0.70}$	0.1543	-11.95	44.39	1.23	1.03	76	
	Combined	G2G3S0S1	347.8947	-21.7512	...	2.10	$2.58^{+0.22}_{-0.21}$	$1.91^{+1.55}_{-0.72}$	0.1543	-11.97	44.35	1.24	1.26	175	
ABELL 2554	84013000	G2G3S0S1	348.0795	-21.5058	7.73	2.09	$6.40^{+0.67}_{-0.55}$	$0.44^{+0.14}_{-0.14}$	0.1111	-11.54	44.74	1.11	0.94	407	
ABELL 2555	86043000	G2G3S0S1	348.1955	-22.1623	6.00	2.03	$2.22^{+0.50}_{-0.44}$	$0.17^{+0.69}_{-0.17}$	0.1385	-12.21	44.01	1.22	0.71	88	
ABELL 2556	84013000	G2G3S0	348.2499	-21.6288	6.01	2.05	$4.13^{+0.29}_{-0.25}$	$0.34^{+0.13}_{-0.11}$	0.0865	-11.29	44.66	1.25	1.05	335	
ABELL 2572	82038000	G2G3S0S1	349.5880	18.7292	7.24	4.69	$3.37^{+0.27}_{-0.24}$	$0.43^{+0.18}_{-0.17}$	0.0403	-11.31	43.93	1.35	1.00	231	

Cluster (1)	Sequence (2)	Instr. (3)	α (4)	δ (5)	R_{ext} (6)	N_H (7)	T_X (8)	Z (9)	z (10)	f_X (11)	L_{bol} (12)	l_{vir} (13)	χ^2_r (14)	d.o.f (15)	Flags (16)
	82038010	G2G3S0S1	349.5907	18.7293	6.75	4.69	$2.97^{+0.15}_{-0.14}$	$0.48^{+0.14}_{-0.13}$	0.0403	-11.34	43.86	1.38	1.10	417	
	83047000	G2G3S0S1	349.6058	18.7255	10.19	4.69	$2.97^{+0.10}_{-0.10}$	$0.36^{+0.07}_{-0.08}$	0.0403	-11.20	44.00	1.20	1.01	746	
	Combined	G2G3S0S1	349.5908	18.7273	...	4.69	$2.91^{+0.07}_{-0.07}$	$0.46^{+0.07}_{-0.06}$	0.0403	-11.26	43.94	1.25	1.54	965	
ABELL 2589	87060000	G2G3S0S1	350.9969	16.7731	10.93	4.15	$3.55^{+0.10}_{-0.09}$	$0.49^{+0.07}_{-0.06}$	0.0414	-10.83	44.44	1.24	1.08	831	
ABELL 2597	83062000	G2G3S0S1	351.3352	-12.1236	11.66	2.49	$3.58^{+0.06}_{-0.07}$	$0.37^{+0.04}_{-0.03}$	0.0852	-10.79	45.10	1.05	1.05	1322	
ABELL 2634	83002000	G2G3S0S1	354.6229	27.0276	15.34	5.07	$3.40^{+0.09}_{-0.08}$	$0.43^{+0.06}_{-0.06}$	0.0310	-10.88	44.13	1.17	1.01	1194	
ABELL 2657	84002000	G2G3S0S1	356.2349	9.1948	16.33	5.66	$3.77^{+0.07}_{-0.07}$	$0.38^{+0.04}_{-0.03}$	0.0402	-10.75	44.51	1.12	1.09	1273	
ABELL 2667	85028000	G2G3S0S1	357.9214	-26.0853	7.00	1.65	$6.31^{+0.29}_{-0.28}$	$0.31^{+0.05}_{-0.06}$	0.2300	-11.21	45.69	1.02	1.07	912	
ABELL 2670	82049000	G2G3S0S1	358.5562	-10.4122	8.96	2.89	$3.98^{+0.17}_{-0.17}$	$0.25^{+0.08}_{-0.07}$	0.0765	-11.18	44.64	1.13	1.08	633	
ABELL 2744	82000000	G2G3S0S1	3.5695	-30.3880	9.45	1.60	$9.61^{+0.64}_{-0.56}$	$0.19^{+0.07}_{-0.07}$	0.3080	-11.41	45.84	0.95	1.02	1002	
ABELL 2798	85008000	G2G3S0S1	9.3771	-28.5461	6.00	1.71	$3.03^{+0.33}_{-0.29}$	$0.36^{+0.23}_{-0.19}$	0.1050	-12.11	43.93	1.15	0.91	211	
ABELL 2801	85007000	G2G3S0S1	9.6278	-29.0921	6.00	1.80	$2.53^{+0.55}_{-0.45}$	$0.56^{+0.71}_{-0.41}$	0.1080	-12.38	43.64	1.19	0.85	124	
ABELL 2811	84003000	G2G3S0S1	10.5324	-28.5318	9.94	1.54	$5.17^{+0.16}_{-0.16}$	$0.30^{+0.05}_{-0.04}$	0.1086	-11.11	45.09	1.07	1.10	1124	
ABELL 3088	87033000	G2G3S0S1	46.7558	-28.6718	7.00	1.36	$6.71^{+0.60}_{-0.53}$	$0.28^{+0.10}_{-0.09}$	0.2534	-11.51	45.49	1.00	1.03	491	
ABELL 3112	81003000	G2G3S0S1	49.4936	-44.2387	12.40	2.60	$4.28^{+0.09}_{-0.08}$	$0.51^{+0.05}_{-0.04}$	0.0750	-10.67	45.17	1.09	1.12	1273	
ABELL 3158	84020000	G2G3S0S1	55.7348	-53.6279	15.59	1.36	$5.49^{+0.12}_{-0.13}$	$0.36^{+0.04}_{-0.04}$	0.0597	-10.60	45.10	1.10	1.17	1529	
ABELL 3266	83023000	G2G3S0S1	67.8300	-61.4383	16.33	1.59	$8.35^{+0.21}_{-0.20}$	$0.32^{+0.04}_{-0.03}$	0.0589	-10.41	45.39	1.13	1.06	1789	
ABELL 3376	84056000	G2G3S0S1	90.4749	-39.9727	13.38	4.85	$4.29^{+0.16}_{-0.16}$	$0.29^{+0.07}_{-0.07}$	0.0456	-10.89	44.51	1.15	1.16	795	
ABELL 3381	85040000	G2G3S0S1	92.4793	-33.6069	6.01	3.16	$1.84^{+0.19}_{-0.19}$	$0.57^{+0.42}_{-0.26}$	0.0359	-12.17	42.80	1.22	0.96	300	
ABELL 3391	72019000	G2G3S0S1	96.5955	-53.6945	13.13	5.51	$6.07^{+0.26}_{-0.24}$	$0.36^{+0.07}_{-0.06}$	0.0514	-10.86	44.75	1.15	1.19	964	
ABELL 3395N	82033000	G2G3S0S1	96.9119	-54.4668	16.08	6.12	$4.72^{+0.16}_{-0.15}$	$0.38^{+0.06}_{-0.05}$	0.0506	-10.87	44.65	1.09	1.02	1097	
ABELL 3395S	82033000	G2G3S0S1	96.7321	-54.5559	18.78	6.35	$5.02^{+0.23}_{-0.21}$	$0.27^{+0.07}_{-0.07}$	0.0506	-10.87	44.67	1.06	1.02	1061	
ABELL 3408	87043000	G2G3S0S1	107.1198	-49.2126	9.21	5.93	$2.78^{+0.14}_{-0.12}$	$0.43^{+0.14}_{-0.13}$	0.0420	-11.46	43.76	1.18	1.04	532	
ABELL 3444	85044000	G2G3S0S1	155.9592	-27.2617	8.47	5.49	$6.87^{+0.47}_{-0.43}$	$0.25^{+0.07}_{-0.08}$	0.2533	-11.30	45.71	0.97	1.00	597	
	85044010	G2G3S0S1	155.9608	-27.2605	7.49	5.49	$6.52^{+0.90}_{-0.72}$	$0.30^{+0.15}_{-0.15}$	0.2533	-11.33	45.67	0.99	1.15	200	
	Combined	G2G3S0S1	155.9531	-27.2571	...	5.49	$6.81^{+0.40}_{-0.37}$	$0.26^{+0.06}_{-0.06}$	0.2533	-11.30	45.71	0.97	1.08	726	
ABELL 3528N	84057000	G2G3S0S1	193.5923	-29.0167	7.73	6.16	$4.80^{+0.26}_{-0.25}$	$0.40^{+0.10}_{-0.09}$	0.0547	-11.14	44.46	1.29	0.99	635	
ABELL 3528S	84057000	G2G3S0S1	193.6650	-29.2266	9.21	6.09	$4.94^{+0.20}_{-0.19}$	$0.34^{+0.06}_{-0.07}$	0.0547	-11.01	44.60	1.24	1.00	816	
ABELL 3530	86015000	G2G3S0S1	193.9100	-30.3300	7.49	5.77	$4.17^{+0.26}_{-0.25}$	$0.30^{+0.12}_{-0.12}$	0.0537	-11.36	44.18	1.25	1.02	460	
ABELL 3532	86014000	G2G3	194.3227	-30.3640	10.43	5.91	$4.48^{+0.17}_{-0.17}$	$0.36^{+0.07}_{-0.08}$	0.0554	-10.98	44.61	1.18	1.01	561	
	86016000	G2G3S0S1	194.3404	-30.3769	13.87	5.91	$4.86^{+0.16}_{-0.17}$	$0.33^{+0.06}_{-0.05}$	0.0554	-10.92	44.69	1.11	1.12	1005	
	Combined	G2G3S0S1	194.3364	-30.3740	...	5.91	$4.64^{+0.12}_{-0.12}$	$0.32^{+0.05}_{-0.04}$	0.0554	-10.95	44.65	1.12	1.02	1200	
ABELL 3556	83046000	G2G3S0S1	201.0313	-31.6677	7.73	4.07	$3.35^{+0.30}_{-0.26}$	$0.36^{+0.21}_{-0.19}$	0.0479	-11.84	43.54	1.17	1.09	357	
ABELL 3558	82046000	G2G3S0S1	201.9885	-31.5054	14.85	3.89	$5.51^{+0.15}_{-0.13}$	$0.31^{+0.04}_{-0.04}$	0.0480	-10.38	45.14	1.19	0.97	1445	
	83058000	G2G3	202.0105	-31.5035	13.63	3.88	$5.48^{+0.13}_{-0.13}$	$0.39^{+0.04}_{-0.04}$	0.0480	-10.40	45.11	1.22	1.02	921	N

Cluster (1)	Sequence (2)	Instr. (3)	α (4)	δ (5)	R_{ext} (6)	N_H (7)	T_X (8)	Z (9)	z (10)	f_X (11)	L_{bol} (12)	l_{vir} (13)	χ^2_r (14)	d.o.f (15)	Flags (16)
	Combined	G2G3S0S1	201.9971	-31.5012	...	3.88	$5.51^{+0.09}_{-0.10}$	$0.33^{+0.03}_{-0.03}$	0.0480	-10.39	45.12	1.20	1.09	1702	
ABELL 3562	84041000	G2G3S0S1	203.3883	-31.6805	8.47	3.85	$4.74^{+0.18}_{-0.17}$	$0.44^{+0.08}_{-0.07}$	0.0490	-10.90	44.60	1.34	1.04	842	
ABELL 3565	61006000	G2S0S1	204.1630	-33.9542	7.00	4.10	$1.16^{+0.11}_{-0.09}$	$0.15^{+0.07}_{-0.04}$	0.0123	-11.72	42.25	1.61	1.92	178	g
ABELL 3570	84074000	G2G3S0S1	206.7043	-37.8897	10.43	4.40	$2.56^{+0.16}_{-0.16}$	$0.43^{+0.17}_{-0.15}$	0.0366	-11.48	43.60	1.16	0.99	418	
ABELL 3571	82047000	G2G3S0S1	206.8620	-32.8593	15.34	3.70	$6.97^{+0.13}_{-0.12}$	$0.36^{+0.03}_{-0.03}$	0.0391	-10.14	45.26	1.30	0.99	1933	
ABELL 3581	81019000	G2S0S1	211.8755	-27.0049	13.87	4.53	$1.70^{+0.05}_{-0.04}$	$0.31^{+0.05}_{-0.04}$	0.0230	-10.68	43.90	1.27	1.19	618	g
ABELL 3602	74044000	G2G3	218.2095	-44.3113	6.01	8.38	$4.17^{+0.35}_{-0.30}$	$0.44^{+0.18}_{-0.17}$	0.1044	-11.55	44.58	1.16	0.95	220	
ABELL 3627	84005000	G2G3S0S1	243.7445	-60.9152	20.25	20.40	$5.83^{+0.08}_{-0.08}$	$0.28^{+0.02}_{-0.02}$	0.0157	-10.21	44.44	1.40	1.32	2016	
ABELL 3667	83054000	G2G3S0S1	303.1279	-56.8290	18.78	4.72	$6.72^{+0.19}_{-0.19}$	$0.29^{+0.04}_{-0.04}$	0.0556	-10.36	45.34	1.09	0.96	1407	
ABELL 3921	83048000	G2G3S0S1	342.4877	-64.4240	11.91	2.95	$5.24^{+0.24}_{-0.23}$	$0.32^{+0.07}_{-0.07}$	0.0936	-10.97	45.10	1.06	1.06	901	
	83048010	G2G3S0S1	342.5067	-64.4214	11.42	2.95	$5.64^{+0.29}_{-0.27}$	$0.31^{+0.07}_{-0.07}$	0.0936	-10.99	45.11	1.07	1.04	873	
	Combined	G2G3S0S1	342.4914	-64.4253	...	2.95	$5.07^{+0.17}_{-0.15}$	$0.36^{+0.04}_{-0.06}$	0.0936	-10.97	45.10	1.06	1.29	1253	
ABELL 3934	85030000	G2G3S0S1	343.3930	-33.7102	6.01	1.24	$5.35^{+0.49}_{-0.42}$	$0.34^{+0.12}_{-0.11}$	0.2241	-11.65	45.19	1.04	1.05	400	
	85030010	G2G3S0S1	343.3923	-33.7233	6.00	1.24	$4.91^{+0.98}_{-0.74}$	$0.58^{+0.32}_{-0.28}$	0.2241	-11.60	45.22	1.08	1.09	99	
	Combined	G2G3S0S1	343.3822	-33.7244	...	1.24	$5.73^{+0.44}_{-0.39}$	$0.35^{+0.09}_{-0.09}$	0.2241	-11.65	45.21	1.05	1.19	466	
ABELL 4038	83004000	G2G3S0S1	356.9330	-28.1434	16.57	1.56	$3.06^{+0.04}_{-0.03}$	$0.43^{+0.03}_{-0.03}$	0.0300	-10.45	44.50	1.20	1.10	1597	
ABELL 4059	82030000	G2G3S0S1	359.2555	-34.7527	11.91	1.10	$3.92^{+0.07}_{-0.06}$	$0.53^{+0.04}_{-0.04}$	0.0475	-10.66	44.76	1.21	0.97	1401	
ABELL 4067	86010000	G2G3S0S1	359.7150	-60.6200	8.47	2.11	$3.45^{+0.22}_{-0.20}$	$0.52^{+0.17}_{-0.15}$	0.0989	-11.45	44.57	1.07	1.10	321	
	86010010	G2G3S0S1	359.7104	-60.6344	9.45	2.12	$3.34^{+0.14}_{-0.13}$	$0.53^{+0.11}_{-0.10}$	0.0989	-11.44	44.57	1.05	1.02	751	
	Combined	G2G3S0S1	359.7079	-60.6260	...	2.12	$3.56^{+0.12}_{-0.10}$	$0.48^{+0.08}_{-0.06}$	0.0989	-11.45	44.58	1.05	1.29	885	
ABELL S0506	83017000	G2G3S0S1	75.2836	-24.4098	6.00	2.56	$9.46^{+3.17}_{-2.78}$	$0.40^{+0.40}_{-0.39}$	0.3220	-12.40	44.90	1.07	1.01	154	
ABELL S0520	86036000	G2G3S0S1	79.1721	-54.5119	6.02	6.82	$6.94^{+0.94}_{-0.73}$	$0.22^{+0.14}_{-0.13}$	*0.2824*	-11.70	45.47	1.02	0.97	309	z
ABELL S0636	85006000	G2G3S0S1	157.5140	-35.3314	12.15	6.52	$2.08^{+0.05}_{-0.05}$	$0.43^{+0.08}_{-0.07}$	0.0087	-10.88	42.90	1.77	1.07	889	
	85010000	G2G3S0S1	157.4407	-35.3311	13.38	6.56	$2.23^{+0.06}_{-0.05}$	$0.50^{+0.08}_{-0.07}$	0.0087	-10.83	42.97	1.68	1.10	925	
	Combined	G2G3S0S1	157.4735	-35.3282	...	6.54	$2.13^{+0.03}_{-0.04}$	$0.41^{+0.05}_{-0.04}$	0.0087	-10.84	42.94	1.73	1.26	1220	
ABELL S0753	65018000	G2G3S0S1	210.9094	-33.9769	9.70	5.46	$2.37^{+0.14}_{-0.13}$	$0.36^{+0.16}_{-0.12}$	0.0142	-11.21	43.03	1.54	1.05	358	
ABELL S1077	83019010	G2G3S0S1	344.7041	-34.8049	7.00	1.30	$8.59^{+0.92}_{-0.80}$	$0.14^{+0.11}_{-0.11}$	0.3130	-11.70	45.54	0.99	1.22	508	
ABELL S1111	72042000	G2G3S0S1	349.7789	-42.1148	6.00	1.98	$2.64^{+0.30}_{-0.35}$	$0.18^{+0.22}_{-0.16}$	0.0450	-11.84	43.43	1.47	0.96	147	
AWM 04	83072000	G2G3S0S1	241.2255	23.9305	9.94	5.00	$2.48^{+0.07}_{-0.06}$	$0.56^{+0.09}_{-0.07}$	0.0328	-11.20	43.77	1.25	1.01	735	
AWM 07	80036000	G2G3S0S1	43.6431	41.5873	19.77	9.82	$3.71^{+0.06}_{-0.05}$	$0.51^{+0.03}_{-0.04}$	0.0178	-10.10	44.47	1.38	1.05	1552	
AX J2239−0429	83018000	G2G3S0S1	339.8916	-4.4909	6.00	4.02	$6.58^{+4.44}_{-2.09}$	$0.17^{+0.35}_{-0.17}$	0.5565	-12.69	44.97	1.03	1.16	131	
CENTAURUS	80032000	G2G3S0S1	192.1976	-41.3079	17.55	8.06	$3.89^{+0.13}_{-0.15}$	$0.54^{+0.05}_{-0.04}$	0.0110	-10.08	44.09	1.79	0.97	986	N
	80033000	G2G3S0S1	192.2110	-41.3191	20.01	8.06	$4.04^{+0.20}_{-0.20}$	$0.56^{+0.06}_{-0.05}$	0.0110	-10.07	44.10	1.62	0.98	646	N
	83026000	G2G3S0S1	192.2004	-41.3137	21.48	8.06	$3.91^{+0.07}_{-0.07}$	$0.53^{+0.02}_{-0.02}$	0.0110	-10.04	44.13	1.56	1.20	1505	N
	Combined	G2G3S0S1	192.1973	-41.3100	...	8.06	$3.96^{+0.06}_{-0.05}$	$0.53^{+0.02}_{-0.01}$	0.0110	-10.05	44.12	1.60	1.27	1598	N

Cluster (1)	Sequence (2)	Instr. (3)	α (4)	δ (5)	R_{ext} (6)	N_H (7)	T_X (8)	Z (9)	z (10)	f_X (11)	L_{bol} (12)	l_{vir} (13)	χ^2_r (14)	d.o.f (15)	Flags (16)
CID 28	86017000	G2G3S0S1	73.7058	-18.1325	7.73	4.11	$2.24^{+0.11}_{-0.11}$	$0.49^{+0.13}_{-0.12}$	0.0335	-11.46	43.50	1.30	1.11	370	
CL 0016+1609	80025000	G2G3S0	4.6461	16.4343	6.00	4.07	$8.99^{+1.41}_{-1.12}$	$0.16^{+0.16}_{-0.15}$	0.5465	-11.89	45.84	0.93	1.05	228	
	84016000	G2G3S0S1	4.6467	16.4397	6.51	4.07	$9.06^{+0.98}_{-0.84}$	$0.22^{+0.10}_{-0.11}$	0.5465	-11.88	45.85	0.91	1.06	518	
	Combined	G2G3S0S1	4.6443	16.4361	...	4.07	$8.74^{+0.80}_{-0.68}$	$0.12^{+0.09}_{-0.09}$	0.5465	-11.88	45.84	0.91	1.12	683	
CL 09104+4109	71002000	G2G3S0S1	138.4390	40.9392	6.00	0.99	$6.61^{+0.63}_{-0.60}$	$0.45^{+0.12}_{-0.12}$	0.4420	-11.86	45.61	0.96	1.14	371	
CL 1938.3+5409	87057000	G2G3S0S1	294.5683	54.1572	7.49	10.70	$7.52^{+0.38}_{-0.37}$	$0.25^{+0.06}_{-0.06}$	*0.2593*	-11.37	45.85	1.00	1.04	980	z
CL 2244−0221	83016000	G2G3S0S1	341.8226	-2.0867	6.00	5.30	$4.85^{+1.25}_{-0.96}$	$0.03^{+0.29}_{-0.03}$	0.3280	-12.39	44.74	1.00	1.12	164	
CYGNUS A	70003000	G2G3S0S1	299.8778	40.7323	14.37	34.80	$9.80^{+0.32}_{-0.28}$	$0.70^{+0.04}_{-0.05}$	0.0561	-10.57	45.45	1.17	1.56	1969	N
	70003010	G2G3S0S1	299.8700	40.7384	16.09	34.70	$9.78^{+0.27}_{-0.26}$	$0.73^{+0.04}_{-0.04}$	0.0561	-10.56	45.46	1.14	1.79	2142	N
	Combined	G2G3S0S1	299.8684	40.7360	...	34.75	$10.44^{+0.22}_{-0.19}$	$0.72^{+0.03}_{-0.02}$	0.0561	-10.56	45.47	1.15	2.42	2287	N
EXSS 0657.5−5551	84009000	G2G3S0S1	104.6240	-55.9488	7.24	6.53	$11.98^{+0.98}_{-0.86}$	$0.30^{+0.09}_{-0.10}$	0.2960	-11.24	46.07	1.03	0.92	822	
	86075000	G2G3S0S1	104.6253	-55.9430	8.96	6.53	$12.25^{+0.86}_{-0.73}$	$0.17^{+0.08}_{-0.07}$	0.2960	-11.22	46.10	0.99	1.05	1173	
	Combined	G2G3S0S1	104.6260	-55.9447	...	6.53	$11.64^{+0.56}_{-0.51}$	$0.23^{+0.06}_{-0.05}$	0.2960	-11.22	46.08	0.99	1.11	1451	
FORNAX	80038000	G2G3S0S1	54.6434	-35.4568	13.13	1.34	$1.35^{+0.03}_{-0.03}$	$0.37^{+0.05}_{-0.04}$	0.0050	-10.67	42.54	2.41	1.41	688	
	80039000	G2G3S0S1	54.6322	-35.4538	11.91	1.34	$1.36^{+0.04}_{-0.03}$	$0.39^{+0.06}_{-0.06}$	0.0050	-10.74	42.48	2.60	1.43	623	
	Combined	G2G3S0S1	54.6204	-35.4601	...	1.34	$1.36^{+0.02}_{-0.02}$	$0.36^{+0.03}_{-0.02}$	0.0050	-10.70	42.52	2.49	1.80	869	
HCG 042	83025000	G2G3S0S1	150.0656	-19.6283	6.00	4.80	$0.78^{+0.04}_{-0.05}$	$0.13^{+0.04}_{-0.03}$	0.0133	-12.02	41.97	2.13	1.34	194	
HCG 051	82028000	G2G3S0S1	170.6130	24.2938	7.00	1.27	$1.35^{+0.05}_{-0.05}$	$0.29^{+0.06}_{-0.05}$	0.0258	-11.77	42.89	1.31	1.19	520	
HCG 057	63000000	G2G3S0S1	174.4508	21.9746	6.00	1.96	$3.63^{+1.11}_{-0.85}$	$0.72^{+1.16}_{-0.49}$	0.0304	-12.78	42.23	1.47	1.22	216	
HCG 062	81012000	G2G3S0S1	193.2691	-9.2053	8.22	3.01	$0.99^{+0.03}_{-0.04}$	$0.14^{+0.03}_{-0.02}$	0.0137	-11.32	42.73	1.62	1.31	416	
	86008000	G2G3S0S1	193.2716	-9.2009	7.24	3.01	$1.21^{+0.08}_{-0.07}$	$0.24^{+0.10}_{-0.07}$	0.0137	-11.42	42.65	1.72	1.38	290	
	86008030	G2G3	193.2768	-9.1974	6.75	3.01	$1.17^{+0.10}_{-0.08}$	$0.29^{+0.17}_{-0.10}$	0.0137	-11.45	42.61	1.80	1.41	144	
	Combined	G2G3S0S1	193.2739	-9.2028	...	3.01	$1.05^{+0.03}_{-0.03}$	$0.15^{+0.02}_{-0.01}$	0.0137	-11.37	42.69	1.67	1.44	630	
HCG 068	85031000	G2G3S0S1	208.3694	40.2952	6.00	0.98	$0.78^{+0.08}_{-0.09}$	$0.09^{+0.06}_{-0.03}$	0.0080	-12.22	41.40	3.96	1.20	144	
HCG 094	82038000	G2G3S0S1	349.3116	18.6965	8.96	4.73	$3.52^{+0.19}_{-0.18}$	$0.44^{+0.15}_{-0.13}$	0.0422	-11.08	44.20	1.28	0.97	364	
	82038010	G2G3S0S1	349.3061	18.7005	10.92	4.73	$3.40^{+0.10}_{-0.09}$	$0.45^{+0.07}_{-0.07}$	0.0422	-11.03	44.25	1.20	1.09	946	
	Combined	G2G3S0S1	349.3065	18.6976	...	4.73	$3.24^{+0.07}_{-0.07}$	$0.47^{+0.06}_{-0.05}$	0.0422	-11.03	44.23	1.21	1.54	1042	
HCG 097	84006000	G2G3S0	356.8438	-2.2963	6.00	3.65	$1.02^{+0.07}_{-0.06}$	$0.12^{+0.03}_{-0.03}$	0.0218	-12.01	42.45	1.39	1.57	314	
HERCULES	83030000	G2G3S0S1	241.1487	17.7263	10.43	3.43	$2.33^{+0.07}_{-0.07}$	$0.45^{+0.09}_{-0.08}$	0.0366	-11.05	44.00	1.22	1.13	742	
HERCULES A	86038000	G2G3S0S1	252.7806	4.9935	6.00	6.40	$4.15^{+0.27}_{-0.25}$	$0.45^{+0.11}_{-0.10}$	0.1540	-11.59	44.87	1.11	1.06	484	
HYDRA A	80015000	G2G3S0S1	139.5205	-12.0949	10.68	4.94	$3.54^{+0.07}_{-0.06}$	$0.35^{+0.03}_{-0.03}$	0.0522	-10.53	44.94	1.25	1.14	1196	
MKW 03S	80011000	G2G3S0S1	230.4547	7.7065	11.91	3.03	$3.41^{+0.05}_{-0.06}$	$0.44^{+0.03}_{-0.04}$	0.0450	-10.62	44.71	1.22	1.03	1306	
MKW 04S	83008000	G2G3S0S1	181.6641	28.1687	9.21	1.69	$2.07^{+0.10}_{-0.05}$	$0.45^{+0.12}_{-0.10}$	0.0236	-11.46	43.19	1.30	0.97	624	
	84017000	G2G3S0S1	181.6498	28.1826	7.98	1.69	$2.23^{+0.15}_{-0.17}$	$0.40^{+0.17}_{-0.14}$	0.0236	-11.56	43.11	1.35	1.08	303	
	84017010	G2G3S0S1	181.6610	28.1670	7.00	1.69	$2.41^{+0.22}_{-0.21}$	$0.65^{+0.28}_{-0.22}$	0.0236	-11.61	43.08	1.42	1.11	156	

Cluster (1)	Sequence (2)	Instr. (3)	α (4)	δ (5)	R_{ext} (6)	N_H (7)	T_X (8)	Z (9)	z (10)	f_X (11)	L_{bol} (12)	l_{vir} (13)	χ^2_r (14)	d.o.f (15)	Flags (16)
	Combined	G2G3S0S1	181.6572	28.1743	...	1.69	$2.16^{+0.04}_{-0.07}$	$0.43^{+0.07}_{-0.07}$	0.0236	-11.50	43.16	1.32	1.07	807	
MKW 04	52027000	G2G3S0S1	181.1130	1.8941	11.91	1.89	$1.85^{+0.04}_{-0.03}$	$0.73^{+0.09}_{-0.07}$	0.0198	-10.95	43.52	1.34	1.19	885	
	82012000	G2G3S0S1	181.1120	1.8893	10.92	1.89	$1.78^{+0.07}_{-0.06}$	$0.45^{+0.11}_{-0.08}$	0.0198	-10.95	43.52	1.40	1.12	556	
	82013000	G2G3S0S1	181.1158	1.8948	10.43	1.89	$1.90^{+0.07}_{-0.07}$	$0.60^{+0.13}_{-0.10}$	0.0198	-10.98	43.50	1.43	1.03	555	
	82014000	G2G3S0S1	181.1114	1.8951	10.92	1.89	$1.74^{+0.06}_{-0.07}$	$0.53^{+0.13}_{-0.10}$	0.0198	-10.95	43.51	1.40	1.03	504	
	82015000	G2G3S0S1	181.1215	1.8895	11.66	1.89	$1.84^{+0.06}_{-0.07}$	$0.49^{+0.12}_{-0.10}$	0.0198	-10.94	43.53	1.36	0.92	525	
	Combined	G2G3S0S1	181.1097	1.8972	...	1.89	$1.83^{+0.02}_{-0.03}$	$0.55^{+0.05}_{-0.03}$	0.0198	-10.94	43.53	1.38	1.45	1261	
MKW 08	84049000	G2G3S0S1	220.1689	3.4805	12.15	2.78	$3.03^{+0.13}_{-0.12}$	$0.41^{+0.10}_{-0.10}$	0.0272	-11.04	43.83	1.25	0.91	660	
MKW 09	83009000	G2G3S0S1	233.1279	4.6945	7.49	4.17	$1.95^{+0.12}_{-0.11}$	$0.55^{+0.18}_{-0.14}$	0.0343	-11.46	43.49	1.30	1.20	731	
MS 0302.5+1717	84028000	G2G3	46.3277	17.4723	6.00	10.80	$10.81^{+\infty}_{-5.24}$	$0.62^{+2.65}_{-0.62}$	0.4250	-12.53	45.09	1.11	1.04	57	
	87055000	G2G3S1	46.3504	17.4772	6.00	10.80	$6.60^{+3.49}_{-2.07}$	$0.10^{+0.43}_{-0.10}$	0.4250	-12.63	44.83	1.07	1.32	99	
	87055010	G2G3S0S1	46.3303	17.4713	6.00	10.80	$7.26^{+5.51}_{-2.51}$	$0.15^{+0.56}_{-0.15}$	0.4250	-12.49	45.00	1.08	0.95	86	
	Combined	G2G3S0S1	46.3304	17.4734	...	10.80	$10.38^{+3.68}_{-2.47}$	$0.14^{+0.25}_{-0.14}$	0.4250	-12.55	45.04	1.11	1.21	240	
MS 0302.7+1658	84028000	G2G3S0S1	46.3859	17.1697	6.00	10.90	$5.28^{+1.98}_{-1.25}$	$0.28^{+0.44}_{-0.28}$	0.4245	-12.54	44.87	1.05	0.99	138	
MS 0353.6−3642	82042000	G2G3S0S1	58.8778	-36.5586	6.00	1.21	$5.35^{+1.14}_{-0.86}$	$0.30^{+0.25}_{-0.23}$	0.3200	-12.02	45.12	1.05	1.35	143	
MS 0418.3−3844	87052000	G2G3S0	65.0274	-38.6296	6.00	2.07	$3.61^{+1.23}_{-0.83}$	$0.38^{+0.68}_{-0.38}$	0.3500	-12.51	44.62	1.02	1.08	156	
MS 0440.5+0204	82026000	G2G3S0S1	70.7949	2.1686	6.00	9.66	$5.02^{+0.61}_{-0.50}$	$0.30^{+0.17}_{-0.16}$	0.1965	-11.93	44.80	1.06	0.94	217	
MS 0451.6−0305	81025000	G2S0S1	73.5492	-3.0158	6.00	5.03	$8.62^{+1.54}_{-1.21}$	$0.28^{+0.17}_{-0.18}$	0.5391	-11.94	45.78	0.93	0.97	217	g
MS 0735.6+7421	83035000	G2G3S0S1	115.4142	74.2460	6.26	3.49	$5.45^{+0.53}_{-0.45}$	$0.37^{+0.14}_{-0.13}$	0.2160	-11.55	45.26	1.04	0.92	253	
MS 0811.6+6301	84061000	G2G3S0S1	124.0094	62.8845	6.00	4.26	$3.53^{+0.91}_{-0.51}$	$1.25^{+0.92}_{-0.70}$	0.3120	-12.35	44.68	1.08	1.21	113	
MS 0821.5+0337	87054000	G2G3S0S1	126.0428	3.4664	6.00	4.07	$4.46^{+2.52}_{-1.40}$	$0.33^{+1.24}_{-0.33}$	0.3470	-13.02	44.15	1.05	1.12	120	
MS 0839.8+2938	82011000	G2G3S0S1	130.7286	29.4571	6.00	4.09	$3.80^{+0.25}_{-0.23}$	$0.59^{+0.16}_{-0.14}$	0.1930	-11.78	44.84	1.06	1.23	362	
MS 1006.0+1202	86057000	G2G3S0S1	152.2046	11.8006	7.00	3.77	$7.03^{+0.86}_{-0.84}$	$0.37^{+0.18}_{-0.15}$	0.2604	-11.70	45.34	1.00	0.86	270	
MS 1008.1−1224	82056000	G2G3S0S1	152.6366	-12.6548	6.00	6.97	$7.47^{+1.56}_{-1.21}$	$0.72^{+0.30}_{-0.26}$	0.3063	-12.02	45.20	1.04	0.99	164	
MS 1054.4−0321	83065000	G2G3S0S1	164.2493	-3.6298	6.00	3.58	$13.21^{+4.04}_{-2.77}$	$0.07^{+0.26}_{-0.07}$	0.8390	-12.41	45.77	0.93	1.15	314	
MS 1111.8−3754	84011000	G2G3S0S1	168.5593	-38.1912	8.72	9.14	$5.79^{+0.22}_{-0.21}$	$0.37^{+0.05}_{-0.05}$	0.1290	-11.35	45.06	1.06	1.14	1086	
MS 1137.5+6625	85046000	G2G3S0S1	175.0913	66.1326	6.00	1.21	$6.94^{+3.82}_{-2.15}$	$0.00^{+0.44}_{-0.00}$	0.7842	-12.81	45.15	1.09	0.73	34	
	85046010	G2G3S0S1	175.0660	66.1227	6.00	1.21	$6.49^{+2.88}_{-1.99}$	$0.52^{+0.72}_{-0.52}$	0.7842	-12.87	45.09	1.10	1.14	55	
	Combined	G2G3S0S1	175.0822	66.1294	...	1.21	$6.70^{+1.84}_{-1.46}$	$0.26^{+0.34}_{-0.26}$	0.7842	-12.84	45.13	1.15	1.09	95	
MS 1147.3+1103	84060000	G2G3S0S1	177.4587	10.7836	6.00	2.75	$6.04^{+1.37}_{-1.04}$	$0.42^{+0.30}_{-0.26}$	0.3030	-12.15	44.97	1.07	0.96	166	
MS 1224.7+2007	82043000	G2G3S0S1	186.8019	19.8643	6.00	2.56	$4.75^{+1.21}_{-1.03}$	$0.31^{+0.58}_{-0.31}$	0.3255	-12.30	44.83	1.00	0.60	77	
MS 1241.5+1710	83067000	G2G3S0S1	190.9997	16.8971	6.00	1.91	$7.22^{+2.70}_{-1.75}$	$0.73^{+0.46}_{-0.40}$	0.5490	-12.32	45.37	0.96	0.92	95	
MS 1244.2+7114	85032000	G2G3S0S1	191.5355	70.9646	6.00	1.63	$3.55^{+0.65}_{-0.49}$	$0.30^{+0.32}_{-0.27}$	0.2250	-11.97	44.76	1.07	1.09	137	
	86046000	G2G3S0S1	191.5259	70.9628	6.00	1.63	$3.33^{+0.41}_{-0.35}$	$0.40^{+0.29}_{-0.23}$	0.2250	-11.97	44.75	1.02	0.93	215	
	Combined	G2G3S0S1	191.5595	70.9551	...	1.63	$4.13^{+0.36}_{-0.32}$	$0.40^{+0.14}_{-0.13}$	0.2250	-12.00	44.77	1.05	1.28	342	

Cluster (1)	Sequence (2)	Instr. (3)	α (4)	δ (5)	R_{ext} (6)	N_H (7)	T_X (8)	Z (9)	z (10)	f_X (11)	L_{bol} (12)	l_{vir} (13)	χ^2_r (14)	d.o.f (15)	Flags (16)
MS 1305.4+2941	91001000	G2G3S0S1	196.9565	29.4278	6.00	1.02	$2.91^{+0.46}_{-0.40}$	$0.62^{+0.58}_{-0.40}$	0.2410	-12.35	44.42	1.04	1.36	195	
MS 1358.4+6245	81032000	G2G3S0S1	209.9495	62.5288	6.00	1.93	$5.95^{+0.62}_{-0.54}$	$0.31^{+0.12}_{-0.11}$	0.3290	-11.90	45.29	1.01	1.03	345	
	83075000	G2G3S0S1	209.9535	62.5177	6.00	1.93	$7.08^{+0.87}_{-0.73}$	$0.32^{+0.14}_{-0.13}$	0.3290	-11.90	45.34	1.05	0.83	339	
	Combined	G2G3S0S1	209.9578	62.5319	...	1.93	$6.70^{+0.55}_{-0.49}$	$0.26^{+0.10}_{-0.08}$	0.3290	-11.90	45.32	1.03	1.02	607	
MS 1426.4+0158	82044000	G2G3S0S1	217.2365	1.7493	6.00	2.75	$8.75^{+2.77}_{-2.23}$	$0.00^{+0.34}_{-0.00}$	0.3200	-12.26	45.00	1.07	1.02	123	
MS 1455.0+2232	82053000	G2G3S0S1	224.3093	22.3430	6.75	3.16	$4.45^{+0.24}_{-0.22}$	$0.37^{+0.08}_{-0.09}$	0.2568	-11.44	45.46	0.96	0.98	545	
	82053010	G2G3S0S1	224.3137	22.3328	6.01	3.16	$4.53^{+0.51}_{-0.47}$	$0.42^{+0.22}_{-0.18}$	0.2568	-11.47	45.44	0.99	1.03	157	
	Combined	G2G3S0S1	224.3096	22.3409	...	3.16	$4.51^{+0.22}_{-0.20}$	$0.35^{+0.07}_{-0.07}$	0.2568	-11.45	45.46	0.97	1.02	641	
MS 1512.4+3647	83066000	G2G3S0S1	228.5933	36.6006	6.00	1.38	$3.59^{+0.89}_{-0.74}$	$0.29^{+0.55}_{-0.29}$	0.3727	-12.26	44.92	1.02	0.85	99	
MS 1532.5+0130	87051000	G2G3S0S1	233.7767	1.3352	6.00	4.90	$3.60^{+0.91}_{-0.68}$	$0.12^{+0.34}_{-0.12}$	0.3200	-12.52	44.52	1.03	0.95	201	
MS 1621.5+2640	85051000	G2G3S0S1	245.9130	26.5684	6.00	3.56	$6.54^{+1.33}_{-1.02}$	$0.49^{+0.24}_{-0.22}$	0.4275	-12.25	45.19	1.00	0.99	209	
MS 1910.5+6736	86058000	G2G3S0S1	287.6157	67.6906	6.00	6.12	$4.45^{+0.79}_{-0.52}$	$0.36^{+0.21}_{-0.22}$	0.2460	-11.98	44.90	1.04	1.07	195	
MS 2053.7−0449	85052000	G2G3S0S1	314.0773	-4.6161	6.00	4.96	$10.03^{+8.73}_{-3.55}$	$0.00^{+0.31}_{-0.00}$	0.5830	-12.93	44.88	1.09	0.83	75	
MS 2137.3−2353	81022000	G2G3S0S1	325.0674	-23.6616	6.00	3.55	$4.57^{+0.41}_{-0.35}$	$0.53^{+0.15}_{-0.14}$	0.3130	-11.60	45.49	0.97	0.77	267	
NGC 0499	61007000	G2G3S0S1	20.7876	33.4483	9.00	5.24	$0.76^{+0.03}_{-0.03}$	$0.13^{+0.02}_{-0.02}$	0.0147	-11.44	42.63	1.41	1.59	268	
	61007010	G2G3S0S1	20.7832	33.4467	9.00	5.24	$0.84^{+0.09}_{-0.09}$	$0.09^{+0.04}_{-0.03}$	0.0147	-11.51	42.58	1.39	1.62	73	
	63026000	G2G3S0S1	20.8120	33.4531	9.00	5.24	$0.78^{+0.02}_{-0.02}$	$0.17^{+0.02}_{-0.02}$	0.0147	-11.44	42.62	1.42	1.24	356	
	Combined	G2G3S0S1	20.7929	33.4513	...	5.24	$0.77^{+0.02}_{-0.02}$	$0.15^{+0.01}_{-0.01}$	0.0147	-11.44	42.62	1.41	1.77	514	
NGC 0507	61007000	G2G3S0S1	20.8952	33.2518	9.00	5.25	$1.20^{+0.03}_{-0.04}$	$0.17^{+0.03}_{-0.02}$	0.0165	-11.07	43.16	1.57	1.28	540	
	61007010	G2G3S0S1	20.9104	33.2497	9.00	5.25	$1.35^{+0.07}_{-0.07}$	$0.44^{+0.15}_{-0.10}$	0.0165	-11.11	43.11	1.56	1.22	182	
	63026000	G2G3	20.9154	33.2685	9.00	5.25	$1.27^{+0.06}_{-0.05}$	$0.26^{+0.08}_{-0.06}$	0.0165	-11.08	43.14	1.57	1.19	325	
	Combined	G2G3S0S1	20.9056	33.2586	...	5.25	$1.27^{+0.03}_{-0.02}$	$0.26^{+0.03}_{-0.02}$	0.0165	-11.08	43.15	1.57	1.52	713	
NGC 0533	62009000	G2G3S0	21.3956	1.7687	6.51	3.10	$1.17^{+0.09}_{-0.10}$	$0.23^{+0.13}_{-0.08}$	0.0181	-11.64	42.66	1.54	1.27	134	
	62009010	G2G3S0S1	21.3807	1.7576	7.49	3.10	$1.17^{+0.07}_{-0.07}$	$0.25^{+0.10}_{-0.06}$	0.0181	-11.57	42.73	1.45	1.18	206	
	Combined	G2G3S0S1	21.3901	1.7626	...	3.10	$1.20^{+0.05}_{-0.06}$	$0.30^{+0.09}_{-0.07}$	0.0181	-11.61	42.69	1.47	1.34	309	
NGC 1132	65021000	G2G3S0S1	43.2290	-1.2750	7.73	5.18	$1.08^{+0.05}_{-0.04}$	$0.21^{+0.05}_{-0.04}$	0.0232	-11.56	42.94	1.34	1.17	347	
NGC 2300	80012000	G2G3S0S1	113.0664	85.7152	15.00	5.28	$1.09^{+0.06}_{-0.12}$	$0.15^{+0.09}_{-0.05}$	0.0064	-11.55	41.84	1.34	1.03	236	
	85005000	G2G3S0	113.0945	85.7113	15.00	5.27	$0.99^{+0.10}_{-0.08}$	$0.09^{+0.04}_{-0.03}$	0.0064	-11.48	41.90	1.35	1.55	500	
	Combined	G2G3S0S1	113.0919	85.7156	...	5.28	$0.98^{+0.06}_{-0.05}$	$0.10^{+0.03}_{-0.02}$	0.0064	-11.49	41.89	1.35	1.35	663	
NGC 2563	63008000	G2G3S0S1	125.1598	21.0724	6.26	4.23	$1.36^{+0.11}_{-0.09}$	$0.27^{+0.11}_{-0.08}$	0.0149	-11.97	42.18	1.50	1.10	310	
NGC 3258	61020000	G2G3S0S1	157.2439	-35.6016	16.82	6.49	$2.04^{+0.09}_{-0.08}$	$0.33^{+0.10}_{-0.08}$	0.0093	-10.94	42.89	1.38	1.05	845	
NGC 4261	74085000	G2G3S0S1	184.8360	5.8226	9.21	1.55	$2.18^{+0.16}_{-0.20}$	$0.33^{+0.08}_{-0.08}$	0.0070	-11.71	41.90	1.41	2.49	553	N
NGC 4325	85066000	G2G3S0S1	185.7782	10.6171	6.26	2.23	$0.95^{+0.02}_{-0.03}$	$0.34^{+0.06}_{-0.04}$	0.0255	-11.35	43.21	1.54	1.20	360	
NGC 5044	80026000	G2G3S0S1	198.8454	-16.3923	11.17	4.92	$0.97^{+0.02}_{-0.01}$	$0.24^{+0.02}_{-0.01}$	0.0082	-10.50	43.06	2.43	1.53	594	
	80026010	G2G3S0S1	198.8488	-16.3934	10.92	4.92	$0.96^{+0.02}_{-0.02}$	$0.24^{+0.02}_{-0.03}$	0.0082	-10.51	43.06	2.48	1.18	357	

Cluster (1)	Sequence (2)	Instr. (3)	α (4)	δ (5)	R_{ext} (6)	N_H (7)	T_X (8)	Z (9)	z (10)	f_X (11)	L_{bol} (12)	l_{vir} (13)	χ^2_r (14)	d.o.f (15)	Flags (16)
	87002000	G2G3S0S1	198.8446	-16.3805	13.88	4.92	$1.05^{+0.02}_{-0.01}$	$0.29^{+0.02}_{-0.03}$	0.0082	-10.48	43.10	1.92	1.49	672	
	87002010	G2G3S0S1	198.8568	-16.3863	12.16	4.93	$1.02^{+0.02}_{-0.01}$	$0.22^{+0.02}_{-0.01}$	0.0082	-10.51	43.07	2.17	1.81	660	
	87002020	G2G3S0S1	198.8606	-16.4030	12.65	4.94	$1.10^{+0.01}_{-0.02}$	$0.33^{+0.03}_{-0.03}$	0.0082	-10.52	43.06	2.07	1.61	670	
	87002030	G2G3S0S1	198.8391	-16.3873	11.17	4.93	$1.02^{+0.02}_{-0.01}$	$0.23^{+0.02}_{-0.01}$	0.0082	-10.52	43.06	2.40	1.49	664	
	Combined	G2G3S0S1	198.8403	-16.3864	...	4.93	$1.01^{+0.01}_{-0.01}$	$0.27^{+0.01}_{-0.01}$	0.0082	-10.49	43.08	2.20	2.65	1286	
NGC 5129	84048000	G2G3S0S1	201.0267	13.9737	9.21	1.76	$0.94^{+0.07}_{-0.07}$	$0.16^{+0.07}_{-0.04}$	0.0240	-11.73	42.82	1.20	1.01	212	
	87058000	G2G3S0S1	201.0355	13.9692	8.96	1.76	$0.84^{+0.03}_{-0.03}$	$0.12^{+0.02}_{-0.02}$	0.0240	-11.75	42.80	1.20	1.32	407	
	Combined	G2G3S0S1	201.0339	13.9729	...	1.76	$0.84^{+0.03}_{-0.03}$	$0.12^{+0.02}_{-0.02}$	0.0240	-11.73	42.82	1.20	1.29	473	
NGC 5813	65019000	G2G3S0S1	225.2921	1.7046	7.00	4.21	$0.73^{+0.02}_{-0.02}$	$0.25^{+0.04}_{-0.03}$	0.0064	-11.16	42.16	3.27	1.42	304	
NGC 5846	61012000	G2G3S0S1	226.6301	1.6154	8.47	4.26	$0.73^{+0.02}_{-0.02}$	$0.21^{+0.02}_{-0.03}$	0.0061	-11.25	42.04	2.36	1.24	431	
NGC 6109	75000000	G2G3S0S1	244.4169	34.9800	11.42	1.41	$2.87^{+0.14}_{-0.13}$	$0.27^{+0.10}_{-0.09}$	0.0301	-11.41	43.54	1.18	1.08	784	
NGC 6173	85069000	G2G3S0S1	247.4304	40.8361	6.00	0.95	$1.00^{+0.07}_{-0.06}$	$0.18^{+0.06}_{-0.05}$	0.0310	-11.85	42.94	1.51	1.24	261	
NGC 6329	84047000	G2G3S0S1	258.5473	43.6973	6.26	2.11	$1.45^{+0.14}_{-0.12}$	$0.33^{+0.16}_{-0.11}$	0.0274	-11.88	42.83	1.33	1.19	268	
OPHIUCHUS	80027000	G2G3S0S1	258.1061	-23.3654	16.57	20.20	$11.79^{+0.31}_{-0.30}$	$0.35^{+0.04}_{-0.03}$	0.0280	-9.79	45.58	1.56	1.07	2057	
PAVO I	81020000	G2G3S0S1	304.6083	-70.8623	6.75	5.17	$0.90^{+0.07}_{-0.07}$	$0.18^{+0.08}_{-0.05}$	0.0126	-11.80	42.14	1.57	1.17	209	
PCC N34−173	85034000	G2G3S0S1	268.9694	62.6124	6.26	3.38	$1.98^{+0.17}_{-0.19}$	$0.52^{+0.25}_{-0.21}$	0.0267	-11.89	42.85	1.35	1.09	260	
PCC N34−175	86071000	G2G3S0S1	258.8331	57.4083	8.96	2.55	$2.31^{+0.07}_{-0.08}$	$0.42^{+0.09}_{-0.08}$	0.0283	-11.04	43.79	1.39	1.28	644	
PCC S34−111	84050000	G2G3S0S1	16.8824	32.4075	8.47	5.40	$2.27^{+0.16}_{-0.13}$	$0.37^{+0.19}_{-0.12}$	0.0173	-11.49	42.90	1.43	1.08	319	
PCC S49−132	84051000	G2G3S0S1	347.6144	7.5803	10.19	4.88	$3.34^{+0.20}_{-0.18}$	$0.25^{+0.12}_{-0.11}$	0.0400	-11.25	43.98	1.20	1.04	482	
PCC S49−140	86070000	G2G3S0S1	29.0995	5.6457	6.26	4.49	$1.90^{+0.17}_{-0.16}$	$0.46^{+0.27}_{-0.19}$	0.0191	-11.91	42.53	1.44	1.00	219	
PCC S49−147	81001000	G2G3S0S1	5.3037	22.3624	8.72	4.09	$1.44^{+0.17}_{-0.13}$	$0.24^{+0.15}_{-0.08}$	0.0191	-11.74	42.65	1.29	1.33	360	
PEGASUS	63017000	G2G3S0S1	350.0816	8.2118	8.47	5.01	$0.92^{+0.03}_{-0.04}$	$0.18^{+0.03}_{-0.03}$	0.0140	-11.65	42.39	1.41	1.22	475	
PKS 0745−19	81016000	G2G3S0S1	116.8800	-19.2934	12.40	42.40	$6.25^{+0.13}_{-0.13}$	$0.35^{+0.02}_{-0.03}$	0.1028	-10.67	45.74	1.06	1.11	1677	
RX J0138.0−2156	86037000	G2G3S0S1	24.5180	-21.9243	6.26	1.18	$6.66^{+0.57}_{-0.67}$	$0.40^{+0.13}_{-0.12}$	*0.3451*	-11.71	45.42	0.97	0.91	367	z
RX J0232.3−4420	83010000	G2G3S0S1	38.0768	-44.3443	7.24	2.49	$7.00^{+0.49}_{-0.45}$	$0.24^{+0.07}_{-0.08}$	0.2386	-11.40	45.55	1.01	1.09	636	
	83010010	G2G3S0S1	38.0709	-44.3443	6.75	2.49	$7.44^{+0.88}_{-0.74}$	$0.23^{+0.12}_{-0.13}$	0.2386	-11.42	45.55	1.03	1.07	319	
	Combined	G2G3S0S1	38.0600	-44.3533	...	2.49	$7.19^{+0.42}_{-0.38}$	$0.22^{+0.07}_{-0.06}$	0.2386	-11.41	45.55	1.02	1.09	824	
RX J0949.8+1708	84008000	G2G3S0S1	147.4697	17.1221	6.26	3.16	$8.44^{+0.88}_{-0.74}$	$0.13^{+0.11}_{-0.10}$	0.3826	-11.73	45.68	0.97	1.09	443	
RX J0952.8+5153	86076000	G2G3S0S1	148.2080	51.8840	6.75	0.89	$4.34^{+0.32}_{-0.29}$	$0.29^{+0.11}_{-0.10}$	0.2140	-11.54	45.20	1.00	1.03	424	
RX J1023.7+0411	80014000	G2G3S0S1	155.9120	4.1896	6.75	3.00	$6.40^{+0.30}_{-0.28}$	$0.31^{+0.05}_{-0.06}$	0.2906	-11.26	45.84	0.98	0.96	834	
RX J1230.7+3440	84052000	G2G3S0S1	187.6862	34.6511	6.00	1.35	$5.71^{+1.54}_{-1.05}$	$0.21^{+0.33}_{-0.21}$	0.3331	-12.00	45.19	0.98	0.87	102	
	84052010	G2G3S0S1	187.6948	34.6715	6.00	1.35	$3.68^{+1.28}_{-0.71}$	$0.97^{+2.07}_{-0.94}$	0.3331	-11.93	45.17	1.04	1.62	30	
	Combined	G2G3S0S1	187.6871	34.6651	...	1.35	$5.62^{+0.53}_{-0.91}$	$0.24^{+0.30}_{-0.21}$	0.3331	-12.00	45.19	1.00	1.04	135	
RX J1314.5−2517	84037000	G2G3S0S1	198.6158	-25.2568	7.24	7.08	$8.38^{+0.83}_{-0.71}$	$0.25^{+0.10}_{-0.11}$	0.2440	-11.51	45.54	1.02	0.85	599	
	84037010	G2G3S0S1	198.6205	-25.2592	6.51	7.07	$8.98^{+0.90}_{-0.77}$	$0.23^{+0.10}_{-0.11}$	0.2440	-11.52	45.54	1.05	0.97	565	

Cluster (1)	Sequence (2)	Instr. (3)	α (4)	δ (5)	R_{ext} (6)	N_H (7)	T_X (8)	Z (9)	z (10)	f_X (11)	L_{bol} (12)	l_{vir} (13)	χ^2_r (14)	d.o.f (15)	Flags (16)
	Combined	G2G3S0S1	198.6299	-25.2650	...	7.08	$10.49^{+0.78}_{-0.68}$	$0.19^{+0.08}_{-0.07}$	0.2440	-11.53	45.58	1.05	1.12	933	
RX J1320.1+3308	83012000	G2G3S0S1	200.0563	33.1454	7.49	1.05	$1.19^{+0.06}_{-0.06}$	$0.17^{+0.04}_{-0.04}$	0.0362	-11.68	43.27	1.20	1.40	383	
	93007040	G2G3S0S1	200.0552	33.1399	6.00	1.05	$1.36^{+0.16}_{-0.21}$	$0.38^{+0.42}_{-0.22}$	0.0362	-11.86	43.08	1.64	1.11	68	
	93007070	...	200.0683	33.1852	6.00	1.05	...	...	0.0362	...	...	...	...	...	
	93007080	G2G3S0S1	200.0624	33.1266	6.00	1.05	$1.21^{+0.20}_{-0.17}$	$0.49^{+0.96}_{-0.28}$	0.0362	-11.73	43.18	1.84	1.28	49	
	Combined	G2G3S0S1	200.0628	33.1506	...	1.05	$1.22^{+0.06}_{-0.05}$	$0.21^{+0.06}_{-0.04}$	0.0362	-11.73	43.22	1.23	1.32	464	
RX J1347.5−1145	83050000	G2G3S0S1	206.8794	-11.7540	7.00	4.85	$10.88^{+0.73}_{-0.66}$	$0.37^{+0.08}_{-0.08}$	0.4510	-11.34	46.29	0.93	1.08	887	
RX J1354.9+7715	84053000	G2G3S0S1	208.6405	77.2488	6.00	2.88	$5.87^{+1.39}_{-1.00}$	$0.32^{+0.26}_{-0.24}$	0.3967	-11.97	45.38	1.00	1.04	139	
RX J1532.9+3021	86067000	G2G3S0S1	233.2238	30.3523	6.26	2.16	$5.44^{+0.33}_{-0.30}$	$0.34^{+0.07}_{-0.08}$	0.3615	-11.49	45.76	0.92	0.98	621	
RX J1716.6+6708	84059000	G2G3S0S1	259.2150	67.1541	6.00	3.68	$9.84^{+5.76}_{-3.22}$	$0.06^{+0.54}_{-0.06}$	0.8090	-13.00	45.08	1.03	0.94	63	
	84059010	G2G3S0S1	259.2601	67.1534	6.00	3.69	$12.61^{+\infty}_{-7.68}$	$0.03^{+1.70}_{-0.03}$	0.8090	-12.75	45.39	1.03	1.31	82	
	Combined	G2G3S0S1	259.2279	67.1402	...	3.69	$10.19^{+5.35}_{-3.01}$	$0.39^{+0.53}_{-0.39}$	0.8090	-12.99	45.10	1.07	1.06	95	
RX J1720.0+2638	86062000	G2G3S0S1	260.0429	26.6269	9.70	4.06	$5.45^{+0.29}_{-0.27}$	$0.26^{+0.07}_{-0.06}$	0.1610	-11.03	45.52	1.00	0.93	729	
RX J1736.4+6804	86054000	G2G3S0S1	264.0962	68.1336	7.73	4.37	$1.76^{+0.35}_{-0.32}$	$0.50^{+0.61}_{-0.29}$	0.0258	-12.07	42.61	1.21	1.13	221	
RX J2129.6+0005	85029000	G2G3S0S1	322.4196	0.0925	7.00	4.28	$6.10^{+0.36}_{-0.34}$	$0.40^{+0.08}_{-0.08}$	0.2350	-11.35	45.57	1.01	0.93	722	
SC 1327−312	83059000	G2G3S0S1	202.4404	-31.6068	8.96	3.89	$3.48^{+0.11}_{-0.11}$	$0.34^{+0.07}_{-0.06}$	0.0508	-11.06	44.38	1.23	1.05	723	
SC 1329−313	84043000	G2G3S0S1	202.8599	-31.8175	8.72	3.93	$3.79^{+0.22}_{-0.20}$	$0.39^{+0.13}_{-0.11}$	0.0429	-11.33	43.99	1.24	0.97	581	
TRI AUST	83060000	G2G3S0S1	249.5716	-64.3569	15.34	13.00	$10.26^{+0.37}_{-0.34}$	$0.26^{+0.05}_{-0.04}$	0.0510	-10.23	45.57	1.23	1.01	1505	
	83060010	G2G3S0S1	249.5981	-64.3649	16.08	13.00	$10.01^{+0.47}_{-0.44}$	$0.29^{+0.06}_{-0.07}$	0.0510	-10.25	45.55	1.20	0.99	1243	
	Combined	G2G3S0S1	249.5922	-64.3634	...	13.00	$10.19^{+0.29}_{-0.28}$	$0.26^{+0.03}_{-0.04}$	0.0510	-10.24	45.56	1.22	1.02	1775	
WBL 184	74036000	G2G3S0S1	128.7319	55.5726	6.02	4.14	$3.87^{+0.25}_{-0.22}$	$0.10^{+0.08}_{-0.08}$	0.0512	-11.66	43.81	1.29	1.14	489	
WBL 224	66000000	G2G3S0S1	141.9950	29.9872	6.00	2.11	$1.43^{+0.28}_{-0.23}$	$0.16^{+0.19}_{-0.09}$	0.0266	-12.30	42.40	1.43	1.09	251	
WBL 225	83011000	G2G3S0S1	143.3515	34.0347	6.00	1.51	$0.74^{+0.06}_{-0.06}$	$0.20^{+0.10}_{-0.06}$	0.0269	-12.12	42.50	1.90	0.99	192	
ZWCL 0024.0+1652	84046000	G2G3S0S1	6.6595	17.1648	6.00	4.23	$5.17^{+1.95}_{-1.34}$	$0.42^{+0.52}_{-0.41}$	0.3949	-12.49	44.82	1.03	1.16	173	
ZWCL 0847.2+3617	86063000	G2G3S0S1	132.5355	36.0706	6.00	3.16	$9.21^{+1.50}_{-1.20}$	$0.35^{+0.17}_{-0.16}$	0.3737	-11.85	45.57	1.01	0.93	291	
ZWCL 1718.1−0108	74037000	G2G3	260.1939	-1.1315	15.59	10.10	$3.58^{+0.14}_{-0.12}$	$0.45^{+0.10}_{-0.08}$	0.0280	-10.97	43.98	1.17	1.17	636	

A.3 Additional Sources Detected

Table A.3 lists serendipitous sources that were detected in each ASCA observation along with its identification, if known. These sources were masked out during the extraction of spectra. Note that the sources identified as clusters or groups are also in Table A.1, usually as being too far off–axis or too close to a bright source.

Table A.3: Additional Sources

Sequence	R.A.	DEC.	Name	ID
60032000	190.8418	2.9178	...	...
61012000	226.8001	1.7789	...	...
62009000	21.2606	1.7714	PMN J0125+0146	QSO
	21.4536	2.0670	...	...
62009010	21.2796	1.7774	PMN J0125+0146	QSO
	21.4726	2.0730	...	...
63000000	174.6257	21.9839	...	...
63008000	125.1786	20.9545	...	...
63017000	349.8914	8.2992	...	...
	350.1796	8.2190	NGC 7626	Galaxy
64008000	190.8397	2.9215	...	...
66000000	141.8994	30.1694	...	...
72042000	349.6115	-42.3664	NGC 7582	Galaxy
73062000	8.3692	-21.6548	...	...
74003000	100.5373	67.9790	Q 0636+680	QSO
	101.4238	67.9257	...	...
74037000	260.1173	-0.9817	3C 353	Galaxy
74044000	218.1674	-44.1616	...	...
74085000	184.6621	5.7659	...	...
	184.9557	5.7556	RX J1219.8+0545	QSO
80010000	40.0126	-1.8383	...	...
	40.2262	-1.6265	4C -02.14	QSO
80035000	128.2883	65.8467	...	...
80038000	54.7257	-35.5906	NGC 1404	Galaxy
80039000	54.7274	-35.5899	NGC 1404	Galaxy
81002000	230.8076	8.5487	...	...
	230.8803	8.8465	...	...
81004000	239.6285	27.2846	...	...
81010000	202.9127	-1.8597	...	...
81013000	199.9396	70.0315	...	...
81023000	227.8954	5.7607	...	...
81032000	209.8847	62.3211	...	...
	210.1492	62.3681	...	...
81033000	335.7491	-1.7463	...	...
	335.8154	-1.6505	...	...
82005000	222.5433	58.2343	...	...
	223.2824	58.1613	...	...
82006000	154.2729	59.4089	SBS 1013+596	QSO
	154.4737	59.4294	...	...
82011000	130.7851	29.7308	...	...
82026000	70.8325	2.3291	...	...
	70.9229	2.2611	...	...
	71.0650	2.2786	...	...
82028000	170.3980	24.0810	...	...
	170.4690	24.1459	...	...
82031000	63.9658	-11.3322	...	...
82033000	96.7093	-54.5382	...	...
	96.9234	-54.4341	...	...
82034000	13.7885	26.4555	...	...
82037000	249.9094	46.8233	...	...
82043000	186.6699	19.8614	...	...
82049000	358.8526	-10.4367	...	...
82052000	210.3588	2.9360	...	...
82052010	210.3601	2.9355	...	...
83000000	219.4718	3.4450	...	...
	219.6685	3.4227	...	...
83002000	354.4974	27.1785	ABELL 2634:[SM98] 02	GClstr
83004000	357.1955	-28.2048	...	...
	357.2224	-28.1279	...	...
83006000	145.5607	8.9972	...	...
83007000	171.0981	21.5180	...	...
83008000	181.9701	28.0565	...	...
83009000	233.1179	4.8990	Q 1529+050	QSO
	233.4233	4.8707	...	...
83010010	38.0888	-44.0020	...	...
83011000	143.4379	34.2266	...	...

Sequence	R.A.	DEC.	Name	ID
83012000	199.9205	33.1148	...	...
	199.9756	33.3129	...	...
83014000	189.4115	62.9857	...	...
83017000	75.3099	-24.3825	...	...
	75.3560	-24.2858	...	...
83018000	340.0842	-4.4909	...	...
83019010	344.6531	-34.9541	...	...
83024000	159.3182	-27.3333	...	...
83024010	159.3117	-27.3299	...	...
83025000	150.2251	-19.5199	...	...
	150.2780	-19.4395	...	...
	150.4485	-19.5986	...	...
83030000	241.2829	17.7310	NGC 6047	Galaxy
83034000	137.3453	10.8824	...	...
83035000	115.4762	74.4375	...	...
	115.7887	74.4927	MS 0737.0+7436	Galaxy
	116.0096	74.5625	MS 0737.9+7441	QSO
83037000	44.3415	5.7607	...	...
83040010	227.9110	5.7530	...	...
83041000	136.5868	16.9905	...	...
	136.6422	16.7673	3C 215	QSO
83047000	349.3261	18.7201	HCG 094	GGroup
83058000	202.4457	-31.6103	SC 1327-312	GClstr
83059000	202.0454	-31.5220	...	...
83061000	202.0388	-27.3205	...	...
83065000	164.0909	-3.5950	...	...
	164.1166	-3.8256	...	...
	164.3386	-3.8542	MS 1054.8-0335	Galaxy
83066000	228.6620	36.8263	...	...
	228.8441	36.6489	...	...
83070000	24.3925	-12.9898	ABELL 0222	GClstr
83072000	241.2206	24.0394	...	...
83074000	240.8852	15.9115	...	...
83075000	209.8885	62.3206	...	...
	210.1530	62.3676	...	...
	210.2832	62.6810	...	...
84003000	10.5567	-28.2948	...	...
	10.7971	-28.5131	...	...
84006000	356.8503	-2.1743	...	...
84012000	257.8776	64.2762	...	...
84012010	257.8737	64.2772	...	...
84013000	348.2569	-21.5779	...	...
84014000	346.9677	-22.5339	...	...
	347.1834	-22.3372	...	...
84015000	347.1820	-22.3383	...	...
84017010	181.9702	28.0565	...	...
84020000	55.4459	-53.7073	...	...
84022000	227.6633	33.5811	...	...
84026000	195.6914	67.4846	...	...
84028000	46.2715	17.2834	Q 0302+170	QSO
	46.5789	17.3012	CL 0303+1706	GClstr
84031000	130.6349	36.2742	...	...
84034000	87.3203	-25.7930	...	...
84036000	162.6290	-2.7001	...	...
84041000	203.6407	-31.5929	...	...
84043000	202.4928	-31.6122	...	...
84047000	258.7429	43.6185	...	...
	258.9841	43.6808	...	...
84048000	200.9876	14.0988	...	...
84052000	187.6425	34.5237	...	...
84052010	187.6309	34.5350	...	...
84057000	193.5990	-29.0161	...	...
	193.6652	-29.2209	...	...
84059000	258.6213	67.1830	...	...
	258.7935	67.1356	...	...
	259.5203	67.4733	...	...
84059010	258.6194	67.1806	...	...
	258.7916	67.1332	...	...
	259.5184	67.4709	...	...
84061000	123.8509	62.7829	...	...
84071000	73.3053	-10.4123	...	...
	73.4651	-10.4243	...	...
84072000	235.0959	-3.2313	...	...
	235.1746	-3.2672	...	...
84073000	71.8822	-20.3470	...	...
84074000	206.9179	-37.8414	...	...
85008000	9.0881	-28.6625	...	...
85010000	157.1309	-35.5224	...	...
	157.2306	-35.6088	NGC 3258	GGroup
85028000	357.6372	-26.3414	...	...
85031000	208.5924	40.2070	[KB98] J1354+402	QSO
85033000	128.2460	65.8551	...	...

Sequence	R.A.	DEC.	Name	ID
85034000	268.9708	62.1874	...	...
85035000	192.8374	-15.5824	...	...
	193.1234	-15.5255	IC 0829	Galaxy
85042000	196.0263	33.5944	...	...
85046000	174.9885	65.7943	3C 263	QSO
85046010	174.9795	65.7965	3C 263	QSO
85047000	347.0647	-1.9275	...	...
	347.1639	-1.9283	...	...
	347.2085	-2.1863	...	...
85048000	28.3166	1.0341	RX J0153.2+0102	GClstr
85052000	313.9681	-4.8518	MS 2053.2-0503	Galaxy
	314.1994	-4.8269	...	...
85056000	205.6343	26.2637	...	...
85062000	15.5566	-22.0429	...	...
	15.7096	-22.1608	...	...
85063000	41.4056	36.9734	...	...
	41.5659	37.1392	...	...
	41.8838	36.8365	...	...
85065000	235.3646	34.1926	...	...
85068000	246.8858	40.8110	...	...
	247.4116	40.8311	...	...
85069000	247.6290	41.0311	...	...
	247.7923	40.8032	KUV 16295+4054	QSO
86010000	359.7575	-60.9116	...	...
86010010	359.7505	-60.9137	...	...
86014000	193.9008	-30.3517	ABELL 3530	GClstr
86015000	194.3248	-30.3664	ABELL 3532	GClstr
86017000	73.6537	-18.3571	...	...
86043000	348.4151	-22.1694	...	...
86048000	216.5087	16.8374	...	...
	216.8729	16.8817	...	...
86053000	245.8352	41.2916	KUV 16217+4124	QSO
	245.9292	41.1057	...	...
	246.4444	41.2953	...	...
86062000	259.9833	26.4945	...	...
86067000	233.0093	30.2846	...	...
	233.5514	30.5827	...	...
86071000	258.8386	57.6550	...	...
86073000	255.2676	34.0601	...	...
	255.7140	33.7430	...	...
87043000	107.1800	-49.5428	...	...
87051000	233.7181	1.5032	Q 1532+016	QSO
	233.8924	1.3034	...	...
87054000	125.9017	3.6559	...	...
	126.0249	3.6491	...	...
87055000	46.0425	17.3311	...	...
	46.2863	17.2856	Q 0302+170	QSO
	46.4072	17.1708	MS 0302.7+1658	GClstr
	46.5937	17.3034	CL 0303+1706	GClstr
87055010	46.0269	17.3264	...	...
	46.2707	17.2809	Q 0302+170	QSO
	46.3916	17.1661	MS 0302.7+1658	GClstr
	46.5781	17.2987	CL 0303+1706	GClstr
93007040	199.9226	33.1137	...	...
	199.9777	33.3118	...	...
93007070	199.9189	33.1155	...	...
	199.9740	33.3136	...	...
93007080	199.9184	33.1157	...	...
	199.9735	33.3138	...	...

A.4 Cooling Flow and Density Profile Data for Clusters

Table A.4 contains data from the literature used in Chapter 5 and Chapter 6. The columns in Table A.4 are as follows:

1. The cluster name from Table A.2.
2. The central cooling time, in units of 10^9 years.
3. The mass deposition rate, in units of $M_\odot$ yr^{-1}.
4. The reference from which the cooling time and mass deposition rate were taken. AF98 refers to Allen & Fabian (1998a). P98 refers to Peres et al. (1998).
5. The central density for a β-model fit to the surface brightness profile by Mohr et al. (1999), in units of 10^{-26} $h_{50}^{1/2}$ g cm^{-3}.
6. The outer slope parameter (β) for the fit.
7. The core radius of the fit, in units of h_{50}^{-1} Mpc.
8. The core radius of the inner component when a double-β model was used, in units of h_{50}^{-1} Mpc.

Table A.4: Cooling Flow and Density Profile Data from the Literature

Cluster (1)	$t_{\rm cool}$ (2)	$\dot{M}$ (3)	Ref (4)	ρ_0 (5)	β (6)	R_1 (7)	R_2 (8)
2A 0335+096	$0.90^{+0.00}_{-0.00}$	325^{+32}_{-43}	P98	...	...	...	...
ABELL 0085	$2.40^{+0.10}_{-0.10}$	198^{+53}_{-52}	P98	$5.10^{+0.32}_{-0.44}$	$0.662^{+0.029}_{-0.024}$	$0.317^{+0.054}_{-0.047}$	$0.063^{+0.011}_{-0.009}$
ABELL 0119	$19.20^{+12.20}_{-8.60}$	0^{+2}_{-0}	P98	$0.27^{+0.01}_{-0.01}$	$0.662^{+0.023}_{-0.022}$	$0.483^{+0.028}_{-0.028}$	...
ABELL 0262	$1.50^{+0.10}_{-0.10}$	27^{+4}_{-3}	P98	$7.29^{+0.55}_{-0.38}$	$0.556^{+0.027}_{-0.025}$	$0.135^{+0.035}_{-0.034}$	$0.014^{+0.004}_{-0.004}$
ABELL 0399	$15.20^{+8.40}_{-5.00}$	0^{+51}_{-0}	P98	...	...	...	...
ABELL 0401	$10.60^{+4.00}_{-1.80}$	42^{+82}_{-42}	P98	$1.14^{+0.08}_{-0.05}$	$0.606^{+0.015}_{-0.016}$	$0.237^{+0.016}_{-0.019}$	...
ABELL 0478	$1.10^{+0.10}_{-0.10}$	810^{+176}_{-195}	AF98	$7.42^{+0.64}_{-0.30}$	$0.713^{+0.030}_{-0.033}$	$0.269^{+0.045}_{-0.045}$	$0.072^{+0.011}_{-0.011}$
ABELL 0496	$1.80^{+0.10}_{-0.10}$	95^{+13}_{-12}	P98	$8.15^{+0.64}_{-0.26}$	$0.650^{+0.021}_{-0.019}$	$0.219^{+0.017}_{-0.019}$	$0.033^{+0.003}_{-0.003}$
ABELL 0520	$16.70^{+24.00}_{-6.20}$	0^{+85}_{-0}	AF98	...	...	...	...
ABELL 0576	$2.80^{+2.40}_{-0.90}$	3^{+13}_{-3}	P98	...	...	...	...
ABELL 0586	$5.50^{+0.70}_{-0.70}$	159^{+69}_{-56}	AF98	...	...	...	...
ABELL 0644	$6.80^{+0.40}_{-0.40}$	189^{+106}_{-35}	P98	$1.79^{+0.08}_{-0.08}$	$0.660^{+0.048}_{-0.048}$	$0.176^{+0.035}_{-0.034}$	...
ABELL 0665	$12.30^{+0.90}_{-0.90}$	0^{+232}_{-0}	AF98	...	...	...	...
ABELL 0754	$7.90^{+9.70}_{-2.10}$	2^{+5}_{-2}	P98	$0.57^{+0.01}_{-0.02}$	$0.614^{+0.361}_{-0.360}$	$0.367^{+0.324}_{-0.309}$	...
ABELL 0773	$9.80^{+13.70}_{-6.60}$	0^{+238}_{-0}	AF98	...	...	...	...
ABELL 0963	$4.10^{+1.30}_{-0.50}$	340^{+129}_{-183}	AF98	...	...	...	...
ABELL 1060	$3.20^{+1.20}_{-0.80}$	8^{+3}_{-2}	P98	$1.66^{+0.10}_{-0.11}$	$0.703^{+0.044}_{-0.036}$	$0.164^{+0.017}_{-0.015}$	$0.043^{+0.005}_{-0.004}$
ABELL 1068	$1.20^{+0.10}_{-0.10}$	408^{+128}_{-90}	AF98	...	...	...	...
ABELL 1367	$25.80^{+13.10}_{-8.00}$	0^{+1}_{-0}	P98	$0.24^{+0.01}_{-0.00}$	$0.607^{+0.044}_{-0.042}$	$0.360^{+0.046}_{-0.043}$	...
ABELL 1413	$8.60^{+0.60}_{-0.70}$	137^{+43}_{-85}	AF98	...	...	...	...
ABELL 1650	$2.40^{+1.20}_{-0.80}$	280^{+464}_{-89}	P98	...	...	...	...
ABELL 1651	$6.50^{+0.70}_{-0.70}$	138^{+48}_{-41}	P98	$1.71^{+0.08}_{-0.08}$	$0.616^{+0.012}_{-0.013}$	$0.160^{+0.009}_{-0.009}$	...
ABELL 1689	$2.90^{+0.50}_{-0.20}$	563^{+185}_{-174}	AF98	$4.22^{+0.45}_{-0.47}$	$0.648^{+0.035}_{-0.024}$	$0.131^{+0.022}_{-0.014}$	...
ABELL 1704	$2.10^{+0.10}_{-0.20}$	306^{+92}_{-73}	AF98	...	...	...	...
ABELL 1736	$7.90^{+15.30}_{-4.60}$	1^{+4}_{-1}	P98	...	...	...	...
ABELL 1795	$1.40^{+0.10}_{-0.10}$	449^{+46}_{-46}	AF98	$5.83^{+0.89}_{-0.29}$	$0.790^{+0.031}_{-0.032}$	$0.344^{+0.024}_{-0.035}$	$0.083^{+0.005}_{-0.009}$
ABELL 1835	$1.50^{+0.50}_{-0.30}$	1154^{+432}_{-482}	AF98	...	...	...	...
ABELL 2029	$1.50^{+0.10}_{-0.10}$	576^{+99}_{-79}	AF98	$7.14^{+1.14}_{-0.36}$	$0.705^{+0.030}_{-0.028}$	$0.334^{+0.022}_{-0.036}$	$0.079^{+0.004}_{-0.009}$
ABELL 2052	$1.30^{+0.30}_{-0.20}$	102^{+108}_{-15}	P98	$6.67^{+1.31}_{-0.55}$	$0.712^{+0.081}_{-0.069}$	$0.203^{+0.045}_{-0.042}$	$0.039^{+0.009}_{-0.009}$
ABELL 2063	$5.00^{+0.40}_{-0.30}$	37^{+7}_{-12}	P98	$2.25^{+0.46}_{-0.17}$	$0.706^{+0.051}_{-0.047}$	$0.255^{+0.045}_{-0.044}$	$0.059^{+0.012}_{-0.020}$
ABELL 2065	$4.40^{+2.20}_{-1.30}$	13^{+14}_{-6}	P98	...	...	...	...
ABELL 2142	$4.30^{+0.80}_{-0.70}$	303^{+167}_{-72}	AF98	$3.08^{+0.34}_{-0.46}$	$0.787^{+0.082}_{-0.093}$	$0.635^{+0.213}_{-0.198}$	$0.164^{+0.054}_{-0.051}$
ABELL 2163	$12.70^{+12.30}_{-4.60}$	0^{+90}_{-0}	AF98	...	...	...	...
ABELL 2199	$1.90^{+0.00}_{-0.10}$	154^{+18}_{-8}	P98	$5.68^{+0.36}_{-0.30}$	$0.663^{+0.012}_{-0.008}$	$0.162^{+0.010}_{-0.008}$	$0.041^{+0.002}_{-0.002}$
ABELL 2204	$0.94^{+0.04}_{-0.04}$	1007^{+98}_{-263}	AF98	$22.70^{+3.40}_{-2.60}$	$0.585^{+0.061}_{-0.045}$	$0.260^{+0.106}_{-0.098}$	$0.035^{+0.015}_{-0.012}$
ABELL 2218	$10.40^{+4.10}_{-2.00}$	0^{+133}_{-0}	AF98	...	...	...	...
ABELL 2219	$9.00^{+18.80}_{-3.80}$	0^{+485}_{-0}	AF98	...	...	...	...
ABELL 2244	$7.30^{+0.60}_{-0.50}$	244^{+49}_{-145}	P98	$2.58^{+0.37}_{-0.57}$	$0.594^{+0.061}_{-0.045}$	$0.117^{+0.047}_{-0.031}$	...
ABELL 2255	$36.90^{+21.00}_{-9.50}$	0^{+4}_{-0}	P98	$0.34^{+0.01}_{-0.02}$	$0.792^{+0.050}_{-0.043}$	$0.584^{+0.046}_{-0.039}$	...
ABELL 2256	$10.80^{+20.50}_{-9.10}$	0^{+16}_{-0}	P98	$0.59^{+0.01}_{-0.01}$	$0.828^{+0.062}_{-0.061}$	$0.486^{+0.042}_{-0.041}$	...
ABELL 2261	$3.00^{+1.40}_{-0.60}$	227^{+238}_{-87}	AF98	...	...	...	...
ABELL 2319	$9.50^{+10.40}_{-3.20}$	0^{+81}_{-47}	AF98	$1.21^{+0.05}_{-0.07}$	$0.536^{+0.061}_{-0.060}$	$0.213^{+0.070}_{-0.069}$	...
ABELL 2390	$4.20^{+0.30}_{-0.20}$	370^{+97}_{-69}	AF98	...	...	...	...
ABELL 2597	$2.30^{+0.10}_{-0.10}$	271^{+41}_{-41}	P98	$10.10^{+1.40}_{-1.50}$	$0.612^{+0.023}_{-0.021}$	$0.044^{+0.007}_{-0.006}$	...
ABELL 2744	$18.80^{+42.00}_{-6.40}$	0^{+101}_{-0}	AF98	...	...	...	...
ABELL 3112	$0.70^{+0.10}_{-0.10}$	415^{+252}_{-174}	P98	$7.04^{+0.89}_{-0.58}$	$0.562^{+0.040}_{-0.040}$	$0.049^{+0.022}_{-0.021}$	...
ABELL 3158	$12.00^{+4.20}_{-2.50}$	25^{+74}_{-25}	P98	$0.81^{+0.05}_{-0.05}$	$0.657^{+0.041}_{-0.036}$	$0.262^{+0.034}_{-0.031}$	...
ABELL 3266	$5.20^{+8.40}_{-1.50}$	3^{+35}_{-3}	P98	$0.46^{+0.02}_{-0.01}$	$0.744^{+0.039}_{-0.037}$	$0.495^{+0.040}_{-0.038}$	...

Cluster (1)	$t_{\rm cool}$ (2)	$\dot{M}$ (3)	Ref (4)	ρ_0 (5)	β (6)	R_1 (7)	R_2 (8)
ABELL 3391	$16.70\ ^{+5.60}_{-3.50}$	$0\ ^{+5}_{-0}$	P98	$0.53^{+0.06}_{-0.05}$	$0.541^{+0.048}_{-0.044}$	$0.216^{+0.045}_{-0.038}$	...
ABELL 3532	$14.00\ ^{+3.30}_{-2.30}$	$0\ ^{+25}_{-0}$	P98	$0.49^{+0.06}_{-0.06}$	$0.589^{+0.086}_{-0.062}$	$0.246^{+0.073}_{-0.057}$	...
ABELL 3558	$10.20\ ^{+0.30}_{-0.20}$	$40\ ^{+39}_{-10}$	P98	$0.96^{+0.04}_{-0.02}$	$0.548^{+0.029}_{-0.029}$	$0.194^{+0.028}_{-0.027}$	...
ABELL 3562	$7.20\ ^{+0.60}_{-0.50}$	$37\ ^{+26}_{-27}$	P98	$1.15^{+0.08}_{-0.05}$	$0.470^{+0.007}_{-0.007}$	$0.097^{+0.006}_{-0.007}$	...
ABELL 3571	$5.80\ ^{+0.90}_{-1.00}$	$72\ ^{+56}_{-31}$	P98	$1.54^{+0.05}_{-0.06}$	$0.610^{+0.024}_{-0.024}$	$0.173^{+0.016}_{-0.015}$	...
ABELL 3667	$13.40\ ^{+6.40}_{-3.40}$	$0\ ^{+11}_{-0}$	P98	$0.71^{+0.02}_{-0.03}$	$0.541^{+0.016}_{-0.016}$	$0.258^{+0.026}_{-0.025}$	...
ABELL 4038	$2.30\ ^{+0.60}_{-0.30}$	$87\ ^{+25}_{-19}$	P98	$2.78^{+0.23}_{-0.16}$	$0.537^{+0.033}_{-0.033}$	$0.056^{+0.012}_{-0.011}$	...
ABELL 4059	$3.40\ ^{+0.60}_{-0.40}$	$130\ ^{+27}_{-21}$	P98	$2.31^{+0.18}_{-0.13}$	$0.558^{+0.019}_{-0.020}$	$0.078^{+0.011}_{-0.011}$	...
ABELL S1077	$16.90\ ^{+32.70}_{-6.20}$	$0\ ^{+120}_{-0}$	AF98	...	...	...	...
AWM 07	$1.90\ ^{+0.20}_{-0.20}$	$41\ ^{+6}_{-6}$	P98	$3.54^{+0.12}_{-0.21}$	$0.678^{+0.030}_{-0.029}$	$0.195^{+0.013}_{-0.011}$	$0.032^{+0.005}_{-0.002}$
CENTAURUS	$0.80\ ^{+0.00}_{-0.00}$	$30\ ^{+10}_{-5}$	P98	$13.30^{+1.50}_{-0.80}$	$0.569^{+0.035}_{-0.036}$	$0.138^{+0.045}_{-0.040}$	$0.012^{+0.005}_{-0.004}$
CL 09104+4109	$2.00\ ^{+0.10}_{-0.10}$	$620\ ^{+147}_{-87}$	AF98	...	...	...	...
CYGNUS A	$2.60\ ^{+0.10}_{-0.10}$	$244\ ^{+26}_{-22}$	P98	$25.20^{+7.10}_{-3.40}$	$0.472^{+0.057}_{-0.057}$	$0.015^{+0.049}_{-0.015}$	...
HYDRA A	$2.00\ ^{+0.00}_{-0.00}$	$264\ ^{+81}_{-60}$	P98	$9.30^{+1.32}_{-0.40}$	$0.766^{+0.021}_{-0.025}$	$0.237^{+0.013}_{-0.024}$	$0.047^{+0.002}_{-0.008}$
MKW 03S	...	...	...	$3.65^{+0.27}_{-0.20}$	$0.562^{+0.038}_{-0.038}$	$0.056^{+0.015}_{-0.015}$	...
MS 1358.4+6245	$2.80\ ^{+1.20}_{-0.60}$	$123\ ^{+369}_{-50}$	AF98	...	...	...	...
MS 1455.0+2232	$1.10\ ^{+0.20}_{-0.10}$	$712\ ^{+185}_{-53}$	AF98	...	...	...	...
MS 2137.3−2353	$1.20\ ^{+0.10}_{-0.10}$	$754\ ^{+263}_{-117}$	AF98	...	...	...	...
OPHIUCHUS	$3.00\ ^{+0.40}_{-0.30}$	$127\ ^{+48}_{-94}$	P98	$3.08^{+0.48}_{-0.27}$	$0.705^{+0.036}_{-0.032}$	$0.266^{+0.028}_{-0.026}$	$0.079^{+0.008}_{-0.025}$
PKS 0745−19	$1.10\ ^{+0.10}_{-0.10}$	$650\ ^{+120}_{-148}$	AF98	$13.30^{+0.90}_{-1.10}$	$0.586^{+0.008}_{-0.009}$	$0.056^{+0.006}_{-0.006}$	...
RX J1023.7+0411	$1.70\ ^{+0.10}_{-0.10}$	$1057\ ^{+117}_{-146}$	AF98	...	...	...	...
RX J1347.5−1145	$2.60\ ^{+0.20}_{-0.10}$	$1378\ ^{+75}_{-316}$	AF98	...	...	...	...
TRI AUST	$10.80\ ^{+7.10}_{-3.10}$	$33\ ^{+87}_{-33}$	P98	$1.28^{+0.24}_{-0.12}$	$0.816^{+0.062}_{-0.060}$	$0.621^{+0.076}_{-0.088}$	$0.212^{+0.025}_{-0.038}$

A.5 Mass Data for Clusters

Table A.5 contains data from the literature used in Chapter 7 for the M–T relationship. The columns in Table A.5 are as follows:

1. The cluster name from Table A.2.
2. The optical virial radius from Girardi et al. (1998a), in units of h_{50}^{-1} Mpc.
3. The virial mass from Girardi et al. (1998a), in units of $10^{14} h_{50}^{-1} M_{\odot}$.
4. The number of galaxy redshifts used to derive the virial mass.
5. The β parameter from a fit to the x-ray cluster surface brightness profile by Fukazawa (1997).
6. The core radius from a fit to the cluster x-ray surface brightness profile by Fukazawa (1997), in units of h_{50}^{-1} Mpc.
7. Radius for temperature resolved mass estimates, in units of h_{50}^{-1} Mpc.
8. Mass within the given radius, in units of $10^{14} h_{50}^{-1} M_{\odot}$.
9. Reference for x-ray mass and radius.

Table A.5: Mass Data from the Literature

Cluster (1)	$R_{\rm vir}$ (2)	$M_{\rm vir}$ (3)	n_z (4)	β (5)	r_c (6)	M_x (7)	R_x (8)	Reference (9)
2A 0335+096	...	...	...	0.60	0.046	1.0	2.2	Ohashi (1997)
ABELL 0085	3.88	$19.76\ ^{+4.50}_{-3.36}$	124	0.60	0.173	...	...	
ABELL 0119	2.72	$5.00\ ^{+1.80}_{-1.48}$	62	0.60	0.462	...	...	
ABELL 0194	1.36	$1.20\ ^{+0.44}_{-0.30}$	29	0.45	0.138	...	...	
ABELL 0262	2.10	$2.64\ ^{+0.60}_{-0.50}$	40	0.50	0.063	...	...	
ABELL 0399	4.46	$26.90\ ^{+5.48}_{-5.26}$	79	...	...	...	...	
ABELL 0400	2.40	$4.98\ ^{+1.46}_{-1.24}$	57	0.45	0.102	...	...	
ABELL 0401	4.60	$27.38\ ^{+5.52}_{-5.00}$	106	...	...	...	...	
ABELL 0478	...	...	...	0.70	0.154	...	...	
ABELL 0496	2.74	$6.40\ ^{+2.08}_{-1.90}$	55	0.55	0.070	1.0	3.0	Mushotzky (1984)
ABELL 0514	3.52	$16.10\ ^{+3.26}_{-2.60}$	80	...	...	...	...	
ABELL 0539	2.52	$4.02\ ^{+1.04}_{-0.84}$	70	0.60	0.164	...	...	
ABELL 0548E	2.28	$4.52\ ^{+1.24}_{-1.10}$	62	...	...	...	...	
ABELL 0576	3.66	$19.04\ ^{+3.14}_{-2.82}$	199	...	...	...	...	
ABELL 0754	2.64	$8.46\ ^{+2.08}_{-1.44}$	62	...	...	...	...	
ABELL 1060	2.44	$3.80\ ^{+0.76}_{-0.66}$	79	0.55	0.080	2.0	3.6	Loewenstein & Mushotzky (1996)
ABELL 1631	2.80	$10.12\ ^{+1.78}_{-1.58}$	58	...	...	...	...	
ABELL 1775	1.92	$4.14\ ^{+2.52}_{-1.86}$	11	...	...	...	...	
ABELL 1795	3.34	$11.72\ ^{+2.66}_{-2.44}$	80	0.65	0.135	2.0	6.0	Mushotzky (1984)
ABELL 2029	4.66	$13.64\ ^{+4.80}_{-4.60}$	73	...	...	1.9	9.4	Sarazin et al. (1998)
ABELL 2063	2.66	$6.08\ ^{+1.18}_{-0.96}$	70	0.60	0.133	...	...	
ABELL 2107	2.48	$5.24\ ^{+1.62}_{-1.54}$	65	...	...	...	...	
ABELL 2142	4.52	$35.68\ ^{+7.98}_{-6.98}$	86	...	...	...	...	
ABELL 2147	...	...	...	0.50	0.218	...	...	
ABELL 2163	...	...	...	...	...	2.0	21.4	Markevitch (1996)
ABELL 2197	2.44	$7.14\ ^{+1.62}_{-1.56}$	36	...	...	...	...	
ABELL 2199	3.20	$11.42\ ^{+3.12}_{-2.42}$	42	0.60	0.080	1.0	2.6	Mushotzky (1984)
ABELL 2256	5.40	$46.24\ ^{+7.90}_{-6.86}$	86	0.75	0.457	3.0	12.0	Markevitch & Vikhlinin (1997)
ABELL 2319	6.18	$79.08\ ^{+11.70}_{-10.24}$	118	0.55	0.271	...	...	
ABELL 2554	3.36	$12.14\ ^{+4.38}_{-2.96}$	27	...	...	...	...	
ABELL 2589	1.88	$1.54\ ^{+1.06}_{-0.90}$	28	...	...	...	...	
ABELL 2634	2.80	$8.62\ ^{+2.70}_{-1.96}$	69	0.50	0.246	...	...	
ABELL 2670	3.40	$11.12\ ^{+1.44}_{-1.16}$	186	...	...	...	...	
ABELL 2798	2.84	$3.78\ ^{+2.28}_{-1.62}$	16	...	...	...	...	
ABELL 3158	3.90	$18.74\ ^{+3.78}_{-3.46}$	123	...	...	...	...	
ABELL 3266	4.42	$23.40\ ^{+3.92}_{-3.30}$	128	...	...	...	...	
ABELL 3376	2.76	$7.28\ ^{+1.56}_{-1.36}$	65	...	...	...	...	
ABELL 3381	1.18	$0.74\ ^{+0.58}_{-0.32}$	13	...	...	...	...	
ABELL 3391	2.66	$7.22\ ^{+4.40}_{-2.70}$	50	...	...	...	...	
ABELL 3528N	1.84	$1.96\ ^{+0.78}_{-0.46}$	24	...	...	...	...	
ABELL 3532	2.96	$6.52\ ^{+2.14}_{-1.72}$	42	...	...	...	...	
ABELL 3556	2.56	$7.00\ ^{+2.30}_{-1.48}$	66	...	...	...	...	
ABELL 3558	3.90	$23.08\ ^{+2.04}_{-1.82}$	338	0.50	0.150	...	...	
ABELL 3562	2.94	$12.06\ ^{+1.68}_{-1.28}$	89	...	...	...	...	
ABELL 3571	4.18	$16.34\ ^{+4.80}_{-4.38}$	69	0.60	0.171	...	...	
ABELL 3667	3.88	$23.50\ ^{+3.20}_{-2.52}$	152	...	...	...	...	
ABELL 3921	1.96	$4.04\ ^{+2.14}_{-1.32}$	24	...	...	...	...	
ABELL 4059	...	...	...	0.65	0.150	1.0	3.0	Ohashi (1997)
ABELL 4067	2.00	$2.12\ ^{+1.06}_{-0.66}$	22	...	...	...	...	
ABELL S0753	2.14	$2.62\ ^{+1.34}_{-1.00}$	32	...	...	...	...	
AWM 04	...	...	...	0.55	0.068	...	...	

Cluster (1)	$R_{\rm vir}$ (2)	$M_{\rm vir}$ (3)	n_z (4)	β (5)	r_c (6)	M_x (7)	R_x (8)	Reference (9)
AWM 07	3.46	$11.54\ ^{+3.60}_{-3.00}$	33	0.55	0.125	2.0	4.0	Loewenstein & Mushotzky (1996)
CENTAURUS	...	...	...	0.50	0.075	1.0	1.6	Ohashi (1997)
HCG 051	...	...	...	0.55	0.115	...	...	
HCG 062	...	...	...	0.40	0.006	...	...	
HYDRA A	...	...	...	0.60	0.071	...	...	
MKW 03S	2.44	$3.20\ ^{+1.08}_{-0.96}$	27	0.65	0.095	2.0	4.0	Ohashi (1997)
MKW 04S	...	...	...	0.40	0.047	...	...	
MKW 04	2.10	$2.30\ ^{+0.70}_{-0.52}$	42	0.45	0.017	...	...	
MKW 09	...	...	...	0.45	0.050	...	...	
NGC 0507	...	...	...	0.45	0.029	...	...	
NGC 2300	...	...	...	0.40	0.049	...	...	
NGC 5044	...	...	...	0.50	0.019	...	...	
OPHIUCHUS	...	...	...	0.60	0.227	...	...	
TRI AUST	...	...	...	0.60	0.252	...	...	

A.6 Optical Data for Clusters

Table A.6 presents optical data from the literature for clusters in the ASCA cluster sample. See Chapter 8 for discussion and more information.

The columns in Table A.6 are as follows:

1. The cluster name from Table A.2.
2. The velocity dispersion in km s^{-1} with 68% confidence levels.
3. The number of galaxy redshifts redshifts used to derive the velocity dispersion.
4. The reference from which the velocity dispersion was taken: BH (Barmby & Huchra 1998), B99 (Borgani et al. 1999), C95 (Collins et al. 1995), D97 (Dantas et al. 1997), D99 (Donahue et al. 1999), DGC (Drinkwater et al. 2001), G01 (Girardi & Mezzetti 2001), G97 (Girardi et al. 1997), G98 (Girardi et al. 1998b), HP2 (Helsdon & Ponman 2000a), L96 (Ledlow et al. 1996), M99 (Mahdavi et al. 1999), MGW (Mohr et al. 1996), MM (Metzger & Ma 2000), O97 (Owen et al. 1997), S98 (Small et al. 1998), SR3 (Struble & Rood 1999), WQI (Way et al. 2000), ZHG (Zabludoff et al. 1990), ZM (Zabludoff & Mulchaey 1998).
5. The Abell richness of the cluster from Abell et al. (1989).
6. The Bahcall galaxy density from Bahcall (1977, 1980, 1981).
7. The amplitude of the two point cross correlation function of the cluster with 1σ errors.
8. The source of the B_{gg} value: YL (Yee & López-Cruz 1999), AO (Andersen & Owen 1994).
9. The total optical luminosity (in the B_j band) of the cluster within the cluster virial radius from Girardi et al. (2000), in units of 10^{12} $L_\odot$.

Table A.6: Optical Data for Clusters

Cluster (1)	σ_r (2)	n_z (3)	Ref. (4)	N_A (5)	N_B (6)	B_{gg} (7)	Ref. (8)	L_{opt} (9)
3C 295	1642^{+224}_{-187}	15	G01	...	...	...	...	...
ABELL 0068	...	...	...	52	...	...	...	...
ABELL 0085	969^{+95}_{-61}	124	G98	59	...	757 ± 174	YC	93.6
ABELL 0115	1074^{+208}_{-121}	13	G01	174	...	...	...	...
ABELL 0119	679^{+106}_{-80}	62	G98	69	18	...	...	70

Cluster (1)	σ_r (2)	n_z (3)	Ref. (4)	N_A (5)	N_B (6)	B_{gg} (7)	Ref. (8)	L_{opt} (9)
ABELL 0133	735^{+87}_{-72}	120	WQI	47	...	...	...	...
ABELL 0194	341^{+57}_{-37}	29	G98	37	15	260 ± 55	A0	12
ABELL 0222	730^{+102}_{-96}	26	G01	155	...	...	...	...
ABELL 0223	868^{+186}_{-124}	14	G01	152	...	...	...	...
ABELL 0262	525^{+47}_{-33}	40	G98	40	14	146 ± 41	A0	...
ABELL 0267	...	...	...	37	...	...	...	...
ABELL 0370	859^{+118}_{-112}	35	G01	40	...	...	...	...
ABELL 0376	519^{+116}_{-98}	14	SR3	36	...	...	...	...
ABELL 0399	1116^{+89}_{-83}	79	G98	57	...	1449 ± 235	YC	...
ABELL 0400	599^{+80}_{-65}	57	G98	58	...	170 ± 56	A0	...
ABELL 0401	1152^{+86}_{-70}	106	G98	90	35	2242 ± 286	YC	...
ABELL 0478	904^{+261}_{-140}	14	ZHG	104	35	...	...	...
ABELL 0483	...	...	...	52	...	...	...	...
ABELL 0496	687^{+89}_{-76}	55	G98	50	14	...	...	44.4
ABELL 0514	882^{+84}_{-64}	80	G98	78	...	946 ± 196	YC	64.4
ABELL 0520	1005^{+229}_{-132}	18	G01	186	...	...	...	...
ABELL 0521	1123^{+146}_{-102}	35	G01	63	...	...	...	...
ABELL 0539	629^{+70}_{-52}	70	G98	50	...	124 ± 40	A0	...
ABELL 0548E	571^{+54}_{-40}	62	G98	...	...	...	...	...
ABELL 0560	...	...	...	69	...	...	...	...
ABELL 0562	...	...	...	70	...	...	...	...
ABELL 0576	914^{+50}_{-38}	199	G98	61	25	300 ± 53	A0	...
ABELL 0586	...	...	...	190	...	...	...	...
ABELL 0611	...	...	...	56	...	...	...	...
ABELL 0644	...	...	...	42	...	...	...	...
ABELL 0665	821^{+233}_{-130}	25	G01	321	...	2186 ± 290	YC	...
ABELL 0697	941^{+296}_{-296}	9	MM	53	...	...	...	...
ABELL 0744	814^{+173}_{-106}	20	ZHG	42	...	...	...	...
ABELL 0750	...	...	...	142	...	...	...	...
ABELL 0754	662^{+77}_{-50}	62	G98	92	30	...	...	...
ABELL 0773	...	...	...	108	...	...	...	...
ABELL 0779	466^{+67}_{-67}	47	M99	32	...	138 ± 41	A0	...
ABELL 0851	1067^{+89}_{-96}	55	G01	71	...	...	...	...
ABELL 0854	...	...	...	59	...	...	...	...
ABELL 0959	...	...	...	55	...	...	...	...
ABELL 0963	1350^{+200}_{-150}	36	SR3	134	...	...	...	...
ABELL 0990	...	...	...	58	...	...	...	...
ABELL 1045	...	...	...	71	...	...	...	...
ABELL 1060	610^{+52}_{-43}	79	G98	50	13	...	...	47.2
ABELL 1068	...	...	...	71	...	...	...	...
ABELL 1111	...	...	...	88	...	...	...	...
ABELL 1204	...	...	...	54	...	...	...	...
ABELL 1246	...	...	...	136	...	...	...	...
ABELL 1300	1034^{+89}_{-104}	53	G01	62	...	...	...	...
ABELL 1367	822^{+69}_{-55}	93	ZHG	117	18	542 ± 78	A0	...
ABELL 1413	...	...	...	196	...	1686 ± 257	YC	...
ABELL 1423	...	...	...	63	...	...	...	...
ABELL 1430	...	...	...	96	...	...	...	...
ABELL 1451	...	...	...	131	...	...	...	...
ABELL 1466	...	...	...	58	...	...	...	...
ABELL 1553	...	...	...	100	...	...	...	...
ABELL 1576	...	...	...	158	...	...	...	...
ABELL 1631	702^{+54}_{-46}	58	G98	34	...	...	...	56.8
ABELL 1650	...	...	...	114	...	1861 ± 263	YC	...
ABELL 1651	965^{+160}_{-107}	29	ZHG	70	...	...	...	...
ABELL 1672	...	...	...	53	...	...	...	...
ABELL 1674	...	...	...	165	...	...	...	...
ABELL 1682	...	...	...	75	...	...	...	...
ABELL 1689	1172^{+123}_{-99}	49	G01	228	...	...	...	...
ABELL 1704	...	...	...	134	...	...	...	...
ABELL 1722	...	...	...	86	...	...	...	...
ABELL 1732	...	...	...	67	...	...	...	...

Cluster (1)	σ_r (2)	n_z (3)	Ref. (4)	N_A (5)	N_B (6)	B_{gg} (7)	Ref. (8)	L_{opt} (9)
ABELL 1736	...	...	...	41	...	...	...	...
ABELL 1763	...	...	...	152	...	...	...	...
ABELL 1775	478^{+117}_{-63}	11	G98	92	...	1018 ± 202	YC	...
ABELL 1795	834^{+85}_{-76}	80	G98	115	27	1430 ± 233	YC	...
ABELL 1835	...	...	...	48	...	...	...	...
ABELL 1851	...	...	...	125	...	...	...	...
ABELL 1885	...	...	...	63	...	...	...	...
ABELL 1895	...	...	...	107	...	...	...	...
ABELL 1913	454^{+128}_{-75}	14	ZHG	53	...	954 ± 192	YC	...
ABELL 1914	...	...	...	105	...	...	...	...
ABELL 1942	...	...	...	138	...	...	...	...
ABELL 1995	...	...	...	56	...	...	...	...
ABELL 2028	434^{+93}_{-57}	20	ZHG	50	...	...	...	...
ABELL 2029	1164^{+98}_{-78}	73	G98	82	32	1736 ± 255	YC	...
ABELL 2033	...	...	...	40	...	...	...	...
ABELL 2034	...	...	...	105	...	...	...	...
ABELL 2052	561^{+87}_{-73}	46	G97	41	...	173 ± 41	A0	...
ABELL 2063	667^{+55}_{-41}	70	G98	63	...	540 ± 78	A0	...
ABELL 2065	1203^{+371}_{-289}	31	S98	109	50	...	...	...
ABELL 2104	...	...	...	89	...	...	...	...
ABELL 2107	622^{+71}_{-64}	65	G98	51	...	...	...	...
ABELL 2111	...	...	...	148	...	...	...	...
ABELL 2142	1132^{+110}_{-92}	86	G98	89	30	...	...	...
ABELL 2147	821^{+68}_{-55}	91	BH	52	12	349 ± 56	A0	...
ABELL 2152	715^{+81}_{-61}	57	BH	60	...	278 ± 50	A0	...
ABELL 2163	...	...	...	119	...	...	...	...
ABELL 2187	...	...	...	49	...	...	...	...
ABELL 2197	612^{+56}_{-53}	36	G98	73	6	403 ± 64	A0	...
ABELL 2199	801^{+92}_{-61}	42	G98	88	19	635 ± 80	A0	...
ABELL 2204	...	...	...	133	34	...	...	...
ABELL 2218	1222^{+147}_{-109}	43	G01	214	...	...	...	...
ABELL 2219	...	...	...	159	...	...	...	...
ABELL 2244	...	...	...	89	...	1698 ± 254	YC	...
ABELL 2255	1266^{+150}_{-135}	44	SR3	102	28	2296 ± 289	YC	...
ABELL 2256	1348^{+86}_{-64}	86	G98	88	32	2174 ± 281	YC	...
ABELL 2259	...	...	...	58	...	...	...	...
ABELL 2261	...	...	...	128	...	...	...	...
ABELL 2319	1545^{+95}_{-77}	118	G98	68	...	...	...	...
ABELL 2390	1294^{+76}_{-67}	200	G01	72	...	...	...	...
ABELL 2440	957^{+199}_{-136}	48	MGW	32	24	1053 ± 207	YC	...
ABELL 2534	...	...	...	110	...	...	...	...
ABELL 2537	...	...	...	51	...	...	...	...
ABELL 2540	...	...	...	70	...	...	...	...
ABELL 2550	...	...	...	122	...	...	...	...
ABELL 2554	840^{+131}_{-68}	27	G98	159	...	1218 ± 222	YC	106.8
ABELL 2555	...	...	...	72	...	...	...	...
ABELL 2556	...	...	...	67	...	828 ± 187	YC	...
ABELL 2572	524^{+121}_{-121}	13	RSL	32	...	208 ± 44	A0	...
ABELL 2589	470^{+120}_{-84}	28	G98	40	20	...	...	...
ABELL 2597	...	...	...	43	...	665 ± 172	YC	...
ABELL 2634	700^{+97}_{-61}	69	G98	52	...	216 ± 46	A0	...
ABELL 2657	829^{+116}_{-103}	31	SR3	51	...	740 ± 170	YC	...
ABELL 2667	...	...	...	165	...	...	...	...
ABELL 2670	852^{+48}_{-35}	186	G98	142	...	1771 ± 257	YC	68.8
ABELL 2744	...	...	...	137	...	...	...	...
ABELL 2798	711^{+181}_{-101}	16	G98	58	...	...	...	42
ABELL 2801	...	...	...	74	...	...	...	...
ABELL 2811	695^{+200}_{-108}	13	C95	73	...	...	...	...
ABELL 3088	...	...	...	83	...	...	...	...
ABELL 3112	552^{+86}_{-63}	49	G98	116	...	...	...	...
ABELL 3158	976^{+70}_{-58}	123	G98	85	...	...	...	104
ABELL 3266	1107^{+82}_{-65}	128	G98	91	...	...	...	115.6

Cluster (1)	σ_r (2)	n_z (3)	Ref. (4)	N_A (5)	N_B (6)	B_{gg} (7)	Ref. (8)	L_{opt} (9)
ABELL 3376	688^{+68}_{-57}	65	G98	42	...	...	...	35.6
ABELL 3381	293^{+110}_{-54}	13	G98	69	...	...	...	8
ABELL 3391	663^{+195}_{-112}	50	G98	40	...	...	...	65.6
ABELL 3408	...	...	...	41	...	...	...	...
ABELL 3444	...	...	...	57	...	...	...	...
ABELL 3528N	461^{+82}_{-36}	24	G98	...	...	...	...	...
ABELL 3530	...	...	...	34	...	...	...	...
ABELL 3532	738^{+112}_{-85}	42	G98	36	...	...	...	69.2
ABELL 3556	642^{+94}_{-49}	66	G98	49	...	...	...	60
ABELL 3558	977^{+39}_{-34}	338	G98	226	...	...	...	222
ABELL 3562	736^{+49}_{-36}	89	G98	129	...	...	...	...
ABELL 3565	...	...	...	64	...	...	...	...
ABELL 3570	...	...	...	31	...	...	...	...
ABELL 3571	1045^{+109}_{-90}	69	G98	126	...	...	...	182.8
ABELL 3581	577^{+82}_{-94}	24	SR3	42	...	...	...	...
ABELL 3602	...	...	...	65	...	...	...	...
ABELL 3627	...	...	...	59	...	...	...	...
ABELL 3667	971^{+62}_{-47}	152	G98	85	...	...	...	160.4
ABELL 3921	490^{+126}_{-73}	24	G98	93	...	...	...	53.6
ABELL 3934	...	...	...	113	...	...	...	...
ABELL 4038	363^{+67}_{-67}	18	RSL	117	...	...	...	...
ABELL 4059	628^{+65}_{-72}	45	SR3	66	...	...	...	...
ABELL 4067	499^{+123}_{-74}	22	G98	72	...	...	...	34.8
ABELL S0506	1356^{+204}_{-150}	21	G01	121	...	...	...	...
ABELL S0520	...	...	...	83	...	...	...	...
ABELL S0636	...	...	...	1	...	...	...	...
ABELL S0753	536^{+127}_{-88}	32	G98	18	...	...	...	22.8
ABELL S1077	1388^{+128}_{-71}	63	G01	92	...	...	...	...
ABELL S1111	...	...	...	25	...	...	...	...
AWM 07	864^{+110}_{-80}	33	G98	...	...	...	...	...
CENTAURUS	791^{+60}_{-62}	93	G98	...	15	...	...	...
CL 0016+1609	984^{+130}_{-95}	42	G01	...	...	...	...	...
CYGNUS A	1581^{+286}_{-197}	41	O97	...	...	...	...	...
EXSS 0657.5−5551	926^{+178}_{-104}	12	G01	...	...	...	...	...
FORNAX	374^{+26}_{-26}	108	DGC	...	...	...	...	...
HCG 042	266^{+37}_{-37}	25	ZM	...	...	...	...	...
HCG 051	263^{+97}_{-97}	5	HP2	...	...	87 ± 32	A0	...
HCG 057	282^{+84}_{-85}	7	HP2	...	...	116 ± 35	A0	...
HCG 062	376^{+52}_{-46}	45	ZM	...	...	...	...	...
HCG 068	170^{+66}_{-66}	5	HP2	...	...	94 ± 35	A0	...
HCG 097	389^{+80}_{-81}	5	RSL	...	...	...	...	...
HERCULES	691^{+37}_{-39}	172	SR3	...	...	...	...	...
MKW 03S	610^{+69}_{-52}	27	G98	...	13	...	...	...
MKW 04	525^{+71}_{-48}	42	G98	...	11	...	...	...
MKW 04S	...	...	...	...	8	...	...	...
MKW 08	422^{+99}_{-53}	15	L96	...	11	161 ± 42	A0	...
MKW 09	...	...	...	...	13	...	...	...
MS 0302.5+1717	664^{+67}_{-77}	24	G01	...	...	...	...	...
MS 0302.7+1658	735^{+109}_{-80}	30	G01	...	...	...	...	...
MS 0440.5+0204	838^{+131}_{-139}	32	G01	...	...	...	...	...
MS 0451.6−0305	1317^{+122}_{-103}	40	G01	...	...	...	...	...
MS 0839.8+2938	980^{+147}_{-113}	47	B99	...	...	...	...	...
MS 1006.0+1202	1017^{+161}_{-103}	30	B99	...	...	...	...	...
MS 1008.1−1224	1033^{+115}_{-105}	65	G01	...	...	...	...	...
MS 1054.4−0321	1178^{+139}_{-113}	32	G01	...	...	...	...	...
MS 1137.5+6625	884^{+185}_{-124}	22	D99	...	...	...	...	...

Cluster (1)	σ_r (2)	n_z (3)	Ref. (4)	N_A (5)	N_B (6)	B_{gg} (7)	Ref. (8)	L_{opt} (9)
MS 1224.7+2007	837^{+100}_{-83}	23	G01	...	...	...	...	...
MS 1358.4+6245	985^{+58}_{-62}	133	G01	...	...	...	...	...
MS 1455.0+2232	1032^{+130}_{-95}	51	B99	...	...	...	...	...
MS 1512.4+3647	776^{+172}_{-103}	35	G01	...	...	...	...	...
MS 1621.5+2640	735^{+53}_{-53}	88	G01	...	...	...	...	...
NGC 0533	464^{+58}_{-52}	36	ZM	...	...	...	...	...
NGC 1132	346^{+56}_{-56}	9	RSL	...	...	...	...	...
NGC 2563	336^{+44}_{-44}	36	ZM	...	...	...	...	...
NGC 4325	265^{+50}_{-50}	23	ZM	...	...	...	...	...
NGC 5129	304^{+43}_{-43}	34	ZM	...	...	...	...	...
NGC 5846	368^{+72}_{-61}	20	ZM	...	...	...	...	...
NGC 6109	524^{+206}_{-205}	8	RSL	...	...	...	...	...
PCC N34−175	589^{+440}_{-31}	7	L96	...	...	...	...	...
PCC S34−111	486^{+53}_{-37}	47	L96	...	...	107 ± 36	A0	...
PCC S49−132	...	...	...	...	...	123 ± 0	A0	...
PCC S49−140	162^{+33}_{-34}	8	RSL	...	...	58 ± 36	A0	...
PCC S49−147	233^{+141}_{-43}	12	L96	...	...	...	...	...
RX J1320.1+3308	446^{+144}_{-144}	5	RSL	...	...	...	...	...
RX J1716.6+6708	1445^{+288}_{-218}	19	G01	...	...	...	...	...
SC 1327−312	580^{+119}_{-118}	16	D97	...	...	...	...	...
WBL 224	104^{+44}_{-43}	5	RSL	...	...	...	...	...
WBL 225	151^{+56}_{-56}	5	RSL	...	...	...	...	...
ZWCL 0024.0+1652	911^{+81}_{-107}	73	G01	...	...	...	...	...

Appendix B

Notes on Individual Sources

This Appendix gives additional information about some sources considered in this thesis. Sources are listed alphabetically by name.

3C 129 The SIS data for this cluster show a sudden steep decline at low energies that is not seen in the GIS data. This observation was taken late 1998 and in 2-CCD mode which increases the calibration uncertainties of SIS observations. Therefore, we ignored the data below 1.5 keV for the fit.

ABELL 119 The SIS data for this cluster show a sudden steep decline at low energies that is not seen in the GIS data. Therefore, we ignored the data below 1.5 keV for the fit. Fukazawa (1997) also notes this problem and ignores the SIS data entirely.

ABELL 1423 We have adopted $z = 0.2138$ as the redshift of this cluster based on Crawford et al. (1995). This is the redshift of radio galaxy 7C 1154+3353, which appears optically as a cD galaxy and is at the centroid of the x-ray emission. However, Struble & Rood (1999) list the redshift of Abell 1423 as $z = 0.0761$ for three galaxies. They reference as the source of this redshift an earlier paper by Postman et al. (1992), who in turn reference an unpublished preprint, so the ultimate source of this redshift is unclear.

The nominal optical position of Abell 1423 is $3'$ northeast of the x-ray centroid, and the ASCA GIS image reveals a low surface brightness "tail" of emission in this direction. The SIS is positioned in such a way that this "tail" goes outside the chip boundary and so is not visible. A ROSAT HRI image of this region does not show this tail, but it may be too short at 19ks (versus 2×38 ks for GIS2 + GIS3) to see such a feature.

Using either redshift results in a good fit to the spectrum (χ^2 between 0.98-1.01) with only small changes to the fitted temperature and abundance. Both the GIS and SIS spectra show a strong Fe-K line at ≈ 5.5 keV, where it should

be for $z = 0.21$. However, the GIS spectra (but not the SIS) also has a faint spectral feature at ≈ 6.2 keV where the Fe-K line would be for a cluster at $z = 0.07$. Therefore, we think that Abell 1423 may be a superposition of a rich cluster at $z = 0.21$ and a poor, x-ray faint, foreground cluster at $z = 0.07$.

ABELL 2537 This cluster has no optical redshift in the literature. However, XBACS (Ebeling et al. 1996) uses a privately communicated redshift from Romer (the Southern Galactic Pole survey) without listing the value, but using the XBACS flux and luminosity values, we estimate that the redshift should be $z = 0.2989$, close to the fitted value of $z = 0.2806$.

ABELL 3558 In ASCA sequence 83058000, the SIS pointed at a region between the cluster and an adjacent cluster, SC 1327-312 (which was not included in sample since it is too far off axis). Since most of the cluster flux is out of the SIS field-of-view, we have ignored the SIS data for this observation.

AX J2019+112 This the $z \sim 1$ "dark cluster" identified by Hattori et al. (1997) as the cause of the gravitational lensing of MG J2019+1127, an AGN at $z = 3.273$. However, Chartas et al. (2001) finds that Chandra observations resolve the emission into point sources with no extended component. Given the unclear nature of this system and its relative faintness in any case, this source has been excluded from the catalog.

CENTAURUS Also known as Abell 3526, Centaurus is a nearby, well-studied, poor cluster. The spectral fits for this cluster using a single temperature MEKAL model give $\chi^2 > 1.3$, with higher χ^2 values for better signal-to-noise observations. The "Combined" fit to the spectra gives $\chi^2 > 2.7$. Centaurus is known to contain multiphase gas and a cooling flow (Ikebe et al. 1999). To minimize this effect and achieve better a better fit, we have ignored the data below 3 keV.

CYGNUS A This cluster is a complicated system. It is at low galactic latitude ($b = 5.7°$), undergoing a merger, and contains an AGN. The single temperature fits are poor and should be interpreted with caution, as indicated by the large values of reduced χ^2 for the fits. See Markevitch et al. (1998) and Markevitch et al. (1999) for detailed analysis of the ASCA observations of this cluster.

HCG 016 This group was excluded from the catalog. The GIS and SIS images show that the emission comes from several sources with some diffuse emission. Saracco & Ciliegi (1995) find that much of the x-ray emission in a ROSAT

PSPC observation originates from point-like sources spatially coincident with galaxies in the group. Ribeiro et al. (1996) reports that HCG 16 is very rich in starburst galaxies and active galactic nuclei.

HGC 048 This group was originally included in the sample but later dropped. A fit to the ASCA data gives an unusually high temperature $T_x \approx 3$ keV for its luminosity. Ponman et al. (1996) finds a ROSAT PSPC temperature of 1.09 keV with a comparable luminosity. The SIS image resolves the emission into several clumps with some diffuse emission while the GIS image shows scattered emission from Abell 1060 (which has a temperature ≈ 3 keV) which is just outside of the field-of-view. Therefore, the extracted spectrum is probably not measuring the diffuse IGM gas of the group, and the fitted parameters are not reliable.

HCG 092 Also known as Stephan's Quintet, we excluded this group from the sample since it contains an AGN which contributes a great deal to the emission. Awaki et al. (1997) and Davis et al. (1999) both include a power law component in the fit to account for the AGN emission to get an IGM temperature of ≈ 0.76 and metal abundance of ≈ 0.10.

NGC 4261 This group contains an AGN which results in a high χ^2 value for a single temperature MEKAL fit. Including a power low component in the fit to account for emission from the AGN gives a temperature of $0.91^{+0.06}_{-0.05}$ and abundance of $0.11^{+0.04}_{-0.05}$ consistent with the results of Sambruna et al. (1999).

NGC 5044 The spectra for this group are likely contaminated by emission from the galaxies within the group. The spectral fits using a single temperature MEKAL model give $\chi^2 \gtrsim 1.5$ for most observations, with higher χ^2 values for better signal-to-noise observations.

BIBLIOGRAPHY

Abell, G. O. 1958, ApJS, 3, 211
Abell, G. O., Corwin, H. G., & Olowin, R. P. 1989, ApJS, 70, 1
Abramopoulos, F., & Ku, W. H. M. 1983, ApJ, 271, 446
Aceves, H., & Perea, J. 1998, in Observational Cosmology: The development of galaxy systems, ed. G. G. et al., ASP Conference Series, in press
Afshordi, N., & Cen, R. 2001, preprint, astro-ph/0105020
Akritas, M. G., & Bershady, M. A. 1996, ApJ, 470, 706
Albert, C. E., White, R. A., & Morgan, W. W. 1977, ApJ, 211, 309
Allen, S. W. 1998, MNRAS, 296, 392
Allen, S. W. 2000, MNRAS, 315, 269
Allen, S. W., & Fabian, A. C. 1998a, MNRAS, 297, L57
Allen, S. W., & Fabian, A. C. 1998b, MNRAS, 297, L63
Anders, E., & Grevesse, N. 1989, Geochim. Cosmochim. Acta, 53, 197
Andersen, V., & Owen, F. N. 1994, AJ, 108, 361
Arabadjis, J. S., Bautz, M. W., & Garmire, G. P. 2001, ApJ, submitted
Arnaud, K. A. 1988, in Cooling Flows in Clusters and Galaxies, ed. A. C. Fabian, 31
Arnaud, M., & Evrard, A. E. 1999, MNRAS, 305, 631
Arnaud, M., Rothenflug, R., Boulade, O., Vigroux, L., & Vangioni-Flam, E. 1992, A&A, 254, 49
Awaki, H., Koyama, K., Matsumoto, H., Tomida, H., Tsuru, T., & Ueno, S. 1997, PASJ, 49, 445
Bahcall, N. A. 1977, ApJ, 217, L77
Bahcall, N. A. 1980, ApJ, 238, L117
Bahcall, N. A. 1981, ApJ, 247, 787
Bahcall, N. A. 1999, in Formation of Structure in the Universe, 135
Bahcall, N. A., Cen, R., Davé, R., Ostriker, J. P., & Yu, Q. 2000, ApJ, 541, 1
Bahcall, N. A., Lubin, L. M., & Dorman, V. 1995, ApJ, 447, L81
Balogh, M. L., Babul, A., & Patton, D. R. 1999, MNRAS, 307, 463
Barmby, P., & Huchra, J. P. 1998, AJ, 115, 6
Bauer, F., & Bregman, J. N. 1996, ApJ, 457, 382

Bautz, L. P., & Morgan, W. W. 1970, ApJ, 172, L149
Bender, R., Ziegler, B., & Bruzual, G. 1996, ApJ, 463, L51
Bird, C. M., Mushotzky, R. F., & Metzler, C. A. 1995, ApJ, 453, 40
Boggs, P. T., Donaldson, J. R., Byrd, R. H., & Schnabel, R. B. 1989, ACM Transactions on Mathematical Software, 15, 348
Böhringer, H., et al. 2000, ApJS, 129, 435
Borgani, S., Girardi, M., Carlberg, R. G., Yee, H. K. C., & Ellingson, E. 1999, ApJ, 527, 561
Bower, R. G., Benson, A. J., Lacey, C. G., Baugh, C. M., Cole, S., & Frenk, C. S. 2001, MNRAS, 325, 497
Bradt, H., Mayer, W., Naranan, S., Rappaport, S., & Spuda, G. 1967, ApJ, 161, L1
Brighenti, F., & Mathews, W. G. 2001, ApJ, 553, 103
Bryan, G. L. 2000, ApJ, 544, L1
Bryan, G. L., & Norman, M. L. 1998, ApJ, 495, 80
Bullock, J. S., Kolatt, T. S., Sigad, Y., Somerville, R. S., Kravtsov, A. V., Klypin, A. A., Primack, J. R., & Dekel, A. 2001, MNRAS, 321, 559
Buote, D. A. 2000, ApJ, 539, 172
Burg, R., Giacconi, R., Forman, W., & Jones, C. 1994, ApJ, 422, 37
Byram, E. T., Chubb, T. A., & Friedman, H. 1966, Science, 152, 66
Carlberg, R. G., Yee, H. K. C., & Ellingson, E. 1997, ApJ, 478, 462
Carlberg, R. G., Yee, H. K. C., Ellingson, E., Abraham, R., Gravel, P., Morris, S., & Pritchet, C. J. 1996, ApJ, 462, 32
Carlberg, R. G., et al. 1997, ApJ, 485, L13
Cavaliere, A., & Fusco-Femiano, R. 1976, A&A, 49, 137
Cavaliere, A., Menci, N., & Tozzi, P. 1997, ApJ, 484, L21
Chartas, G., Bautz, M., Garmire, G., Jones, C., & Schneider, D. P. 2001, ApJ, 550, L163
Cirimele, G., Nesci, R., & Trevese, D. 1997, ApJ, 475, 11
Collins, C. A., et al. 2000, MNRAS, 319, 939
Collins, C. A., Guzzo, L., Nichol, R. C., & Lumsden, S. L. 1995, MNRAS, 274, 1071
Crawford, C. S., Edge, A. C., Fabian, A. C., Allen, S. W., Bohringer, H., Ebeling, H., McMahon, R. G., & Voges, W. 1995, MNRAS, 274, 75
Dalton, G. B., Maddox, S. J., Sutherland, W. J., & Efstathiou, G. 1997, MNRAS, 289, 263
Dantas, C. C., de Carvalho, R. R., Capelato, H. V., & Mazure, A. 1997, ApJ, 485, 447
David, L. P., & Blumenthal, G. R. 1992, ApJ, 389, 510
David, L. P., Forman, W., & Jones, C. 1991, ApJ, 380, 39

David, L. P., Forman, W., & Jones, C. 1999, ApJ, 519, 533
David, L. P., Jones, C., & Forman, W. 1995, ApJ, 445, 578
David, L. P., Slyz, A., Jones, C., Forman, W., Vrtilek, S. D., & Arnaud, K. A. 1993, ApJ, 412, 479
Davis, D. S., Mulchaey, J. S., & Mushotzky, R. F. 1999, ApJ, 511, 34
De Grandi, S., et al. 1999a, ApJ, 514, 148
De Grandi, S., et al. 1999b, ApJ, 513, L17
De Grandi, S., & Molendi, S. 2001, ApJ, 551, 153
Dell'Antonio, I. P., Geller, M. J., & Fabricant, D. G. 1995, AJ, 110, 502
Dickey, J. M., & Lockman, F. J. 1990, ARA&A, 28, 215
Donahue, M., et al. 2001, ApJ, 552, L93
Donahue, M., Voit, G. M., Scharf, C. A., Gioia, I. M., Mullis, C. R., Hughes, J. P., & Stocke, J. T. 1999, ApJ, 527, 525
Dressler, A. 1980, ApJS, 42, 565
Drinkwater, M. J., Gregg, M. D., & Colless, M. 2001, ApJ, 548, L139
Ebeling, H., Edge, A. C., Böhringer, H., Allen, S. W., Crawford, C. S., Fabian, A. C., Voges, W., & Huchra, J. P. 1998, MNRAS, 301, 881
Ebeling, H., Voges, W., Böhringer, H., Edge, A. C., Huchra, J. P., & Briel, U. G. 1996, MNRAS, 281, 799
Edge, A. C., & Stewart, G. C. 1991a, MNRAS, 252, 428
Edge, A. C., & Stewart, G. C. 1991b, MNRAS, 252, 414
Edge, A. C., Stewart, G. C., & Fabian, A. C. 1992, MNRAS, 258, 177
Edge, A. C., Stewart, G. C., Fabian, A. C., & Arnaud, K. A. 1990, MNRAS, 245, 559
Eke, V. R., Cole, S., & Frenk, C. S. 1996, MNRAS, 282, 263
Eke, V. R., Navarro, J. F., & Frenk, C. S. 1998, ApJ, 503, 569
Enoki, M., Takahara, F., & Fujita, Y. 2001, ApJ, 556, 77
Ettori, S., & Fabian, A. C. 1999, MNRAS, 305, 834
Evrard, A. E., & Henry, J. P. 1991, ApJ, 383, 95
Evrard, A. E., Metzler, C. A., & Navarro, J. F. 1996, ApJ, 469, 494
Fabian, A. C. 1994, ARA&A, 32, 277
Fabian, A. C., Crawford, C. S., Edge, A. C., & Mushotzky, R. F. 1994, MNRAS, 267, 779
Fabian, A. C., Mushotzky, R. F., Nulsen, P. E. J., & Peterson, J. R. 2001, MNRAS, 321, L20
Fairley, B. W., Jones, L. R., Scharf, C., Ebeling, H., Perlman, E., Horner, D., Wegner, G., & Malkan, M. 2000, MNRAS, 315, 669
Fernley, J. A., & Bhavsar, S. P. 1984, MNRAS, 210, 883
Finoguenov, A., David, L. P., & Ponman, T. J. 2000, ApJ, 544, 188
Finoguenov, A., Reiprich, T. H., & Böhringer, H. 2001, A&A, 368, 749

Forman, W., Kellogg, E., Gursky, H., Tananbaum, H., & Giacconi, R. 1972, ApJ, 178, 309
Frenk, C. S., White, S. D. M., Efstathiou, G., & Davis, M. 1990, ApJ, 351, 10
Fujita, Y. 2001, ApJ, 550, L7
Fukazawa, Y. 1997, Ph.D. thesis, University of Tokyo
Fukazawa, Y., Makishima, K., Tamura, T., Ezawa, H., Xu, H., Ikebe, Y., Kikuchi, K., & Ohashi, T. 1998, PASJ, 50, 187
Gaetz, T. J., Salpeter, E. E., & Shaviv, G. 1987, ApJ, 316, 530
Giacconi, R., Murray, S., Gursky, H., Kellogg, E., Schreier, E., & Tananbaum, H. 1972, ApJ, 178, 281
Gioia, I. M., Maccacaro, T., Schild, R. E., Wolter, A., Stocke, J. T., Morris, S. L., & Henry, J. P. 1990, ApJS, 72, 567
Girardi, M., Borgani, S., Giuricin, G., Mardirossian, F., & Mezzetti, M. 1998a, ApJ, 506, 45
Girardi, M., Borgani, S., Giuricin, G., Mardirossian, F., & Mezzetti, M. 2000, ApJ, 530, 62
Girardi, M., Escalera, E., Fadda, D., Giuricin, G., Mardirossian, F., & Mezzetti, M. 1997, ApJ, 482, 41
Girardi, M., Giuricin, G., Mardirossian, F., Mezzetti, M., & Boschin, W. 1998b, ApJ, 505, 74
Girardi, M., & Mezzetti, M. 2001, ApJ, 548, 79
Gotthelf, E. V., Ueda, Y., Fujimoto, R., Kii, T., & Yamaoka, K. 2000, ApJ, 543, 417
Grego, L., Carlstrom, J. E., Reese, E. D., Holder, G. P., Holzapfel, W. L., Joy, M. K., Mohr, J. J., & Patel, S. 2001, ApJ, 552, 2
Groth, E. J., & Peebles, P. J. E. 1977, ApJ, 217, 385
Gunn, J. E., & Gott, J. R. I. 1972, ApJ, 176, 1
Gunn, J. E., Hoessel, J. G., & Oke, J. B. 1986, ApJ, 306, 30
Hatsukade, I. 1989, Ph.D. thesis, Osaka University
Hattori, M., et al. 1997, Nature, 388, 146
Heckman, T. M. 2001, in To appear in "Extragalactic Gas at Low Redshift", ed. J. Mulchaey and J. Stocke, ASP Conf. Series, 7438
Helsdon, S. F., & Ponman, T. J. 2000a, MNRAS, 319, 933
Helsdon, S. F., & Ponman, T. J. 2000b, MNRAS, 315, 356
Henry, J. P. 1997, ApJ, 489, L1
Henry, J. P. 2000, ApJ, 534, 565
Henry, J. P., & Arnaud, K. A. 1991, ApJ, 372, 410
Hickson, P. 1982, ApJ, 255, 382
Hjorth, J., Oukbir, J., & Van Kampen, E. 1998, MNRAS, 298, L1
Horner, D. J., Mushotzky, R. F., & Scharf, C. A. 1999, ApJ, 520, 78

Hradecky, V., Jones, C., Donnelly, R. H., Djorgovski, S. G., Gal, R. R., & Odewahn, S. C. 2000, ApJ, 543, 521
Hwang, U., Mushotzky, R. F., Burns, J. O., Fukazawa, Y., & White, R. A. 1999, ApJ, 516, 604
Hwang, U., Mushotzky, R. F., Loewenstein, M., Markert, T. H., Fukazawa, Y., & Matsumoto, H. 1997, ApJ, 476, 560
Ikebe, Y., Makishima, K., Fukazawa, Y., Tamura, T., Xu, H., Ohashi, T., & Matsushita, K. 1999, ApJ, 525, 58
Irwin, J. A., & Bregman, J. N. 2000, ApJ, 538, 543
Irwin, J. A., & Bregman, J. N. 2001, ApJ, 546, 150
Isobe, T., Feigelson, E. D., Akritas, M. G., & Babu, G. J. 1990, ApJ, 364, 104
Jones, C., & Forman, W. 1999, ApJ, 511, 65
Jones, L. R., Scharf, C., Ebeling, H., Perlman, E., Wegner, G., Malkan, M., & Horner, D. 1998, ApJ, 495, 100
Kaastra, J. S., Ferrigno, C., Tamura, T., Paerels, F. B. S., Peterson, J. R., & Mittaz, J. P. D. 2001, A&A, 365, L99
Kaiser, N. 1986, MNRAS, 222, 323
Katgert, P., Mazure, A., Den Hartog, R., Adami, C., Biviano, A., & Perea, J. 1998, A&AS, 129, 399
Kellogg, E., Gursky, H., Tananbaum, H., Giacconi, R., & Pounds, K. 1972, ApJ, 174, L65
Kepner, J., Fan, X., Bahcall, N., Gunn, J., Lupton, R., & Xu, G. 1999, ApJ, 517, 78
King, I. R. 1972, ApJ, 174, L123
Komatsu, E., & Seljak, U. 2001, MNRAS, preprint, astro-ph/0106151
Kravtsov, A. V., & Yepes, G. 2000, MNRAS, 318, 227
Lacey, C., & Cole, S. 1993, MNRAS, 262, 627
Ledlow, M. J., Loken, C., Burns, J. O., Hill, J. M., & White, R. A. 1996, AJ, 112, 388
Lewis, A. D., Ellingson, E., Morris, S. L., & Carlberg, R. G. 1999, ApJ, 517, 587
Lilje, P. B. 1992, ApJ, 386, L33
Loewenstein, M. 2000, ApJ, 532, 17
Loewenstein, M., & Mushotzky, R. F. 1996, ApJ, 471, L83
Lubin, L. M., & Bahcall, N. A. 1993, ApJ, 415, L17
Lumsden, S. L., Nichol, R. C., Collins, C. A., & Guzzo, L. 1992, MNRAS, 258, 1
Mahdavi, A., Geller, M. J., Böhringer, H., Kurtz, M. J., & Ramella, M. 1999, ApJ, 518, 69
Markevitch, M. 1996, ApJ, 465, L1
Markevitch, M. 1998, ApJ, 504, 27
Markevitch, M., Forman, W. R., Sarazin, C. L., & Vikhlinin, A. 1998, ApJ, 503,

77
Markevitch, M., Mushotzky, R., Inoue, H., Yamashita, K., Furuzawa, A., & Tawara, Y. 1996, ApJ, 456, 437
Markevitch, M., Sarazin, C. L., & Vikhlinin, A. 1999, ApJ, 521, 526
Markevitch, M., & Vikhlinin, A. 1997, ApJ, 491, 467
Mazure, A., et al. 1996, A&A, 310, 31
Merritt, D. 1988, in ASP Conf. Ser. 5: The Minnesota Lectures on Clusters of Galaxies and Large-Scale Structure, 175
Metzger, M. R., & Ma, C. 2000, AJ, 120, 2879
Metzler, C. A., & Evrard, A. E. 1994, ApJ, 437, 564
Mewe, R., Kaastra, D. S., & Liedahl, D. A. 1995, Legacy, 6, 16
Miller, N. A., Owen, F. N., Burns, J. O., Ledlow, M. J., & Voges, W. 1999, AJ, 118, 1988
Mitchell, R. J., Culhane, J. L., Davison, P. J. N., & Ives, J. C. 1976, MNRAS, 175, 29P
Mohr, J. J., & Evrard, A. E. 1997, ApJ, 491, 38
Mohr, J. J., Geller, M. J., & Wegner, G. 1996, AJ, 112, 1816
Mohr, J. J., Mathiesen, B., & Evrard, A. E. 1999, ApJ, 517, 627
Molendi, S., & Pizzolato, F. 2001, ApJ, preprint, astro-ph/0106552
Morgan, W. W., Kayser, S., & White, R. A. 1975, ApJ, 199, 545
Muanwong, O., Thomas, P. A., Kay, S. T., Pearce, F. R., & Couchman, H. M. P. 2001, ApJ, 552, L27
Mulchaey, J. S., & Zabludoff, A. I. 1998, ApJ, 496, 73
Mushotzky, R., Loewenstein, M., Arnaud, K., & Fukazawa, Y. 1994, in AIP Conference Proceedings, Vol. 336, Dark Matter, ed. S. S. Holt & C. L. Bennett (College Park, MD 1994: AIP), 231
Mushotzky, R. F. 1984, Phys. Scr, 7, 157
Mushotzky, R. F., & Loewenstein, M. 1997, ApJ, 481, L63
Mushotzky, R. F., & Scharf, C. A. 1997, ApJ, 482, L13
Navarro, J. F., Frenk, C. S., & White, S. D. M. 1995, MNRAS, 275, 720
Navarro, J. F., Frenk, C. S., & White, S. D. M. 1996, ApJ, 462, 563
Neumann, D. M., & Arnaud, M. 1999, A&A, 348, 711
Nevalainen, J., Markevitch, M., & Forman, W. 2000, ApJ, 532, 694
Ohashi, T. 1997, in ASCA/ROSAT Workshop on Clusters of Galaxies, ed. T. Ohashi (Hakone-Yumato: Japan Society for the Promotion of Science), 201
Olsen, L. F., et al. 1999, A&A, 345, 363
Ostrander, E. J., Nichol, R. C., Ratnatunga, K. U., & Griffiths, R. E. 1998, AJ, 116, 2644
Owen, F. N., Ledlow, M. J., Morrison, G. E., & Hill, J. M. 1997, ApJ, 488, L15
Patel, S. K., et al. 2000, ApJ, 541, 37

Peres, C. B., Fabian, A. C., Edge, A. C., Allen, S. W., Johnstone, R. M., & White, D. A. 1998, MNRAS, 298, 416
Peterson, J. R., et al. 2001, A&A, 365, L104
Ponman, T. J., Bourner, P. D. J., Ebeling, H., & Böhringer, H. 1996, MNRAS, 283, 690
Ponman, T. J., Cannon, D. B., & Navarro, J. F. 1999, Nature, 397, 135
Postman, M., Huchra, J. P., & Geller, M. J. 1992, ApJ, 384, 404
Postman, M., Lubin, L. M., Gunn, J. E., Oke, J. B., Hoessel, J. G., Schneider, D. P., & Christensen, J. A. 1996, AJ, 111, 615
Raymond, J. C., & Smith, B. W. 1977, ApJS, 35, 419
Renzini, A. 1997, ApJ, 488, 35
Ribeiro, A. L. B., de Carvalho, R. R., Coziol, R., Capelato, H. V., & Zepf, S. E. 1996, ApJ, 463, L5
Romer, A. K., et al. 2000, ApJS, 126, 209
Rood, H. J., & Sastry, G. N. 1971, PASP, 83, 313
Rosati, P., Della Ceca, R., Norman, C., & Giacconi, R. 1998, ApJ, 492, L21
Roussel, H., Sadat, R., & Blanchard, A. 2000, A&A, 361, 429
Sambruna, R. M., Eracleous, M., & Mushotzky, R. F. 1999, ApJ, 526, 60
Saracco, P., & Ciliegi, P. 1995, A&A, 301, 348
Sarazin, C. L. 1988, X-ray Emissions from Clusters of Galaxies (Cambridge: Cambridge University Press)
Sarazin, C. L., Wise, M. W., & Markevitch, M. L. 1998, ApJ, 498, 606
Scharf, C. A., Jones, L. R., Ebeling, H., Perlman, E., Malkan, M., & Wegner, G. 1997, ApJ, 477, 79
Scharf, C. A., & Mushotzky, R. F. 1997, ApJ, 485, L65
Schechter, P. 1976, ApJ, 203, 297
Serlemitsos, P. J., et al. 1995, PASJ, 47, 105
Serlemitsos, P. J., Smith, B. W., Boldt, E. A., Holt, S. S., & Swank, J. H. 1977, ApJ, 211, L63
Small, T. A., Ma, C., Sargent, W. L. W., & Hamilton, D. 1998, ApJ, 492, 45
Stanford, S. A., Holden, B., Rosati, P., Tozzi, P., Borgani, S., Eisenhardt, P. R., & Spinrad, H. 2001, ApJ, 552, 504
Struble, M. F., & Rood, H. J. 1999, ApJS, 125, 35
Tamura, T., et al. 2001, A&A, 365, L87
Tanaka, Y., Inoue, H., & Holt, S. S. 1994, PASJ, 46, L37
The, L. S., & White, S. D. M. 1986, AJ, 92, 1248
Thomas, P. A., Muanwong, O., Pearce, F. R., Couchman, H. M. P., Edge, A. C., Jenkins, A., & Onuora, L. 2001, MNRAS, 324, 450
Tozzi, P., & Norman, C. 2001, ApJ, 546, 63
Tozzi, P., Scharf, C., & Norman, C. 2000, ApJ, 542, 106

Valageas, P., & Silk, J. 1999, A&A, 350, 725
Vikhlinin, A., Forman, W., & Jones, C. 1999, ApJ, 525, 47
Vikhlinin, A., McNamara, B. R., Forman, W., Jones, C., Quintana, H., & Hornstrup, A. 1998, ApJ, 502, 558
Voit, G. M. 2000, ApJ, 543, 113
Voit, G. M., & Donahue, M. 1998, ApJ, 500, L111
Way, M. J., Quintana, H., & Infante, L. 2000, preprint, astro-ph/9709036
White, D. A. 2000, MNRAS, 312, 663
White, D. A., & Fabian, A. C. 1995, MNRAS, 273, 72
White, D. A., Jones, C., & Forman, W. 1997, MNRAS, 292, 419
White, R. A., Bliton, M., Bhavsar, S. P., Bornmann, P., Burns, J. O., Ledlow, M. J., & Loken, C. 1999, AJ, 118, 2014
Wu, K. K. S., Fabian, A. C., & Nulsen, P. E. J. 2000, MNRAS, 318, 889
Wu, X., Xue, Y., & Fang, L. 1999, ApJ, 524, 22
Wu, X.-P., Fang, L.-Z., & Xu, W. 1998, A&A, 338, 813
Xu, H., Jin, G., & Wu, X. 2001, ApJ, 553, 78
Xu, H., Makishima, K., Fukazawa, Y., Ikebe, Y., Kikuchi, K., Ohashi, T., & Tamura, T. 1998, ApJ, 500, 738
Xue, Y., & Wu, X. 2000, ApJ, 538, 65
Yee, H. K. C., Ellingson, E., & Carlberg, R. G. 1996, ApJS, 102, 269
Yee, H. K. C., & López-Cruz, O. 1999, AJ, 117, 1985
Zabludoff, A. I., Huchra, J. P., & Geller, M. J. 1990, ApJS, 74, 1
Zabludoff, A. I., & Mulchaey, J. S. 1998, ApJ, 496, 39
Zaritsky, D., Nelson, A. E., Dalcanton, J. J., & Gonzalez, A. H. 1997, ApJ, 480, L91
Zwicky, F., Herzog, E., Karpowicz, M., Kowal, C. T., & Wild, P. 1961-1969, Catalogue of Galaxies and Clusters of Galaxies (Pasadena: Caltech)